universität wien

# DISSERTATION | DOCTORAL THESIS

Titel | Title

Statistically Learning Dispersed New Physics at the LHC

verfasst von | submitted by

Sahana Narasimha

angestrebter akademischer Grad | in partial fulfilment of the requirements for the degree of

Doktorin der Naturwissenschaften (Dr.rer.nat.)

Wien | Vienna, 2026

| | |
|---|---|
| Studienkennzahl lt. Studienblatt \| Degree programme code as it appears on the student record sheet: | UA 796 605 411 |
| Dissertationsgebiet lt. Studienblatt \| Field of study as it appears on the student record sheet: | Physik |
| Betreut von \| Supervisor: | Dipl.-Ing. Dr. Wolfgang Waltenberger Privatdoz. |

# Abstract

The quest for physics beyond the Standard Model is one of the primary goals of the Large Hadron Collider since its discovery of the Higgs Boson in 2012. Despite extensive experimental efforts, no clear evidence for new physics has emerged. Yet, we know that the Standard Model of particle physics is not the final description of nature. Fundamental questions such as the nature of dark matter and the origin of neutrino masses remain unanswered. Though numerous theoretical extensions to the Standard Model have been proposed, we are currently unsure which model would ultimately prevail.

This thesis presents a novel, data-driven, bottom-up approach to address this problem. Instead of testing specific theoretical models against experimental data, we develop a *statistical learning* algorithm that systematically searches for potential *dispersed signals*. Dispersed signals are defined as weak effects of new physics that manifest across multiple LHC analyses, which might be dismissed as statistical fluctuations when examined individually. The algorithm then constructs candidate *proto-models* that explain these mutually compatible dispersed signals across different signal regions while remaining consistent with all experimental constraints.

The methodology is inspired by model selection techniques from statistical literature and employs a random walk through the proto-model parameter space, stochastically adding or removing particles, and modifying their cross sections and branching ratios. This is coupled with a combinatorial algorithm that identifies sets of analyses and signal regions exhibiting maximum deviation from Standard Model predictions. Crucial to this approach is the construction of global likelihoods in proto-model parameter space, utilising both upper limit and efficiency map results from the SModelS database of simplified-model results mostly published by ATLAS and CMS experiments.

This thesis builds upon an initial proof-of-concept study that introduced this methodology and presents significant algorithmic improvements. These include enhanced statistical rigour through the implementation of Reversible Jump Markov Chain Monte Carlo principles, improved computational efficiency, and an expanded database of analyses incorporating recent LHC Run 2 results. We demonstrate the algorithm's capability to identify the potential dispersed signals in regions where traditional channel-by-channel searches may lack sensitivity, thus providing a complementary approach to the ongoing quest for new physics at the LHC.

# Kurzfassung

Die Suche nach Physik jenseits des Standardmodells ist eines der Hauptziele des Large Hadron Collider seit der Entdeckung des Higgs-Bosons im Jahr 2012. Trotz umfangreicher experimenteller Bemühungen sind bisher keine eindeutigen Hinweise auf neue Physik aufgetreten. Dennoch wissen wir, dass das Standardmodell der Teilchenphysik nicht die endgültige Beschreibung der Natur sein kann. Fundamentale Fragen wie die Natur der dunklen Materie und der Ursprung der Neutrinomassen bleiben unbeantwortet. Da zahlreiche theoretische Erweiterungen des Standardmodells vorgeschlagen wurden, ist derzeit unklar, welches Modell sich letztendlich durchsetzen wird. Diese Dissertation präsentiert einen neuartigen, datengetriebenen Bottom-up Ansatz zur Bewältigung dieses Problems: anstatt spezifische theoretische Modelle gegen experimentelle Daten zu testen, entwickelten wir einen *statistischen Lernalgorithmus*, der systematisch nach potenziellen *verteilten Signalen* sucht. Verteilte Signale sind hier definiert als schwache Effekte neuer Physik, die sich über mehrere LHC-Analysen manifestieren und bei isolierter Betrachtung zumeist als statistische Fluktuationen abgetan werden. Der Algorithmus konstruiert dann *Protomodelle*, die diese miteinander kompatiblen verteilten Signale über verschiedene Signalregionen hinweg erklären und gleichzeitig mit allen experimentellen Ausschlüssen konsistent bleiben.

Die Methodik ist von Modellauswahlverfahren aus der statistischen Literatur inspiriert und verwendet einen Random Walk durch den Parameterraum der Protomodelle, wobei stochastisch Teilchen hinzugefügt oder entfernt und ihre Wirkungsquerschnitte und Verzweigungsverhältnisse modifiziert werden. Dies ist mit einem kombinatorischen Algorithmus gekoppelt, der Sätze von Analysen und Signalregionen identifiziert, die maximale Abweichungen von den Vorhersagen des Standardmodells aufweisen. Entscheidend für diesen Ansatz ist die Konstruktion globaler Likelihoods im Parameterraum der Protomodelle, wobei sowohl Upper-Limit- als auch Efficiency-Maps aus der SModelS-Datenbank verwendet werden, die zumeist von ATLAS und CMS veröffentlicht wurden. Diese Dissertation baut auf einer ursprünglichen Machbarkeitsstudie auf, die diese Methodik einführte, und präsentiert signifikante algorithmische Verbesserungen. Dazu gehören ein rigoroserer Ansatz durch die Implementierung eines Reversible Jump Markov Chain Monte Carlo Algorithmus, verbesserte Recheneffizienz und eine erweiterte Datenbank von Analysen, die aktuelle Ergebnisse des LHC Run 2 miteinbezieht. Wir demonstrieren die Fähigkeit des Algorithmus, potenzielle verteilte Signale in Regionen zu identifizieren, in denen individuelle Suchen möglicherweise weniger sensitiv sind, und bieten somit einen komplementären, holistischeren Ansatz zur fortlaufenden Suche nach neuer Physik am LHC.

# Acknowledgements

I would first and foremost like to thank my supervisor, Wolfgang, without whom I would have had absolutely no idea how to approach this project. His trust and confidence in me and my work were always encouraging, even when I failed to meet some deadlines. I wish I could have spent more time developing this project further, but honestly I do not think I would have enjoyed it so much if not for him. I learned not only physics, but also about European (especially Austrian) history, languages, movies, and much more. His cheerfulness and good humour always brought a smile to my face, and I feel very lucky to have met such a wonderful professor. To me, he was the poster picture of the "absent-minded professor" I had only read about as a child, and seeing and working with one in real life has been truly delightful. Before this project, I had mainly worked on theoretical physics, and I always found statistics to be painful, something I simply could not wrap my head around. Thanks to Wolfgang's patience and willingness to explain concepts again (and again), I can now confidently say I am no longer intimidated by statistics. I have overcome my mental block with statistical concepts, and I have him to thank for that.

Second, I would like to thank Sabine for being my co-supervisor. I deeply appreciate her patience and constant guidance. Although I extended the writing of this thesis far longer than expected, she always managed to correct, push, and motivate me just when I needed it. I have always admired her sharp insights and ability to see the bigger picture. I am also very grateful for her hospitality when she hosted me in Grenoble. Although I struggled to keep up with her, whether during hikes or at work, it helped me realise how much I still have to learn. I would also like to thank André. Though our interactions were brief compared to the others, his incisive critiques and insights helped me refine this project considerably. I am also grateful to Timothée, Mohammad, Humberto, and Jamie and I would like to thank them for their support and friendship.

There are many others I would like to thank. First and foremost, my parents, without whose support I do not think I would have made it this far. Even though they have little idea what I actually do, they have always been eager to learn and incredibly supportive. Their confidence in me has given me immense faith in myself. I know I sometimes take it for granted, but when I reflect, I see how much they've given me. I hope they will continue to support my decisions in the future, even if they do not completely understand the paths I choose.

To the family I built here in Vienna: my friends Christina and Maryam, who joined MBI (then HEPHY) on the same day, and with whom I navigated the confusing corridors of the PSK building. We shared so many wonderful memories together, and the three years we spent flew by in what feels like an instant. They taught me how to adjust to the cold, introduced me to ice skating, and so much more. Mangesh, who

I later discovered attended the same university as I did back in India, helped me immensely in adjusting to Vienna. He never hesitated to help or reach out, even when I was distant. I am truly grateful for his friendship, it made adjusting to Vienna far easier. Kaan, with his quirky humor and unexpected remarks, always made discussions lively and fun. Garance and Stefan, with whom I navigated the puzzling bureaucracies of the University of Vienna, were always ready to discuss theoretical questions. Dorian and Niels, who joined later, also made these years memorable.

I also want to thank my flatmates, Ayah and Maias, who truly gave me a home away from home. Their kindness and generosity touched me deeply, and they cared for me in ways I never expected. I could not have asked for better flatmates. They respected my space while always being there when needed. They introduced me to wonderful Middle Eastern food and music, shared stories about their culture, and brought warmth even during the most stressful times.

To my friends back home, especially Varsha, Nafisa, Lakshmi, Praniti, Rishabh, and Lokamruth: even though I am terrible at keeping in touch, they have always looked out for me, pestering me to join on trips or simply to stay connected. Few friends would go to such lengths and I am grateful for them all.

Finally, I want to remember those I lost during this project: my grandparents and my dear friend Sugat, who left us far too soon. I hold fond and precious memories of them, each enriching my life in their own way. Life is short, and I have learned it is more important to appreciate its beauty than to be constantly weighed down by worries.

# Contents

**Abstract** iii

**Kurzfassung** v

**Acknowledgements** vii

**1 Introduction** 1

**2 The Standard Model and Beyond** 5
2.1 Historical Overview . . . 5
2.2 Theoretical Formulation of the Standard Model . . . 7
2.3 Shortcomings of the Standard Model . . . 10
2.4 Overview of BSM models . . . 13
2.4.1 Supersymmetry . . . 13
2.4.2 Extra Dimensional Models . . . 16
2.4.3 Composite Higgs . . . 17
2.4.4 Vector-like Fermions . . . 18
2.4.5 Leptoquarks . . . 19
2.5 Experimental Particle Physics at the LHC . . . 21

**3 Statistics for High Energy Physics** 27
3.1 Frequentist Approach . . . 27
3.1.1 Hypothesis testing . . . 28
3.2 Bayesian Inference . . . 31
3.2.1 Markov Chain Monte Carlo . . . 33
3.3 Model Selection . . . 34
3.3.1 Akaike Information Criterion . . . 35
3.3.2 Reversible Jump Markov Chain Monte Carlo . . . 36

**4 Reinterpretation of LHC results using SModelS** 39
4.1 Simplified Models . . . 39
4.2 SModelS: Working Principle . . . 41
4.2.1 Running SModelS . . . 46
4.3 Likelihood computation in SModelS . . . 48
4.3.1 Likelihood for individual SRs . . . 48
4.3.2 Likelihood for combined SRs . . . 49
4.3.3 Combining likelihoods of uncorrelated analyses . . . 51
4.4 Impact of combining analyses on the electroweakino sector of the MSSM 52
4.4.1 Parameter space . . . 53
4.4.2 Combination strategy . . . 55
4.4.3 Results . . . 57
4.5 Conclusion and Outlook . . . 59

**5 Artificial Proto-modelling: an Introduction** **63**
5.1 What is a Proto-model? . . . 64
5.1.1 Particle Spectrum . . . 65
5.1.2 Decay Channels and Branching Ratios . . . 66
5.1.3 Production cross sections . . . 67
5.2 Constructing likelihoods for proto-models . . . 67
5.3 Walker v1 . . . 68
5.4 Builder v1 . . . 69
5.5 Critic v1 . . . 71
5.6 Combiner v1 . . . 72
5.7 Results from v1 . . . 76
5.7.1 Fake database . . . 76
5.7.2 Real data . . . 77
5.8 Conclusions and Outlook . . . 81

**6 Artificial Proto-modelling v2** **83**
6.1 A look into the database . . . 84
6.2 Walker v2 . . . 88
6.3 Builder v2 . . . 92
6.3.1 Additions to the Proto-models Parameter Space . . . 92
6.3.2 Random changes to the proto-model . . . 94
6.3.3 Prior Distributions . . . 99
6.4 Combiner v2 . . . 100
6.5 Critic v2 . . . 103
6.5.1 Fast Critic . . . 104
6.5.2 Slow Critic . . . 105
6.6 Running the Proto-model framework . . . 106
6.7 Results . . . 107
6.7.1 Runs across fake SM Databases . . . 108
6.7.2 Runs across SModelS database v3.1.0 . . . 109
6.7.3 Closure tests . . . 120
6.7.4 Finding the global optimum . . . 121
6.8 Conclusions . . . 123

**7 Conclusions and Outlook** **127**

**A Neutralino and chargino masses** **131**

**B Complete list of analyses in the SModelS database v3.1.0** **133**

**C Combination Matrix** **137**
C.1 ATLAS 13 TeV . . . 137
C.2 CMS 13 TeV . . . 143

**Bibliography** **145**

# List of Abbreviations

| | |
|---|---|
| **AIC** | **A**kaike **I**nformation **C**riterion |
| **BSM** | **B**eyond the **S**tandard **M**odel |
| **CL** | **C**onfidence **L**evel |
| **DM** | **D**ark **M**atter |
| **EM** | **E**fficiency **M**ap |
| **KDE** | **K**ernel **D**ensity **E**stimate |
| **LBP** | **L**ightest **B**SM **P**article |
| **LHC** | **L**arge **H**adron **C**ollider |
| **LSP** | **L**ightest **S**upersymmetric **P**article |
| **MCMC** | **M**arkov **C**hain **M**onte **C**arlo |
| **MSSM** | **M**inimal **S**upersymmetric **S**tandard **M**odel |
| **RJMCMC** | **R**eversible **J**ump **M**arkov **C**hain **M**onte **C**arlo |
| **SM** | **S**tandard **M**odel |
| **SMS** | **S**implified **M**odel **S**pectra |
| **SR** | **S**ignal **R**egion |
| **SSM** | **S**ignal **S**trength **M**ultiplier |
| **SUSY** | **S**uper**s**y**y**mmetry |
| **UL** | **U**pper **L**imit |

# Chapter 1

# Introduction

The Standard Model (SM) of particle physics represents our most precise understanding of fundamental particles and their interactions to date. It has been established over decades of interplay between theoretical predictions and experimental observations. It has been remarkably successful in explaining the physics observed at experimental colliders and has been tested to a great degree of precision by various experiments. Despite its impressive predictive power, it is evident that the Standard Model is not the complete description of nature. Several fundamental questions remain unanswered: What is the nature of dark matter? What stabilizes the mass of the Higgs boson? These open questions clearly indicate that physics beyond the Standard Model (BSM) must exist. Despite numerous proposed theories beyond the Standard Model, we remain uncertain which, if any, will ultimately prevail.

The search for physics beyond the Standard Model has been one of the primary goals of the Large Hadron Collider (LHC) since the discovery of the Higgs boson in 2012. Traditional searches for new physics at the LHC are typically pursued on a channel-by-channel basis, and outcomes are often interpreted as limits on new physics parameters within the context of specific theoretical models. While this top-down approach has proven effective for testing well defined theories, it has a significant limitation: only a small fraction of the overall available data is utilized in any single analysis. Consequently, weak effects of new physics that manifest simultaneously across different final states or signal regions, which we term as *dispersed signals*, are easily missed or dismissed as statistical fluctuations when analysed in isolation. In the absence of clear signs of new physics in individual channels, and facing an ever-growing number of theoretical proposals, the task of mapping theoretical parameter space to experimental signatures has become increasingly challenging. Moreover, the wealth of experimental constraints from LHC Run 2 makes it crucial to develop methods that can leverage the full body of available data.

This thesis adopts an entirely new and more global approach to address this challenge. Rather than testing specific BSM theories against experimental data, we develop a *statistical learning* algorithm that systematically searches for potential dispersed signals across a collection of published LHC analyses. The goal is to construct candidate "proto-models", collections of simplified model components not constrained by higher-level theoretical assumptions, that explain small excesses in the data while remaining consistent with all other experimental constraints. This bottom-up methodology exploits SModelS [1–6], a public tool designed for fast reinterpretation of LHC searches based on simplified-model results. SModelS decomposes the signatures of full BSM scenarios into simplified-model components and confronts them against

a comprehensive database of experimental results from ATLAS and CMS. Recent enhancements enable the combination of approximately uncorrelated analyses, allowing for increased statistical robustness and the ability to probe different search channels simultaneously through a single, global likelihood.

While no $5\sigma$ discovery of BSM physics has been made since the Higgs boson, small excesses have been reported across multiple channels by different experimental collaborations. Intriguingly, some of these excesses appear in overlapping parameter spaces. These observations provide compelling motivation for our approach: by systematically identifying mutually consistent over-fluctuations across different search channels, we can construct proto-models that may reveal patterns of new physics hidden within the data. Should such patterns exist, we envisage the proto-models to act as a guide for future dedicated analyses and help unravel the concrete underlying BSM theory.

This thesis presents both the proof-of-concept implementation of the proto-model algorithm and significant improvements to the methodology. We demonstrate how this data-driven approach can identify interesting regions of parameter space where traditional channel-by-channel searches might overlook dispersed signals. Ultimately, we work towards a more complete understanding of what the LHC data tell us about potential new physics beyond the Standard Model.

This thesis is organised as follows. Chapter 2 introduces the Standard Model of particle physics, provides an overview of beyond the Standard Model theories, and concludes with a brief description of experimental particle physics at the LHC. Chapter 3 presents important statistical concepts typically used in experimental particle physics and introduces certain methodologies extensively used in this thesis. Chapter 4 introduces the SModelS v3 tool for reinterpretation of LHC experimental results and describes its statistical inference framework, concluding with a case study demonstrating the impact of combining experimental results on the electroweak-ino sector of the Minimal Supersymmetric Standard Model (MSSM). Chapter 5 introduces the bottom-up methodology for constructing proto-models as mentioned above and summarises the proof-of-concept study conducted in the paper [7]. Chapter 6 presents the new algorithmic developments and updated results.

As a complement, the thesis includes three appendices. Appendix A describes the neutralino and chargino mixing matrices in MSSM. Appendix B lists all the analyses implemented in the SModelS database v3.1.0; Appendix C details the construction of the combination matrices used in Chapter 6.

### My contributions

Within the SModelS collaboration, I contributed to extending the database of experimental results. I was extensively involved in implementing and validating new experimental analyses. In particular, I assisted in implementing and validating the first experimental search to use the Simplified Likelihood v2 [8] (presented in Section 4.3.2) for combination of signal regions and the first experimental search to be described by the graph based description in SModelS v3. For the study presented at the end of Chapter 4, I assisted in cross-validating the analysis combinations for the electroweak-ino parameter scan by integrating the PathFinder algorithm, which is subsequently utilized extensively in Chapter 6. Additionally, I helped identify and

resolve bugs in the statistical computation modules and assisted in debugging issues during the transition from SModelS v2 to v3.

My principal contributions of this thesis are presented in Chapter 6 and comprise the following key developments:

1. **Redesigning the algorithm structure:** Restructuring the algorithm flowchart to significantly improve computational efficiency throughout the iteration process.

2. **Improving the statistical inference:** Integration of Reversible Jump Markov Chain Monte Carlo (RJMCMC) methods to enhance the proposal distributions and prior distributions, and improve the acceptance criteria.

3. **Extending the proto-model parameter space:** Addition of off-shell decay modes for certain BSM particles to capture the new signatures implemented in the SModelS database v3.1.0.

4. **Validating across different parameter spaces:** Extensive testing of the algorithm across diverse scenarios to establish baseline expectations.

5. **Extending the combination matrix:** Extension of the analysis combination matrix to incorporate new experimental results from recent LHC Run 2 searches.

6. **Improving the search for the best combination:** Integration of the PathFinder algorithm into the proto-model algorithm to enable more efficient search for the best combination of experimental results.

While the proto-modelling algorithm is not a published tool so far, the code of the proto-model builder is publicly available at `https://github.com/SModelS/protomodels`.

In addition, the work of this thesis was also a part of the following publications, which will not be discussed in detail, as it is not the main topic of this thesis:

1. SModelS v2.3: Enabling global likelihood analyses, M. M. Altakach, S. Kraml, A.Lessa, **S. Narasimha**, T. Pascal, W. Waltenberger, SciPost Phys. 15 (5) (2023) 185. `doi:10.21468/SciPostPhys.15.5.185`, `arXiv:2306.17676`.

2. Global LHC constraints on electroweak-inos with SModelS v2.3, M. M. Altakach, S.Kraml, A. Lessa, **S. Narasimha**, T. Pascal, T. Reymermier, W. Waltenberger, SciPost Phys. 16 (2024) 101. `doi:10.21468/SciPostPhys.16.4.101`, `arXiv:2312.16635`.

3. SModelS v3: Going Beyond $\mathcal{Z}_2$ Topologies, M. M. Altakach, S. Kraml, A. Lessa, **S. Narasimha**, T. Pascal, C. Ramos, Y. Villamizar, W. Waltenberger. `doi:10.1007/JHEP11(2024)074`, `arXiv:2409.12942`

# Chapter 2

# The Standard Model and Beyond

The goal of modern particle physics is to understand how nature behaves at the most fundamental energy scales. This is not an easy task, as it requires knowledge of the interactions of the elementary particles of nature with one another, and the energy scales at which these interactions occur. Since the early 1900s, the scientific community has pursued increasingly sophisticated approaches to investigate these phenomena. Through the interplay of building theoretical models and experimental validation, physicists have been able to construct our current best description of the fundamental laws of nature with the Standard Model of particle physics. This model contains the set of presently known fundamental particles and the description of their interactions with one another. It has been tested to a great degree of precision and has been remarkably successful. However, certain unanswered questions and flaws persist. It is clear that the Standard Model is incomplete, and there should be some physics beyond the Standard Model that explains the inconsistencies and answer the remaining questions. Despite numerous theoretical efforts to construct BSM models that address the Standard Model's deficiencies, no experiment has yet provided a clear evidence for any new physics model. We may thus need to rely on empirical results to act as a guide for advancing theoretical understanding.

To understand what particle physics is working towards, it is illustrative to examine its current state and historical development. Section 2.1 provides a brief historical overview of the SM, tracing how theoretical predictions, experimental confirmations, and unexpected discoveries led to successive theoretical reformulations and expansions. We then present the mathematical formulation of the SM in Section 2.2, followed by a list of its shortcomings in Section 2.3. In Section 2.4, we explore certain BSM models that aim to address the limitations of the SM. Finally, we conclude with a brief description of experimental particle physics at the Large Hadron Collider in Section 2.5.

## 2.1 Historical Overview

Research into electromagnetic interactions began in the late 19th century with Thomson's discovery of the electron [9], the first known elementary particle. When Maxwell's wave theory of light describing it in terms of oscillating electric and magnetic fields [10] failed to explain certain experimental observations, Planck and later Einstein proposed that light energy comes in discrete, quantised packets called photons [11]. The particle nature of photons was confirmed experimentally through Compton scattering

experiments in 1932 [12]. By the mid-20th century, the development of Quantum Electrodynamics (QED) [13–15] provided a complete theoretical framework for describing electromagnetic interactions. In this theory, the photon was identified as a massless spin-1 particle (boson) that mediated the electromagnetic interactions between spin-1/2 particles (fermions) that carried an electric charge. QED was the first quantum field theory (QFT) to be based on the principle of a gauge symmetry $U(1)$ and had successfully accounted for apparent divergences by requiring the theory to be renormalizable.[1]

The study of weak interactions can be traced first to 1914 when it was observed that the energy spectrum of the electrons in $\beta$ decays was continuous, inconsistent with the assumption that only an electron is emitted in the decay [16]. In 1930, Pauli postulated the existence of the neutrino to explain the missing energy and angular momentum spectrum in $\beta$ decays [17], which was later confirmed in 1953 in reactor experiments. Fermi developed the first theoretical description of $\beta$ decay in 1933, modelling it as a four-fermion contact interaction [18, 19]. This theory could accurately describe weak interactions at low energies but failed at high energies above $O(100\ \text{GeV})$. The scalar interaction initially proposed by Fermi was later superseded by $V - A$ theory, which introduced spin-1 $W^{\pm}$ bosons as the mediators of weak interactions [20–22]. Inspired by QED's remarkable success at explaining electromagnetic interactions, physicists sought a renormalizable gauge theory for weak interactions as well. The first breakthrough came with Yang-Mills theories which extended the $U(1)$ gauge invariance to include local non-abelian (i.e. non-commuting) transformations such as $SU(2)$ [23]. In 1961, Glashow proposed an extended symmetry group $SU(2) \times U(1)$ to construct a unified gauge theory of electroweak interactions, and proposed 4 vector bosons to describe both the parity conserving (photon) and parity violating weak interactions ($W^{\pm}, Z$) [24]. In all the theories proposed, the gauge bosons were required to be massless in order for them to be renormalizable. However, the short-range nature of the weak interactions implied that the bosons that mediate this interaction must be very massive, as opposed to the massless photon mediating the long-range electromagnetic force. The apparent paradox was solved by the formulation of the "Higgs mechanism" [25–28] which incorporated the notion of spontaneous symmetry breaking [29] and was proven to be renormalizable [30]. In 1983, both the $W^{\pm}$ and the $Z$ bosons were discovered in the CERN collider, thus verifying the electroweak theory [31–34].

In parallel, theoretical understanding of strong interactions began with Yukawa's 1935 proposal that $\pi$-mesons (pions) mediate the force binding protons and neutrons together [35]. These particles were later detected in cosmic rays and produced at the Berkeley Cyclotron. However, the search for cosmic-ray pions led to an unexpected discovery in 1936, the muon, which was later identified to be the heavier version of the electron. The matter fields were then classified into leptons (electron, muon), mesons (pions) and baryons (protons, neutrons). The 1950s witnessed rapid development in experimental particle physics, revealing numerous particles that interacted through the strong force. To organize this "particle zoo", Gell-Mann arranged the observed particles into an octet pattern [36] and predicted the existence of the $\Omega^{-}$ particle, which was subsequently discovered at Brookhaven in 1963. The underlying structure of this octet representation inspired Gell-Mann [37] and Zweig [38] to independently propose in 1964 that all these particles were composed of fundamental

[1] A QFT is called renormalizable, if all infinities can be absorbed into a redefinition of a finite number of coupling constants and masses.

constituents called quarks. The Stanford Linear Accelerator (SLAC) confirmed the existence of quarks in 1968 by deep inelastic scattering experiments in which they bombarded protons with high-energy electrons. Greenberg introduced the concept of color charge for quarks [39] to resolve the apparent violation of Pauli's exclusion principle in particles like the $\Omega^-$ baryon, which contained three identical quarks. Following the discovery of muon and muon neutrino [40], the observed pattern in lepton families prompted Bjorken and Glashow to predict a fourth quark in 1964 [41], an idea that was further worked on by Glashow, Iliopoulos and Maiani [42] in 1970. The predicted "charm" quark was discovered in 1974 through the $J/\psi$ resonance, corresponding to a charm-containing meson [43, 44]. By 1973, Quantum Chromodynamics (QCD) was formulated as a quantum field theory that describes strong interactions, based on a $SU(3)$ gauge symmetry [45]. The strong interactions between quarks carrying the color charge is described via the exchange of color octet vector bosons, the massless gluons. The theory based on two generations of matter fields experienced problems with the experimental discovery of the tau lepton in 1975 [46], the bottom quark in 1977 [47, 48] and the unexpectedly heavy top quark in 1995 [49, 50]. The last particle of the third generation of matter fields, the tau neutrino, was discovered in 2000 [51].

The last major discovery came in 2012 [52, 53] with the observation of a particle that corresponds to the Higgs boson predicted by the Standard Model. This particle, hypothesized in 1964 to explain how massive particles acquire their mass, represents the physical manifestation of the Higgs mechanism discussed earlier. The discovery of the Higgs boson thus completed the Standard Model's theoretical framework by confirming the existence of the field responsible for spontaneous symmetry breaking.

This brief review of particle physics discoveries illustrates the crucial interplay between theoretical predictions and experimental verification. It is important to note that experimental observations have repeatedly challenged and refined theoretical frameworks. Given this rich history of unexpected experimental discoveries that have repeatedly surprised the theoretical community, it is reasonable to consider that our current understanding may still be incomplete, despite the apparent stability of recent decades. History demonstrates the patience required for such endeavours: the journey from theoretical prediction to experimental confirmation spanned 25 years for neutrinos, half a century for the Higgs boson, and a full century for gravitational waves.

## 2.2 Theoretical Formulation of the Standard Model

The Standard Model of particle physics is a renormalizable quantum field theory that is invariant under the local gauge symmetry $G_{SM}$ as given in Eq. (2.1), which is spontaneously broken:

$$G_{SM} = SU(3)_C \otimes SU(2)_L \otimes U(1)_Y \Rightarrow SU(3)_C \otimes U(1)_{EM}\,. \tag{2.1}$$

Each symmetry in the above equation is a group of field transformations under which the SM Lagrangian is invariant. Each symmetry group is associated with an interaction mediated by spin-1 particles called the bosons, while the matter content of the SM is constituted of spin-1/2 particles called the fermions. $SU(3)_C$ describes the strong interactions, where the subscript $C$ denotes the color charge of the interactions and are

mediated by the massless gluons. The $SU(2)_L \otimes U(1)_Y$ gauge group collectively describes the electroweak interactions mediated by the massive weak gauge bosons and the massless photon. The subscript $L$ implies that only left-chiral fermions interact via the weak force. Left-chiral fermions are described by the projection operator

$$P_L = \frac{1-\gamma_5}{2}\,, \tag{2.2}$$

where the operator $\gamma^5$ is the product of four Dirac matrices: $\gamma^5 = i\gamma^1\gamma^2\gamma^3\gamma^4$. Left-chiral fermions are doublets under $SU(2)_L$ whereas the right-chiral counterparts are singlets. $Y$ denotes the hypercharge of each multiplet and can be calculated from the relation $Q = T_3 + Y$, where $Q$ is the electric charge and $T_3$ is the third component of the weak isospin. Fermions can be further subdivided into particles that interact via the strong and electroweak forces (quarks) and particles that only interact via electroweak force (leptons). Each fermion has a specific representation under the three gauge groups in Eq. (2.1). The spontaneous breaking of the electroweak group $SU(2)_L \otimes U(1)_Y$ to the electromagnetic subgroup $U(1)_{EM}$ gives rise to the scalar field – the Higgs field – which generates the masses of the weak gauge bosons and the fermions. The complex scalar Higgs field is a $SU(2)_L$ doublet and color singlet. The field content of the SM along with their transformations under $G_{SM}$ is summarized in Table 2.1.

| **Name** | **Symbol** | $SU(3)_C$, $SU(2)_L$, $U(1)_Y$ |
|---|---|---|
| Quarks | $Q = (u_L\ d_L)^T$ | $(\mathbf{3},\mathbf{2},\frac{1}{6})$ |
| | $u_R$ | $(\mathbf{3},\mathbf{1},\frac{2}{3})$ |
| | $d_R$ | $(\mathbf{3},\mathbf{1},-\frac{1}{3})$ |
| Leptons | $L = (\nu_L\ e_L)^T$ | $(\mathbf{1},\mathbf{2},-\frac{1}{2})$ |
| | $e_R$ | $(\mathbf{1},\mathbf{1},-1)$ |
| Gluon | $G$ | $(\mathbf{8},\mathbf{1},0)$ |
| $W$ boson | $(W^1\ W^2\ W^3)^T$ | $(\mathbf{1},\mathbf{3},0)$ |
| $B$ boson | $B$ | $(\mathbf{1},\mathbf{1},0)$ |
| Higgs | $H = (\phi^+\ \phi^0)^T$ | $(\mathbf{1},\mathbf{2},\frac{1}{2})$ |

TABLE 2.1: Field content of the Standard Model and their gauge quantum numbers. There are three generations (families) of quarks and leptons, differing by their mass.

We can thus write the SM Lagrangian that contains the fermionic and bosonic degrees of freedom that is invariant under the symmetry in Eq. (2.1):

$$\mathcal{L} = -\frac{1}{4}(F^a_{\mu\nu})^2 + \bar{\psi}(i\not{D})\psi - |D_\mu H|^2 + y_{ij}\bar{\psi}_i\psi_j H - V(H)\,. \tag{2.3}$$

Here, the first term constitutes the field strength tensors $F^a_{\mu\nu}$ and describes the propagation and self-interaction of the gauge bosons. The second term is the kinetic term for all the fermions and the third term describes the kinetic term for the Higgs field $H$. The fourth term describes the Yukawa interactions which connect all fermions to

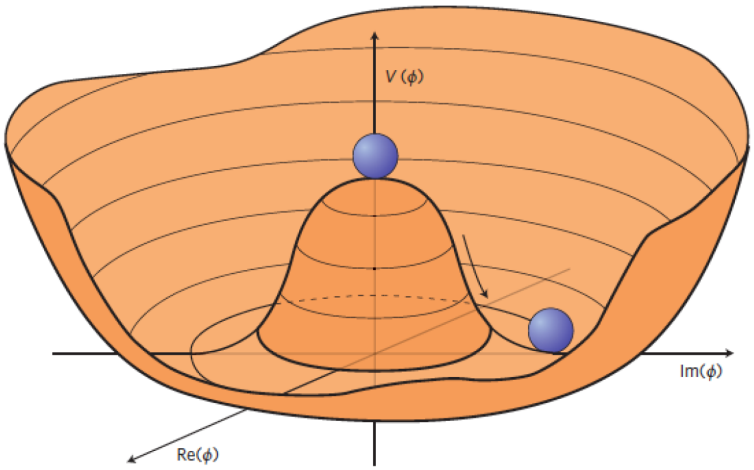


FIGURE 2.1: The Higgs potential described in Eq. (2.4) in the case that $\mu^2 < 0$ [54]

one another via the Higgs scalar field and the Yukawa couplings $y_{ij}$, where $i$ and $j$ represent different fermion generations. The last term gives the Higgs scalar potential

$$V(H) = \mu^2 H^\dagger H + \lambda (H^\dagger H)^2 , \tag{2.4}$$

where $\mu$ and $\lambda$ are parameters that determine the shape of the Higgs potential. This Lagrangian provides our best understanding of the fundamental particles and their interactions.

The electrically charged fermions and the electroweak gauge bosons acquire their masses through the Higgs mechanism, which spontaneously breaks the $SU(2)_L \otimes U(1)_Y$. To realise this, we require the parameters in the Higgs potential in Eq. (2.4) to be $\mu^2 < 0$ and $\lambda > 0$. The resulting scalar potential has a mexican-hat shape, as shown in Figure 2.1. Before the electroweak symmetry breaking, the Higgs field sits at the origin which is symmetric in the weak isospin space, but not the minimum. The minimum of the Higgs potential lies at $-\mu^2/2\lambda \equiv v^2/2$, where we define $v$ as the vacuum expectation value (vev) of the Higgs field. In order for the photon to remain massless, we can choose to give a vev to the electrically neutral scalar component:

$$\langle H \rangle = \begin{pmatrix} 0 \\ \frac{v}{\sqrt{2}} \end{pmatrix} . \tag{2.5}$$

When the Higgs field sits at the minimum of the potential, it acquires a vev and thus is no longer invariant under the electroweak interactions and breaks the electroweak symmetry. We can describe the system as fluctuations around the minimum:

$$H(x) = e^{-ig\theta_i \sigma^i/2} \begin{pmatrix} 0 \\ v + h(x) \end{pmatrix} . \tag{2.6}$$

Here, $g$ is the $SU(2)_L$ coupling constant, $\theta$ corresponds to the degrees of freedom associated to Nambu-Goldstone bosons, $\sigma$ the Pauli matrices and $h$ is a real scalar field

corresponding to the physical massive Higgs state. Substituting Eq. (2.6) in the kinetic term for the Higgs boson in the SM Lagrangian generates the mass terms for three of the electroweak gauge bosons, the charged $W^{\pm}$ and the neutral $Z$ boson:

$$M_W^2 = \frac{g^2 v^2}{4}, \quad M_Z^2 = \frac{(g^2 + g'^2)v^2}{4} = \frac{M_W^2}{\cos^2\theta_W}, \tag{2.7}$$

where $\theta_W$ is the Weinberg angle that parameterises the mixing between the $W^3$ and $B$ gauge eigenstates of $SU(2)_L \times U(1)_Y$ giving rise to the photon and $Z$ mass eigenstates. $g'$ is the $U(1)_Y$ coupling constant.

We obtain the mass terms for the fermions through the Yukawa interaction term after the electroweak symmetry breaking. Diagonalizing the matrix of coupling constants $y_{ij}$, we find

$$m_{f,i} = \frac{y_i v}{\sqrt{2}}, \tag{2.8}$$

with $f = u, d, e$ corresponding to the fermion flavor and $i = 1, 2, 3$ corresponding to the mass generations. With massless neutrinos, it suffices to take the charged leptons mass matrices as diagonal. However, two distinct sets of unitary matrices, $V_{u,d}$, are required to diagonalize the Yukawa matrices for the up- and down-type quarks. This difference leads to the flavor changing nature of the charged current interactions, described by the Cabbibo-Kobayashi-Maskawa (CKM) matrix $V_{CKM} = V_L^u V_L^{d\dagger}$. This $3 \times 3$ unitary matrix is parameterised by three mixing angles and a complex phase which characterizes weak $CP$-violation.

The SM has a total of 19 free parameters: the nine charged fermion masses, the three mixing angles and the $CP$-violating phase of the CKM matrix, the three gauge couplings, $\mu^2$ and $\lambda$ from the Higgs potential, and the $CP$-violating vacuum angle of the strong interaction.

## 2.3 Shortcomings of the Standard Model

Although the SM has a strong theoretical foundation and has been experimentally verified to a great degree of precision, certain flaws still persist. Experimental observations and theoretical considerations motivate us to look for physics beyond the Standard Model (BSM).

#### Neutrino masses

The Higgs mechanism gives us a procedure to generate masses for electrically charged leptons through the Yukawa interaction terms. Neutrinos do not get masses through this mechanism and thus remain massless in the SM. However, recent experimental observations point to small but non-negligible masses for neutrinos via neutrino oscillations [55–57]. The mechanism that gives this mass is still unclear and is a subject of current research. Adding a Yukawa interaction term to the SM Lagrangian such that the neutrinos acquire a mass via the Higgs mechanism requires the introduction of right–handed neutrinos. This points to certain BSM physics. So far, there has been no conclusive evidence for right–handed neutrinos. Neutrino masses could also be

explained if they are Majorana fermions. A Majorana fermion is its own antiparticle, in contrast to the Dirac fermions of the SM, which are distinct from their antiparticles. To confirm the Majorana nature of the neutrinos, we would need to experimentally detect neutrino-less double–beta decay [58] which has not yet been observed.

### Dark Matter

The SM fails to provide a candidate for an invisible and hypothetical form of matter, commonly known as Dark Matter (DM), that has been observed in the Milky Way and in the Universe at large scale. Initial evidence for this type of matter emerged from studies of galactic dynamics, where the gravitational effects observed could not be explained by visible matter alone [59]. This led to hypothesizing the existence of a type of matter that interacts gravitationally but is invisible to electromagnetic radiation. This hypothesis was strengthened later by the observations of galaxy rotation curves [60–63]. With increasing distance from the center of the galaxy $r$, one expected the velocity of a star to drop as $1/\sqrt{r}$. However, observations pointed to a constant velocity distribution at large distances from the center, as shown in Figure 2.2. This discrepancy could be explained by the presence of an invisible massive matter.

Further observations from gravitational lensing measurements give more credence to the presence of dark matter. Today, observations indicate that DM accounts for approximately 84% of all matter in the universe. Explanation for a particle-like nature of dark matter requires us to go beyond the SM, as there is no appropriate candidate for a dark matter particle within the SM.

Though the abundance of DM in the universe has been determined, most properties of DM are still unclear. All current evidence for DM stems from gravitational effects alone. We can infer that dark matter must be stable (or at least extremely long-lived), weakly self-interacting, electrically neutral, and cold, i.e. behaves non-relativistically at temperatures around the keV scale. Theoretical models propose a wide range for DM masses, spanning from $10^{-22}$eV up to the Planck mass.

### Dark Energy

Astronomers in the 1920s observed that nearby galaxies recede from us at velocities proportional to their distances – a first evidence for the expanding nature of the universe. Subsequent observations revealed that this expansion is actually accelerating. Through the measurements of explosions of white dwarfs called Type 1a supernovae [64, 65], scientists proposed the existence of dark energy in 1998. This accelerating expansion implied the existence of an unknown force that counteracts the effect of gravity.

Dark energy was conceived as a homogeneous field that has the effect of a negative pressure pushing space outward. The standard cosmological model, called the Lambda Cold Dark Matter ($\Lambda$CDM) model, provides an explanation of most cosmological observations by including ordinary matter, cold dark matter (CDM), and dark energy by harnessing the lambda parameter, a simple global constant in General Relativity (GR). However, recent findings from the Dark Energy Spectroscopic Instrument (DESI) suggest a deviation from the $\Lambda$CDM model and hint at an evolving dark energy [66].

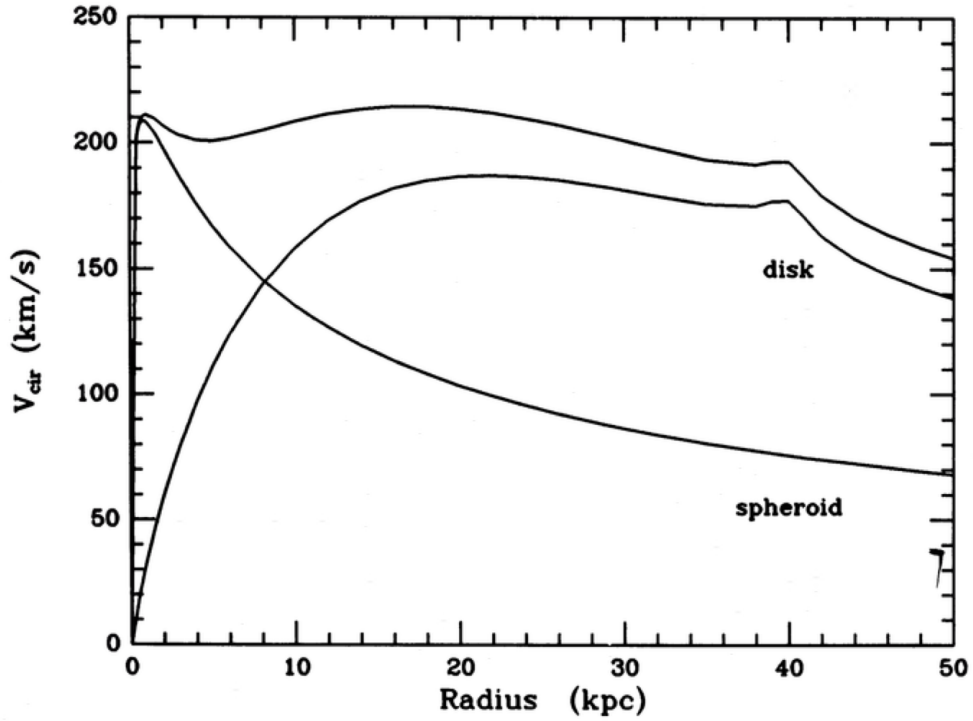


FIGURE 2.2: Distribution of the star velocities in the galaxy NGC 3198 with respect to the distance from the centre of the same galaxy [63].

Its true nature, however, remains a mystery, neither explained by the Standard Model of cosmology nor by the Standard Model of particle physics. This theoretical gap has motivated numerous proposals for modified gravity theories that attempt to explain dark matter and dark energy observations through alterations to gravitational physics alone, though none have achieved definitive success.

**Hierarchy Problem**

The absence of an explanation for gravitational interaction means that the SM is only valid below the (reduced) Planck scale $M_P \approx 2.4 \times 10^{18}$ GeV. The Planck scale is the energy scale at which quantum corrections to gravitational effects become dominant and a quantum theory of gravity is required, which is currently non-existent.

The high energy scale for gravity is puzzling given the characteristic energy scales for interactions in the SM. The running of the strong coupling determines its characteristic scale at 200 MeV, which is also the mass of the hadrons made of light quarks. The electroweak scale is an order of magnitude higher, at the Higgs vev of 246 GeV, similar to the masses of the Higgs, W and Z bosons. The existence of a "gauge desert", i.e. no emergent scales between the electroweak and gravitational forces, seems largely unnatural. This apparent hierarchy of different gauge strengths remains an open theoretical question today and is often referred to as the Hierarchy Problem. Even if we accept this unnatural hierarchy, the stability of it is under question in the context of quadratically divergent corrections to the Higgs Mass, as discussed in the next subsection.

**Higgs Mass**

The tree-level SM Higgs mass is a free parameter, measured to be around 125 GeV. Quantum corrections to the squared mass of the Higgs stem from loop Feynman diagrams in the Higgs propagator, which grow at most logarithmically in $\Lambda_{UV}$, where $\Lambda_{UV}$ represents the cut-off scale up to which the SM is valid. The Higgs mass is therefore heavily dependent on the scale of new physics. If we set this to the Planck scale, it is clear that the squared mass of the Higgs should be around 30 orders of magnitude larger than the observed value. Thus, an enormous fine-tuning is required for the radiative corrections to cancel each other almost completely without invoking new physics below the Planck scale. In order to avoid fine-tuning, all the solutions to the hierarchy problem require new physics at a rather low energy scale (not far from the EW scale). This is by far the strongest argument in favour of new physics at the TeV scale.

## 2.4 Overview of BSM models

### 2.4.1 Supersymmetry

Supersymmetry (SUSY) is an internal symmetry that relates fermionic states to bosonic states and vice versa. The single-particle states of SUSY fall into groups called supermultiplets where each supermultiplet contains an equal number of boson and fermion degrees of freedom. One of the primary motivations for SUSY is that it provides a solution to the hierarchy problem. This symmetry protects the Higgs mass from receiving large corrections, as each fermionic (bosonic) contribution gets cancelled by a contribution with opposite sign from the corresponding bosonic (fermionic) degrees of freedom.

If SUSY were an exact symmetry of nature, the masses of the superpartners would be, in principle, the same as their SM counterparts. However, no such particles have been discovered by experiments at colliders or elsewhere. SUSY must therefore be a broken symmetry with superpartner masses heavier than current SM particles. This breaking of SUSY must be "soft", meaning that the Lagrangian can be written as

$$\mathcal{L} = \mathcal{L}_{\text{SUSY}} + \mathcal{L}_{\text{soft}}\,, \tag{2.9}$$

where $\mathcal{L}_{\text{SUSY}}$ preserves supersymmetry invariance and $\mathcal{L}_{\text{soft}}$ breaks supersymmetry. This soft breaking does not change the dimensionless terms in the Lagrangian and only logarithmic divergences are introduced for the squared mass of the Higgs ($m_h^2$), thus still providing a solution to the hierarchy problem. There are many proposed SUSY extensions to the SM. The one that introduces the smallest number of particles while still giving a reasonable solution to the hierarchy problem is the Minimal Supersymmetric extension of the Standard Model (MSSM) [67–69]. Due to its relative simplicity, the MSSM serves as a useful benchmark. The following discussion of MSSM is based on [70].

Within the MSSM, there are two types of supermultiplets: (a) a *chiral* supermultiplet which combines a two-component Weyl fermion and a complex scalar field and (b) a

*gauge* supermultiplet that combines spin-1/2 Weyl fermionic partners, called gauginos, with the spin-1 gauge bosons which share the same gauge transformation properties. The SM fermions reside in the chiral supermultiplet since their left- and right-handed parts transform differently under the gauge groups. Thus, the bosonic partners of quarks and leptons are spin-0, and not spin-1 vector bosons. Since the Higgs boson is a scalar field, it resides in a chiral supermultiplet. However, this implies that the complex conjugates belong to multiplets of opposite chirality. Thus, a single Higgs doublet cannot give mass simultaneously to up- and down-type quarks, as multiplets of different chiralities cannot couple together in a supersymmetric model. Additionally, since scalars sit in chiral multiplets together with spin-1/2 fields, the cancellation of anomalies requires the presence of an additional doublet. The vector bosons of the SM reside in gauge supermultiplets with their fermionic superpartners. Table 2.2 summarizes the particle content of the MSSM.

| Names | | Spin-0 | Spin-1/2 | Spin-1 | $SU(3)_C, SU(2)_L, U(1)_Y$ |
|---|---|---|---|---|---|
| Chiral Supermultiplets | | | | | |
| squarks, quarks (×3 families) | $\widehat{Q}$ | $\widetilde{Q} = (\widetilde{u}_L\ \widetilde{d}_L)$ | $(u_L\ d_L)$ | | $(\mathbf{3}, \mathbf{2}, \frac{1}{6})$ |
| | $\widehat{u}$ | $\widetilde{u}_R^*$ | $u_R^\dagger$ | | $(\mathbf{3}, \mathbf{1}, -\frac{2}{3})$ |
| | $\widehat{d}$ | $\widetilde{d}_R^*$ | $d_R^\dagger$ | | $(\mathbf{3}, \mathbf{1}, \frac{1}{3})$ |
| sleptons, leptons (×3 families) | $\widehat{L}$ | $\widetilde{L} = (\widetilde{\nu}_{eL}\ \widetilde{e}_L)$ | $(\nu_{eL}\ e_L)$ | | $(\mathbf{1}, \mathbf{2}, -\frac{1}{2})$ |
| | $\widehat{e}$ | $\widetilde{e}_R^*$ | $e_R$ | | $(\mathbf{1}, \mathbf{1}, 1)$ |
| Higgs, higgsinos | $\widehat{H}_u$ | $H_u = (H_u^+\ H_u^0)$ | $(\widetilde{H}_u^+\ \widetilde{H}_u^0)$ | | $(\mathbf{1}, \mathbf{2}, \frac{1}{2})$ |
| | $\widehat{H}_d$ | $H_d = (H_d^0\ H_d^-)$ | $(\widetilde{H}_d^0\ \widetilde{H}_d^-)$ | | $(\mathbf{1}, \mathbf{2}, -\frac{1}{2})$ |
| Gauge Supermultiplets | | | | | |
| gluino, gluon | | | $\widetilde{g}$ | $g$ | $(\mathbf{8}, \mathbf{1}, 0)$ |
| winos, W bosons | | | $\widetilde{W}^\pm\ \widetilde{W}^0$ | $W^\pm\ W^0$ | $(\mathbf{1}, \mathbf{3}, 0)$ |
| bino, B boson | | | $\widetilde{B}$ | $B$ | $(\mathbf{1}, \mathbf{1}, 0)$ |

TABLE 2.2: Particle content of the MSSM. The particles that are new compared to the SM are written in blue. The rows are organised in supermultiplets. For chiral supermultiplets, a symbol representing the whole supermultiplet is denoted in the "Names" column. Adapted from [70].

The superpotential of the MSSM is given by

$$\mathcal{W} = \mu \hat{H}_u \hat{H}_d + \mathbf{y}_u \epsilon_{ab} \hat{Q}^a \hat{H}_u^b \hat{U}^c + \mathbf{y}_d \hat{Q} \hat{H}_d \hat{D}^c + \mathbf{y}_e \hat{L} \hat{H}_d \hat{E}^c\,, \tag{2.10}$$

where the chiral superfields are given in Table 2.2, $\mathbf{y}_u, \mathbf{y}_d, \mathbf{y}_e$ are $3 \times 3$ matrices and $\mu$ is a mass parameter for the Higgs superfield, determining the higgsino mass. Certain terms that violate baryon ($B$) and lepton ($L$) numbers have been omitted from the superpotential as they are strongly constrained by experiments, in particular through the non-observation of proton decay. These terms can be forbidden by introducing a new discrete symmetry, $R$-parity, defined as

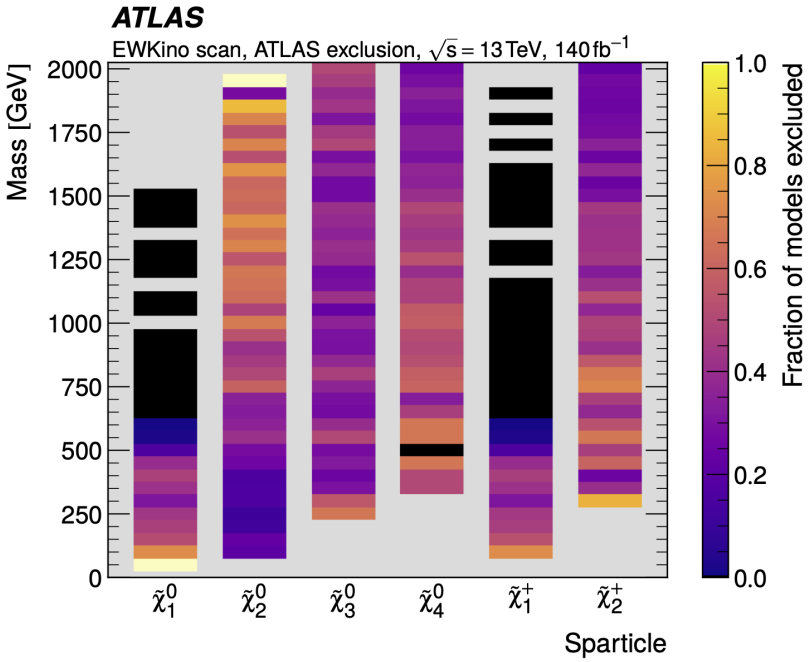


FIGURE 2.3: Fraction of pMSSM electroweakino model points excluded by ATLAS across the masses of each electroweakino particle. Figure adapted from [71].

$$R = (-1)^{3(B-L)+2s}, \tag{2.11}$$

where $s$ is the particle spin. It follows that all SM particles and the Higgs boson are even ($R = 1$), while their superpartners are odd ($R = -1$) under this parity. Invariance of $R$-parity is of great experimental relevance since it implies that all superpartner fields must be produced in pairs and decay to states, at least one of which must be a $R$-parity odd particle. This in turn implies that the lightest supersymmetric particle (LSP) must be absolutely stable.

The superpartners listed in Table 2.2 are not necessarily the mass eigenstates of the theory. Once electroweak symmetry breaking and supersymmetry breaking effects are incorporated, mixing occurs between the electroweak gauginos and the higgsinos, and within the various sets of squarks and sleptons and Higgs scalars that have the same electric charge. The gluino is the lone exception, as it lacks the appropriate quantum numbers to mix with other particles. The neutral electroweak components – comprising the bino, wino, and higgsino fields – undergo mixing to produce four mass ordered states called the neutralinos ($\tilde{\chi}^0_{1,2,3,4}$). Similarly, the charged electroweak states of the wino and the higgsino sectors mix to create two mass ordered states called the charginos ($\tilde{\chi}^\pm_{1,2}$). Mixing also occurs in the sfermion sector, where the left- and right-chiral flavour states $\tilde{f}_L$ and $\tilde{f}_R$ combine to form mass ordered states $\tilde{f}_1$ and $\tilde{f}_2$. For the first two generations, this mixing is typically negligible, allowing the mass eigenstates to coincide with the flavor eigenstates. Mixing of the third generation sfermions is not usually neglected, resulting in mass eigenstates that differ from their corresponding flavor eigenstates.

The MSSM introduces over 100 new *free* parameters, making it difficult to constrain in

the absence of specific evidence for supersymmetry. Therefore, we often simplify the MSSM model space to phenomenologically relevant parts. A popular version of a simplified but phenomenologically rich model is the phenomenological MSSM (pMSSM) [72]. The pMSSM reduces the number of new parameter to 19. The ATLAS collaboration recently presented a summary of constraints from searches for electroweak production of charginos and neutralinos interpreted within the pMSSM, see [71].

### 2.4.2 Extra Dimensional Models

Models with Large Extra Dimensions (LED) have been postulated to explain the large difference between the electroweak unification scale and the Planck scale. In such models, the Planck scale $M_P$ is not regarded as a fundamental scale, but can arise from the electroweak scale by considering that gravity propagates in $n$ extra compact spatial dimensions. Arkani-Hamed, Dimopoulos, and Dvali proposed the ADD model of LED [73] as a solution for the hierarchy problem. The model proposes that our universe, with its four dimensions (three spatial plus time), exists on a membrane within a higher-dimensional space. The Standard Model particles and gauge interactions (electromagnetic force, strong interaction, and weak interaction) are confined to this membrane and operate within the ordinary 3+1 space-time dimensions, while gravity, mediated by the hypothetical graviton, can propagate across the extra dimensions. The strength of the gravitational force in 3 + 1 dimensions is effectively weakened.

In the ADD framework, the Planck scale $M_P$ is not a fundamental scale, but instead is a consequence of the large size of new dimensions. The Planck scale in 4 dimensions can be explained via the presence of $n$ extra dimensions of size $R$ and the Planck scale in $4+n$ dimensions by $M_P^2 \sim M_D^{2+n} R^n$, where $M_D$ represents the Planck scale of the $4+n$ dimensional theory. The hierarchy problem is resolved by appropriately selecting the compactification radius $R$ such that it reproduces the observed four-dimensional Planck scale $M_P$ while simultaneously constraining the effective Planck scale $M_D \sim m_{EW}$. Unlike many exotic extra dimensional theories that involve relevant scales around the Planck scale, the ADD model features dimension sizes on the order of the TeV scale, making it experimentally accessible to current collider experiments. The fields that propagate in this $(4+n)$ dimensional bulk are the $(4+n)$ dimensional graviton. If produced in high-energy proton–proton collisions in association with a jet of hadrons, this graviton can escape undetected into the extra dimensions and its presence can be inferred from $E_T^{\text{miss}}$. For recent constraints on ADD models in monojet and monophoton channels, see [74, 75].

While the ADD model does address the hierarchy between the electroweak scale and the Planck scale, it introduces a new hierarchy between the compactification scale $(1/R)$ which is much smaller than the electroweak scale. This was noted by Randall and Sundrum who then proposed a distinct higher dimensional scenario [76]. In Randall–Sundrum models (RS) (also called 5-dimensional warped geometry theory) the four-dimensional metric is not factorisable, but instead is scaled by a "warp" factor that rapidly changes as a function of an additional dimension:

$$ds^2 = e^{-2kr_c\phi}\,\eta_{\mu\nu}\,dx^\mu dx^\nu + r_c^2 d\phi^2\,. \tag{2.12}$$

Here $k$ is a scale of the order of the Planck scale, $x^\mu$ are the four-dimensional coordinates, $0 \leq \phi \leq \pi$ is the coordinate for an extra dimension, and $r_c$ sets the size of this extra dimension. In this framework, four-dimensional mass scales are connected to

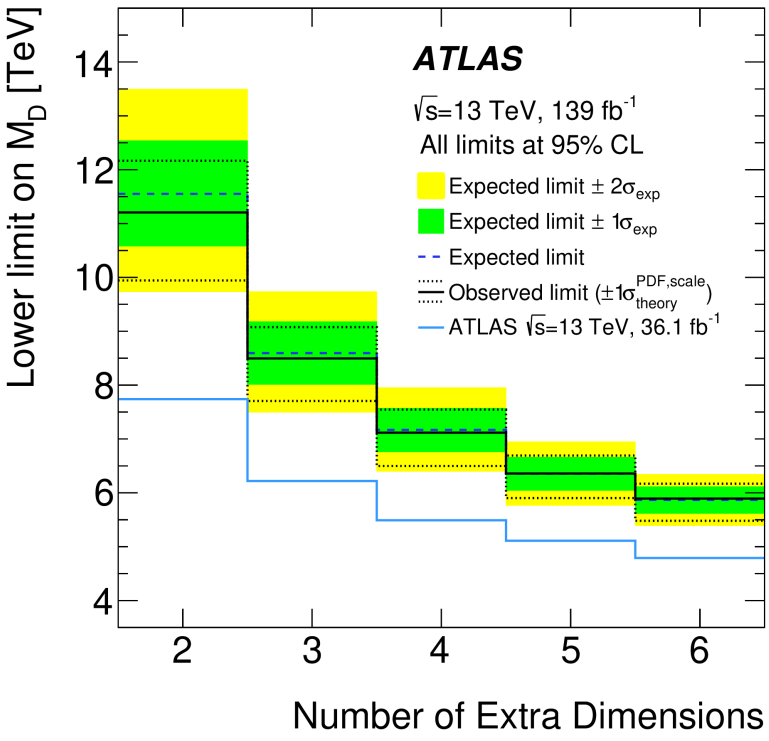


FIGURE 2.4: 95% CL lower limits on the fundamental Planck scale in $4+n$ dimensions, $M_D$, as a function of the number of extra dimensions. Figure adapted from [74].

five-dimensional input mass parameters through the warp factor, $e^{-2kr_c\phi}$. The model does not need extremely large values of $r_c$ to produce the observed large hierarchy between scales. This is because the hierarchy arises from an exponential function of the compactification radius. The small exponential factor shown above can generate the large hierarchy between the observed Planck and weak scales. One distinct prediction of the model, which provides a way to test its validity, is the prediction of a tower of TeV-scale excitations with spin-2, called Kaluza-Klein states, that could be observed in high energy experiments.

### 2.4.3 Composite Higgs

An alternative non-supersymmetric approach to confronting the hierarchy problem is the idea that the Higgs boson is in a composite state arising from a new strongly interacting sector. Here, the Higgs is thought to be a composite object with a compositeness scale (or geometric size) of TeV order. This scenario is historically inspired by QCD for its ability to explain the chiral symmetry and its breaking at low energies. The low energy spectrum of QCD contains scalars with $m \sim \text{GeV} \ll M_{Planck}$ without running into the hierarchy problem, as quantum corrections to composite state masses are naturally cut off at the confinement scale of approximately 1 GeV.

Initial insights regarding a composite Higgs boson that could be lighter than other resonances were first given by Georgi and Kaplan [77]. Current composite Higgs scenarios assume the existence of a strongly coupled sector with a global symmetry larger than the SM gauge group. These theories propose that the Higgs is not merely any composite state from strong dynamics, but specifically a pseudo-Nambu-Goldstone

boson that appears upon spontaneous breaking of approximate global symmetries [78, 79]. In this framework, a new composite sector is described by a global symmetry group $G$ that interacts weakly with the elementary sector (fermions and gauge bosons of the Standard Model). We them spontaneously break this global symmetry $G$ to a subgroup $H$ containing at least the $SU(2)$ doublet necessary to describe the SM type Higgs boson. The Higgs boson thus can be thought of as a pseudo-Nambu-Goldstone boson whose mass is controlled by this breaking mechanism. As a pseudo-Goldstone boson, the Higgs can be naturally light and, in particular, lighter than other new bound states in the theory. The minimal framework to achieve successful electroweak symmetry breaking, resulting in a Higgs doublet of $SU(2)_L$ with the observed Higgs mass, can be described by the symmetry breaking pattern $SO(5) \rightarrow SO(4)$ [78].

Fermion mass generation in composite Higgs models operates through the mechanism of partial compositeness [80], which replaces the direct SM Yukawa couplings with linear mixing between elementary fermions and heavy composite partners. In this scenario, the physical fermion states are linear superpositions of elementary and composite degrees of freedom, where the masses of the composite partners arise from confinement in the strong sector and must be vector-like (having the same quantum numbers for both chiralities) to allow Dirac mass terms. The hierarchy in quark masses emerges naturally as a consequence of varying degrees of partial compositeness: light quark masses result from tiny compositeness fractions, while larger fractions give rise to the large Yukawa coupling observed for the top quark. Since the Higgs mass is related to the mass of these heavy resonances, the framework provides an upper bound on partner masses, with typical models requiring top partners to have masses around 1 TeV [81], making these scenarios potentially accessible to current and future collider experiments. The impact of LHC Run 2 data on CHM scenarios is summarised in [82].

### 2.4.4 Vector-like Fermions

Vector-like fermions are hypothetical particles whose left- and right-handed components transform in the same way under the weak-isospin $SU(2)$ symmetry group [83–86]. Thus, a mass term in the Lagrangian that couples the left- and right-handed components – $\bar{\psi}_L \psi_R$ – is not forbidden by any symmetry. This implies that their mass need not be generated by the SM Higgs mechanism, and they are thus not constrained by electroweak precision data. They are the simplest possible extensions to the SM which can have mass close to the electroweak scale. Further, additions of one or more vector-like families to the SM may provide a dark matter candidate [87–90], and also explain the mass hierarchy between different generations of particles in the SM via mixings with SM fermions [91, 92].

Vector-like Quarks (VLQ) can be realised in composite Higgs models [78, 93] that propose a new strongly interacting sector to break the electroweak symmetry. VLQs may be produced at the LHC either in pairs or singly, along with a third generation quark and a light jet. The most prominent such searches have been for top-partners $T$ decaying via $Zt$, $Ht$, and $Wb$. The primary pair-production mechanisms involve gluon-gluon fusion and quark-antiquark annihilation, leading to the creation of VLQ pairs. The production cross-sections for such processes are highly dependent on the VLQ mass, with minimal dependence on their couplings or decay modes. Single production of VLQs occurs via EW interactions and is highly sensitive to the specific couplings between VLQs and SM quarks. So far, no evidence for these particles have been found and lower limits on their masses above the TeV scale have been placed by

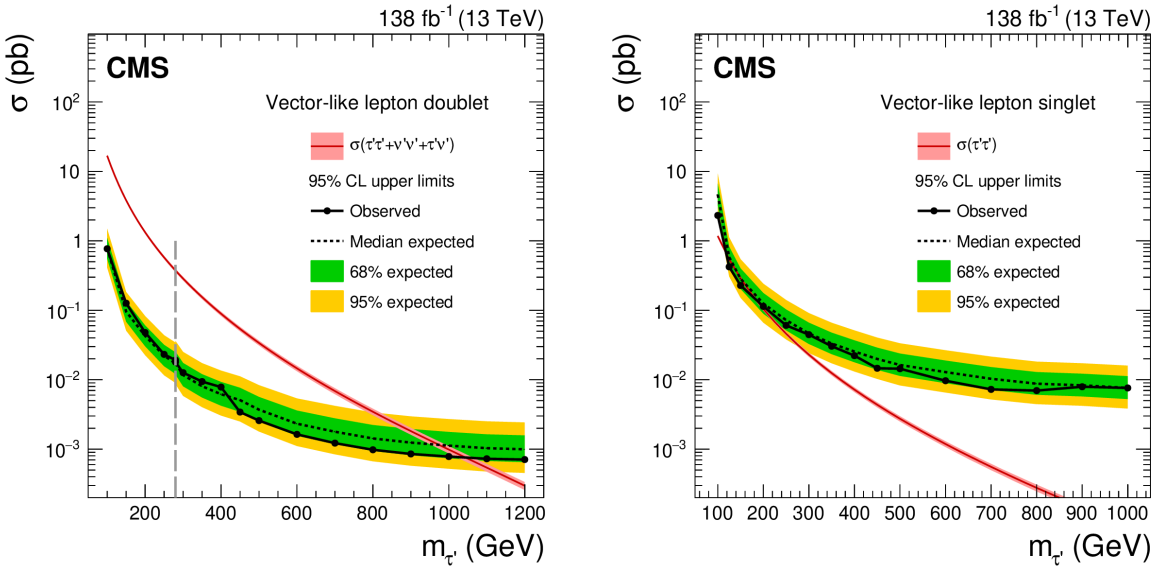


FIGURE 2.5: 95% CL upper limits on the production cross section for the vector-like leptons coupled to third-generation SM leptons in the doublet model (left) and singlet model (right). Figures adapted from [105].

experimental searches. For a review of experimental searches for VLQs during Run 2 by the ATLAS and CMS collaborations, see [94, 95]. For a phenomenological review comparing the exclusion limits on the masses of VLQs from both experiments, refer to [96].

Vector-like leptons (VLL) arise in a wide variety of BSM models such as models with extra spatial dimensions [97], grand unified theories [98], and also weak-scale supersymmetry [99, 100]. VLLs are also proposed solutions to the observed tensions between experimental measurement and SM prediction of the anomalous magnetic moment of the muon [100–104]. Searches for VLLs are challenging compared to VLQs as they are produced via electroweak interactions and thus have lower production cross sections. The production mechanisms and decay channels for VLLs depend on the assumption of the $SU(2)$ representation. A $SU(2)$ VLL doublet model contains an electrically neutral and electrically charged VLL ($L' = (\nu'_{\tau'}, \tau')$), where both the VLLs are assumed to be mas degenerate. The singlet model consists of just charged VLLs with additional coupling that allow it to decay to SM neutrinos, in addition to charged leptons. These models are characterised by final states involving multiple light leptons, jets and missing transverse energy ($E_T^{\text{miss}}$). For an overview of experimental searches for VLLs and future prospects, see [95].

### 2.4.5 Leptoquarks

The Standard Model groups leptons and quarks separately in order to account for their different observed properties. However, their similar structure prompts the proposal of a BSM symmetry that connects the two sectors. One such proposal is Leptoquarks (LQs), which are hypothetical color-triplet scalar or vector bosons carrying both baryon and lepton quantum numbers and having fractional electric charge. Leptoquark states are expected to exist in various extensions of the SM such as grand unified theories based on $SU(5)$ [106] and $SO(10)$ [107], and $R$-parity violating SUSY

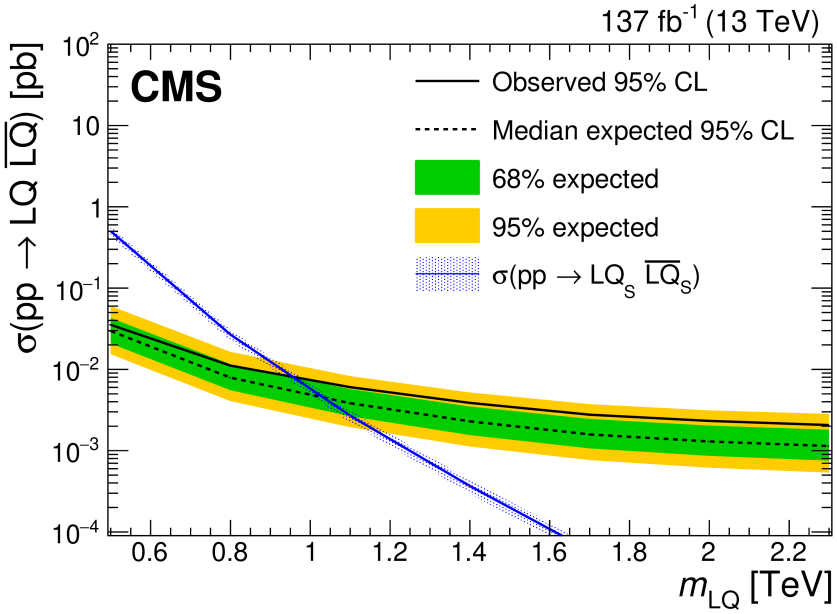


FIGURE 2.6: 95% CL upper limits on pair production cross sections for scalar leptoquarks ($LQ_S$) as a function of the mass of the LQ. The solid blue curve indicates the theoretical predictions for pair-produced $LQ_S$. Figure adapted from [116].

models [108–110]. Since they have both baryon and lepton numbers, they have the ability to transform quarks into leptons and vice versa. They thus can mediate processes that violate the principle of lepton flavour universality. This principle asserts that couplings of leptons to gauge bosons are flavour independent in the SM. However, slight deviations from this principle have been observed in precision measurements of certain $B$-meson decays by the LHCb, Belle and BaBar collaborations [111–113]. LQs were proposed as a possible explanation for such anomalies [114]. In addition, a scalar LQ can also explain the discrepancy between the measured and predicted values of the muon's anomalous magnetic moment [115].

Direct probes of LQs can be conducted at the LHC by investigating their production mechanisms and subsequent decay patterns. Leptoquarks can be pair-produced at the LHC via strong interactions with large production cross sections. This is independent of the LQ coupling to quarks and leptons but is suppressed for large LQ masses. Single LQ can also be produced along with a quark/lepton. Searches for LQs at the LHC focuses on models where LQs interact with leptons and quarks of the same generation, preferentially with third generation fermions.[2] Thus, searches at the LHC usually investigate decays of LQs to a top/bottom quark and tau/tau neutrino, see [116–118]. Scalar LQs coupling to top quarks and individual lepton flavors (electron, muon, and tau) have also been searched for in a recent CMS analysis [105], and LQs with masses below 1120 GeV are excluded at 95% confidence level.

[2]The motivation for considering couplings to third generation fermions is to test lepton flavour universality principle.

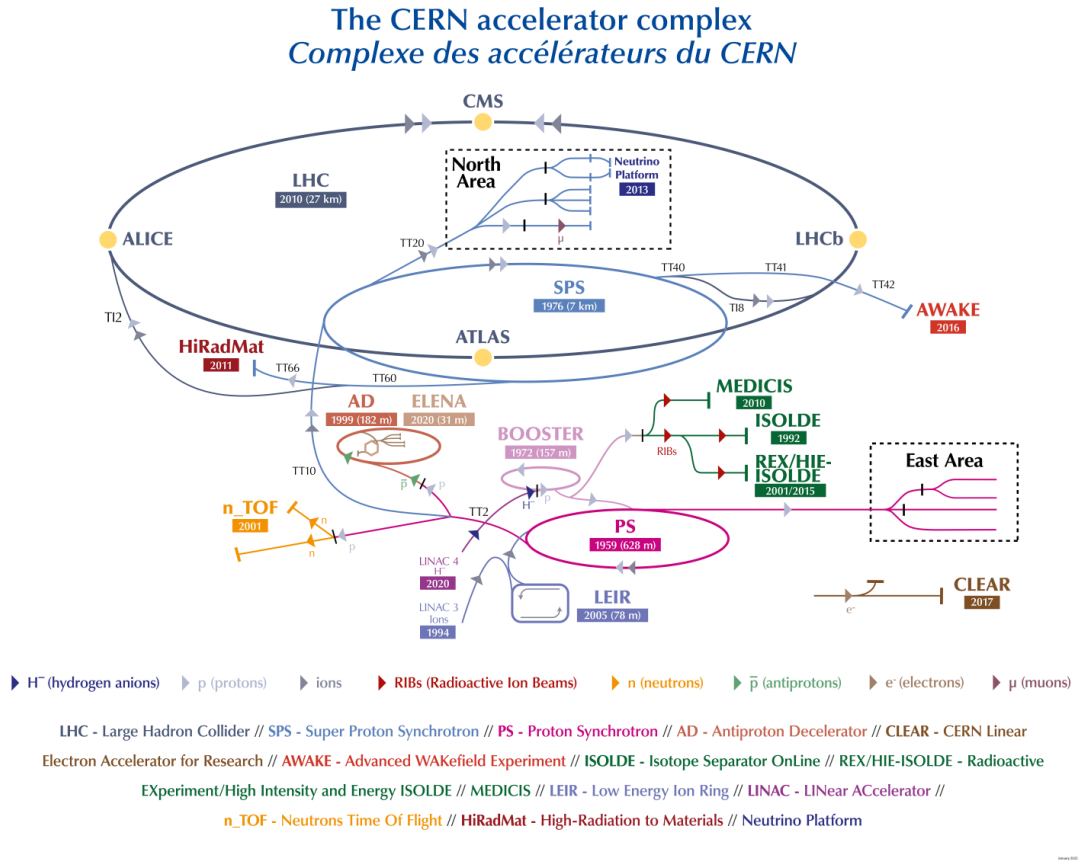


FIGURE 2.7: The CERN accelerator complex [120].

## 2.5 Experimental Particle Physics at the LHC

The Large Hadron Collider is an underground circular hadron collider based at the European Council for Nuclear Research (CERN) and located at the border between France and Switzerland [119]. With a circumference of approximately 27 km, it is currently the most powerful particle collider in the world, achieving proton-proton collisions with a center-of-mass energy approaching 14 TeV. The LHC represents the final stage in CERN's multi-tier acceleration complex, as illustrated in Figure 2.7. The protons or heavy ions (Pb) undergo sequential acceleration through several machines. Starting with a linear accelerator, particles are then passed through three circular accelerators: the Proton Synchrotron Booster (PSB), Proton Synchrotron (PS), and Super Proton Synchrotron (SPS), before entering the LHC for the final acceleration to maximum energy. Two beams (each beam containing many proton bunches) are simultaneously accelerated in this way, but in opposite directions, and collisions occur when these two beams cross each other at specific interaction points.

At the interaction points, the intensity of collisions is described by the instantaneous luminosity. The designed luminosity of the LHC is $10^{34}\text{cm}^2\text{s}^{-1}$. Luminosity in scattering theory is a measure of the number of collisions. Instantaneous luminosity $\mathcal{L}$ can be defined as the ratio of the number of events detected in a particle accelerator, over a certain period of time, to the cross section:

$$\mathcal{L} = \frac{1}{\sigma}\frac{dN}{dt}\,. \tag{2.13}$$

The integrated luminosity $L$ is the integral of the instantaneous luminosity over time: $L = \int \mathcal{L} dt$. The number of collision events for any given process is then given by multiplying the integrated luminosity by the cross section of the process. For most processes of interest, the cross sections are several orders of magnitude below the total hadronic cross sections at the LHC. Therefore, it is crucial to collect a large amount of data to enhance the probability of observing a rare process.

The collider complex houses four large particle detectors where the two particle beams intersect. The specialized detectors LHCb [121, 122] and ALICE [123] are designed to study b-physics and heavy-ion physics, respectively. The other two detectors, ATLAS [124] and CMS [125] are general purpose detectors designed to precisely measure the properties of all light leptons, photons, and hadrons emerging from proton-proton collisions. The work presented in this manuscript relies on the results published by the ATLAS and CMS collaborations. Thus, a brief overview of the two detectors is presented in the next section.

#### ATLAS and CMS detectors

The ATLAS and CMS detectors are designed to identify and study new physics phenomena emerging from proton-proton collisions at the LHC. To achieve this goal, both detectors are optimized for detecting and reconstructing all particle types. Each detector employs a cylindrical, multi-layered architecture with end-cap components, where individual layers serve specialized detection functions. Particles produced during the collisions leave characteristic signatures as they pass through the layers sequentially: starting with the tracking system, followed by an electromagnetic (ECAL) and a hadronic calorimeter (HCAL), and concluding with a muon detection system. A transverse representation of the ATLAS detector and the CMS detector with the different layers is shown in Figures 2.8 and 2.9 respectively.

All the layers are immersed in a high-intensity magnetic field to bend the tracks of electrically charged particles. A particle's electric charge and momentum are then reconstructed from track curvature measurements. Particles that interact only weakly with matter, such as neutrinos, traverse the entire detector without depositing energy or creating tracks. Such particles are referred to as invisible particles.

Though ATLAS and CMS detectors share the same scientific goals, the main difference in their designs comes from the way they produce and maintain a stable magnetic field. ATLAS comprises a thin superconducting central solenoid magnet producing a 2 T axial magnetic field and surrounded by a barrel toroid and two end-cap toroids. On the other hand, the CMS detector is built around a huge solenoid magnet which takes the form of a cylindrical coil of superconducting cable that generates a field of 4 T. The strong magnetic field allows for the precise measurement of the momentum of muons. Both detectors incorporate sophisticated online trigger systems and event filters capable of processing collision events in real time. These systems rapidly evaluate each collision and select only events of scientific interest, which are then stored at the CERN computer centre for detailed offline analysis.

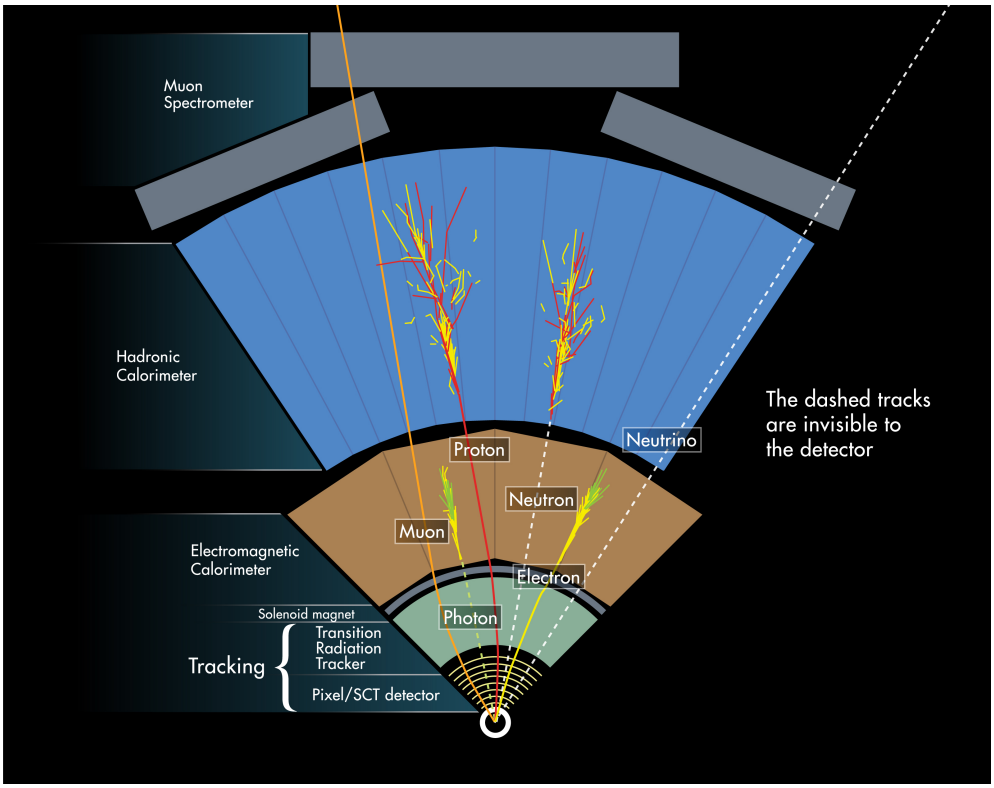


FIGURE 2.8: Particle interactions in a transverse slice of the ATLAS detector [126] from the beam interaction region to the muon detector.

At ATLAS and CMS, an event can be defined as the occurrence of a combination of the final-state particles identified by the detector, together with their kinematic properties such as their four momenta. It is useful to transform the four-momenta into coordinates that reflect the detector geometry. With the beam axis defined as the $z$-direction, the $x-y$ plane forms the transverse plane, allowing particle three-momentum to be expressed as $\mathbf{p} = (\vec{p}_T, p_z)$, where $\vec{p}_T$ represents the transverse momentum component. Due to the beams travelling in the symmetry axis of the cylinder-shaped detectors, only the transverse momenta, $p_T$, can be fully reconstructed. Another observable of interest is the stransverse mass ($m_{T2}$) which is useful to compute masses of pair-produced particles where each decays into one invisible and one directly observable particle.

The four-stage design of ATLAS and CMS permits the identification of the following (quasi-) stable particles in the final-states of the proton collision:

- **Jets**: They are made of travelling bunches of hadrons resulting from the showering and hadronization of the initially produced partons. The jet components can be electrically charged, in which case they are detected in the tracking chamber and ECAL before depositing remaining momentum in the HCAL. The neutral jet components can only be detected by the HCAL.

- *b*-**jets**: They are jets originating from hard bottom quarks. The relatively long lifetime of $b$-hadrons allows them to travel a measurable distance before decaying, enabling identification through reconstruction of secondary vertices associated with $b$-hadron decay.

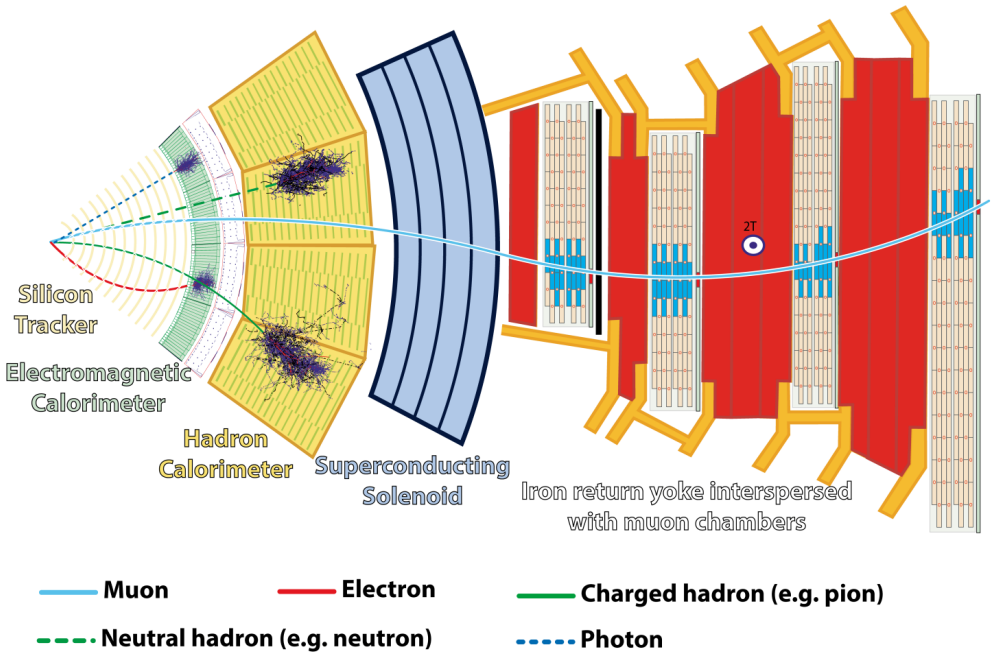


FIGURE 2.9: Particle interactions in a transverse slice of the CMS detector [127] from the beam interaction region to the muon detector.

- **Photons**: Since they are electrically neutral, they do not leave a track in the inner chamber, and only deposit energy in the ECAL.
- **Electrons**: After leaving a track in the inner chamber, they deposit most of their energy in the ECAL.
- **Muons**: They leave tracks in the inner chamber, lose some energy at the ECAL, but deposit most of their energy in the muon chambers.
- **Missing Energy**: The missing transverse energy $E_T^{\text{miss}}$ quantifies the transverse energy of the undetected particles produced in a collision event. It is defined as:

$$E_T^{\text{miss}} = |\vec{p}_T^{\,miss}| = -\left|\sum_i \vec{p}_T^{\,i}\right|, \tag{2.14}$$

  where $\vec{p}_T^{\,miss}$ is the negative vector sum of the transverse momentum $\vec{p}_T$ of all detected particles. In the SM, the only particles that would pass undetected are the neutrinos.

The statistical distributions of these reconstructed events, combined with their measured physical properties, can be compared against theoretical predictions. This comparison is essential for detailed analysis of the fundamental theories governing particle interactions. Through this comprehensive particle identification framework, ATLAS and CMS can reconstruct collision scenarios and systematically search for potential experimental signatures of new physics phenomena beyond the Standard Model.

### Searches for new physics at the LHC

When looking for new physics signals at the LHC, searches are often interpreted in a given theoretical context or, in other words, the data is confronted with a given BSM model. This comparison requires simulating how the BSM signals would interact with the collider and detectors. Typically, simulations consider a large number of events to obtain statistically significant yields after applying kinematic selection criteria. Though this is a heavy computational burden, such detailed simulation is essential for faithful comparison with experimental searches.

At the LHC, the colliding particles are protons composed of quarks and gluons.[3] These collisions are described by the parton model, where protons are viewed as dynamic systems of constantly interacting partons (quarks and gluons). To calculate a process involving quarks in the initial state, one must account for the probability to get a quark within the proton with appropriate momentum. The QCD factorization theorem enables decomposition of the hadron scattering amplitude into the parton-level scattering amplitude and the parton distribution functions (PDFs). Integrating over the phase space converts the scattering amplitudes into cross sections, giving the following hadron cross section:

$$\sigma(AB \to FX) = \sum_{a,b} \int dx_a dx_b \; f_{a/A}(x_a, Q^2) f_{b/B}(x_b, Q^2) \; \hat{\sigma}(ab \to F) \; . \tag{2.15}$$

Here, $A$ and $B$ are the initial state hadrons, the protons in the case of LHC. The sum runs over all partons $a(b)$ contained in the hadron $A(B)$. The proton is composed of two up quarks and one down quark, giving $a, b \in \{u, u, d\}$. The function $f_{a/A}(x_a, Q^2)$ represents the PDF of the parton $a$ inside the hadron $A$. This quantifies the probability to find a parton $a$ inside $A$ with a momentum fraction $x_a$. The PDFs depend on the energy scale $Q$ and are studied in deep inelastic scattering (DIS) experiments. Finally, $\hat{\sigma}(ab \to F)$ is the cross section for the hard scattering process involving the isolated partons $a$ and $b$.

The simulating of high energy collisions at the LHC can then be divided into four stages:

- **Parton-level event generators**: Event simulation begins with computation of the hard-scattering cross section in Eq. (2.15) at a given order in perturbation theory. Parton-level event generators take as input the properties of the BSM model to be simulated and compute the scattering matrix elements characterizing the hard process. The resulting cross sections and kinematic distributions provide the probabilities needed to randomly generate events.

- **Showering and hadronization**: The initial quarks and gluons from the hard process undergo successive radiative emissions, cascading into additional partons with progressively lower momentum through parton showering. Eventually, these partons must form color-neutral hadrons due to QCD confinement, a process called hadronization. Hadronization occurs at momentum scales of approximately 200 MeV, where perturbative QCD breaks down. Showering and

[3] In principle, the LHC also runs proton-lead and lead-lead collisions for the ALICE experiment.

| SR-ISR | |
|---|---|
| Cut | $\left(m(\tilde{\chi}_1^{\pm}/\tilde{\chi}_2^0), m(\tilde{\chi}_1^0)\right)$ = (200, 100) GeV |
| Initial number of events ($\mathcal{L} \times \sigma$) | 251230 |
| Initial number of events ($\mathcal{L} \times \sigma \times \mathcal{B}$) | 8206 |
| Generator filters ($\mathcal{L} \times \sigma \times \mathcal{B} \times \epsilon$) | 6017 |
| 3 leptons with at least one same flavor, opposite-charge pair | 1370 |
| Dilepton triggers | 1343 |
| $b$-jet veto | 1319 |
| $m_{3\ell} > 105$ GeV | 1280 |
| lepton $p_{\mathrm{T}}$ >25,25,20 GeV | 1024 |
| $m_{\ell\ell} \in [75, 105]$ GeV | 1000 |
| $N_{\mathrm{jets}} > 0$ | 478 |
| $N_{\mathrm{jets}} < 4$ | 467 |
| $\lvert\Delta\phi\left(E_{\mathrm{T}}^{\mathrm{miss}}, \mathrm{jets}\right)\rvert > 2.0$ | 314 |
| $R\left(E_{\mathrm{T}}^{\mathrm{miss}}, \mathrm{jets}\right) \in [0.55, 1.0]$ | 104 |
| $p_{\mathrm{T}}^{\mathrm{jets}} > 100$ GeV | 57.3 |
| $E_{\mathrm{T}}^{\mathrm{miss}} > 80$ GeV | 54.8 |
| $m_{\mathrm{T}} > 100$ GeV | 23.3 |
| $p_{\mathrm{T}}^{\mathrm{soft}} < 25$ GeV | 17.8 |

FIGURE 2.10: SR event selection criteria and Monte Carlo (MC) generator-weighted yields defined for a BSM model point in ATLAS-SUSY-2018-06 [128].

hadronization generators therefore use approximate models based on experimental data to describe this process. The output consists of stable hadrons and leptons, constituting truth-level or particle-level events.

- **Detector simulation**:While the physics of the collision is simulated in the previous stages, comparison with experimental data requires simulating the detector response. Detector simulation accounts for the acceptance, resolution, and reconstruction efficiency of the LHC detector systems. This transforms the particle-level events into detector-level observables.

- **Event selection**: LHC searches usually employ cut-based analyses that categorise events into signal regions (SRs) using kinematic requirements on reconstructed objects. The complexity of event selection varies: some CMS analyses define over 100 signal regions, while ATLAS analyses typically employ $\mathcal{O}(10)$ regions. The efficiency $\epsilon_i$ for each SR is defined as the fraction of generated events passing all selection requirements. This is then combined with the cross section and integrated luminosity to predict the expected number of signal events in that region.

Figure 2.10 displays a cutflow table for a signal region SR-ISR in an ATLAS search for chargino-neutralino production in three-lepton final states [128]. The table details the complete sequence of event selection requirements and the corresponding Monte Carlo (MC) generator-weighted yields for a specific BSM model point, beginning with an initial sample of 40000 events. For each SR, experimentalists note the number of observed events ($n_{obs}$) passing the required kinematic selections. The interpretation of this number is then done by comparing it against the background expectations obtained from MC predictions. Further, uncertainties on the predicted background yields are also required to perform proper statistical inference. The next chapter details the statistical methods typically used in particle physics to either assess the significance of an excess or constrain BSM parameter spaces.

# Chapter 3

# Statistics for High Energy Physics

Testing new theories in high energy physics experiments not only depends on collecting high quality experimental data but also requires rigorous statistical methods. In high energy physics, we are often concerned with distinguishing events of interest (signal) from other types of events (background). This in turn necessitates the development and application of sophisticated statistical techniques to discern signals from background noise and to make precise predictions. As the LHC at CERN continues to provide a wealth of data from particle collisions at unprecedented energy scales, analysing such data involves overcoming several challenges. The sheer volume of data, combined with the intricate nature of the underlying physical processes, makes it essential to have rigorous statistical methods to quantify the significance of a discovery or to place constraints on BSM theories.

The statistical interpretation of probability falls into two broad categories, depending on the choice of the analysts. The *frequentist* interpretation of probability is associated with the observed data $X$ and represents the relative frequency of an event when an experiment is repeated multiple times under identical conditions. In *Bayesian* statistics, probability often represents the analyst's *degree of belief* of a hypothesised model, and thus is associated with both the observed data and the model.

This chapter is organized as follows. Section 3.1 discusses frequentist inference as typically employed in high energy physics, including limit-setting procedures. Section 3.2 presents Bayesian inference and introduces Markov Chain Monte Carlo algorithms commonly used for sampling. Section 3.3 introduces model selection methods for comparing models with different degrees of freedom, presenting the Akaike Information Criterion and Reversible Jump Markov Chain Monte Carlo.

## 3.1 Frequentist Approach

In frequentist statistics, the probability $p$ of an event occurrence is defined in the limit of a large number of independent, identical trials. If an event $A$ is observed to occur $n$ times out of $N$ identical trials, its probability is given by:

$$P(A) = \lim_{N\to\infty} \frac{n}{N}\,. \tag{3.1}$$

Suppose we have a sample of observed events $X = (x_1, \ldots, x_n)$ and we try to model

these observations based on a probability density function $f(X|\theta)$ where the functional form of $f$ is known, but the parameter(s) $\theta$ (or a parameter vector $\vec{\theta}$) is unknown. We can then define a *likelihood* as a function of the model parameters, from which optimal parameter values are estimated by evaluating the likelihood at the observed data:

$$L(\theta) = f(X|\theta)\,. \tag{3.2}$$

The most common method of estimating the parameter values compatible with the observed data $X$ in the frequentist paradigm is the maximum likelihood estimate (MLE). This method expects a high probability for the observed data if the hypothesized p.d.f. and parameter values are correct. Conversely, a low probability for the data obtained is expected if the parameter value is far away from the true value. We can then define the maximum likelihood estimators for the parameters to be those which maximize the likelihood function:

$$\hat{\theta} = \underset{\theta}{\operatorname{argmax}}(L(\theta))\,. \tag{3.3}$$

### 3.1.1 Hypothesis testing

The goal of a statistical test is to quantify how well the observed data is in agreement with a given hypothesis. Hypothesis tests determine, with a given confidence level (CL), whether the observed data provide sufficient evidence to reject an initial hypothesis, called the null hypothesis ($H_0$), typically in favour of an alternative hypothesis ($H_1$). In high-energy physics, the null hypothesis $H_0$ usually refers to the expectations from fixed theoretical predictions (could be SM or BSM physics). The alternative hypothesis $H_1$ represents potential models that could explain observations that the null hypothesis could not account for.

In this thesis, we will consider two distinct modes of hypothesis testing. In the *exclusion* mode, the null hypothesis represents a given BSM model point that we aim to constrain or rule out. This is used in Section 4.4 in Chapter 4 and in formulating certain blocks of the Walker algorithm in Chapters 5 and 6. In the *discovery/anomaly detection* mode, the null hypothesis corresponds to the SM predictions. This is mainly used in Chapters 5 and 6.

To quantify the difference between the predictions of $H_0$ and $H_1$, we construct a test statistic $T$ based on experimental observations. We can then formulate a statement on the compatibility of the data and the different hypotheses based on a decision to accept or reject the null hypothesis $H_0$. To do so, we choose a *critical region* for $T$ and if the value of $T$ observed is in the critical region, we reject the null hypothesis $H_0$. This critical region is defined such that the probability of $T$ to be observed in this region, under the null hypothesis, is some value $\alpha$, also called the significance level of the test.

The Neyman-Pearson (NP) likelihood-ratio framework provides a formal method for evaluating hypotheses based on data, establishing a systematic procedure to decide between competing statistical models. The Neyman-Pearson Lemma [129] asserts that for simple hypotheses (where both $H_0$ and $H_1$ are fully specified), the most powerful test at a given significance level $\alpha$ is the likelihood ratio test. Formally, the lemma states the optimal test statistic to distinguish between two simple hypotheses is given

by the ratio of the likelihood functions $L(H_1|X)$ and $L(H_0|X)$ evaluated for the observed data sample $X$ under the two hypotheses:

$$\Lambda(X) = \frac{L(H_1|X)}{L(H_0|X)}\,. \tag{3.4}$$

The null hypothesis $H_0$ is rejected in favour of the alternate hypothesis $H_1$ at significance level $\alpha$ if the quantity $\Lambda(X)$ exceeds a critical value $k$:

$$P(\Lambda(X) > k \,|\, H_0) = \alpha\,. \tag{3.5}$$

One of the commonly used parameters to characterise the hypotheses in high energy physics is the signal strength parameter $\mu$, defined as the ratio of a given BSM signal cross section to a reference cross section:

$$\mu = \frac{\sigma_{sig}}{\sigma_{ref}}\,. \tag{3.6}$$

Thus, $\mu = 1$ corresponds to the signal of the given BSM hypothesis, and $\mu = 0$ corresponds to the SM background-only hypothesis. We can then define a $p$-value as the probability of observing data at least as extreme as the test statistic under $H_0$, and this is often used to assess the evidence against the null hypothesis:

$$p = P(T \geq t_{obs}|H_0)\,, \tag{3.7}$$

where $t_{obs}$ is the observed value of $T$. When the $p$-value is small, it suggests that the observed data is unlikely under $H_0$, thus rejecting $H_0$ in favour of the alternative hypothesis $H_1$. In experimental particle physics, $p$-values are often converted into a quantity called "significance", $Z$, defined as the number of standard deviations above the mean of a Gaussian distributed variable whose upper tail probability equals $p$, that is,

$$Z = \Phi^{-1}(1-p)\,. \tag{3.8}$$

Here, $\Phi^{-1}$ is the quantile function of the standard Gaussian distribution. To claim a discovery, a $p$-value threshold corresponding to a "5-sigma" ($5\sigma$) significance level is typically used. This corresponds to a $p = 2.87 \times 10^{-7}$. The calculation of the $p$-value often involves generating distributions of the test statistic under the null hypothesis using Monte Carlo simulations. These simulations model the expected background processes without any signal. The $p$-value is then obtained by integrating the tail of the distribution beyond the observed value of the test statistic. In cases where the test statistic follows a known distribution (e.g., a chi-squared distribution), the $p$-value can be computed analytically. This method will be used extensively in Chapter 5 and Chapter 6 where $p$-values are extracted from an unknown distribution.

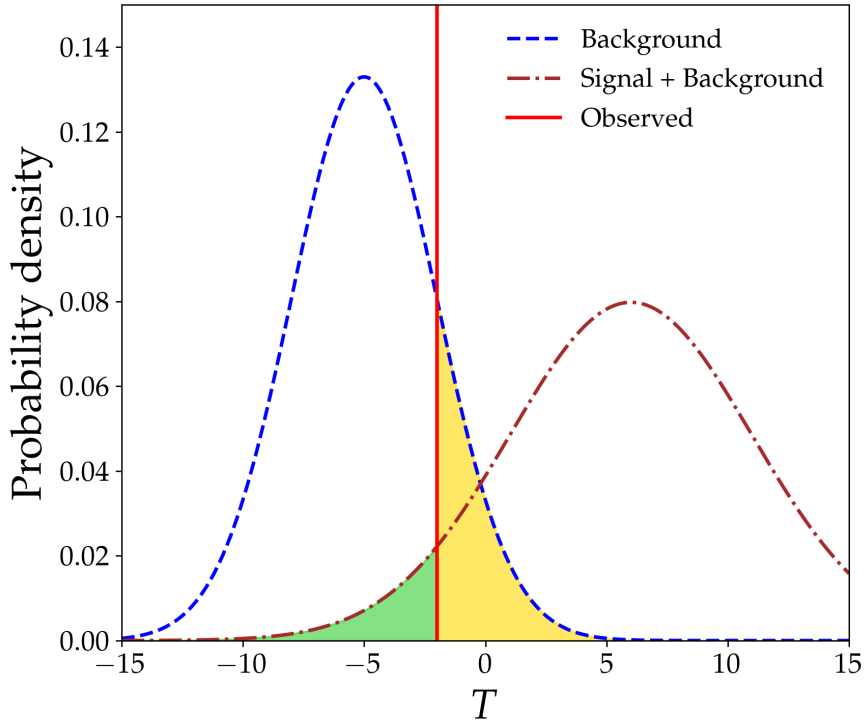


FIGURE 3.1: Illustration of the $CL_s$ method.

To test a hypothesised value of $\mu$, experimental analyses frequently use the *profile likelihood* ratio test based on the NP lemma to quantify discovery significance or exclusion limits:

$$T = -2\ln\lambda(\mu) = -2\ln\frac{L(\mu,\hat{\hat{\theta}})}{L(\hat{\mu},\hat{\theta})}. \tag{3.9}$$

Here, $\hat{\hat{\theta}}$ in the numerator is the value of $\theta$ that gives the maximum likelihood for the specified $\mu$, and $\hat{\mu},\hat{\theta}$ are the ML estimators of the likelihood function, as mentioned in Eq. (3.3). From Eq. (3.9), we can see that $0 \leq \lambda \leq 1$. When $\lambda$ approaches one, this indicates a strong agreement between the observed data and the hypothesized signal strength value $\mu$. Thus, lower values of $T$ corresponds to increasing compatibility between the data and $\mu$. An important property of this test statistic is that, under certain regularity conditions, the asymptotic distribution of $T$ converges to a $\chi^2$ distribution under the null hypothesis (Wilks' Theorem [130]). This is advantageous as the null distribution of $T$ can be determined analytically without requiring Monte Carlo or toy simulations to estimate it, thus reducing the computational burden.

To reject a signal hypothesis in particle physics, the $CL_s$ method [131] is used to set a confidence level. This statistic combines the SM background $p_b$ and signal plus SM background hypotheses $p_{s+b}$ to reduce the impact of statistical fluctuations in the data:

$$CL_s = \frac{p_{s+b}}{1-p_b}, \tag{3.10}$$

where $p_{s+b}$ and $p_b$ are defined as:

$$p_{s+b} = P(T \geq t_{obs} \,|\, s+b)\,, \tag{3.11}$$
$$p_b = P(\,T \leq t_{obs}\,|b)\,. \tag{3.12}$$

Using the above method, upper limits are then set for the signal strength parameter $\mu$ in searches for new physics models at the LHC. The signal hypothesis with signal strength $\mu$ is then excluded at 95% confidence if $\mathrm{CL}_s < 0.05$. Figure 3.1 illustrates Eq. (3.10) for an example distribution of the test statistic $T$ under the signal + background (brown dash-dotted line) and background-only (blue dashed line) hypothesis. The vertical red line is the observed value of $T$. The green and yellow shaded regions correspond to $1 - p_{s+b}$ and $1 - p_b$ respectively.

## 3.2 Bayesian Inference

The Bayesian approach allows the probabilities of specific events to be based on subjective reasoning or degrees of belief. Here, randomness is attributed not only to the data collected $D$, but also to the unknown parameters $\theta_M$ of a model $M$.

Suppose that the data collected $D$ consists of $n \in \mathbb{N}$ measurements of real observables that can be represented by a $n$ vector $X = (x_1, x_2, ..., x_n)^T \in \mathbb{R}^n$. We then aim to statistically describe this data using a model $M$ parameterised by a vector $\vec{\theta}_M = (\theta_1, \theta_2, ..., \theta_m)^T_M \in \mathbb{R}^m$. One can then construct a probabilistic model $P(X \,|\, \vec{\theta}_M, M)$ to describe the data based on the parameters $\vec{\theta}_M$ of the underlying model $M$. This object is often interpreted as a likelihood function of the parameters $\vec{\theta}_M$ based on the fixed observations $X$, as given in Eq. (3.2). With different choices of $\vec{\theta}_M$, we get different likelihood functions, allowing us to infer which parameter values best describe the data.

The Bayesian approach to modelling builds on subjective reasoning on the values of the unknown parameters $\vec{\theta}_M$. The uncertainty about the values of the true parameters $\vec{\theta}_M$ before analysing the data is modelled as a probability distribution $\pi(\vec{\theta}_M)$, where $\pi(\vec{\theta}_M)$ is called the prior density on the parameters $\vec{\theta}_M$. The information contained in the data is then used to update our knowledge of the parameters. However, selecting an appropriate prior distribution is of the utmost importance and can vary depending on the analyst's true understanding of the data. In general, one can classify Bayesian priors into broadly two categories (a) informative – where the personal belief of the analyst is encoded in the prior and (b) uninformative – where the prior is constructed according to some formal rules, not encoding any kind of subjective belief of the analyst.

All things considered, we are interested in the flipped quantity $P(\vec{\theta}_M|X, M)$ in Bayesian inference. This describes the posterior probability that the parameters underlying our assumed model $M$ are actually $\vec{\theta}_M$ upon conditioning on the data. The computation of this quantity relies on both the likelihood function in Eq. (3.2) and the prior density $\pi(\vec{\theta}_M)$ of the unknown parameters. Following Bayes' Theorem, we can write this posterior density as

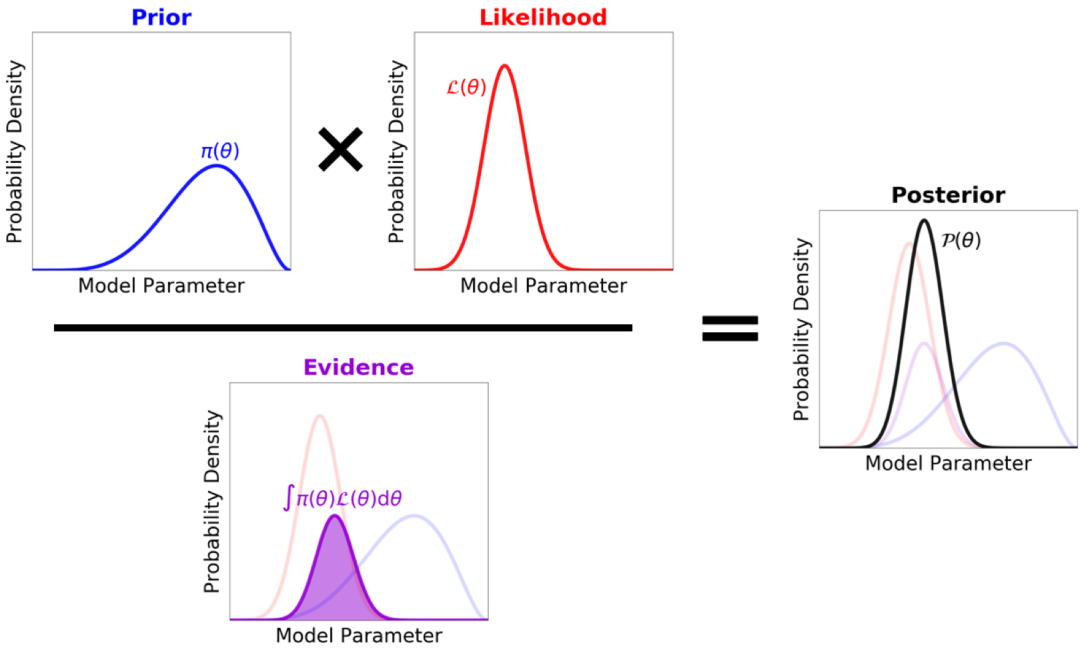


FIGURE 3.2: Illustration of Bayes' Theorem. The posterior density $P(\theta)$ of model parameters $\theta$ results from combining the prior distribution $\pi(\theta)$ (blue) with the likelihood $L(\theta) = P(X|\theta)$ (red), normalised by the overall evidence $Z = \pi(\theta)L(\theta)d\theta$ (purple) for the particular model. Figure adapted from [132].

$$P(\vec{\theta}_M|X, M) = \frac{P(X|\vec{\theta}_M, M)\pi(\vec{\theta}_M|M)}{P(X|M)}\,. \tag{3.13}$$

The denominator represents the likelihood for our model $M$ marginalised over all possible parameter values $\vec{\theta}_M$ and is often called model evidence $Z$:

$$P(X|M) \;=\; Z \;=\; \int P(X|\vec{\theta}_M, M)\;\pi(\vec{\theta}_M|M)\;d\vec{\theta}_M\,. \tag{3.14}$$

The posterior density $P(\vec{\theta}_M|X, M)$ quantifies our belief in $\vec{\theta}_M$ after taking into account the current observations and combining our prior beliefs $\pi(\vec{\theta}_M|M)$, normalizing by the overall evidence $Z$.

For simple problems, posterior densities can sometimes be derived analytically. However, more often than not, the posterior density does not have a closed-form solution. Computational Bayesian inference is a challenging problem, as any algorithm that aims to compute the posterior has to master the difficulty that it has limited access to the full posterior. This is because the posterior density cannot be evaluated directly and one needs to compute the likelihood function for certain parameter values individually. Even if the prior densities take on a simple distribution, this individual computation of likelihood is a major constraint that all attempts have to tackle. Further, to reduce computational budget, we are often necessitated to choose appropriate parameter spaces for the evaluation of the likelihood function.

One of the most popular approaches to get samples directly from the posterior is through Markov Chain Monte Carlo.

### 3.2.1 Markov Chain Monte Carlo

A Markov Chain Monte Carlo (MCMC) algorithm [133] is a sampling procedure allowing one to characterize a distribution without knowing its closed form by randomly sampling values out of this distribution. The name MCMC combines two properties – Monte Carlo and Markov Chain. Monte Carlo is a method to estimate properties of a distribution by studying random samples from the distribution. The benefit of this approach is most realized when the analytic form of the distribution is unfeasible to work with and when the random samples are easy to draw. The Markov property refers to the fact that each new sample generated depends on the one preceding it but does not depend on any samples before the preceding sample. Each random sample is used as a stepping stone to generate the next random sample.

MCMC aims to generate samples that converge to the posterior distribution. It accomplishes this by creating a chain of correlated parameter values $\vec{\theta}_1 \rightarrow ...\vec{\theta}_n$ over $n$ iterations so that the number of iterations spent in a particular region $\delta_{\vec{\theta}_i}$ centered on $\vec{\theta}_i$ is proportional to the posterior density contained in that region. As $n \rightarrow \infty$, the distribution of the final samples $\rho(\vec{\theta})$ should be stationary and equal to the target distribution, i.e., the posterior $P(\vec{\theta})$. This can be satisfied by invoking the *detailed balance* condition. The detailed balance condition states that our chain has achieved stationarity if the flow of probability is conserved when moving from one model state $\mathcal{X} = \vec{\theta}_i$ to the next $\mathcal{X}' = \vec{\theta}_{i+1}$, i.e., the process is reversible. Formally, this reduces to factoring of probability:

$$P(\mathcal{X}'|\mathcal{X})P(\mathcal{X}) = P(\mathcal{X}', \mathcal{X}) = P(\mathcal{X}|\mathcal{X}')P(\mathcal{X}')\,, \tag{3.15}$$

where $P(\mathcal{X}'|\mathcal{X})$ is the probability of moving from state $\mathcal{X} \rightarrow \mathcal{X}'$ and $P(\mathcal{X}|\mathcal{X}')$ is the reverse probability of moving from state $\mathcal{X}' \rightarrow \mathcal{X}$. Rearranging the above terms, we get the following:

$$\frac{P(\mathcal{X}'|\mathcal{X})}{P(\mathcal{X}|\mathcal{X}')} = \frac{P(\mathcal{X}')}{P(\mathcal{X})}\,. \tag{3.16}$$

To move to new states, we first define a proposal distribution $q(\mathcal{X}'|\mathcal{X}) = q(\mathcal{X} \rightarrow \mathcal{X}')$, which proposes a new state $\mathcal{X}'$ in our parameter space conditioned on our current state $\mathcal{X}$. We then either decide to accept this new state, i.e., $\mathcal{X}' = \vec{\theta}_{i+1}$ or reject it, i.e., $\mathcal{X}' = \vec{\theta}_i$ by defining an acceptance probability $\alpha(\mathcal{X} \rightarrow \mathcal{X}')$. Combining the proposal distribution together with the acceptance probability, we get the probability of moving to the new state $\mathcal{X}'$

$$P(\mathcal{X}'|\mathcal{X}) = q(\mathcal{X} \rightarrow \mathcal{X}')\alpha(\mathcal{X} \rightarrow \mathcal{X}')\,. \tag{3.17}$$

Substituting the above expression into our detailed balance condition in Eq. (3.15), the acceptance probability must satisfy:

$$\frac{\alpha(\mathcal{X} \to \mathcal{X}')}{\alpha(\mathcal{X}' \to \mathcal{X})} = \frac{P(\mathcal{X}')}{P(\mathcal{X})} \frac{q(\mathcal{X}' \to \mathcal{X})}{q(\mathcal{X} \to \mathcal{X}')} . \tag{3.18}$$

We then get the Metropolis-Hastings criterion:

$$\alpha(\mathcal{X} \to \mathcal{X}') = min\left[1, \frac{P(\mathcal{X}')}{P(\mathcal{X})} \frac{q(\mathcal{X}' \to \mathcal{X})}{q(\mathcal{X} \to \mathcal{X})}\right] . \tag{3.19}$$

This approach forms the basis of the Metropolis-Hastings (MH) [134, 135] algorithm to generate samples from the posterior distribution via the following iterative steps:

- Initialize the chain at a certain starting point $\mathcal{X}^* = \vec{\theta}^*$, which is either a prior expected value or randomly drawn from the prior distribution of $\vec{\theta}$.
- Given the current state of the chain to be $\mathcal{X}$, propose a new state $\mathcal{X} \to \mathcal{X}'$ by sampling from the proposal distribution $q(\mathcal{X} \to \mathcal{X}')$.
- Compute the acceptance probability $\alpha(\mathcal{X} \to \mathcal{X}')$ defined in Eq. (3.19).
- Generate a random number $u$ from a Uniform distribution between $[0, 1]$.
- If the random number generated $u \leq \alpha(\mathcal{X} \to \mathcal{X}')$, accept the move and set $\mathcal{X}' = \vec{\theta}_{i+1}$. Else, reject the move and set $\mathcal{X}' = \vec{\theta}_i$.
- Repeat the process for the next steps.

Although the above procedure sounds simple in practice, it does suffer from some major problems. One of the issues in generating a sequential set of states is the fact that our chain only has a finite length and needs a starting position $\mathcal{X}^*$. If our chain were infinitely long, we would expect it to visit every possible position in parameter space, rendering the exact starting position unimportant. However, in practice, we terminate the sampling after $n$ iterations, and starting from a location $\mathcal{X}^*$ that has an extremely low probability means that a large fraction of our $n$ samples would occupy this low-probability region and possibly bias our final results. Since we have limited knowledge beforehand about the posterior distribution, we often remove the initial chain of states (burn-in period) once we are confident that our chain has begun sampling from higher-probability regions. Further, the construction of an appropriate proposal distribution is a non-trivial task, and tuning is often required to get an efficient algorithm. Additionally, if the posterior distribution is non-convex, or multimodal (containing multiple peaks), the algorithm may get stuck in local modes for many iterations, thus failing to explore the full parameter space.

## 3.3 Model Selection

The main challenge addressed in this manuscript is the problem of choosing the "best" model among a class of competing models with different numbers of parameters. Model selection criteria provide a useful tool in identifying a model of appropriate structure and dimension among a collection of candidate models. These criteria assess whether a fitted model offers an optimal balance between goodness-of-fit and parsimony. An effective selection criterion will eliminate candidate models that are

either too simplistic to adequately accommodate the data or unnecessarily complex. The vast literature on model selection criteria (for a review, see [136]) is fundamentally grounded in *Occam's razor*, which advocates for choosing the simplest model that maintains a given level of predictive accuracy.

Achieving this balance between accuracy and parsimony presents significant challenges without systematic model selection approaches. This section discusses two established model selection criteria that guide certain features of the algorithm described in Chapter 6.

### 3.3.1 Akaike Information Criterion

The Akaike information criterion (AIC) [137] was the first model selection criterion to gain widespread attention in the statistical community. It is one of the most widely known information criterion. Developed by Akaike, AIC builds on the established maximum likelihood framework, which provides a robust approach for parameter estimation when the model structure and dimensionality are fixed. For a parametric candidate model of interest, the likelihood function reflects how well the model explains the observed data. As the size and complexity of the model are increased, the model becomes more capable of adapting to the nuances and subtleties of the data. As a consequence, choosing the fitted model that maximizes the empirical likelihood will invariably lead to the selection of the largest and most complex model in the candidate collection. Thus, model selection based on the likelihood principle requires an extension of the traditional likelihood framework. Akaike thus extended this framework with which one could perform model estimation and selection concurrently.

Consider a statistical model that describes a particular dataset, where the model is characterized by a $n$ dimensional parameter vector $\vec{\theta}_n$. The likelihood function reaches its maximum value at $\widehat{\vec{\theta}}_n$, the maximum likelihood estimate. The AIC value for this model is then given by:

$$\mathrm{AIC} = -2 \ln L(\hat{\vec{\theta}}_n) + 2n \,. \tag{3.20}$$

When evaluating a set of candidate models for the dataset, the model with the minimum AIC value is chosen as the best fit model. Thus, AIC makes a compromise with the model performance (measured through the likelihood function) by including a penalty on complexity that increases with the number of estimated parameters. This penalty discourages overfitting, which is important because increasing the number of parameters in the model almost always improves the goodness of the fit.

It is important to note that AIC evaluates the "goodness" of a candidate model *relative* to other models in a set. It cannot be used to assess the absolute fit of the model. If all candidate models perform poorly, AIC offers no indication of this limitation. Therefore, it is typically recommended to validate the absolute quality of an AIC-selected model using additional diagnostic methods.

### 3.3.2 Reversible Jump Markov Chain Monte Carlo

The MCMC sampler is not useful in Bayesian model determination where the dimension of the parameter vector $\vec{\theta}$ being sampled is not fixed. Green first proposed a reversible Markov Chain sampler [138] which extended the Metropolis-Hastings framework to allow for jumps between parameter subspaces of differing dimensionality.

Suppose that we have a countable set of candidate models $\{M_k, k \in \mathbb{N}\}$, where model $M_k$ is parameterised by a vector $\vec{\theta}^{(k)}$ of unknown parameters with parameter space $\vec{\theta}^{(k)} \subset \mathbb{R}^{d_k}$. The dimension of the model $d_k$ varies from model to model in the set. Once we observe some data sample $X$, we want one of our candidate models to describe this data. Then we can model the joint distribution of $(k, \vec{\theta}^k, y)$ as

$$P(k, \vec{\theta}^{(k)}, X) = P(X|k, \vec{\theta}^{(k)})\pi(\vec{\theta}^{(k)}|k)\pi(k)\,. \tag{3.21}$$

The above joint distribution is the product of the likelihood $L(k, \vec{\theta}^{(k)}) = P(y|k, \vec{\theta}^{(k)})$ given the data $y$, a discrete prior on the choice of model $M_k$ or model probability $\pi(k)$, and prior on the parameters given model $M_k$, $\pi(\vec{\theta}^{(k)}|k)$. The joint inference problem over this candidate model space can be set in the form of a simple Bayesian hierarchical model, based on the joint posterior distribution of $k$ and $\vec{\theta}^{(k)}$,

$$P(k, \vec{\theta}^{(k)}|X) = \frac{L(k, \vec{\theta}^{(k)}|X)\pi(k)\pi(\vec{\theta}^{(k)}|k)}{\sum_i \{\int L(i, \vec{\theta}^{(i)}|X)\pi(\vec{\theta}^{(i)}|i)d\vec{\theta}^{(i)}\}\pi(i)}\,. \tag{3.22}$$

We can often factorise this posterior as

$$P(k, \vec{\theta}^{(k)}|X) = P(k|X)P(\vec{\theta}^{(k)}|k, X)\,, \tag{3.23}$$

that is, as the product of posterior probabilities on the model and posterior probabilities on model-specific parameters.

Let the state space in which our sampler has to traverse be denoted by $\Theta$, where $\Theta = \bigcup_k \vec{\theta}^{(k)}$. Our aim is to construct an aperiodic and irreducible sampler on this union parameter space. Therefore, we require that our chain satisfies the detailed balance condition similar to the one defined for MCMC algorithms (Eq. (3.15)). Like the usual Metropolis-Hastings algorithm, we can build a chain where at a specific iteration we suppose that the chain is in model $M_k$ of dimension $d_k$ parameterised by vector $\vec{\theta}^{(k)}$. We then propose to move to model $M_{k'}$ of dimension $d_{k'}$ parameterised by vector $\vec{\theta}^{(k')}$. We can split this task into two parts – first, as a selection move between models $M_k \to M_{k'}$, and then propose $\vec{\theta}^{(k')}$. For convenience, we will denote the current state as $\mathcal{X} = (k, \vec{\theta}^{(k)})$ with dimension $d_k$ and the proposed new state as $\mathcal{X}' = (k', \vec{\theta}^{(k')})$ with dimension $d_{k'}$.

We now need to establish an acceptance probability for a reversible jump move. However, unlike in regular MCMC, we typically need multiple types of moves to traverse the whole parameter space $\Theta$. We consider that each move type is chosen independently for each sweep of the sampler, and extend the conventional MH algorithm to

allow for probabilities of each move type to depend on the current state. A particular move type $m$ consists of both the forwards move from state $\mathcal{X} \to \mathcal{X}'$ and the reverse $\mathcal{X}' \to \mathcal{X}$.

However, we encounter a problem while constructing a proposal density $q_m(\mathcal{X} \to \mathcal{X}')$ for each move type $m$. Since $\mathcal{X}$ and $\mathcal{X}'$ have potentially different dimensions, it becomes difficult to construct a reversible proposal mechanism. One way to tackle this problem is to introduce latent random variables $u$ and $u'$ of dimension $d_u$ and $d_{u'}$ generated from known distributions $g_m$ and $g'_m$, respectively, such that we match the dimensions $d_k + d_u = d_{k'} + d_{u'}$. We can then construct the proposal density $q_m$ on the extended parameter space $(\mathcal{X}, u)$ and $(\mathcal{X}', u')$ so that $q((\mathcal{X}, u) \to (\mathcal{X}', u'))$ is reversible, via a 1-1 differentiable mapping, i.e.,

$$(\mathcal{X}', u') = h_m(\mathcal{X}, u) \quad \Longleftrightarrow \quad (\mathcal{X}, u) = h'_m(\mathcal{X}', u'); \quad \text{where } h'_m = h_m^{-1}. \tag{3.24}$$

The construction of the proposal density then reduces to the generation of the latent random variables followed by the mapping function. Let $j_m(\mathcal{X})$ denote the probability that move $m$ is attempted at state $\mathcal{X}$, then the detailed balance condition for each specific move type becomes

$$\int_{((\mathcal{X},u),(\mathcal{X}',u'))} P(\mathcal{X}) j_m(\mathcal{X}) g_m(u) \alpha_m(\mathcal{X} \to \mathcal{X}') d\mathcal{X} du = \int_{((\mathcal{X},u),(\mathcal{X}',u'))} P(\mathcal{X}') j_m(\mathcal{X}') g'_m(u') \alpha_m(\mathcal{X}' \to \mathcal{X}) d\mathcal{X}' du'. \tag{3.25}$$

Ensuring that the detailed balance condition holds for each move type $m$ is sufficient to ensure reversibility of the chain [1]. If the transformation $h_m$ and its inverse $h'_m$ from $(\mathcal{X}, u)$ to $(\mathcal{X}', u')$ and vice versa, respectively, are differentiable, we can then apply the standard change-of-variable formula to the right hand side of Eq. (3.25). Then the integral equality holds if

$$P(\mathcal{X}) j_m(\mathcal{X}) g_m(u) \alpha_m(\mathcal{X} \to \mathcal{X}') = P(\mathcal{X}') j_m(\mathcal{X}') g'_m(u') \alpha_m(\mathcal{X}' \to \mathcal{X}) \left| \frac{\partial(\mathcal{X}', u')}{\partial(\mathcal{X}, u)} \right|. \tag{3.26}$$

where the last factor is the Jacobian of the transformation $h_m : (\mathcal{X}, u) \to (\mathcal{X}', u')$

$$\left| \frac{\partial(\mathcal{X}', u')}{\partial(\mathcal{X}, u)} \right| = \left| \frac{\partial h_m(p, q)}{\partial(\mathcal{X}, u)} \right|_{p=\mathcal{X}, q=u}. \tag{3.27}$$

Thus, we can define the acceptance probability $\alpha_m(\mathcal{X}, \mathcal{X}')$ to move from state $\mathcal{X}$ to $\mathcal{X}'$ with move type $m$ as

[1] For a complete proof of this condition, see Section 3.2 in [138].

$$\alpha_m(\mathcal{X} \to \mathcal{X}') = \min\left\{1, \frac{P(\mathcal{X}')}{P(\mathcal{X})} \frac{j_m(\mathcal{X}')}{j_m(\mathcal{X})} \frac{g'_m(u')}{g_m(u)} \left| \frac{\partial(\mathcal{X}', u')}{\partial(\mathcal{X}, u)} \right| \right\}. \tag{3.28}$$

Note that at state $\mathcal{X} = (k, \vec{\theta}^{(k)})$, only a limited number of moves $m$ are typically available, namely those for which $j_m(\mathcal{X}) > 0$. With probability $1 - \sum_m j_m(\mathcal{X})$, no move type is attempted.

Some additional remarks about the above procedure are in order. The acceptance probability simplifies if one of $u$ or $u'$ is a null vector, thus needing to generate only one set of latent variables. The proposal mechanisms can be generalised by allowing the distributions of $u$ or $u'$ to depend on the states $\mathcal{X}$ or $\mathcal{X}'$. Under such a generalisation, $g(u)$ and $g(u')$ are replaced by $g(u|\mathcal{X})$ and $g(u'|\mathcal{X}')$ in the acceptance probability. We can also generate these random variables from the prior distribution on the parameters, which helps facilitate cancellation in the acceptance probability. Furthermore, in a move that increases the dimension of the state space, it may be feasible to set the new parameters precisely equal to these random variables, i.e., the proposed parameter vector $\vec{\theta}^{(k')}$ is formed by concatenating $\vec{\theta}^{(k)}$ and $u$. In this case, the Jacobian of the transformation is 1. For a simple example of the RJMCMC procedure applied to model selection between Poissonian (1 d.o.f.) and binomial (2 d.o.f.) distributions, see Section 3.1 in [139].

# Chapter 4

# Reinterpretation of LHC results using SModelS

In Chapter 2, we have seen a range of BSM theories that have been proposed to address the shortcomings of the SM. The diverse nature of these theories translates into a variety of different new physics signals that could potentially be searched for at the LHC. Characterizing the signals from these theories is no easy feat, as it would not be immediately clear what particles are producing them, what are the dominant decay modes and other questions. Hence, many LHC searches for new physics often interpret their results in terms of *simplified models*, each with a small set of unambiguous parameters. However, constraints on such simplified models do not directly translate to full theoretical models. It is thus necessary to systematically quantify how the current experimental data constrains these full theories, especially in the absence of a strong deviation from the SM in the LHC data. Consequently, many reinterpretation software packages have been developed that allow phenomenologists to interpret experimental results in more generic scenarios.

There are two approaches that are considered by the reinterpretation community at large. One way is to reproduce experimental analyses through Monte Carlo simulations, and thus requires a (lightweight) version of the data processing performed in the experimental analyses, such as signal and background selections. Such "recasting" tools are often computationally expensive. The second approach focuses on reusing simplified model results through streamlined analysis inputs, such as efficiency and acceptance maps. While typically less sensitive to detailed kinematic variables, it offers significantly faster performance than the first method. The SModelS software package [1–6] falls into this category and will be the primary focus of this chapter.

This chapter is organised as follows. Section 4.1 provides a brief overview of the simplified models framework. Section 4.2 details the SModelS working principle, its database structure, and its outputs. Section 4.3 reviews the likelihood calculation in SModelS. Lastly, Section 4.4 summarises the study on global LHC constraints on electroweakinos with SModelS v2.3 [6]. The current version of SModelS and its database is version 3.1.0.

## 4.1 Simplified Models

A simplified model is defined by a set of hypothetical particles with specific production processes and decay channels. They are designed to characterize new physics

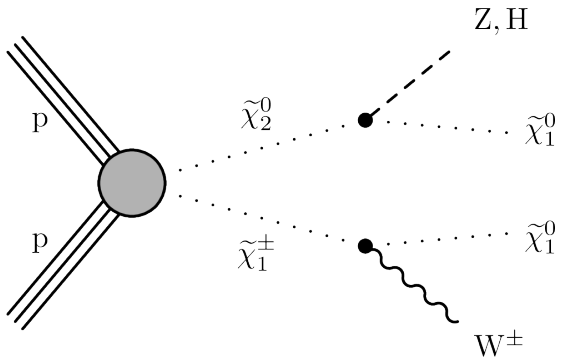


FIGURE 4.1: An example of a CMS search for electroweak production of charginos and neutralinos using simplified models [143]. The simplified model topology depicting chargino-neutralino pair production and their subsequent decays is shown in the top plot. Here, the chargino always decays to a $W$ boson and the lightest neutralino $\tilde{\chi}_1^0$ while the heavier neutralino decays 100% of the time to either a $Z$ or Higgs boson along with the $\tilde{\chi}_1^0$.

signatures with a small number of parameters related to collider physics, such as particle masses, production cross sections and branching ratios. In practice, the decay branching ratios are often fixed to 100%.

The simplified model framework can quantify the dependence of an experimental limit on the particle spectrum or a particular sequence of particle production and decays in a manner that is more general than most BSM theories. They show a clear relation between the free parameters of the model and the detector signatures. In this way, the theory dependence of the interpretations is reduced, allowing for generic descriptions of the final state signatures. Simplified models were first introduced to have a useful description of any $R$-parity conserving (RPC) "SUSY-like" new physics signal [140–142]. RPC "SUSY-like" includes theories that introduce new particles which carry SM quantum numbers (partner particles) and a parity under which partner particles are odd, such that the lightest such partner particle is stable. Their application was then extended from "SUSY-like" searches to Dark Matter searches, LLP searches, and resonant searches for exotic particles.

For each simplified model mass point, the product of experimental acceptance and efficiency ($\mathcal{A} \times \epsilon$) is calculated to convert the number of signal events into a signal cross section. This information is then used to derive a 95% confidence level upper limit on the product of the cross section and branching fraction ($\sigma \times$ BR) as a function of particle masses using the $CL_s$ prescription described in Section 3.1.1. The top plot of Figure 4.1 illustrates an example of a simplified model topology depicting chargino-neutralino pair production and their subsequent decays. Here, the chargino always decays to a $W$ boson and the lightest neutralino $\tilde{\chi}_1^0$ while the heavier neutralino decays 100% of the time to either a $Z$ or Higgs boson along with the $\tilde{\chi}_1^0$.

The corresponding 95% CL upper limit on the cross section as a function of the mass parameters presented by a CMS search [143] is shown in Figure 4.2. The thick black line in the chargino-neutralino mass plane represents the 95% exclusion limit. This limit is derived by comparing the observed cross section to the corresponding BSM reference cross section. All mass points under the thick black curve have a $CL_s$ value smaller than 0.05, and all points above it have a $CL_s$ value larger than 0.05. The solid

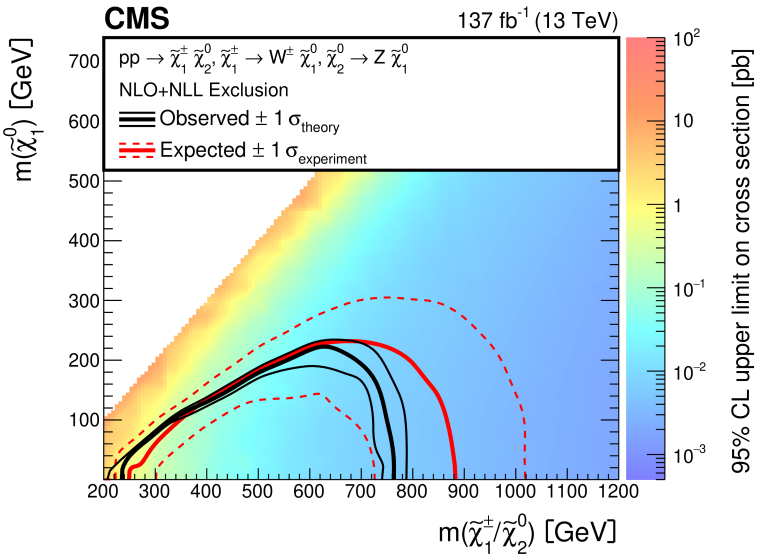


FIGURE 4.2: The 95% CL exclusion contour from CMS-SUS-21-002 [143] for the simplified model topology depicted in Figure 4.1.

red line shows the *expected* 95% exclusion limit evaluated using the SM background predictions instead of the observed values. This expected limit is used to estimate the sensitivity of a search. The two red dotted curves shows how the expected limit would vary if the SM prediction varies within its $1\sigma$ uncertainty. These contour lines are practical for comparing exclusion reaches between different analyses, but are not usable for reinterpretation. However, upper limits (ULs) on the cross section as well as efficiency maps (EMs) are reusable. The heatmap represents the upper limit on the cross sections at 95% exclusion CL. This limit is determined by scaling the predicted cross section until the exclusion confidence level equals 95%. All points outside the exclusion contour have a cross section upper limits larger than their nominal values, while points inside the contour have upper limits smaller than their nominal values.

## 4.2 SMODELS: Working Principle

SMODELS is an automatic public tool for the fast reinterpretation of simplified model results from the LHC. It is based on a general procedure to decompose BSM theories into Simplified Model Spectrum (SMS) topologies and obtain constraints from relevant experimental results implemented in the SMODELS database. This method allows a user to test BSM predictions for the LHC in a model independent framework, confronting them against the relevant results. As depicted in Figure 4.3, it comprises three main components:

- Decomposition of the input BSM spectrum into SMS topologies.
- Matching the decomposed SMS topologies with those from the experimental results implemented in the database.
- Performing statistical inference for the relevant SMS topologies using the limits provided by the experimental results.

This procedure assumes that the experimental results used to constrain simplified models are model-independent enough to be used to constrain other models with

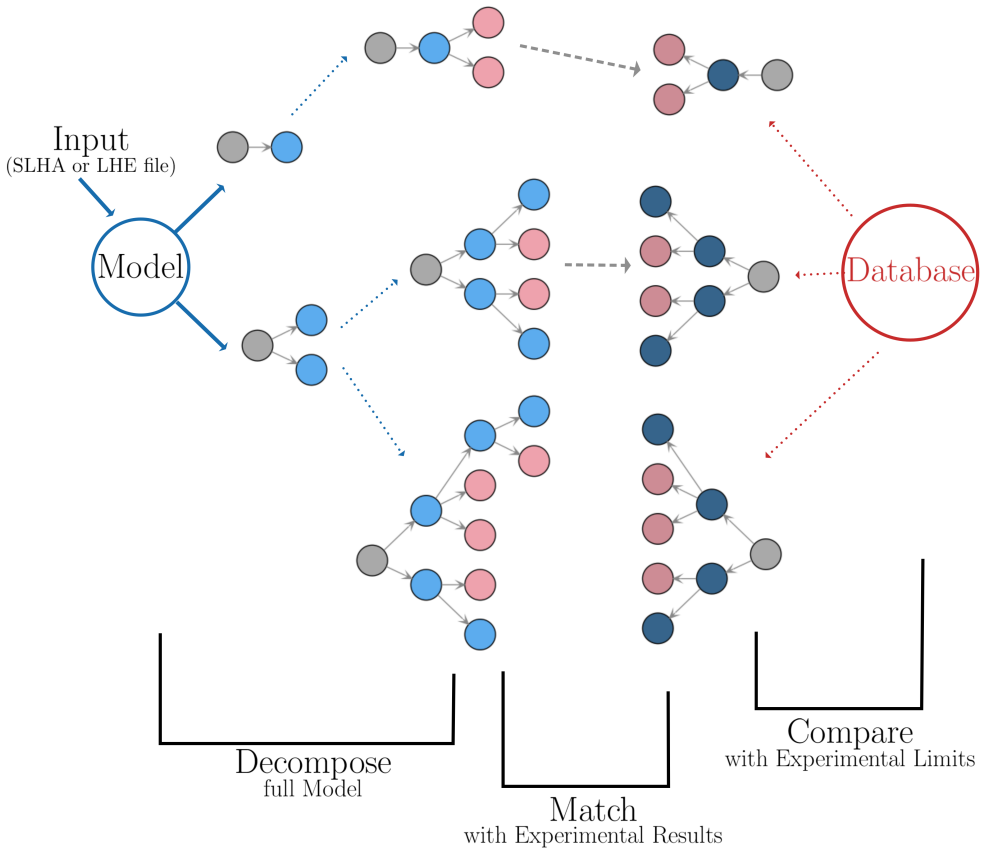


FIGURE 4.3: Schematic representation of the working principle of SModelS.

similar decay products and quantum numbers, independently of the kinematics. This allows us to map the signals of the input BSM model to its SMS-equivalent topologies and use the latter to constrain the BSM model. In particular, we assume that the details of the production mechanism can be ignored, taking into account only the total cross section of the production and the new particles produced in the $pp$ collisions.

Under these assumptions, SModelS v3 allows for SMS topologies to be represented by graphs, i.e. directed rooted trees, as shown in Figure 4.4. The root node labelled "PV" stands for the primary vertex and stands for the hard scattering collision ($pp \rightarrow$ produced particles). The other graph nodes represent all the BSM and SM particles appearing in the SMS topology. The decays from the parent particle to the daughter particle are represented by edges connecting the corresponding nodes. Further, all the required information about a specific particle is stored in the node, i.e. quantum numbers, mass, and total decay width. The decays of SM states are not specified in the graph.

The input file to SModelS must contain information about the particle content of the BSM model along with its parameters (masses, cross sections, ...) described in either a SUSY Les Houches Accord (SLHA) file format [144] or a Les Houches event (LHE) file format [145]. Once the input model is provided, SModelS begins the decomposition procedure, starting from the production cross sections for all the BSM particles and then generating all the possible decays according to the information provided. All such SMS topologies are constructed until the final decay particle states are stable. During the decomposition procedure, a weight is assigned to each SMS topology

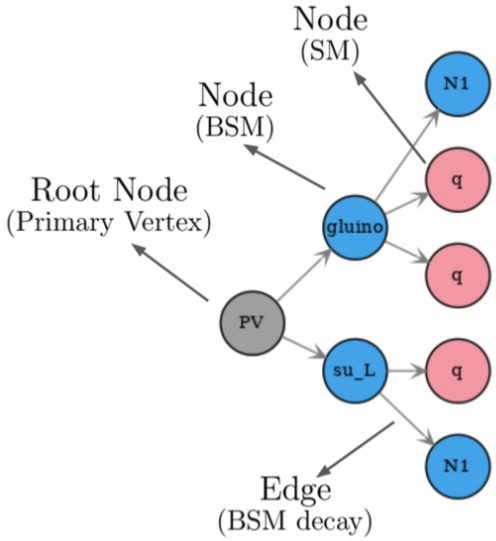


FIGURE 4.4: The representation of a simplified model topology as a graph in SModelS v3 along with its elements: root node, SM and BSM nodes, and edges representing the decays.

which multiplies the production cross section with the product of all the branching ratios ($\prod_i \mathrm{BR}_i$):

$$w_{\mathrm{SMS}} \equiv \sigma \times \prod_i \mathrm{BR}_i \,. \tag{4.1}$$

Upon decomposition, SModelS automatically compares each topology from the decomposition with those constrained by the experimental analyses in the SModelS database.[1] We then need to compute the relevant signal cross sections or theory predictions to compare against the experimental limits. SModelS presents such constraints by means of a $r$-value:

$$r_{(\mathrm{exp})} = \frac{\sigma^{\mathrm{BSM}}}{\sigma^{\mathrm{UL}}_{(\mathrm{exp})}} \,. \tag{4.2}$$

If $r_{(\mathrm{exp})} \geq 1$, then the model is (expected to be) excluded, otherwise it is not. In Eq. (4.2), $\sigma^{\mathrm{BSM}}$ is the effective cross section predicted by the BSM model and $\sigma^{\mathrm{UL}}_{(\mathrm{exp})}$ is the 95% confidence level (expected) upper limit on the effective cross section. The effective cross sections are compared against the signal upper limits obtained from two types of experimental results implemented in the SModelS database:

1. **Upper Limit (UL) type results:** These provide constraints on the cross section times branching ratio ($\sigma \times \mathrm{BR}$) for a simplified model. Such constraints are usually given in the format of UL maps that correspond to 95% CL upper limits on $\sigma \times \mathrm{BR}$ as a function of the BSM parameter space (typically the masses or slices over the mass planes). To obtain the $r$-value from UL results, we can directly

[1] For more details on the matching procedure, refer to **SMS Matching** section in [146].

compare the weight of the SMS topology to the corresponding upper limit on $\sigma \times \text{BR}$:

$$r = \frac{\sigma^{\text{BSM}}}{\sigma^{\text{UL}}} = \frac{w_{\text{SMS}}}{\sigma^{\text{UL}}} \,. \tag{4.3}$$

If upper limits on the expected $\sigma \times \text{BR}$ are given along with the observed, we can then compute the expected $r$-value. However, the disadvantage of having only UL results is that their interpretation is limited to constraining individual signal topologies, as not enough information is available to build a likelihood for the signal.

2. **Efficiency Map (EM) type results:** These provide constraints on the total number of signal events in a specific signal region ($N_s^{\text{SR}}$). Equivalently, we can consider this as a limit on the effective cross section $\sigma^{\text{SR}} = N_s^{\text{SR}}/\mathcal{L} = \sigma \times (\epsilon \times \mathcal{A})^{\text{SR}} \times \prod_i \text{BR}_i$ where $\mathcal{L}$ is the integrated luminosity of the search. The term $(\epsilon \times \mathcal{A})^{\text{SR}}$ corresponds to the simulated efficiency times acceptance values, which are provided as a grid over the BSM parameter space for a specific signal region and a specific simplified model. The $r$-value is then obtained by comparing the effective signal region cross section to the signal upper limit for the respective signal region:

$$r = \frac{\sigma^{\text{BSM}}}{\sigma^{\text{UL}}} = \frac{w_{\text{SMS}} \times (\epsilon \times \mathcal{A})^{\text{SR}}}{\sigma^{\text{SR,UL}}} \,, \tag{4.4}$$

where $\sigma^{\text{SR,UL}} = N_s^{\text{SR,UL}}/\mathcal{L}$. The expected $r$-value can be computed by substituting the expected SM events in place of the signal events in the upper limit. A useful property of these type of results is that they can be used to constrain combinations of SMS topologies that contribute to the same SR. Moreover, given the observed and expected number of events per SR, one can build a likelihood for the signal strength per SR. Additionally, if correlations of background uncertainties across SRs are provided by the experiment, we can build a combined likelihood for the entire search (refer to Section 4.3 for more details).

The structure of the SModelS database is depicted in Figure 4.5. Database entries are categorised according to the center-of-mass energy (8 or 13 TeV) and the experiment collaboration (ATLAS or CMS) of their analyses. Depending on the reinterpretation material provided by the experimental collaborations, UL- or EM-type results, or both, are implemented for an individual analysis. If both types of results are implemented, two different database entries are added, where a suffix "-eff" is appended to the name of the folder containing the EM-type results. The name of the folder corresponds to the name/ID of the analysis being implemented (ex: ATLAS-SUSY-2018-11, CMS-SUS-21-002).

Each database entry has a `globalinfo.txt` file which contains the general information such as the name of the analysis, the energy scale of the $pp$ collisions and the integrated luminosity. The UL-type results contain a sub-folder which collects the upper-limit maps for all the simplified topologies constrained by the analysis. Such maps are stored in a `TxName.txt` file, where "TxName" stands for a shorthand notation

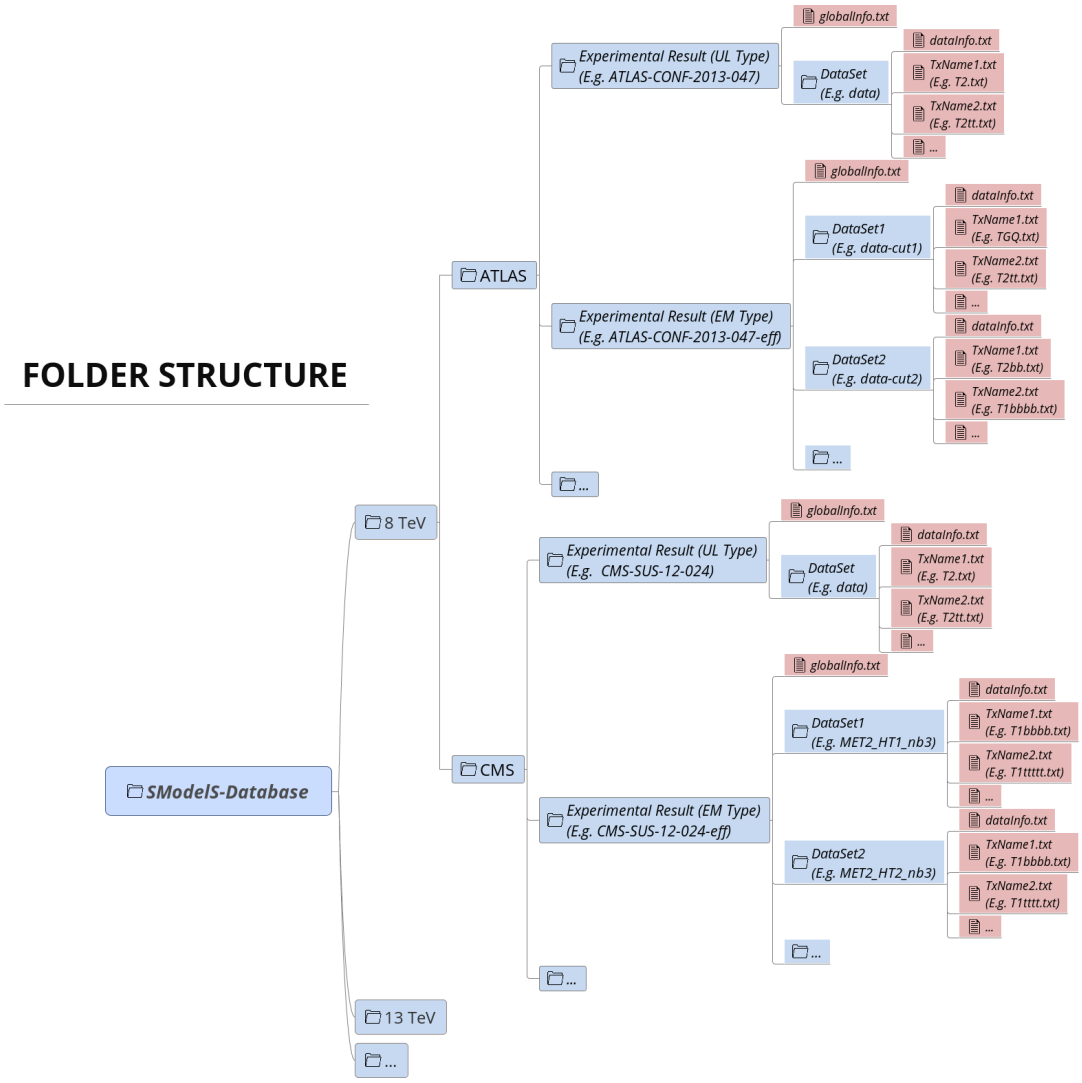


FIGURE 4.5: The structure of the SModelS database. Database entries are categorised according to the center-of-mass energy (currently, 8 or 13 TeV) and the experiment (ATLAS or CMS) of their analyses. They are further categorised based on the type of results they contain (UL- or EM-type results).

given to a SMS topology.[2] The file additionally contains a string representation of the SMS topology with the final state signatures. For EM-type results, a sub-folder is assigned to each SR designed by the experimental collaborations. These folders contain similar `TxName.txt` files as in the UL-type results, where instead of upper-limit maps, they contain the efficiency maps for the corresponding SR and simplified model. In addition, a `dataInfo.txt` file is present in each sub-folder indicating the name of the SR, the number of expected SM events, its uncertainty and the actual number of events observed, as well as the 95% CL on the expected and observed cross section upper limits. The full list of analyses implemented in SModelS database v3.1.0 can be found in Appendix B.

[2]For a complete list of TxNames considered in SModelS, see `smodels.github.io/docs/SmsDictionary`.

### 4.2.1 Running SModelS

When the user provides SLHA files or LHE files as an input, they can then run a command-line tool `runSModelS.py`, whose output reports on the SMS decomposition and theory predictions of the input BSM model. A typical usage is:

```
./runSModelS.py -f FILENAME -p PARAMETERFILE -o OUTPUTDIR
```

Here, `FILENAME` is the path to the input file, while `PARAMETERFILE` is the path to a file containing a list of SModelS parameters that allows the user to change the default options in SModelS depending on the use case. `OUTPUTDIR` specifies the path to the directory where the output of the SModelS results would be stored. The last two arguments are optional, and if not specified, the default ones will be used. More information on the execution of the command can be obtained by running `./runSModelS.py -h`.

As mentioned above, the user can change some default parameters while running SModelS with the help of a parameter file. A subset of the most relevant parameters for the user is listed below:

- `combineSRs`: If set to `True`, compute the constraints by combining the SRs when possible (for EM-type results, see Section 4.3). Else, only the constraint from the most sensitive SR is used, i.e. the one that gives the highest $r_{\text{exp}}$.[3]

- `combineAnas`: This is an optional argument that takes in a list of analysis IDs separated by commas to be combined. All the analyses in the list are assumed to be fully uncorrelated, so it is up to the user to make sure that the analyses can be safely combined.

- `reportAllSRs`: If set to `True`, return constraints from all matched SRs. Else, return according to condition set by `combineSRs`.

- `model`: Provide a path to a file that defines the particle content of the BSM model. If not defined, SModelS reads the particle content from the input BSM model specified via `FILENAME`.

- `ignorePromptQNumbers`: Provide a list of quantum numbers that can be ignored for promptly decaying particles. Many experimental searches are insensitive to the properties of particles with prompt decays. Hence, SModelS has the option to ignore such properties, which can greatly reduce the running time. This is a new option that is available from SModelS v3.0.0 onward.

- `sigmacut`: Specify the minimum SMS weight $w_{\text{SMS}}$. SMS topologies with a weight below this value are not taken into account during the decomposition procedure. The default value is 0.005 fb.

- `minmassgap`: Specify the maximum mass difference between BSM particles to compress topologies. When the mass difference between a parent BSM particle and the daughter BSM particle is small, the decay often produces soft SM final states that cannot be detected. As a good approximation, we neglect such soft final states and compress the respective decay. The default value is 5 GeV.

[3] The most sensitive SR is defined as the one that *is expected* to most constrain the BSM model.

- `minmassgapISR`: Specify the maximum value of the mass difference (in GeV) for performing mass compression leading to ISR signatures. If not defined, a default value of 1 GeV is assumed. This is only used if we enforce mass compression. This is a new option that is available from SModelS v3.0.0 onward.

- `path`: Input the path to the SModelS database, which can be supplied by specifying the directory name of the database, the path to a pickle file or a URL path.

- `analyses`: If set to `all`, compare against all experimental analyses in the database. Otherwise, only a list of analysis IDs can be given to test the input model against a reduced database.

- `txnames`: If set to `all`, compare against all SMS topologies implemented in the database. Otherwise, only a list of TxNames given is considered for comparison.

- `dataselector`. If set to `upperLimits` (`efficiencyMaps`), return constraints only from UL-type (EM-type) results. Else, if set to `all`, return constraints from both types of results.

- `outputType`: List the output formats to present the SModelS results.

The results of SModelS are then printed in `OUTPUTDIR` according to the formats specified in `outputType`. The available outputs are a human-readable screen output (stdout), a log output (a stdout redirected to a .log file), a Python dictionary, a XML file and a SLHA file. If the user runs over multiple files, an additional text output (`summary.txt`) is generated which provides a summary of the results for each input file.

The output typically contains the following information for each matched simplified model and database entry:

- the name of the database entry.

- the type of data constraining the model – "upper limit" for UL-type results, name of SR which best constrains the model for EM-type results, or "combined" if SRs are combined.

- TxName(s) of the constrained SMS topology(ies).

- the center-of-mass energy.

- the theory prediction of the BSM model (given by values in the numerator in Eq. (4.3) or Eq. (4.4) depending on the data type).

- the observed experimental limit on the theoretical prediction (given by values in the denominator in Eq. (4.3) or Eq. (4.4) depending on the data type).

- the observed and expected $r$-values (no expected $r$-value is computed for UL-type results if expected upper limit maps are not provided).

In addition, the likelihoods under the SM and BSM hypothesis, as well as the maximum likelihood, are returned for EM-type results. Further, if the user provides a list of analyses that can be considered to be combined, the aforementioned quantities are also computed and printed for the said combination. The output file also contains information about unconstrained simplified models. It comprises the theoretical

prediction and the SMS topology of the simplified models for which no match was found in the database (both for prompt and displaced decays), or for which a match was found but the particle parameters were outside the experimental UL and/or EM grid(s).

## 4.3 Likelihood computation in SModelS

As mentioned in the previous section, SModelS can provide additional statistical information about the constrained model for EM-type results by computing likelihoods for the tested signal. This likelihood describes the plausibility for a signal strength $\mu$ given data $D$:

$$L(\mu, \theta|D) = P(D|\mu s + b + \theta)p(\theta)\,. \tag{4.5}$$

Here, $s$ and $b$ refer to the number of predicted signal and background events, respectively. $\theta$ refers to the nuisance parameters that arise due to systematic effects, with $p(\theta)$ describing the probability distribution of the nuisances.

### 4.3.1 Likelihood for individual SRs

If no information regarding correlation of signal regions is available, we compute a simplified likelihood [3] for the most sensitive (a.k.a. best) signal region. The most sensitive SR is defined as the one that gives the highest $r_{\text{exp}}$ value. A simplified likelihood assumes $p(\theta)$ to follow a Gaussian distribution centered around zero with a variance of $\delta^2$, and $P(D)$ corresponds to a counting variable and is thus described by a Poissonian. The likelihood for an individual SR thus takes the form:

$$L(\mu, \theta|D) = \frac{(\mu s + b + \theta)^{n_{\text{obs}}} e^{-(\mu s + b + \theta)}}{n_{\text{obs}}!} \exp\left(-\frac{\theta^2}{2\delta^2}\right), \tag{4.6}$$

where $n_{\text{obs}}$ is the number of observed signal events in the SR and $\delta$ is the one sigma background uncertainty. By default, we profile over the nuisance parameters $\theta$. We take the values for $n_{\text{obs}}, b$ and $\delta$ from the published information on HEPData. From this likelihood, we can then compute a 95% CL limit on $\mu$ using the $CL_s$ limit from the test statistic $q_\mu$ [147],

$$q_\mu = \begin{cases} -2\ln\left(\frac{L(\mu,\hat{\hat{\theta}})}{L(\hat{\mu},\hat{\theta})}\right), & \hat{\mu} \leq \mu\,; \\ 0\,, & \hat{\mu} > \mu\,, \end{cases} \tag{4.7}$$

where $\hat{\mu}$ and $\hat{\theta}$ are the maximum likelihood estimators and $\hat{\hat{\theta}}$ is the value of $\theta$ that maximises $L$ at the specific $\mu$. The upper limit on the cross section is then obtained by multiplying the fiducial cross section with the upper limit on $\mu$: $\sigma^{\text{UL}} = \mu^{\text{UL}}\sigma^{\text{BSM}}$. The expected upper limits for both the signal strength and the cross section can be computed by assuming all the observed yields to come from the SM background, i.e. $n_{\text{obs}} = b$. In addition to the upper limits, SModelS also reports the likelihood values for $L_{\text{BSM}} \equiv L(\mu = 1)$, $L_{\text{SM}} \equiv L(\mu = 0)$ and $L_{\text{max}} \equiv L(\hat{\mu})$.

### 4.3.2 Likelihood for combined SRs

If background correlations across SRs for a search are provided by the experimental collaborations, then SModelS can go a significant step further to compute the likelihood for the entire analysis by combining information from all the SRs. Such information is usually provided in the form of a correlation or covariance matrix (usually by the CMS collaboration) or in the form of a full statistical model (usually by the ATLAS collaboration, and more recently by the CMS collaboration). Depending on the type of information provided, SModelS can compute combined SR likelihoods using three different approaches.

#### Simplified likelihood v1: Gaussian uncertainties

This likelihood computation framework was initially introduced in [148] and is available in SModelS since v1.1.3 [4]. Here, all nuisance parameters are consolidated into a single distribution using a multivariate Gaussian. Poissonians are still used to describe the counting variables in the individual signal regions. The likelihood for the signal hypothesis when combining $N$ SRs takes the form:

$$L(\mu, \theta|D) = \prod_{i=1}^{N} \frac{(\mu s_i + b_i + \theta_i)^{n^i_{\text{obs}}} e^{-(\mu s_i + b_i + \theta_i)}}{n^i_{\text{obs}}!} \exp\left( -\frac{1}{2}\vec{\theta}^T V^{-1} \vec{\theta} \right). \tag{4.8}$$

Here, $\mu$ is the overall signal strength and $V$ represents the covariance matrix provided. From here on, this approach of computing likelihood is referred to as SLv1. To compute the observed and expected upper limits on the signal strength and the cross section, we follow the same procedure as described in Section 4.3.1.

As long as the Gaussian approximation for the nuisances is valid, SLv1 demonstrates satisfactory performance. It is however not a good approximation for very low expected events.

#### Simplified Likelihood v2: Gaussian with a skew

To account for non-Gaussian effects in the nuisances, we can incorporate a skewness term in the Gaussian distribution. This was first proposed in [149], where a Poissonian was once again used to model the observed events, while the distribution of the nuisances was slightly modified:

$$L(\mu|D) = \prod_{i=1}^{N} \text{Pois}(\mu s_i + a_i + b_i\theta_i + c_i\theta_i^2) \cdot \frac{e^{-\frac{1}{2}\vec{\theta}^T \rho^{-1} \vec{\theta}}}{\sqrt{(2\pi)^N}}. \tag{4.9}$$

In the above equation, $a_i$ represents the number of background events originally labeled as $b_i$ in Eq. (4.8). The nuisances have been relabeled as $\theta_i \to b_i\theta_i + c_i\theta_i^2$. The coefficients $a_i, b_i$ and $c_i$ are related to the first three statistical moments. The first moment is the mean, the second moment is the covariance $V_{ij} = b_i b_j \rho_i j + 2c_i c_j \rho_{ij}^2$ and the diagonal element of the third moment is $m_{3,i} = 6b_i^2 c_i + 8c_i^3$. To extend the SLv1 framework to the SLv2, all that is needed are the third moments $m_3$. This can be computed from a bifurcated Gaussian given asymmetric background uncertainties $\delta_-$ and $\delta_+$ [150]

$$m_3 = \frac{2}{\delta_- + \delta_+}\left[\delta_- \int_{-\infty}^{0} x^3\,\mathrm{Gauss}(x;0,\delta_-^2)\,dx + \delta_+ \int_{0}^{\infty} x^3\,\mathrm{Gauss}(x;0,\delta_+^2)\,dx\right]. \quad (4.10)$$

The SLv2 has been technically available in SModelS for a while, but was not used due to lack of experimental information. The CMS-SUS-20-004 analysis is the first analysis to provide the required information and SModelS is the first reinterpretation tool to make effective use of the formalism of [149].

#### HistFactory statistical models

The ATLAS collaboration has started to publish full statistical models using a JSON serialisation for Run 2 results with $139 fb^{-1}$ luminosity on HEPData. This full statistical model is based on HistFactory [151] and has the complete set of nuisance parameters, describing systematic and statistical uncertainties and their correlations across signal regions at the same fidelity as used in the searches. Since SModelS v1.2.4 [152], these statistical models have been implemented via an interface to the pyhf package [153], a pure-Python implementation of the HistFactory workspaces. Whenever a HistFactory statistical model is available in the database, SModelS then relegates the evaluation of the likelihood to pyhf where, internally, the calculation is again based on the asymptotic formulas of [147]. More technically, the full likelihood takes the form:

$$L(\eta,\chi|n,a) = \prod_{c\,\in\,\text{channels}}\prod_{b\,\in\,\text{bins}} \mathrm{Pois}(n_{cb}|\nu_{cb}(\eta,\chi)) \prod_{\chi} c_\chi(a_\chi|\chi)\,, \quad (4.11)$$

where $\eta, \chi, n, a$ represent the free parameters, the constrained parameters, the number of observed events, and the additional global observables from auxiliary measurements, respectively. The first two products contain the simultaneous measurement of multiple channels (defined as disjoint binned distributions), while the third product is over the constrained parameters $\chi$ with a constraint term $c$ based on the auxiliary data $a$. $\nu_{cb}(\eta,\chi)$ represents the expected rate of events as a function of the unconstrained parameters $\eta$ and constrained parameters $\chi$.

The evaluation of full HistFactory models, that can have hundreds of nuisance parameters ($\theta = \{\eta,\chi\}$), can be very CPU intensive, especially when combining analyses. For this reason, the official SModelS database contains mostly simplified versions of the HistFactory models [154], which were derived from the full ones using the simplify tool [155]. There are however certain cases – ATLAS-SUSY-2018-16 analysis [156] and the ATLAS-SUSY-2019-08 analysis [157] – where we use the full HistFactory models instead of the simplified ones when the latter does not reproduce the results from the former well enough.

Figure 4.6 depicts the importance of combining SRs over using the likelihood constructed from the best SR to reproduce the experimental limits. In addition, it also shows how the simplified statistical model works well for one analysis (ATLAS-SUSY-2019-09 [158]), while it fails for another (ATLAS-SUSY-2018-16 [156]) forcing the use of the full HistFactory statistical model.

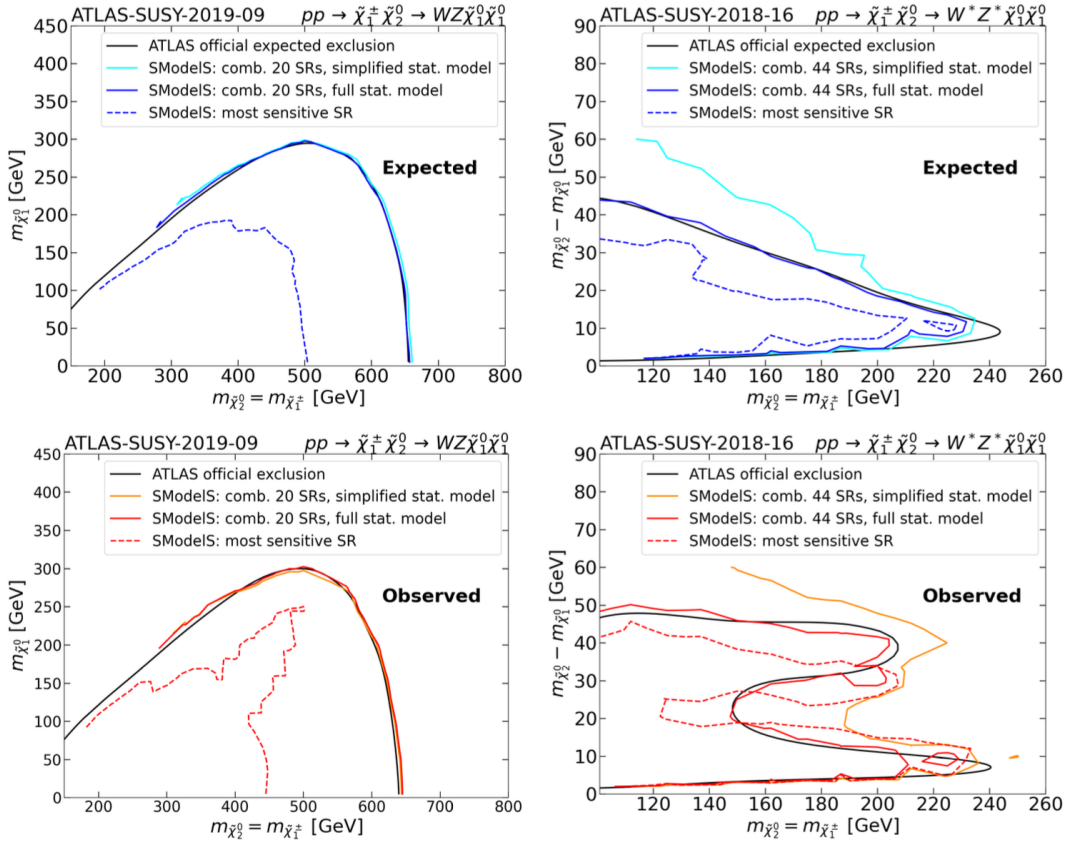


FIGURE 4.6: SModelS reproducing the expected (top) and observed (bottom) experimental limits using the most sensitive SR, the full statistical model and the simplified one. The plots on the left shows the simplified likelihood working well for ATLAS-SUSY-2019-09 [158] and plots on the right shows the failure of the simplified likelihood computation for ATLAS-SUSY-2018-16 [156].

### 4.3.3 Combining likelihoods of uncorrelated analyses

SModelS also provides the possibility to combine likelihoods from different analyses when the given analyses can be considered to be approximately uncorrelated. Two analyses are considered to be approximately uncorrelated if their SRs do not overlap and we can neglect inter-analyses correlations of systematic uncertainties (stemming from, e.g., luminosity measurements). Though overlaps of SRs of one analysis with the control regions of another in the combination can in principle induce correlations of systematic uncertainties, we generally expect such effects to be negligible compared to other uncertainties in SModelS. We can then build a combined likelihood $L_c$ for all such combinable analyses by simply taking the product of the individual analyses $L_i$:

$$L_c(\mu) = \prod_i L_i(\mu s_i)\,, \tag{4.12}$$

where $\mu$ is the common signal strength assumed for all analyses. The individual likelihoods can be computed either from the best signal region likelihoods and/or combined signal region likelihoods (as explained in the previous sections).

To construct a global likelihood for all experimental results at the LHC, one would need to know the mutual correlations across experiments on top of having the likelihood for individual analyses. However, to quantify correlations across analyses is a difficult task and dedicated effort is required by experimental collaborations. For now, the user needs to determine which analyses can be combined and provide it as an input to the SModelS parameter file. Generally, results from different experiments (ATLAS and CMS), different LHC runs (8 and 13 TeV), as well as fully hadronic and fully leptonic analyses are regarded as approximately uncorrelated [7], at least within the approximations of SModelS. More sophisticated combinations of analyses could be constructed through detailed examination of signal (and control) region definitions; an approach based on Monte Carlo simulation is presented in [159].

The combination of analyses is interesting for two reasons. First, the signal of a particular BSM scenario may be manifest in different final states, which are constrained by different analyses. Combining them uses more of the available data and thus provides more robust, and usually stronger, constraints. Second, experimental analyses can always be subject to over- or under-fluctuations of the backgrounds. In the former case, the observed limit is weaker, in the latter case stronger, than the expected limit. Again, the combination of different, approximately independent analyses can mitigate this effect and provide more robust constraints. The next section describes the impact of combining different LHC results to constrain the electroweakino sector of the MSSM.

## 4.4 Impact of combining analyses on the electroweakino sector of the MSSM

Experimental searches at the LHC usually search for SUSY signals by targeting final state signatures of specific simplified-model scenarios. While this approach facilitates straightforward interpretation, this often comes at the cost of sacrificing the richness of SUSY phenomenology. If we even just study the MSSM, its decay patterns and thus signatures can be quite complex, and limits on specific simplified model scenarios may not be sufficient to cover its vast parameter space. With the ever increasing amount of constraints, it becomes necessary to aggregate all the results to see what the data actually tells us. Global reinterpretations of this vast set of experimental results are essential to either rigorously rule out parameter spaces or shine light on interesting phase space regions.

Both experimentalists and phenomenologists stress the importance of combining experimental results. The ATLAS and CMS collaborations performed statistical combinations of results from searches in different exclusive final state using LHC Run 1 data (see [160, 161]) and studied their impact on constraining the pMSSM phase space. More recently, ATLAS published their summary of constraints on the electroweak production of charginos and neutralinos from LHC Run 2 data, also interpreted within the pMSSM [71].

Phenomenologists too have conducted independent studies of combining experimental results by through reinterpretation of existing searches in different theoretical scenarios. The GAMBIT collaboration, for example, has conducted global fits not only on SUSY parameter space [162–164] but also on simplified dark matter scenarios [165].

In this section, we explore how SModelS can be used for global reinterpretation of LHC results, particularly in constraining the electroweakino parameter space of the MSSM. The following discussion summarizes the study presented in [166].

### 4.4.1 Parameter space

We reuse the electroweakino (henceforth referred to as EW-ino) points scanned in the study [5] to set the global constraints on the EW-ino sector of the MSSM using SModelS v2.2 database. This is done as it allows for direct comparison with the earlier studies while also saving CPU time. Section 4.2 of [5] details the random scan of the following parameters within the corresponding ranges:

$$\begin{aligned} 10\,\text{GeV} < \quad & M_1 \quad < 3\,\text{TeV}\,; \\ 100\,\text{GeV} < \quad & M_2 \quad < 3\,\text{TeV}\,; \\ 100\,\text{GeV} < \quad & \mu \quad < 3\,\text{TeV}\,; \\ 5 < \quad & \tan\beta \quad < 50\,. \end{aligned} \tag{4.13}$$

All other SUSY breaking parameters were fixed to 10 TeV, assuming that the stop-sector parameters can always be adjusted such that $m_h \simeq 125$ GeV without influencing the EW-ino sector. We chose the lower limits on $M_2$ and $\mu$ to avoid the LEP constraints on light charginos, while the bounds on $\tan\beta$ were chosen to avoid Yukawa couplings from becoming non-perturbatively large. SOFTSUSY 4.1.11 was used to compute the mass spectra and decay tables, where we set $m_h = 125$ GeV for consistency of the decay calculations. All points have a neutralino LSP.

The complete scan in [5] consisted of close to 100k points. In this study, we selected the subset of points with only prompt decays (no long-lived particles, all decay widths $\Gamma_{\text{tot}} > 10^{-11}$ GeV). Further, to focus on the regions to which the current prompt EW-ino searches are sensitive, we imposed $m_{\tilde{\chi}_1^0} < 500$ GeV and $m_{\tilde{\chi}_1^\pm} < 1200$ GeV. We also removed a few points with $m_{\tilde{\chi}_1^\pm} < 103$ GeV and points with erroneous branching ratios in SOFTSUSY 4.1.11.[4] A total of 18544 points then constituted the EW-ino dataset which was then analysed with SModelS v2.3.

As bino-like LSP and non-bino-like LSP exhibit different phenomenology, it is often relevant to distinguish such scenarios. For a bino-like LSP, we consider a $m_{\tilde{\chi}_1^0}$ with at least 50% bino component, i.e. $N_{11}^2 \geq 0.5$, where $N$ is the neutralino mixing matrix (see Eq. (A.4) in Appendix A). Non-bino-like LSP points ($N_{11}^2 < 0.5$) feature a mostly higgsino-like, mostly wino-like, or strongly mixed $\tilde{\chi}_1^0$. The distributions of the values of $M_1$, $M_2$, and $\mu$ considered in our dataset are shown in Figure 4.7 where the left plot consists of points with a bino-like LSP and right plot consists of points with a non-bino-like LSP. Requiring $m_{\tilde{\chi}_1^0} < 500$ GeV results in the cutoff at $M_1 \approx 500$ GeV shown in the left plot, while the edges around $M_2$, $\mu \approx 1.2$ TeV come from imposing $m_{\tilde{\chi}_1^\pm} < 1200$ GeV. The edge at $\mu \approx 500$ GeV in the right plot comes from requiring $m_{\tilde{\chi}_1^0} < 500$ GeV along with promptly decaying $\tilde{\chi}_1^\pm$, whereas the range of $M_1$ and $M_2$ go from small to very large values. That the $M_2$ distribution is suppressed towards small values, instead of showing an edge around 500 GeV, is due to the fact that light

[4] This bug, which was then corrected, occurred in the transition from 2-body to 3-body neutralino decays https://ballanach.github.io/softsusy/.

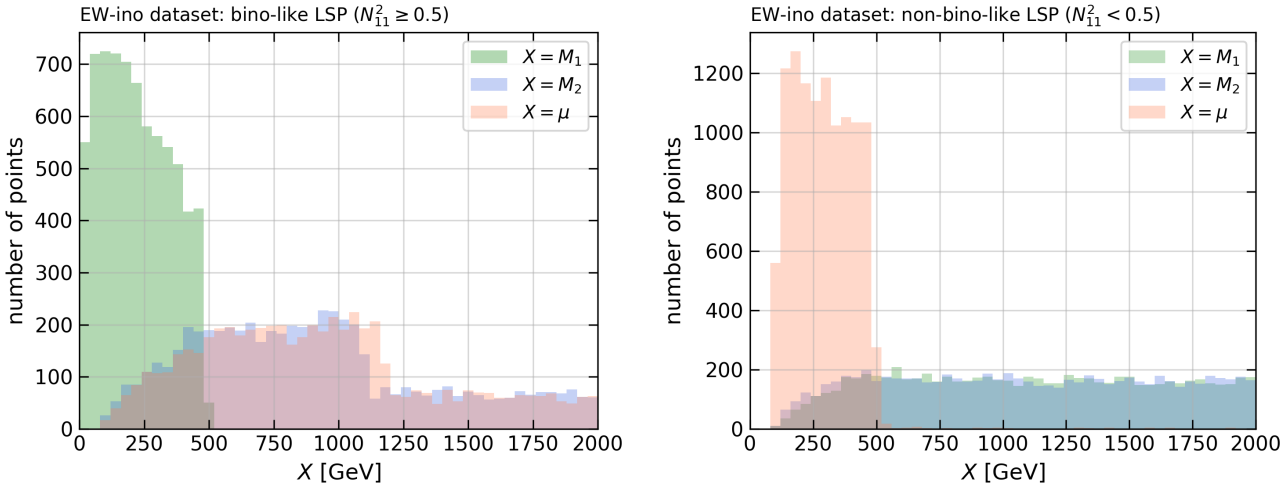


FIGURE 4.7: Distributions of $M_1$, $M_2$ and $\mu$ in the set of EW-ino scan points used in this study; on the left for points with a bino-like LSP, on the right for points with a non-bino-like LSP. Only values up to 2 TeV are shown.

winos are generally long-lived; as mentioned we removed these cases from the scan. Also, there is no edge around 1.2 TeV, because for non-bino-like LSP points the $\tilde{\chi}_1^\pm$ is always close in mass to the $\tilde{\chi}_1^0$ and thus $m_{\tilde{\chi}_1} < 540$ GeV.

The properties of non-bino-like LSP points can be understood from Figure 4.8, which shows these points in the $\mu$ vs. $M_2$ plane (left) and the $M_2/M_1$ vs. $M_2/\mu$ plane (right). The higgsino content of the LSP is indicated by the colour code: for red points the $\tilde{\chi}_1^0$ is mostly higgsino, while for purple points it is mostly wino. In between, from yellow to green to turquoise, the $\tilde{\chi}_1^0$ is a strongly mixed state of higgsino and wino ($\mu \approx M_2$), higgsino and bino ($\mu \approx M_1$) or wino and bino ($M_2 \approx M_1$). The sparsity of points at low $M_2$ (visible in the left plot) is due to removing long-lived charginos from the scan. In fact, for all the remaining points in the region $M_2 < 500$ GeV and $\mu \gtrsim M_2 + 100$ GeV in Figure 4.8, the bino mass parameter $M_1$ is close to $M_2$, roughly $M_1 \in [1, 1.2] \times M_2$. This increases the splitting between the $\tilde{\chi}_1^0$ and the $\tilde{\chi}_1^\pm$, such that the latter is no longer long-lived.

We confront each point in the EW-ino dataset is against the experimental results of the analyses detailed in Section 3 of [6]. All the analyses in this list provide reinterpretation material for SModelS to compute the likelihood $L(\mu, \theta|D)$ for the respective SUSY signal. As mentioned in Section 4.2, SModelS reports the result in the form of $r$-values, with $r$ defined as the ratio of the predicted fiducial cross section of the signal over the corresponding upper limit ($r \equiv 1/\mu_{95}$). Often, a point is considered excluded if the highest observed $r$-value $r_{obs}^{\max} \geq 1$. This corresponds to an exclusion by the *most constraining* analysis. The statistically more robust approach is to base the exclusion on the *most sensitive* (or "best") analysis, i.e. the analysis with the highest $r_{exp}$; a point is then considered as excluded if the corresponding observed $r$-value $r_{obs}^{\text{best}} \geq 1$. As discussed in [6], either approach is quite sensitive to statistical fluctuations, which motivates us to attempt a global combination.

A few comments on the parameter settings while running SModelS are in order. We set the parameter `sigmacut` to be $10^{-3}$ fb and `minmassgap` to be 10 GeV (which differs

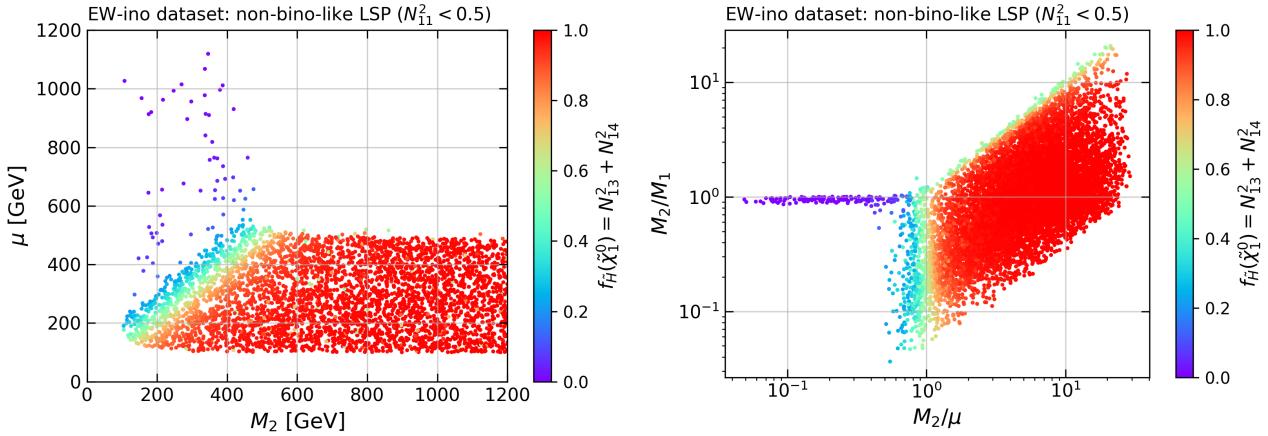


FIGURE 4.8: Non-bino-like LSP points, on the left in the $\mu$ vs. $M_2$ plane and on the right in the $M_2/M_1$ vs. $M_2/\mu$ plane. The colour code shows higgsino content of the LSP. In the left plot, the $x$- and $y$-axes go only up to 1.2 TeV for better visibility of the mixed region, but in both directions scan points extend up to 3 TeV.

from the default value of 5 GeV). The `minmassgap` setting is relevant in particular if one or more SUSY particles have mass close to the mass of the LSP, as is the case for non-bino-like LSP points.

### 4.4.2 Combination strategy

We now need to construct a global likelihood from the individual analysis likelihoods. As detailed in Section 4.3.3, a combined likelihood $L_C$ for a combination of analyses $C$ is the product of the individual likelihoods $L_i$. As we do not have access to inter-analyses correlations, we consider two analyses to be combinable only if they are approximately uncorrelated. We then have to address two questions: i) which analyses can be treated as uncorrelated and ii) how to select the optimal combination from all possible combinations.

For i), we treat analyses from different LHC runs, and from distinct experiments (ATLAS or CMS) as uncorrelated. Furthermore, we treat analyses with non-overlapping signal regions as approximately uncorrelated by carefully examining SR definitions (see Appendix C) to determine orthogonality or overlap, yielding the combinability matrix in Figure 4.9. This approximation neglects inter-analysis correlations of systematic uncertainties (e.g., luminosity measurements) and potential correlations from SR/control region overlaps between analyses. Such effects require full recasts including signal and control regions, which is beyond current capabilities. However, we expect these effects to be small compared to other uncertainties in SModelS and reinterpretation studies in general.

For ii), since not all analyses can enter the same combination, multiple combinations can be built based on this combinability matrix. We define the "best combination" as the most sensitive one – that with the lowest expected signal strength limit $\mu_{95}^{\text{exp}}$ (or highest $r_{\text{exp}}$). Since computing $\mu_{95}^{\text{exp}}$ is time-consuming, we assume the combination that minimizes

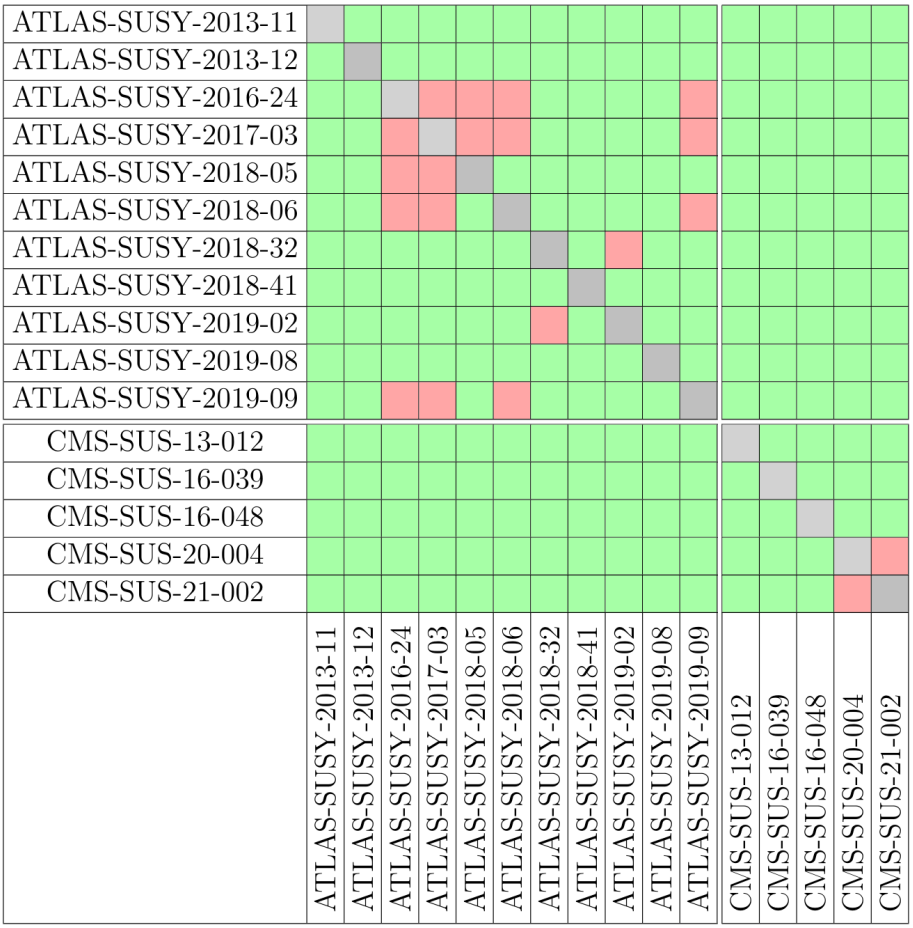


FIGURE 4.9: Matrix displaying the combinability of the searches considered in this study. Green means the two analyses are assumed to be approximately uncorrelated and can be combined, while red means that they are not and shouldn't be combined.

$$w = \frac{L^{\text{exp}}(\text{BSM})}{L^{\text{exp}}(\text{SM})}, \tag{4.14}$$

is the one with the lowest $\mu_{95}^{\text{exp}}$. Here, $L^{\text{exp}}(\text{H})$ is the expected combined likelihood under the H hypothesis. To find the best combination of analyses given a model point, we follow the following steps:

1. Select analyses which are sensitive to the model point, i.e, $\mu_{95}^{\text{exp}} \leq 10$. Though insensitive analyses can be considered for the combination, they do not impact the final result and were removed for computational efficiency and stability.

2. List all potential combinations according to the combinability matrix, Figure 4.9. If there is only one analysis sensitive to the tested model, the "combination" corresponds to that individual analysis.

3. Remove all combinations that are subsets of other combinations. This ensures that all available information is used to build the combination.

4. Compute $w$ for all the remaining combinations and select the one that gives the lowest value.

In practice, the combiner algorithm from [7] was used with minimal modifications to determine the best combination for each point in our EW-ino dataset. We cross-checked the procedure with a second method, based on the PATHFINDER algorithm from [159] (for more details on this algorithm, see Section 6.4), which we adapted for this study to find the best combination of analyses, instead of the optimal SR combination in [159]. Both methods gave identical results.

In the following, we will refer to the best combination of analyses simply as "the combination".

### 4.4.3 Results

We investigated the impact of analysis combination on the EW-ino sector of the MSSM using the scanned parameter points and the combination strategy discussed in the previous subsections. Figure 4.10 shows the impact of combining analyses over the individual results in excluding the EW-ino parameter space. The left plot of Figure 4.10 depicts the gain in expected reach due to the combination, where a point is expected to be excluded if a result gives $r_{\text{exp}} \geq 1$. The plot also shows the individual analysis which mainly drive the expected exclusion: ATLAS-SUSY-2019-09 ($3\ell + \not{E}_T$ search), ATLAS-SUSY-2018-41 and CMS-SUS-21-002 (all hadronic searches). Due to the accumulation of statistics in the combination, the expected reach is enhanced, resulting in an increase of 48% in the expected number of excluded points (from 3081 to 4549 points). The right plot of Figure 4.10 depicts the impact of the combination on the observed number of excluded points with respect to the most sensitive and most constraining analyses (the analyses that give the highest $r_{\text{exp}}$ and $r_{\text{obs}}$ respectively).[5]

It is interesting to note that the combination excludes more points than the most constraining analysis up to $m_{\tilde{\chi}_1^\pm} \approx 700$ GeV. For higher masses, the under-fluctuations recorded by the hadronic ATLAS analysis result in a more aggressive exclusion when considering the most constraining analysis. All in all, the most sensitive analysis, the most constraining analysis and the combination exclude 3046, 3949, and 4124 points, respectively. We also note the importance of using NLO cross sections as 611 points ($\approx 15\%$) would not have been excluded by the combination had we used LO instead of NLO cross sections.

Figure 4.11 shows the different combination sets for excluded points featuring a bino-like LSP in the $m_{\tilde{\chi}_1^0}$ vs. $m_{\tilde{\chi}_1^\pm}$ plane. We note that the combinations form clusters in different regions of this parameter space, thus proving the stability of our procedure. Additionally, fewer analyses enter the combination as masses of $\tilde{\chi}_1^0$ or $\tilde{\chi}_1^\pm$ become larger, since most analyses are insensitive to high masses. This can be seen as we move from one colour patch to the next representing an analysis becoming (in)sensitive to the tested signal when $m_{\tilde{\chi}_1^0}$ or $m_{\tilde{\chi}_1^\pm}$ (increases) decreases. There are small overlapping regions due to the composition of the produced particles: for the wino-bino scenario, production cross sections are larger and the sensitivity of the analyses are extended, while for the higgsino-bino scenario the sensitivity is suppressed. Finally, the grey points constitute of many different combinations and are concentrated at low masses due to a large number of analyses being sensitive only in this region.

[5] We point out that using the largest $r_{\text{obs}}$ is not statistically sound, as it favours analyses which observed under-fluctuations in the data, thus artificially increasing the constraining power.

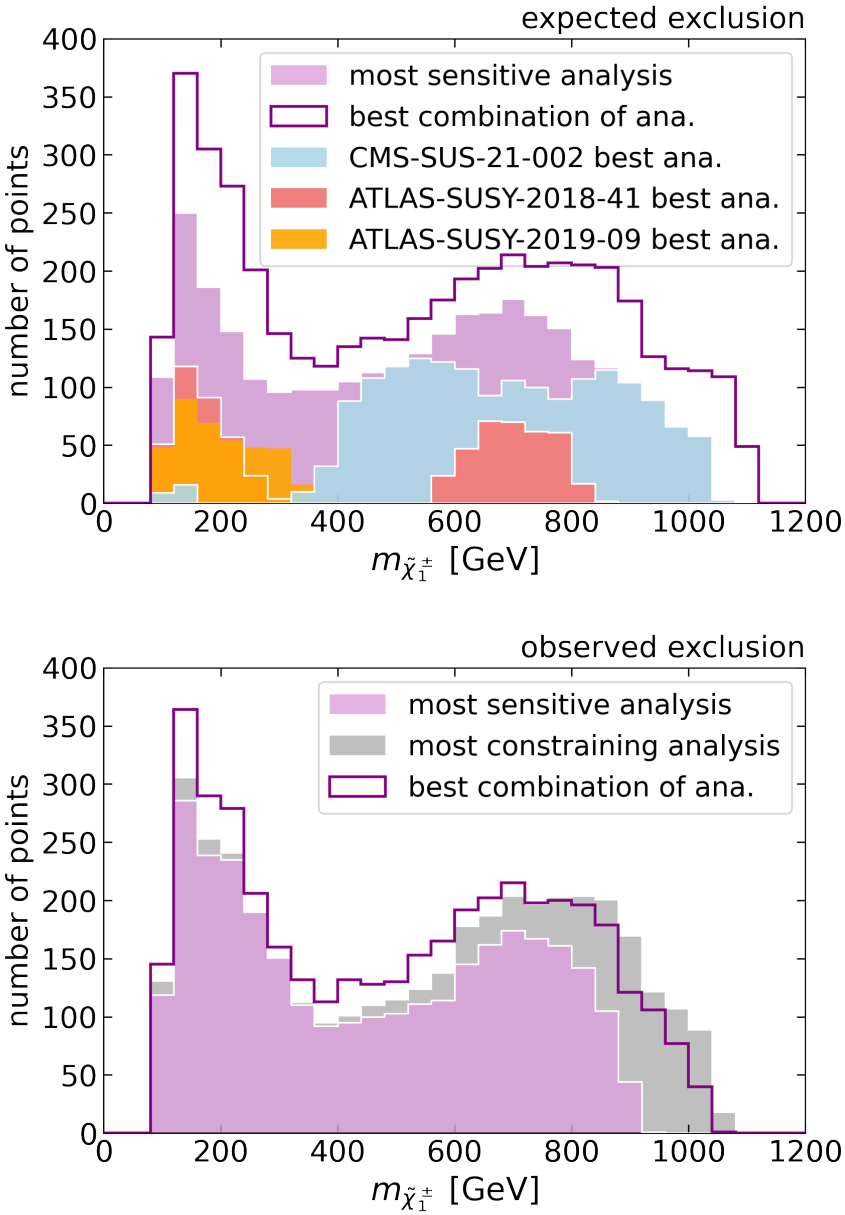


FIGURE 4.10: Number of points expected to be excluded (top) and number of points actually excluded (bottom) as determined by the most sensitive analysis (pink area) and the best combination of analyses (purple line). In addition, the left panel shows the impact of the two hadronic searches: CMS-SUS-21-002 (light blue) and ATLAS-SUSY-2018-41 (light red), along with the $3\ell + \not{E}_T$ search ATLAS-SUSY-2019-09 (orange). On the other hand, the right panel also displays the observed exclusion with respect to the most constraining analysis (grey).

A similar plot for points with a non-bino-like LSP is shown in Figure 4.12. Since we keep only points with promptly decaying $\tilde{\chi}_1^\pm$, the majority of points have a higgsino-like LSP. The number of points excluded by the combination is highly reduced for these scenarios.This is due to the fact that the higgsino-like LSP scenario produces a large number of final state topologies, many of which have no available LHC results. As already seen in Figure 4.11, the low mass region is populated by combinations made up of many analyses, while only four analyses are sensitive enough to enter the

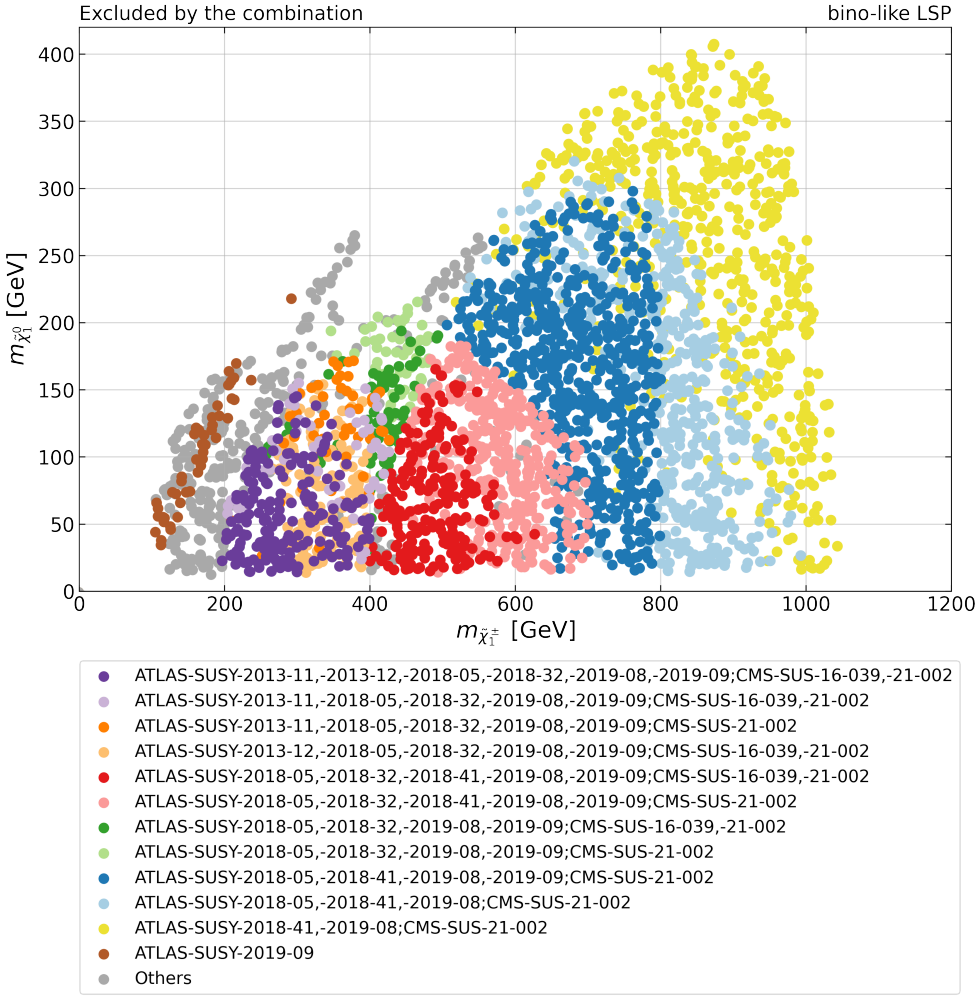


FIGURE 4.11: Most sensitive combinations in the $m_{\tilde{\chi}_1^0}$ vs. $m_{\tilde{\chi}_1^\pm}$ plane for points excluded by the combination and featuring a bino-like LSP. Only the combinations appearing at least 25 times are shown. The combinations that appeared less than 25 times fall into the "Others" category.

combination at high masses. The grey points at low LSP masses contain a sufficiently large $m_{\tilde{\chi}_1^\pm} - m_{\tilde{\chi}_1^0}$ mass gap and are excluded by higgsinos ($\tilde{\chi}_1^\pm$ and $\tilde{\chi}_2^0$) decays to off-shell gauge bosons. Finally, the two brown points at large $m_{\tilde{\chi}_2^\pm}$ are constrained by a combination of analyses sensitive to off-shell higgsino decays and on-shell wino decays. For further details on the impact of analysis combination for both scenarios, see the "Results" section in the paper [146].

The EW-ino sector of the MSSM is difficult to constrain at the LHC in a generic manner, as mixing effects lead to large variations in production cross sections and decay branching ratios. As a consequence, limits on charginos and neutralinos in the context of simplified models do not hold in general. Thus, a global picture combining the wealth of experimental results from searches in different final states is necessary.

## 4.5 Conclusion and Outlook

The wealth of experimental constraints on new physics from Run 2 of the LHC makes global reinterpretation studies increasingly important. These studies help determine

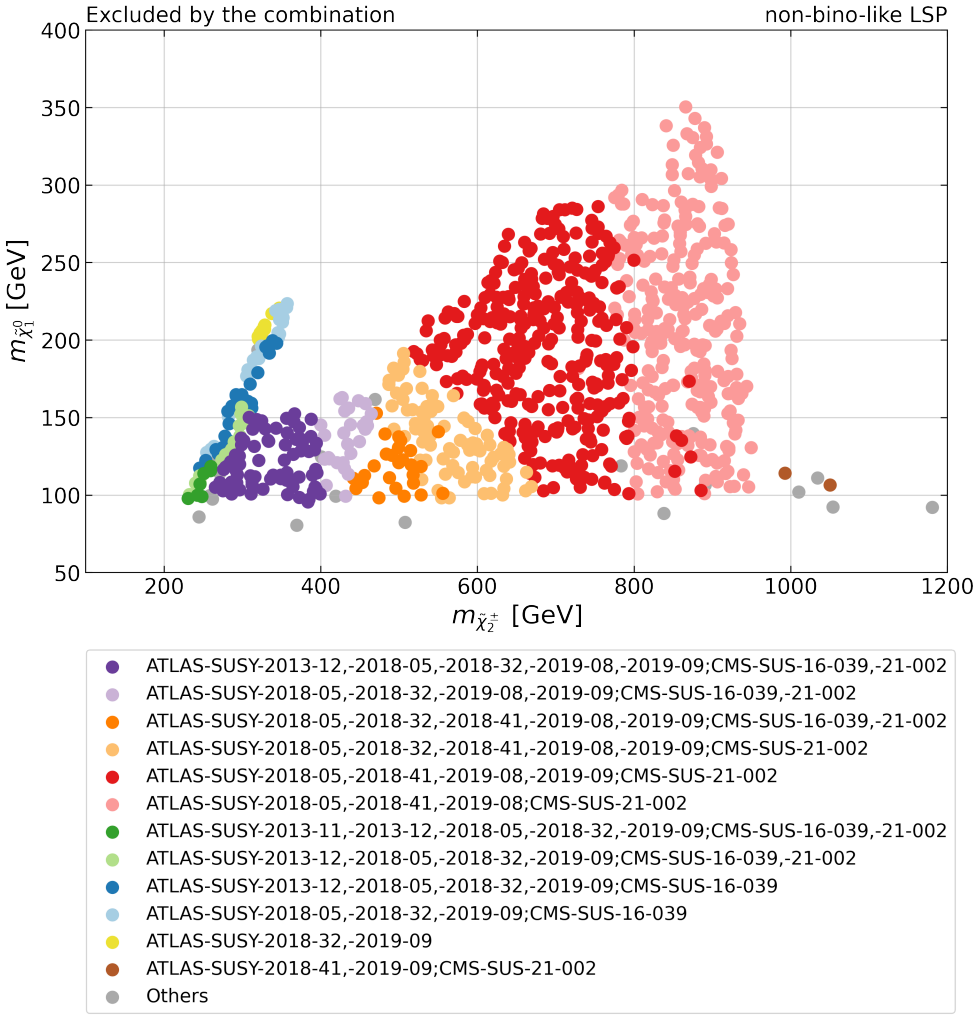


FIGURE 4.12: Most sensitive combinations in the $m_{\tilde{\chi}_1^0}$ vs. $m_{\tilde{\chi}_2^\pm}$ plane for points excluded by the combination and featuring a non-bino-like LSP. Only the combinations appearing at least 2 times are shown. The other combinations that appeared 2 times or less fall into the "Others" category.

how the full body of experimental information constrains complex BSM scenarios. It is also useful in identifying the most promising parameter regions where new physics may still manifest at the LHC. This endeavour requires software tools that encompass searches across as many final states as possible and can construct global likelihoods from them. The SModelS package is a publicly available tool designed for this purpose. It enables fast reinterpretation of LHC searches for new physics based on simplified model results. Its computational efficiency makes it particularly well-suited for large parameter space scans and comprehensive model surveys.

A key advantage of SModelS is its ability to perform likelihood combination across different analyses. This capability enables statistically more rigorous constraints and facilitates global likelihood analyses of LHC searches. The methodology encompasses various approaches for computing likelihoods from publicly available experimental information and establishes a framework for their systematic combination within SModelS. The physics impact of such global studies was demonstrated through a comprehensive case study of the electroweakino sector of the MSSM, summarized in

the previous section. It highlights the importance of combining approximately independent analyses to average out statistical fluctuations, leading to more robust exclusion limits. An extensive global study of the EW-ino sector of the MSSM is covered in the paper [166]. This study exemplifies a top-down approach, starting with well-established BSM theories and systematically constraining their parameter spaces through comprehensive comparison with experimental data.

The next two chapters shift to a complementary bottom-up approach that utilizes the full breadth of available results. Rather than testing specific theoretical models, this inverse methodology systematically searches for signatures that exhibit strong deviations from Standard Model predictions, allowing the data itself to guide the discovery of potential new physics signals.

# Chapter 5

# Artificial Proto-modelling: an Introduction

Inverse problems arise across scientific disciplines when researches must determine quantities that cannot be directly observed by measuring related, observable quantities. This process involves inferring causal factors and underlying principles from experimental data – a task that is both fundamental to scientific inquiry and notoriously challenging to execute. In particle physics, this inverse problem translates to constructing the fundamental Lagrangian that governs physical processes based on experimental observations. Within the SM framework, precise theoretical predictions have largely transformed this inverse problem into classical hypothesis testing, as exemplified by the successful determination of Higgs boson properties through direct experimental verification.

However, should experimental evidence for BSM physics emerge at the LHC or other facilities, the situation becomes considerably more complex. The mapping from experimental signatures to the parameter space of underlying theoretical models is not straightforward. This complexity stems from two primary factors. First, the number of proposed extensions to the Standard Model continues to grow, with many models containing numerous free parameters. Second, there will likely be too few experimental observables to establish direct connections between experimental results and theoretical frameworks.

Searches for new phenomena at the LHC typically proceed on a channel-by-channel basis, with experimental analyses performed across many different final states. While this approach has proven successful for establishing limits on specific theoretical models, it suffers from a significant drawback: only a small fraction of the available experimental data is utilised in any given analysis. This limitation becomes particularly problematic for *dispersed signals* – effects of new physics that manifest simultaneously across different final states or signal regions. Such signals are easily missed or dismissed as statistical fluctuations when analysed in isolation, despite potentially representing signatures of new physics when considered collectively. Recent efforts toward more global approaches include effective field theory (EFT) interpretations and model-independent searches. However, EFT methods lose validity in the presence of on-shell new physics, while current model-independent searches focus on significant deviations in particular kinematic distributions and may still miss dispersed signals that require global likelihood analysis to identify.

This motivates the development of a data-driven approach to model building. In

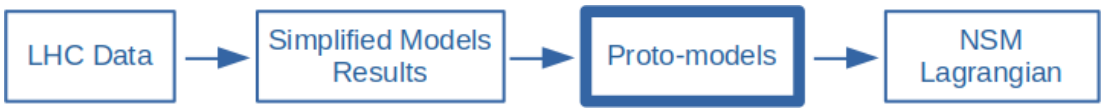


FIGURE 5.1: A strategy of how we may envisage to construct a Next Standard Model (NSM) Lagrangian from LHC data: the outcomes of specific searches, which are interpreted through simplified models, can be used to construct proto-models.

this chapter, we introduce an automated method for constructing new physics models which we call "proto-models" from small excesses observed in the experimental searches implemented in the SModelS database, as illustrated in Figure 5.1. The algorithm, dubbed the "Walker", generates proto-models that are consistent with the observed LHC data.

This chapter introduces the proto-model concept and describes the algorithm used in the initial proof-of-concept study and summarises the results obtained in [7]. Section 5.1 introduces the idea of a proto-model defining its parameters and the underlying assumptions. Section 5.2 describes the methodology for constructing likelihoods for a given proto-model. Section 5.3 presents the working principle of the prototype algorithm developed in [7]. The last section summarises the results presented in [7] when applying this algorithm to the SModelS database v1.2.4. Readers already familiar with this work may proceed directly to Chapter 6, which presents recent improvements to this approach.

## 5.1 What is a Proto-model?

We define a 'proto-model' to refer to collections or stacks of simplified models that propose the existence of new particles and/or interactions beyond the SM. We emphasize that these proto-models are not intended to be ultraviolet (UV) complete theories or a consistent effective field theory, i.e. they need not obey higher order mathematical principles like gauge symmetries. They are meant to serve as templates or prototypes to guide future experimental and theoretical searches for new physics, and could perhaps be further developed to construct the Next Standard Model (NSM) Lagrangian. They are motivated by small excesses in the searches for simplified models across experiments at the LHC and the reinterpretation of these searches by the SModelS collaboration. As mentioned in the introduction, inverse problems in particle physics are particularly difficult to tackle and this approach simplifies the problem by focusing on the basic, physically observable components rather than fully developed theories.

In the proof of concept paper [7], proto-models were generated using a MCMC-like random walk algorithm. The number of BSM particles in the proto-model, their masses, production cross sections and decay branching ratios were taken as free parameters. These proto-models were then tested against experimental results implemented in the SModelS database. The idea was to capture the small excesses across the searches to construct proto-models that maximally violate the SM hypothesis while still remaining compatible with the ATLAS and CMS constraints.

The MCMC-type walk involved randomised steps in the parameter space of the proto-model, corresponding to random changes in the values of the free parameters of the

proto-model. To test the proto-model hypothesis against the SM, approximation likelihoods were built using the statistical tools available in SModelS. Further, comparison between proto-models with different numbers of degrees of freedom at each step of the walk was performed using a test statistic based on the Akaike Information Criterion [137].

As mentioned above, we consider the number and type of BSM particles, their masses, production cross section, and decay branching ratios as free parameters. However, certain assumptions about the particle content were made. The particle spectrum introduced was inspired by SUSY partner particles, as we were confronting these models against a database (v1.2.4) containing extensive simplified model results from searches for SUSY. Therefore, the following constraints were imposed:

1. $\mathbb{Z}_2$ **symmetry:** We assume that all the BSM particles entering our proto-model are odd under $\mathbb{Z}_2$ symmetry. This is due to the fact that the majority of experimental results implemented in the SModelS database (v1.2.4) present constraints on simplified model topologies that follow this symmetry. They thus have to be pair-produced and cascade decay to the lightest state

2. **The lightest BSM particle (LBP):** The lightest BSM particle is stable and does not carry color and electrical charges. It therefore can be considered as a dark matter candidate

3. **Prompt Decay:** Most of the experimental results implemented in the database present constraints for promptly decaying particles. All BSM particles decay promptly, except for the LBP.

4. **Maximum Mass:** Masses of the particles are restricted to be within the reach of the LHC. Thus, only particles with a mass below 2.4 TeV are taken into account.

With such constraints imposed, we consider up to 20 BSM particles in both versions of the algorithm.

### 5.1.1 Particle Spectrum

When introducing BSM particles, we do not specify the spin and multiplicity of states for each particle as they are mostly relevant for the production cross section, which we consider a free parameter. Following the above constraints, we define 20 SUSY-inspired particles for building proto-models:

- Light quark partners $X_q$ ($q = u, d, c, s$): For each light flavor quark, we introduce a single partner particle. Unlike SUSY models, we do not consider two independent particles (left and right-handed squarks) for each flavor. A possible multiplicity of (degenerate) states is accounted for by rescaling the production cross section.

- Heavy quark partners $X_b^i$, $X_t^i$ ($i = 1, 2$): Unlike the light quark partners, we consider two independent particles for each flavor. Since these particles have extensively been searched for at the LHC, we include two states in order for the proto-models to have enough degrees of freedom to accommodate the data.

- Gluon partner $X_g$: We introduce one new color-octet particle, analogous to a gluino in SUSY.

| Particle | Decay Channels | Particle | Decay Channels |
|---|---|---|---|
| $X_q$ | $qX_Z^j,\ q'X_W^i,\ qX_g$ | $X_W^1$ | $WX_Z^j$ |
| $X_t^1$ | $tX_Z^j,\ bX_W^i,\ WX_b^1,\ tX_g$ | $X_W^2$ | $WX_Z^j,\ ZX_W^1,\ hX_W^1$ |
| $X_b^1$ | $bX_Z^j,\ tX_W^i,\ WX_t^1,\ bX_g$ | $X_Z^{j\neq 1}$ | $WX_W^i,\ ZX_Z^k,\ hX_Z^k$ |
| $X_t^2$ | $tX_Z^j,\ bX_W^i,\ ZX_t^1,\ WX_b^1,\ tX_g$ | $X_\ell$ | $\ell X_Z^j,\ \nu_\ell X_W^i$ |
| $X_b^2$ | $bX_Z^j,\ tX_W^i,\ ZX_b^1,\ WX_t^1,\ bX_g$ | $X_{\nu_\ell}$ | $\nu_\ell X_Z^j,\ \ell X_W^i$ |
| $X_g$ | $q\bar{q}X_Z^i,\ q\bar{q}'X_W^i,\ b\bar{b}X_Z^i,\ t\bar{t}X_Z^j,\ btX_W^i,\ qX_q,\ bX_b,\ tX_t$ | | |

TABLE 5.1: The BSM particles and their decay channels considered for building proto-models in the paper [7].

- Electroweak partners $X_W^i$, $X_Z^j$ ($i = 1,2$; $j = 1,2,3$): We allow for two electrically charged and three neutral states. These might correspond to charginos and neutralinos in the MSSM (with the neutral higgsinos being exactly mass-degenerate), or to the scalars of an extended Higgs sector with a new conserved parity. The lightest neutral state ($X_Z^1$) is assumed to be the LBP.
- Charged lepton partners $X_\ell$ ($\ell = e, \mu, \tau$): Similar to light-flavor quarks, we consider a single partner for each lepton flavor.
- Neutrino partners $X_{\nu_\ell}$: We consider one partner for each neutrino flavor($\nu_e, \nu_\mu, \nu_\tau$).

Since the LBP is $X_Z^1$, all other BSM particle masses must satisfy $m(X) \geq m(X_Z^1)$. We further require mass ordering for states with multiple partners, e.g., $m(X_t^2) > m(X_t^1)$.

Additional requirements are imposed on the masses for colored new particles to avoid biasing the algorithm to "discover" light states in phase-space regions that are poorly covered in the database. Most of the simplified model results in the SMODELS database does not constrain colored new colored states with masses below 310 GeV. Therefore, we impose that the masses for $X_g$ and $X_q$ are heavier than this value. In addition, for $X_t$ masses below 280 GeV, we disallow a "corridor" region 150 GeV $< m(X_t) - m * X_Z^1 <$ 200 GeV. Events in such corridor regions are too similar to SM $t\bar{t}$ events, and thus many CMS analyses do not provide any statements for those regions (refer to [167] for example).

### 5.1.2 Decay Channels and Branching Ratios

The decay modes of each new particle introduced is ensured to be consistent with its quantum numbers. Table 5.1 lists the possible decay channels for each BSM particle. Not all possible decays were considered. In v1, only on-shell decays were allowed, and in particular, decays of $X_W$ and $X_Z$ into $X_\ell + \ell/\nu$, $X_\nu + \nu/\ell$, and $X_{W,Z} + \gamma$ were not considered.

If a given decay is kinematically forbidden, or one of the daughter BSM particles in the decay mode is not present in the proto-model, they are turned off. The branching ratios to the remaining allowed decay channels are taken as free parameters, which are then normalised to unity. If no decay channel is allowed for a BSM particle (except the LBP), it is removed from the proto-model.

### 5.1.3 Production cross sections

As mentioned before, production cross sections for the BSM particles can vary freely. Along with pair production of particles, we consider associated production for certain BSM particles. To have sensible starting values, cross sections are first initialised using the corresponding MSSM-like cross section, and then are freely rescaled by a signal strength multiplier (SSM) $\kappa$. For example, we set the cross section for the pair production of $X_g$ as:

$$\sigma(pp \to X_g X_g) = \kappa_{X_g X_g} \times \sigma(pp \to \tilde{g}\tilde{g})\,, \tag{5.1}$$

where the cross section for the gluino pair production is evaluated at the $X_g$ mass. Hence, we consider the rescaling factors $\kappa$ to be the free parameters instead of the total cross section. In v1, these cross sections were evaluated during runtime using Pythia 8.2 [168] and NLLFast 3.1 [169–176].

In practice, we create a template SLHA input file containing all the BSM particles and their decay channels, similar to a MSSM SLHA input file. We do not set the masses or the branching ratios for the particles. During runtime, this template file is modified by the algorithm depending on the parameter content of the proto-model. Particles not present in the proto-model are decoupled by setting their masses to $10^6$ GeV. Decay branching ratios, production modes and their cross sections are also written in this template file once set. It is then sent as an input BSM model file to SModelS for further statistical inference.

## 5.2 Constructing likelihoods for proto-models

The degree to which likelihoods can be built critically depends on the amount of information published by the experimental collaborations. As mentioned in Chapter 4, the SModelS database contains two types of experimental results: UL-type results that provide upper limits on signal cross section times branching ratio, and EM-type results that provide efficiency maps for the simplified model searches. Starting with the least amount of information available, we make use of the data published for inference in the following ways:

- If only observed ULs are given, then no likelihood can be built. In v1, such type of results were used to provide a constraint at 95% CL, which then played a role in determining the maximal allowed signal strength $\mu_{max}$ (see Section 5.5).

- If expected ULs are given in addition to the observed ULs, an approximate likelihood as a truncated Gaussian [177] was constructed:

$$L(\mu|D) = \frac{c}{2\pi}\frac{\sigma_{pred}}{\sigma_{obs}} \exp\left(-\frac{(\mu\sigma_{pred} - \sigma_{max})^2}{2\sigma_{obs}^2}\right), \quad \text{for } \mu \geq 0\,. \tag{5.2}$$

  Here, the likelihood is a function of the signal strength $\mu$ for any cross section $\sigma_{pred}$ predicted for a given proto-model. The observed cross section value $\sigma_{obs}$ was approximated by using the standard deviation of the expected Gaussian likelihood for the cross section, i.e $\sigma_{\text{obs}} \approx \sigma_{\text{exp}} = \sigma_{exp}^{UL}/1.96$, with $\sigma_{exp}^{UL}$ being the expected 95% CL upper limit on the signal cross section. $\sigma_{max}$ was chosen such

that the above likelihood correctly reproduces the observed 95% CL upper limit on the production cross section $\sigma_{obs}^{UL}$. The normalization constant $c \geq 1$ is to ensure that the integral over the likelihood from $\mu = 0$ to infinity equals unity. Since this was a crude approximation, such a likelihood is *no longer being built* in v2.

- When efficiency maps for simplified model topologies are published by experimental searches, we have more information to construct a likelihood for a signal strength $\mu$, as described in Eq. (4.6).
- The optimal case is when we have efficiency maps along with a statistical model that details correlations of uncertainties across signal regions, as described in Section 4.3.2.
- Upon further having a combination matrix detailing which analyses can be combined, we can build a global likelihood for a given proto-model as described in Section 4.3.3.

The constraints from all other analyses that do not enter the combination were used to provide a limit on the global signal strength $\mu$ in v1.

## 5.3 Walker v1

The Walker algorithm in v1 followed a MCMC-type random walk in the proto-model 's parameter space and was composed of certain blocks that interacted with each other. A procedural flow-chart is presented in Figure 5.2, which follows a single iteration of the walk described below:

1. **Builder**: This block is responsible for defining the particle content and other parameters of the proto-model. It also contains functions that allow for random changes in the proto-model regarding any of its free parameters.
2. **Critic**: Once a proto-model is defined by the builder, it is then sent to the **Critic** block. This confronts the proto-model against the constraints in the SModelS database to compute an upper bound on the overall signal strength $\mu_{\max}$.
3. **Combiner**: This block collects the set of experimental results in the SModelS database that provide theory predictions for the proto-model. It then identifies the combination of experimental results that maximally violate the SM hypothesis, while still being compatible with the constraints from the **Critic**.
4. **Test Statistic**: Similar to the MH algorithm for MCMC sampling, we compute an acceptance probability that decides whether we keep the current proto-model or return to the previous one. However, unlike a typical MCMC walk, the proto-models at different steps may have potentially different degrees of freedom. We therefore define a test statistic $K$ (detailed in Section 5.6) for each proto-model, and compute the acceptance probability as:

$$\alpha(\mathbf{M}_i \to \mathbf{M}_{i+1}) = \min\left\{1, \frac{1}{2}(K_{i+1} - K_i)\right\}, \tag{5.3}$$

where $i$ is the index of the current step.

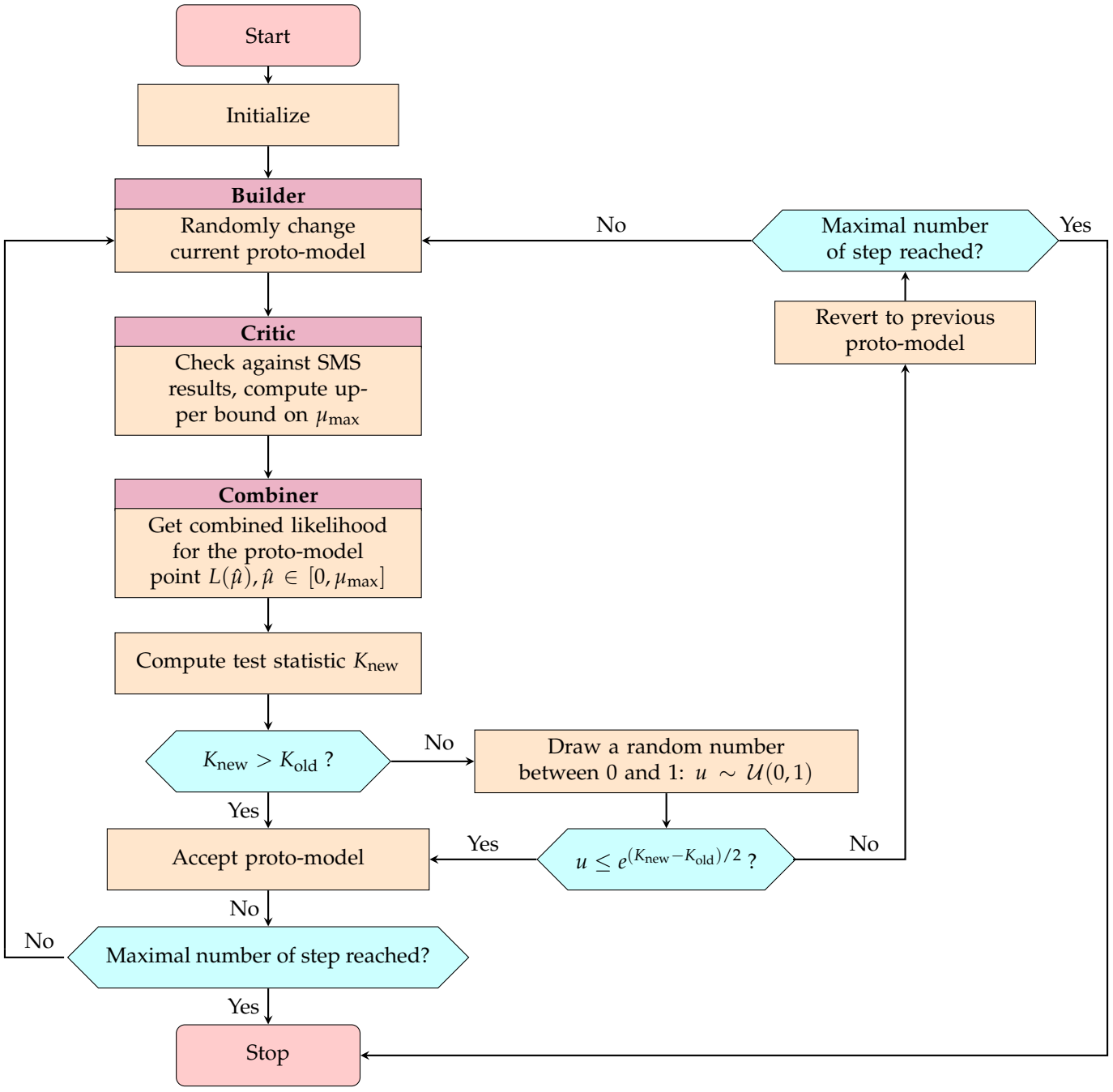


FIGURE 5.2: Simplified flowchart of the Walker algorithm v1.

## 5.4 Builder v1

The builder's task is to define the BSM particle content, the masses of the constituent particles, their production cross sections and decay channels of a proto-model at each step of the walk. The content, features, and attributes related to a specific proto-model is contained in the `Protomodel` class. Random changes are applied to the proto-model in each iteration of the walk with the functions implemented in the `Manipulator` class. The following random actions on a proto-model were executed with a certain probability:

1. **Adding a new particle**: From the list of BSM particles in 5.1, any particle not

yet present in the proto-model could be randomly chosen to be added. Upon including the new particle, the particle mass is drawn from a uniform distribution between the LBP mass and 2.4 TeV. For particles with multiple generations, e.g., $X_W^1, X_W^2$, mass ordering was required such that $m_{X_W^1} < m_{X_W^2}$.

Branching ratios for each particle are initialized by drawing from a Gaussian distribution with mean $= 1/N_{decay}$ where $N_{decay}$ is the number of allowed decay channels (for the corresponding decays listed in 5.1), and a variance equal to $0.5/\sqrt{N_{decay}}$. Once the branching ratios were initialised, they were normalised to add up to unity. Lastly, the signal strength multipliers for the pair and associated production modes were set to 1.0.

To control the rate of addition, the algorithm limited new particles from being added when the test statistic $K$ is high and/or when the proto-model already contains a large number of particles.

2. **Removing a particle**: Amongst the BSM particles present in the proto-model, a randomly chosen particle can be removed. Upon removal, the corresponding production modes and decays involving the particle were also deleted and the remaining branching ratios were normalized. A lower generation particle was not removed if the corresponding higher generation was still present in the proto-model.

   To control the rate of removal, the algorithm removed more particles if the test statistic $K$ was low and/or too many particles were present in the proto-model.

3. **Changing the branching ratio**: The branching ratios for the decay channels of a randomly chosen particle in the proto-model was allowed to be changed with a probability of 20%. This change could occur in one of three distinct ways, each with a certain probability: (i) assign a 100% branching ratio to a randomly chosen decay channel and close all other decay channels, (ii) close a random decay channel by setting the branching ratio to 0 and, (iii) the BR for each decay channel could be modified by a distinct random number $\delta_{\text{BR}}$ drawn from Uniform$[-b, b]$, where $b = 0.1/N_{decay}$. Upon any of these changes, the algorithm made sure that there was at least one decay channel present, and that all the remaining BRs were normalised.

4. **Changing the signal strength multipliers**: With a 25% chance, random changes in the signal strength multipliers ($\kappa$) were made in one of three possible ways: (i) a randomly chosen production mode in the proto-model could have its SSM rescaled by a value drawn from a Gaussian distribution centered around 1 and with width 0.1, (b) a randomly chosen production mode could have its SSM set to zero, one, or to the SSM of another mode and (c) all the production modes involving a randomly chosen particle could have their SSMs rescaled by a random uniform number between 0.8 and 1.2.

5. **Changing the mass of an existing particle**: If none of the above changes were implemented, the mass of a randomly chosen particle in the proto-model was forcibly changed. Otherwise, this was done with a 20% chance. The mass of the particle was changed by a value $\delta_m$ drawn from a uniform distribution where the interval depended on the test statistic $K$ and the number of particles present in

the proto-model. For better performing models with large number of particles, the value of $\delta_m$ was small.

## 5.5 Critic v1

The Critic tests the proto-model given from the Builder against the constraints from the SModelS database. In v1, an upper limit on the global signal strength $\mu$ was computed using constraints from all analyses, defined by:

$$\mu < \mu_{\text{max}} = 1.3 \frac{\sigma^{\text{UL}}_{\text{obs}}}{\sigma^{\mathbf{M}}} \,. \tag{5.4}$$

Here, $\sigma^{\mathbf{M}}$ is the relevant proto-model signal cross section. The upper limit on the signal cross section ($\sigma^{\text{UL}}_{\text{obs}}$) is obtained from the most sensitive analysis/signal region.[1] The factor 1.3 was introduced to allow for a 30% violation of the 95% CL observed UL. Such violations were allowed to take into account the fact that when simultaneously checking for constraints from a large set of results, a few are statistically allowed to be violated. Although this was an approximate constraint, it allowed the limits from correlated analyses as well as those for which no approximate likelihood could be computed to be taken into account. This constraint was then used to truncate the combined likelihood ($L_c^{\mathbf{M}}(\hat{\mu})$) built for a combination of results obtained from the Combiner such that:

$$\hat{\mu} = \min(\hat{\mu}_c, \mu_{\text{max}}) \,, \tag{5.5}$$

with $\hat{\mu}_c$ the value maximising $L_c^{\mathbf{M}}$.

The above procedure is illustrated in Fig. 5.3. The left panel in this figure shows how likelihoods are combined for a proto-model when it is possible to construct a likelihood for all the relevant results, which can all be considered as uncorrelated. In the example shown, "Result A" represents an analysis which favours $\mu > 0$, while "Result B" corresponds to a *constraining analysis*. This means that the latter observed an under fluctuation in the data with respect to the expected SM background, thus favouring $\mu \leq 0$. The grey line shows the maximum of the combined likelihood ($\hat{\mu}$), while the red line corresponds to the limit on $\mu$ ($\mu_{max}$) obtained from "Result B" alone. The right panel in Figure 5.3 displays our approximation for the case when it is not possible to construct a proper likelihood for the most constraining analysis ("Result B" in this example) or it cannot be considered as uncorrelated with the other results. In this case we truncate the likelihood for "Result A" at ($\mu_{max}$) obtained from "Result B". Hence, the value of $\hat{\mu}$ for the truncated likelihood shifts slightly with respect to the full result. In v1, this approximation was applied whenever it is not possible to construct a full likelihood.

[1] As mentioned before, the most sensitive result corresponds to the one with the highest $r_{\text{exp}}$ value.

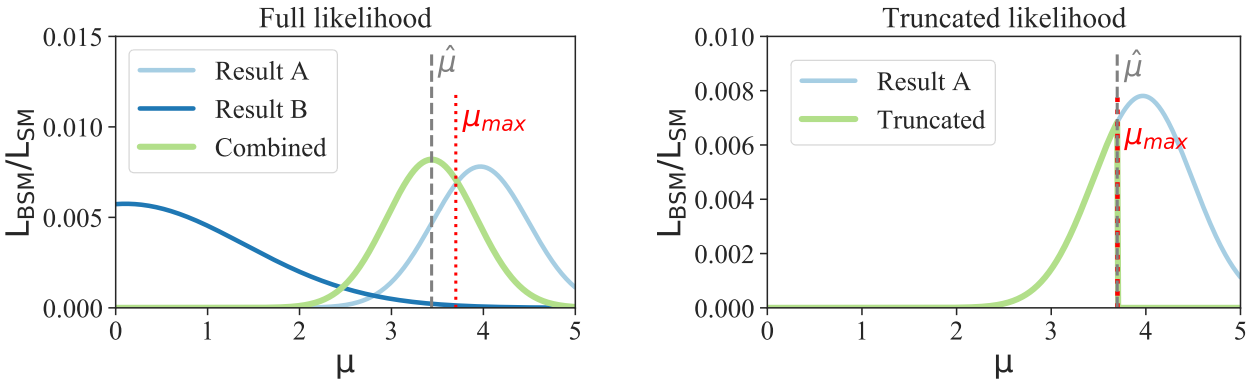


FIGURE 5.3: Left: an illustration of the signal likelihood as a function of the signal strength ($\mu$) for two results (A and B) and the corresponding combined likelihood. The value of $\hat{\mu}$ given by the maximum of the combined likelihood (green curve) is also shown as well as the upper limit on $\mu$ ($\mu_{max}$) given by Result B alone. Right: a similar example, but where it is not possible to combine both likelihoods, or the likelihood for Result B is not available. In this case, the likelihood for Result A is truncated at $\mu_{max}$ (obtained from Result B). All the curves are normalised to the corresponding SM likelihood value ($\mu = 0$).

## 5.6 Combiner v1

The Combiner's role is to collect all the experimental results from the SMODELS database that provide theory predictions for the proto-model and determine the optimal combination of results. For this, a combination matrix was built that specified which experimental results could be combined with each other. Only experimental results providing sufficient information for likelihood construction were included in this matrix.

To build the combination matrix, correlations across analyses/signal regions were treated in a binary way. If a given pair of results have considerable overlap in their signal region definitions, a joint likelihood could not be computed. If the pair of results could be considered to be approximately uncorrelated, a joint likelihood was computed by trivially multiplying their likelihoods. This feature of computing joint likelihoods was inbuilt in the Combiner v1 as this was not yet available in SMODELS v1.2.4.

Several criteria were used to identify approximately uncorrelated results. Experimental results from different runs (8 TeV and 13 TeV) and from different experiments (ATLAS and CMS) were considered to be approximately uncorrelated. Additionally, results with clearly different final state signatures were taken to be approximately uncorrelated (ex: fully leptonic versus fully hadronic final states). The combination matrix considered for v1 of the Walker algorithm is shown in Figure 5.4.

Under the above assumptions, all possible combinations for subsets of LHC results were constructed by the Combiner in v1. A combinable set of analyses was defined as follows:

1. Each analysis in the combination can be considered uncorrelated with any other analyses in the combination.

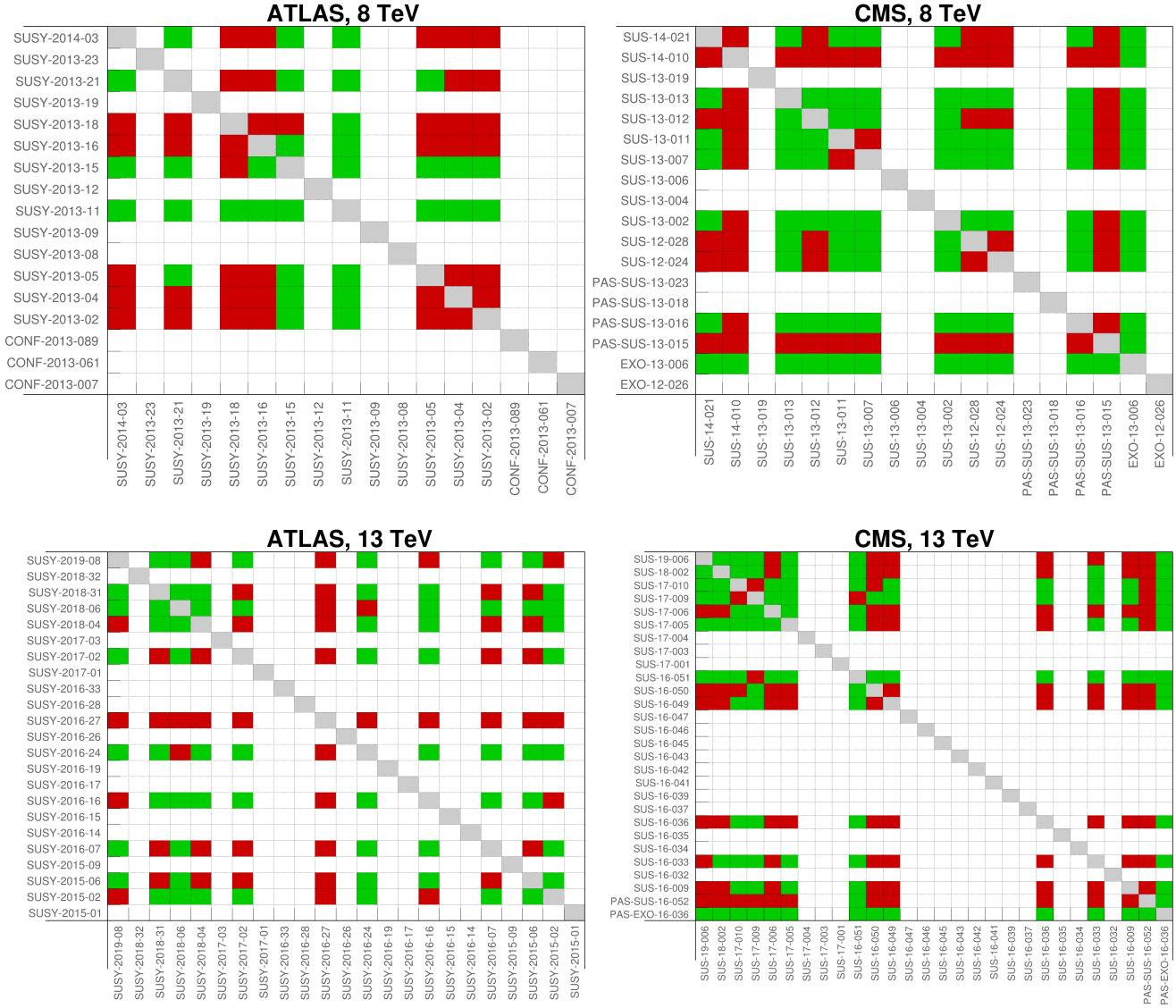


FIGURE 5.4: Binary combination matrices used in v1, that describes which analyses are considered to be approximately uncorrelated (green bins) and which are not (red bins). Analyses from different LHC runs or different experiments are always taken as uncorrelated. White bins denote analyses, for which no likelihood can be computed (observed UL only).

2. Any analysis that can be added to the combination is required to be added, i.e., subsets of combinations were not allowed.

To build the joint likelihood for a given combination, the likelihoods of individual analysis in the combination were trivially multiplied, i.e.,

$$L_c(\mu) = \prod_{i=1}^{N} L_i(\mu)\,, \tag{5.6}$$

where the product is over all $N$ uncorrelated analyses and $\mu$ is the global signal strength. For each combination, the Combiner computed the value of $\mu = \hat{\mu}_c$ that maximises

the proto-model likelihood $L_c^{\mathbf{M}}$. If $\hat{\mu}_c$ was greater than the constraint computed by the critic ($\mu_{\max}$), then the combined likelihood was evaluated at $\mu_{\max}$ by defining $\hat{\mu}_c = \mu_{\max}$.

The optimal combination, which we henceforth refer to as the *most significant combination*, is defined as the one that captures the most deviation from SM predictions. To identify the most significant combination, a quantity $Z$ was defined:

$$Z = \sqrt{2 \ln \frac{L_c^{\mathbf{M}}(\mu = \hat{\mu}_c)}{L_c^{\mathrm{SM}}(\mu = 0)}}\,. \tag{5.7}$$

The most significant combination was identified as the one that gave the maximum $Z$, i.e., the one that maximally deviated from the SM hypothesis.

The disadvantage of the above procedure is that it was computationally expensive to find all possible combinations and compute the combined $\hat{\mu}_c$ for each set. Moreover, as additional analyses with more complex statistical models are incorporated into the SModelS database, this step would greatly affect the computational load. Therefore, the above method of finding the most significant combination is no longer followed in proto-models v2.

### Test Statistic

At each step of the walk, the random changes implemented by the Builder on the current proto-model was either accepted or rejected. Since the proto-models at different steps could have potentially different dimensions, this acceptance/rejection criteria needed to take into account not only the deviations from SM predictions but also the dimensionality of the proto-model at different steps. Thus, a test statistic $K$ was designed such that it was higher for those models that satisfy all constraints while simultaneously giving a larger deviation from the expected SM predictions. Additionally, it was desirable to lower $K$ for those models with too many degrees of freedom, following the law of parsimony, i.e., Occam's razor. Thus, for a given proto-model, for each combination of results $c$, we computed the auxiliary quantity $K_c$,

$$K_c = 2 \ln \frac{L_c^{\mathbf{M}}(\hat{\mu}_c) \cdot \pi(\mathbf{M})}{L_c^{\mathbf{SM}} \cdot \pi(SM)}\,. \tag{5.8}$$

Here $L_c^{\mathbf{M}}$ is the joint likelihood for a combination set $c$ of experimental results *given* the proto-model $\mathbf{M}$. It is evaluated at the signal strength value $\hat{\mu}_c$, which maximizes the likelihood and satisfies $0 \leq \hat{\mu}_c < \mu_{max}$. The corresponding SM likelihood is computed by setting the signal strength value of the joint likelihood to 0, i.e $L_c^{\mathrm{SM}} := L_c^{\mathbf{M}}(\mu = 0)$. The priors on the proto-model and the SM are given respectively by $\pi(\mathbf{M})$ and $\pi(\mathrm{SM})$. The combination set of results, $c$, refers to the most significant combination determined by the Combiner.

The priors assumed the role of penalty factors punishing the proto-model for new degrees of freedom introduced. The prior on the SM was considered a common factor for all proto-models and for all different combinations of results. As it did not influence the comparison between distinct proto-models, we set $\pi(\mathrm{SM}) = 1$. The distinction between proto-models of different dimensions was thus defined by the prior on the

| Proto-model parameters | $n_{particles}$ | $n_{BRs}$ | $n_{SSMs}$ | $\Delta K$ |
|---|---|---|---|---|
| One new particle, one non-trival BR, two production modes | 1 | 1 | 2 | $-2$ |
| Two new particles, trivial BRs, five production modes | 2 | 0 | 5 | $-3.25$ |
| Three new particles, non-trivial branchings and SSMs | 3 | 3 | 8 | $-6.5$ |

TABLE 5.2: The effect on the proto-model test statistic $K$ by the choice of prior in Eq. (5.9) for different proto-model parameters. The last column displays the decrease in the test statistic: $\Delta K = 2 \ln \pi(\mathbf{M})$.

proto-model. The proto-model prior $\pi(\mathbf{M})$ penalized the test statistic for newly introduced particles, branching ratios, or production cross sections, and was formulated as:

$$\pi(\mathbf{M}) = \exp\left[-\left(\frac{n_{\text{particles}}}{a_1} + \frac{n_{\text{BRs}}}{a_2} + \frac{n_{\text{SSMs}}}{a_3}\right)\right]. \tag{5.9}$$

Here $n_{\text{particles}}$, $n_{\text{BRs}}$ and $n_{\text{SSMs}}$ is the number of new particles, (non-trivial) branching ratios [2] and signal strength multipliers present in the proto-model respectively. Since particle-particle and particle-antiparticle production modes can have different signal strength multipliers in this algorithm, they are counted as distinct degrees of freedom. In order to favour democratic decays, if two decay channels for a given particle have BRs differing by less than 5%, they are counted only once. The parameters $a_1$, $a_2$, and $a_3$ were chosen to be 2, 4, and 8, respectively. This was chosen so that the above prior for a proto-model with one particle having one non-trivial decay channel and two production modes could be considered equivalent to the Akaike Information Criterion [137] for one free parameter. Note that to obtain the prior on the SM from Eq. (5.9), setting $n_{\text{particles}} = n_{\text{BRs}} = n_{\text{SSMs}} = 0$ gives the normalisation condition $\pi(\text{SM}) = 1$. The test statistic $K$ thus roughly corresponded to a $\Delta\chi^2$ of the proto-model with respect to the SM, penalizing for the new degrees of freedom.

Table 5.2 illustrates the influence of the prior on $K$ for a few parameter choices. With the introduction of the Critic and the selection of the most significant combination of results, it was difficult to have a clear probabilistic interpretation of $K$ since its exact distribution was unknown. Negative values of $K$ were also probable. Such an outcome was interpreted as a preference for the SM over the proto-model.

Once $K$ was computed for a proto-model at each step, it was compared with the corresponding $K$ value of the proto-model in the previous step. The proto-model was then accepted or rejected based on the acceptance criterion defined in Eq. (6.2). In addition, for each walk, ten proto-models yielding the highest $K$ values were recorded in a separate file for more detailed analysis.

[2] This means, for only one decay mode with 100% BR, $n_{\text{BRs}} = 0$.

## 5.7 Results from v1

The Walker algorithm v1 was executed over the full SModelS v1.2.4 database. This included simplified model constraints from 40 ATLAS and 46 CMS analyses detailed in Appendix A.3 in [7]. All v1 results were obtained using 50 parallel walkers, each running for 1000 steps. Each walker had a runtime of 12h to 24h on a single core.

The proto-models with the highest $K$ values generated by the Walker in each walk were recorded. Interpreting the significance of these $K$ values required knowledge of the distribution of $K$ under the SM hypothesis. To this end, an ensemble of "fake SM databases" was created in which the observed data was replaced by values sampled from the expected SM backgrounds. The Walker was then run on such databases to determine the density of $K$ under the SM hypothesis. The significance of $K$ obtained from walking on the real data could then be evaluated using this density. This section details the methodologies used to obtain and evaluate the results in v1.

### 5.7.1 Fake database

To interpret the significance of the test statistic $K$ and estimate its global $p$-value, "MC toy" versions of the SModelS database were produced. In particular, the observed data was replaced by the values sampled from the SM background in three different ways listed below:

1. EM-type results contain information on the expected SM background and its uncertainty for each SR. For each SR, a value was sampled from a normal distribution with the SM background as the mean and the squared uncertainty as the variance. The sampled value was used as the expected event count ($\lambda$) in a Poisson distribution that models the observed number of events. The "fake" observation was then obtained by sampling from this Poissonian.

2. UL-type results that contain information on expected upper limits could be used to estimate the SM uncertainty on the expected limit. This was done by assuming large number of observed events and small systematical uncertainties [177]. The observed upper limits were then obtained by sampling from a Gaussian distribution:

$$\sigma_{\text{obs}}^{\text{UL}} \sim \text{Norm}\left(\sigma_{\text{exp}}^{\text{UL}}, (\delta\sigma_{\text{exp}}^{\text{UL}})^2\right), \tag{5.10}$$

   where $\delta\sigma_{\text{exp}}^{\text{UL}} = \sigma_{\text{exp}}^{\text{UL}}/1.96$ is the estimated width of the distribution.

3. UL-type results that do not provide any information on the expected upper limits enter the fake database without any modifications, as not enough information is available to estimate the SM uncertainty.

With the above sampling procedure, an ensemble of 50 fake SM databases was produced, on which the Walker algorithm was then executed. Collecting the proto-models with the highest $K$ values, the density of $K$ under the SM hypothesis was then estimated via a Kernel density estimator (KDE):

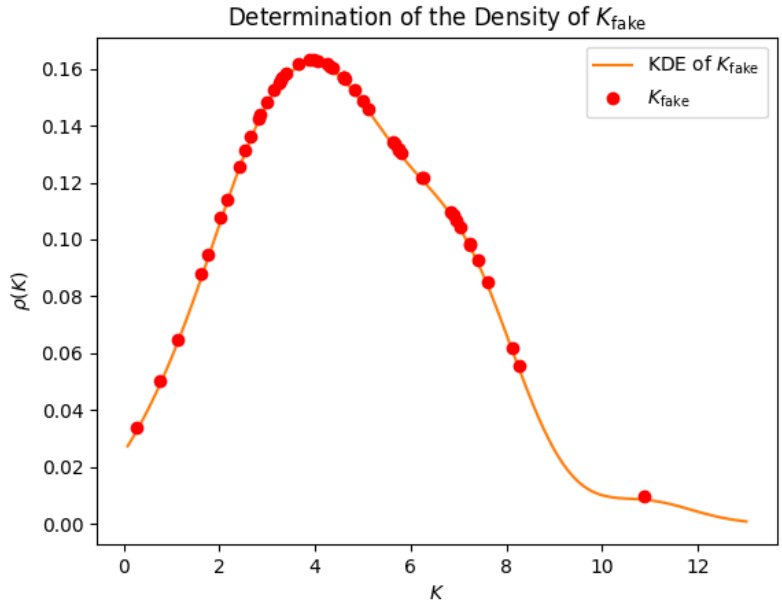


FIGURE 5.5: The density of the test statistic $K$ under the SM-only hypothesis obtained using a Kernel Density Estimator (KDE). The red points denote the $K$ values generated by the runs over 50 fake databases.

$$\rho(K) := \frac{1}{Nw} \sum_{i=1}^{N} \text{kern}_w(K - K^i_{\text{fake}}) \,. \tag{5.11}$$

Here, $N = 50$ represents the number of runs with the fake databases, where each run employs 50 parallel walkers with 1,000 steps per walker. $K^i_{\text{fake}}$ stands for the highest test statistic value obtained from a proto-model generated from the $i^{\text{th}}$ run. A Gaussian with a width $w$ determined by Scott's rule [178] was chosen as the Kernel $\text{kern}_w$ for the KDE.

As mentioned in Section 5.6, the Walker algorithm was optimised to search for dispersed signals with a maximum deviation from the SM hypothesis. This was done by defining $K$ to be maximum over all possible combinations of results for a proto-model. Hence, large $K$ values were expected to be found even under the SM hypothesis, as over-fluctuations in the background could mimic the effects of dispersed signals. This can be seen in Figure 5.5 which depicts the $K^i_{\text{fake}}$ values generated for each walk and the resulting density $\rho(K)$ under the SM hypothesis. Values of up to $K \approx 11$ were expected even under the SM hypothesis with the density peaking at $K \approx 4$.

### 5.7.2 Real data

With the actual SMODELS database having the real LHC results, 10 runs were executed where each run employed 50 walkers with 1000 steps per walker. The proto-models with the highest $K$ values obtained from each run is shown in Figure 5.6. One can see that all runs generated similar highest scoring proto-models. All the highest scoring proto-models include a top-partner $X^1_t$, a light-flavor quark partner $X_{d,c}$ along with the LBP $X^1_Z$. A lepton partner $X_\mu$ was introduced in run 5 due to small $\approx 1\sigma$ excesses

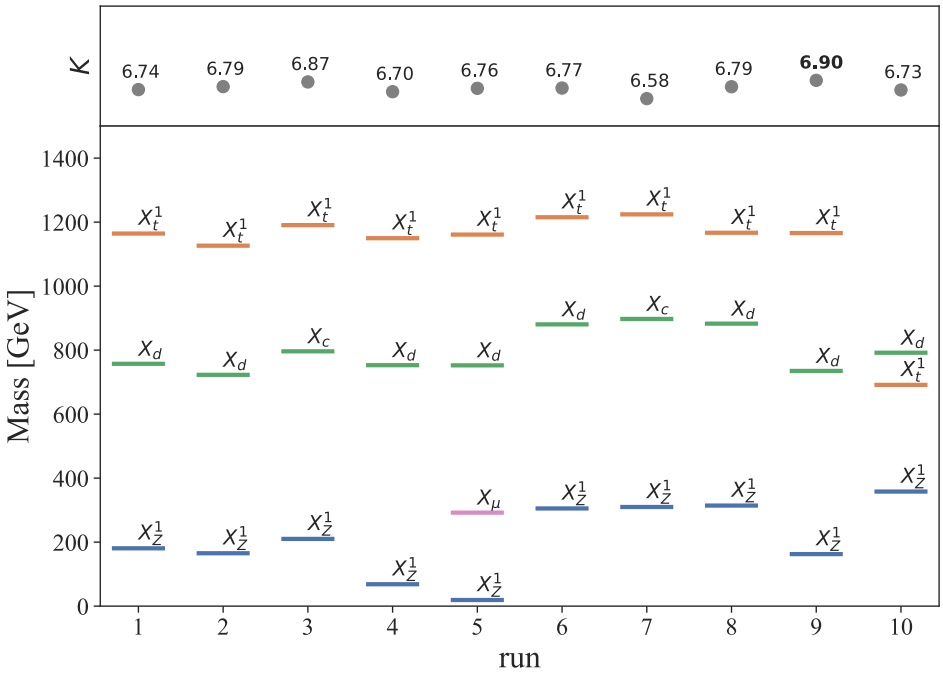


FIGURE 5.6: The particle content and mass spectrum for the proto-models having the highest test statistic $K$ obtained from each of the 10 runs over real SMODELS database. The top block displays the corresponding $K$ for each proto-model and the highest $K$ is highlighted in bold text for walker 9.

in the CMS search for sleptons, CMS-SUS-17-009 [179] and the ATLAS search for electroweakinos, ATLAS-SUSY-2016-24 [180]. Although the introduction of an additional particle resulted in a prior penalty of $\Delta K = -1.25$, this was overruled in favour of the increase in the likelihood ratio $\Delta Z^2 = 1.94$. The average test statistic of the highest scoring proto-models from these runs stood at $K = 6.76 \pm 0.08$.

The "winning" proto-model from these runs, i.e., the one with the highest $K = 6.90$ was generated in step 582 of the 29th walker in run 9. This proto-model consisted of the LBP $X_Z^1$ of mass 163 GeV, a $X_d$ with mass 735 GeV and $X_t^1$ with mass 1166 GeV. It produces signals in the $t\bar{t} + E_T^{\text{miss}}$ and jets$+E_T^{\text{miss}}$ final states with SUSY-like cross sections. The effective signal strength multipliers for the corresponding production cross-sections were put at $\hat{\mu} \times \kappa_{X_t^1 \bar{X}_t^1} \approx 1.2$ and $\hat{\mu} \times \kappa_{X_d \bar{X}_d} \approx 0.5$, corresponding to the cross-section values $\sigma(pp \to X_t^1 \bar{X}_t^1) \approx 2.6$ fb and $\sigma(pp \to X_d \bar{X}_d) \approx 24$ fb at $\sqrt{s} = 13$ TeV. Both the $X_t^1$ and $X_d$ directly decay to the lightest state ($X_Z^1$) with 100% BR.

The analyses in SMODELS database v1.2.4 that contributed to this proto-model is listed in Table 5.3. The observed excesses in the multijet (i.e., $0\updownarrow$ + jets) + $E_T^{\text{miss}}$ analyses from ATLAS at $\sqrt{s} = 8$ and 13 TeV [181, 182] and from CMS at $\sqrt{s} = 8$ TeV [184] motivate the introduction of the light quark partner $X_d$ around 700 GeV. The obtained $K$ value is mostly driven by the $\approx 1.5\sigma$ and $2\sigma$ excesses observed in the 13 TeV ATLAS and CMS stop searches [183, 185]. These searches motivate the introduction of the top partner, $X_t^1$, with a mass around 1.2 TeV.

| Analysis | Dataset | Obs | Exp | Z | P | Signal |
|---|---|---|---|---|---|---|
| ATL multijet, 8 TeV [181] | SR6jtp | 6 | $4.9 \pm 1.6$ | $0.4\,\sigma$ | $X_d$ | 0.25 |
| ATL multijet, 13 TeV [182] | 2j_Me ... | 611 | $526 \pm 31$ | $2.2\,\sigma$ | $X_d$ | 44.18 |
| ATL $1\ell$ stop, 13 TeV [183] | tN_high | 8 | $3.8 \pm 1$ | $1.9\,\sigma$ | $X_t$ | 3.93 |
| CMS multijet, 8 TeV [184] | | 30.8 fb | 19.6 fb | $1.1\,\sigma$ | $X_d$ | 2.66 fb |
| CMS $0\ell$ stop, 13 TeV [185] | | 4.5 fb | 2.5 fb | $1.6\,\sigma$ | $X_t$ | 2.62 fb |

TABLE 5.3: Analyses that contribute to the $K$ value of the highest scoring proto-model from Fig. 5.6. The **Dataset** column lists the contributing signal region (SR) where applicable. The **Obs** and **Exp** columns list the number of observed events or the observed upper limit and the expected background and its uncertainty or the expected upper limit, respectively. The column **Z** lists the significance of the excess, and the column **P** lists the proto-model particle introduced for fitting the observed data. The last column, **Signal** shows the predicted contribution of the proto-model, in number of events for EM results (ATLAS, ATL for short) and in fb for UL results (CMS).

Another interesting point to note in Table 5.3 is the notably smaller signal prediction contribution of the proto-model to the number of events than the one favoured by the excesses, as seen when comparing the **Obs** and **Signal** columns. This is due to tension with the constraints imposed on the signal strength by the Critic. Table 5.4 lists the analyses that mostly contribute to this tension for the proto-model. The 13 TeV CMS multijet analyses for 36 fb$^{-1}$ [186, 187] and 137 fb$^{-1}$ [188] observe under-fluctuations with respect to the expected background and yield the maximum constraint to the proto-model. The proto-model is maximally constrained by the limits of [188] in the 2 jets + $E_T^{\text{miss}}$ and $t\bar{t}+$ $E_T^{\text{miss}}$ channels. In these channels, the proto-model signal cross sections exceeded both the observed and expected UL, as shown in Table 5.4.

| Analysis (all CMS 13 TeV) | Prod | $\sigma_{XX}$ (fb) | $\sigma^{\text{UL}}_{\text{obs}}$ (fb) | $\sigma^{\text{UL}}_{\text{exp}}$ (fb) | $r_{\text{obs}}$ |
|---|---|---|---|---|---|
| CMS multijet, $M_{H_T}$, 137 fb$^{-1}$ [188] | $(\bar{X}_d, X_d)$ | 23.96 | 18.45 | 21.57 | 1.30 |
| CMS multijet, $M_{H_T}$, 137 fb$^{-1}$ [188] | $(\bar{X}_t, X_t)$ | 2.62 | 2.04 | 2.08 | 1.28 |
| CMS multijet, $M_{H_T}$, 36 fb$^{-1}$ [186] | $(\bar{X}_d, X_d)$ | 23.96 | 19.26 | 28.31 | 1.24 |
| CMS multijet, $M_{\text{T2}}$, 36 fb$^{-1}$ [187] | $(\bar{X}_d, X_d)$ | 23.96 | 26.02 | 31.79 | 0.92 |
| CMS $1\ell$ stop, 36 fb$^{-1}$ [189] | $(\bar{X}_t, X_t)$ | 2.62 | 2.91 | 4.44 | 0.90 |

TABLE 5.4: List of the most constraining results for the highest scoring proto-model. The second column displays the constrained production mode, while the third column shows the respective cross section value. The corresponding observed and expected upper limits and the ratio $r_{\text{obs}} = \sigma_{XX}/\sigma^{\text{UL}}_{\text{obs}}$ are also presented.

Similar conclusions were drawn for all the highest scoring proto-models in Figure 5.6. The significance of the highest scoring proto-models was estimated by computing a global $p$-value using the Kernel Density Estimator for the test statistic $K$ defined in Eq. (5.11). Figure 5.7 shows the $K$ distribution under the SM-only hypothesis and the observed $K$ values from the real runs. The green stars represent the $K$ values for the 10 highest scoring proto-models obtained with the real database. Despite occupying the tail of the distribution, these values do not show a strong tension with the SM-only hypothesis. To quantify this compatibility, a $p$-value was computed based on the relative frequency of $K$ values under the SM hypothesis above the observed $K$ values

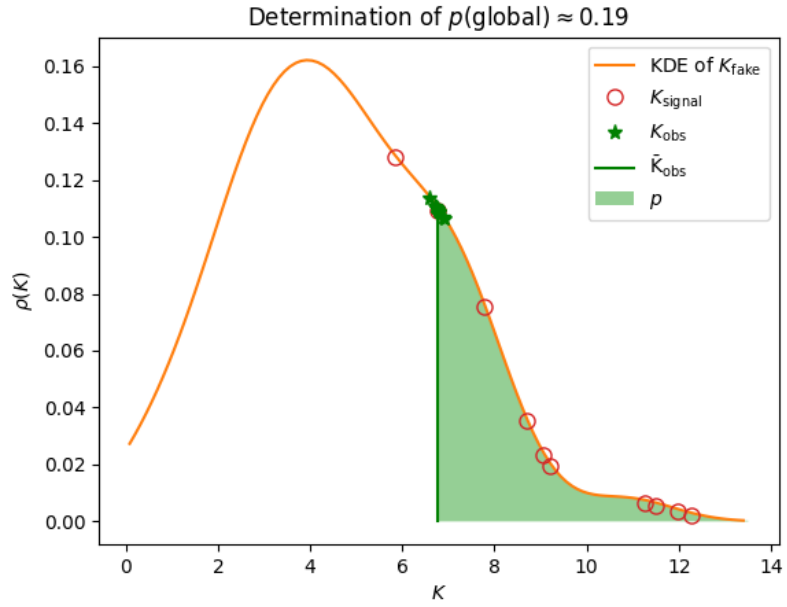


FIGURE 5.7: Values of the test statistic $K$ obtained for the walks discussed in the text. The green stars represent the $K$ values for the highest scoring proto-models from 10 runs over the real database, while the red open circles show the values obtained under the "BSM hypothesis" (see Section 5.3 in [7]). The solid orange curve shows the distribution obtained under the SM-only hypothesis. The shaded green area corresponds to the global $p$-value for average $K$ from the runs over the real database.

$(K_{\text{obs}})$:

$$p_{\text{global}} := \lim_{N\to\infty} \frac{1}{N} \sum_{i=1}^{N} \mathbb{1}_{[\overline{K}_{\text{obs}},\infty]}(K^i_{\text{fake}}) \approx \int_{\overline{K}_{\text{obs}}}^{\infty} dK\rho(K) \,. \tag{5.12}$$

Here, $N = 50$ is the number of fake SM only runs, $\mathbb{1}_X(x)$ is the indicator function which is unity for all $x \in X$ and zero otherwise, $\overline{K}_{\text{obs}}$ is the average of $K_{\text{obs}}$ obtained from the 10 runs over the real database, and $\rho(K)$ refers to the estimated density of the test statistic defined in Eq. (5.11). The shaded area under the curve in Figure 5.7 corresponds to the global $p$-value for the SM hypothesis:

$$p_{\text{global}} \approx 0.19 \,. \tag{5.13}$$

This indicates approximately a 19% probability of observing the experimental data under the SM hypothesis. In this context, the $p$-value quantifies the likelihood of observing data at least as extreme as the recorded results assuming no new physics beyond the SM exists. This result indicated a very mild disagreement with the SM hypothesis as it falls well short of the threshold typically required for claiming a significant discovery (corresponding to $5\sigma$ significance or $p < 0.00003\%$). This conservative result was expected due to potentially overestimated background uncertainties. While not statistically conclusive evidence for new physics, this $p$-value suggested potential

anomalies that merit further investigation.

## 5.8 Conclusions and Outlook

Searches for new physics typically adopt a top-down approach, where theoretically motivated models are tested against various experimental constraints. In the absence of a clear BSM signal, and with the ever-increasing number of models, it becomes relevant to adopt a more model-independent, data-driven approach. The approach discussed in this chapter tackles this inverse problem by relying on SModelS features and its large database of simplified model results to search for feeble signals dispersed across several search channels, and to explain them by means of simpler models called proto-models.

This chapter presented a summary of the study in Ref. [7], which introduced a novel statistical learning algorithm capable of identifying potential dispersed signals across the collection of published LHC analyses. The algorithm's objective is to construct candidate proto-models from small excesses present in the various searches implemented in the SModelS database while maintaining consistency with all other experimental constraints. The proto-model generation is based on the simplified model framework, exploiting the SModelS software and its extensive database of simplified model results from ATLAS and CMS searches for new physics. The Walker algorithm v1 employed a random walk through the proto-model parameter space, stochastically adding or removing particles and modifying their cross sections and branching ratios. This was coupled with a combinatorial algorithm that identified the set of analyses and signal regions which exhibit the strongest deviation from the SM hypothesis, drawing from a total of 86 ATLAS and CMS search results.

Upon running the Walker algorithm v1 over the SModelS database v1.2.4, it identified small excesses at $\approx 2\sigma$ in stop and multijet + $E_T^{\text{miss}}$ searches from ATLAS and CMS. These excesses were explained by a SUSY-like top partner $X_t^1$ and quark partner $X_q$ at mass scale of roughly 1 TeV, along with a neutralino-like lightest particle $X_Z^1$ below 400 GeV. This proto-model signal did not violate any constraints from other searches implemented in the database. The best performing proto-model obtained from these runs has a test statistic $K = 6.9$, while the global $p$-value for the SM hypothesis stood at $p_{\text{global}} \approx 0.19$. The test statistic $K$ accounts for both the deviation from the SM hypothesis and the penalty for new degrees of freedom introduced in the proto-model.

While these results were interesting in their own right, they were viewed primarily as a proof of principle. This implementation of the Walker algorithm (v1) faced several limitations stemming from the variety and type of available simplified model results in SModelS database v1.2.4.

First, the SModelS database has undergone significant upgrades since v1.2.4 (currently v3.1.0) and now contains an extensive collection of experimental searches from ATLAS and CMS (see Appendix B for a detailed list). Searches for long-lived particles (LLPs), monojets, and resonances have been added, increasing the types of final state signatures included in the database. These signatures cannot be captured by the parameter space considered in v1; thus, extensions to the parameter space are required to enable these results to drive proto-model generation.

Second, and perhaps most importantly, only efficiency map results, that provide acceptance times efficiency ($\mathcal{A} \times \epsilon$) information, allow for proper likelihood construction. Analyses providing only 95% CL upper limits on signal cross sections necessitate crude approximations that can significantly distort the statistical evaluation. In SModelS database v1.2.4, merely one-third of available simplified model results are provided as efficiency maps. The number of experimental searches providing efficiency maps has since increased in SModelS database v3.1.0, and thus the next iteration of the Walker algorithm benefits from an expanded collection of results.

Third, with increasing number of experimental searches, the number of possible combinations grows exponentially, making the enumeration of all combination sets computationally expensive. Moreover, many searches now provide detailed statistical models for combining signal regions. While this is more robust, it significantly increases the computational burden of identifying the combination that most deviates from the expected SM background. To address this computational bottleneck, v2 implements an alternative method based on the PathFinder algorithm to accelerate this process.

Fourth, apart from the test statistic $K$, we could not assign statistical significance to the proto-models generated by the Walker algorithm. Although the Walker algorithm followed a MCMC-type walk, there was no robust probability framework for accepting or rejecting proto-models at each step. In particular, since the dimension of the proto-model changed at each step, the acceptance probability depended only on $K$ and did not account for the proposal densities and prior distributions on model parameters. Consequently, we did not expect the walks to converge over the parameter space. Further, we did not check whether the walk adequately explored the available parameter space. Therefore, in the next iteration, significant upgrades to this acceptance procedure are made, following ideas from Reversible Jump Markov Chain Monte Carlo (RJMCMC) sampling methods.

The next chapter introduces the Artificial Proto-modelling framework v2, which addresses these limitations and presents major improvements. While the core ideas remain the same, significant improvements to each block have been made, and these changes required major restructuring of the Walker algorithm.

# Chapter 6

# Artificial Proto-modelling v2

In the previous chapter, we discussed a data-driven methodology for identifying mutually compatible signals dispersed across various searches for new physics at the LHC. These dispersed signals were interpreted in terms of *proto-models*, which parameterised potential new physics through BSM particle content, masses, production cross sections, and branching ratios while remaining independent of specific theoretical assumptions. These proto-models were generated using a Walker algorithm, which combined search channels from the SModelS database (v1.2.4) that exhibited the most significant deviations from the expected SM background while remaining compatible with all other experimental constraints.

In this chapter, we present several major improvements to the artificial proto-modelling framework, pushing it beyond the proof-of-concept stage. First, we expand the proto-model parameter space to target new signatures that were not present in the earlier versions of the SModelS database. These additions are described in Section 6.3.1. Second, as the number of experimental results with complex statistical models increased, enumerating all possible combinations and identifying those with the largest deviations from the expected SM background became computationally expensive. To address this, we implement the PathFinder algorithm [159] to accelerate the search process and modify our method to identify optimal combinations, as outlined in Section 6.4. Third, we make substantial upgrades to both the builder and critic blocks to improve statistical rigour. In the builder block, we construct well motivated proposal densities and priors that guide the acceptance or rejection of proto-models at each iteration of the walk. The critic block is divided into two types depending on the experimental constraints used.

A critical aspect requiring careful consideration is the interpretation of the posterior proto-model space. In the initial implementation, the Walker algorithm ran on varying dimensional proto-model parameter space through a random walk procedure, where the acceptance of proto-models was determined by the test statistic $K$. However, this acceptance criterion did not guarantee the reversibility of the chain, making probabilistic interpretation of the posterior proto-model distribution and convergence assessment challenging. While this limitation did not significantly impact the initial version, which focused primarily on proto-model generation, it became crucial to address for proper statistical inference. We therefore redesigned the acceptance methodology by incorporating principles from the Reversible Jump Markov Chain Monte Carlo (RJMCMC) algorithm, described in Section 3.3.2.

In this chapter, we present the updated framework architecture and validate it on

ensembles of fake SM databases to establish baseline expectations under the SM only hypothesis. We then apply it to the real SModelS database v3.1.0 to identify and characterize potential BSM signals with proper statistical significance. All these comprehensive modifications necessitated a major restructuring of the algorithm flowchart, which is presented in Figure 6.5.

The remainder of this chapter is organized as follows. Section 6.1 motivates the need for a consistent explanation of excesses found in different ATLAS and CMS results. We first discuss the broader phenomenological community's perspective and then focus on which of these experimental results are implemented in the SModelS database. Sections 6.2 - 6.5 describe the updated acceptance criterion and major algorithmic blocks of the Walker framework, with significant improvements made to enhance statistical rigour and computational efficiency. Section 6.6 outlines the software architecture of the proto-modelling framework and commonly used run configurations. Finally, Section 6.7 presents the results of running this updated algorithm on the SModelS database v3.1.0. Most importantly, we discuss not only the best fit proto-models, but also emphasize the type and variety of proto-models generated, their coverage, and the significance of the best fit proto-models.

## 6.1 A look into the database

The primary motivation of artificial proto-modelling is to build candidate models that are consistent with the LHC data. Comparing against all the LHC data is currently outside the scope of this thesis, as we would require a lot more information from experiments. We thus select certain interesting phase space regions, where hints of excesses have been identified by the community at large. This section explains the motivation for selecting these regions as the primary focus for building proto-models.

### Excesses in monojets and soft lepton LHC searches

Although no significant deviation from the SM has been reported by experimental collaborations, small excesses have been recorded in several ATLAS and CMS searches, most notably in searches for single, hard jets plus missing energy (henceforth referred to as "monojets") and soft leptons plus missing energy.

In the searches for soft leptons plus $E_T^{\text{miss}}$, the excesses predominantly appear in events containing two leptons ($2\ell$) with a dilepton invariant mass in the range of 10–20 GeV. On the ATLAS side, the search for events with two soft opposite-sign same-flavour (OSSF) leptons plus $E_T^{\text{miss}}$ (ATLAS-SUSY-2018-16 [190]) observed a small excess, particularly evident when combined with results from a search for $3\ell$ + $E_T^{\text{miss}}$ (ATLAS-SUSY-2019-09 [191]). On the CMS side, two analyses observed similar excesses in the same region: one searching for 2 or 3 low $p_T$ leptons plus $E_T^{\text{miss}}$ (CMS-SUS-18-004 [192]), and another searching for 3 or 4 leptons plus $E_T^{\text{miss}}$, with up to 2 hadronically decaying $\tau$ leptons or 2 same-sign light leptons (CMS-SUS-19-012 [193]). All these analyses utilize the full Run 2 luminosity and have been interpreted in terms of simplified supersymmetric scenarios in which the light electroweakinos are composed mostly of higgsino or wino-binos. Surprisingly, the excesses appear in nearly the same regions of simplified higgsino and bino-wino MSSM parameter space across both collaborations. This overlap suggests that a model producing a good fit to one soft-lepton analysis may also fit the other searches.

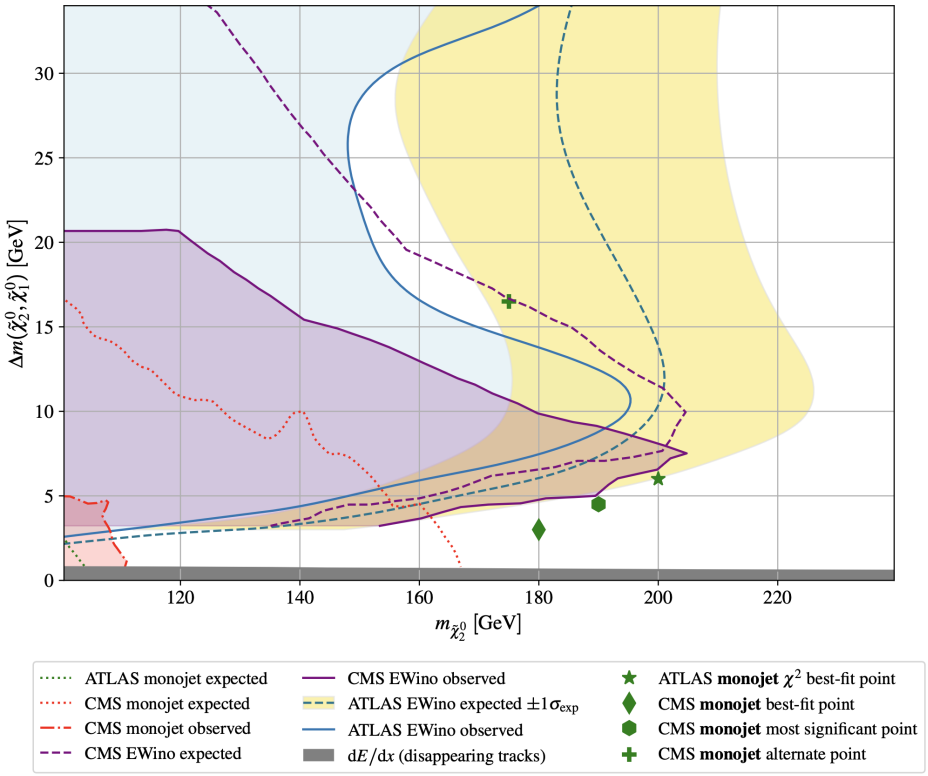


FIGURE 6.1: Exclusion regions in the $(m_{\tilde{\chi}_2^0}, \Delta m)$ plane presented in the study [195] through the reinterpretation of the results of several LHC analyses.

In the monojet searches, excesses have been recorded by ATLAS (ATLAS-EXOT-2018-06 [74]) and CMS (CMS-EXO-20-004 [194]). In the ATLAS analysis, the excesses occur for $E_T^{\text{miss}} > 400$ GeV. The CMS analysis records significant excesses in the 2018 dataset, with some SRs of the 2016 dataset also reporting slight excesses. While these searches were originally interpreted within different model frameworks, they can be reinterpreted for electroweakino pair production followed by decays to the LSP and soft SM fermions. The rejection of leptons and additional jets with $p_T$ above a few GeV in these analyses makes them particularly sensitive to very small electroweakino mass splittings, and thus are complementary to the soft lepton searches discussed above.

A series of studies conducted in the papers [195–198] demonstrated that the signatures targeted by these searches overlap and could be explained by simple models. In particular, these studies have examined the compatibility of these excesses in the context of higgsino and wino-bino simplified models. The study in [195], based on MADANALYSIS 5, found the soft lepton excesses to be surprisingly compatible with the monojet excesses from both ATLAS and CMS when interpreting the monojet signals in terms of "simplified higgsino" scenarios.[1] Figure 6.1 illustrates the compatibility of these excesses in simplified pure-higgsino scenarios as studied by [195]. In the Figure, 'ATLAS EWino' refers to the combined ATLAS soft lepton analyses [190, 191], while 'CMS EWino' refers to the CMS soft lepton analysis [192]. The disappearing track constraints are from [199], and the monojet exclusions are from the ATLAS and CMS monojet searches mentioned above. Four statistically significant benchmark points

[1] Here, the lightest supersymmetric particle (LSP) $\tilde{\chi}_1^0$, the next-to-lightest supersymmetric particle (NLSP) $\tilde{\chi}_1^\pm$ and the second lightest neutralino $\tilde{\chi}_2^0$ constitute a triplet of "pure" higgsinos.

that potentially explain the observed excesses are marked for the monojet searches (for details of the "best-fit" points, see [195]). Thus, for a higgsino-like LSP, the excesses correspond to chargino-LSP mass splittings of roughly 5–15 GeV. Furthermore, when these soft-lepton search results are considered alongside the disappearing-track analysis, there exists a gap in the parameter space for modest mass splittings of a few GeV, where neither higgsinos nor winos are excluded at any mass above the long-standing LEP limit of approximately 93 GeV. A complementary study in [196, 198] interpreted the excesses in the wino-bino scenario where the light electroweakinos are composed entirely of gauginos, i.e., the higgsinos are decoupled. For a bino-like LSP, the excesses can be explained with best-fit points having NLSP-LSP mass splittings of roughly 10–20 GeV.

While such excesses are expected to appear in searches due to statistical fluctuations, several factors make these particular excesses worthy of investigation: first, they appear consistently across different experiments and search channels; second, they lie in a parameter region that could provide a viable dark matter candidate, and may offer an explanation for the measured value of the muon's magnetic dipole moment. These features have sparked considerable interest in the phenomenological community.

### Excesses in the SModelS database v3.1.0

The discussion in the previous subsection motivates an investigation into the types of proto-models capable of consistently explaining the observed excesses. Such an investigation necessarily relies on reinterpreting the mentioned search results within the SModelS database. However, practical limitations exist in the available reinterpretation material. From the soft lepton searches, only the ATLAS analysis has published sufficient information for SModelS to construct a likelihood. Specifically, efficiency maps and a full statistical model are available for the ATLAS analysis, while only upper limit maps are available for the CMS 2-3$\ell$ + $E_T^{\text{miss}}$ search, and neither upper limit maps nor efficiency maps are available for the CMS 3-4$\ell$ + $E_T^{\text{miss}}$ search. From the monojet searches, only the CMS search provides reinterpretation material in the form of simplified-likelihood yields and a covariance matrix. while only upper limit maps on the observed cross section are available for the ATLAS monojet search. While the best-fit points from the monojet searches were shown to be compatible with the excesses from soft-lepton searches in [195], no global likelihood could be constructed due to missing information from the experiments. To address this limitation, "home-grown" efficiency maps were generated for the ATLAS monojet search from electroweakino production and included in the current SModelS v3.1.0 database. [2]

Figure 6.2 presents the distribution of per-SR significances under the SM hypothesis, i.e. the observed deviation from the SM prediction in units of error on the SM prediction, for the EM-type results present in the SModelS database v3.1.0. These significance values were computed from the observed event counts, expected event counts, and background uncertainties provided by the experiments for individual signal regions. The top plot presents the distribution for all validated EM-type results, while the bottom plot restricts to searches for electroweakinos (EWinos) and monojets. If no new physics is observed, this distribution is expected to follow the standard normal distribution as depicted by the black dotted line. The peak around 0 above the standard normal distribution reflects the conservativeness of the experiments. Positive

[2] Here, "home-grown" refers to using the recast from MadAnalysis 5 and a custom EMCreator tool.

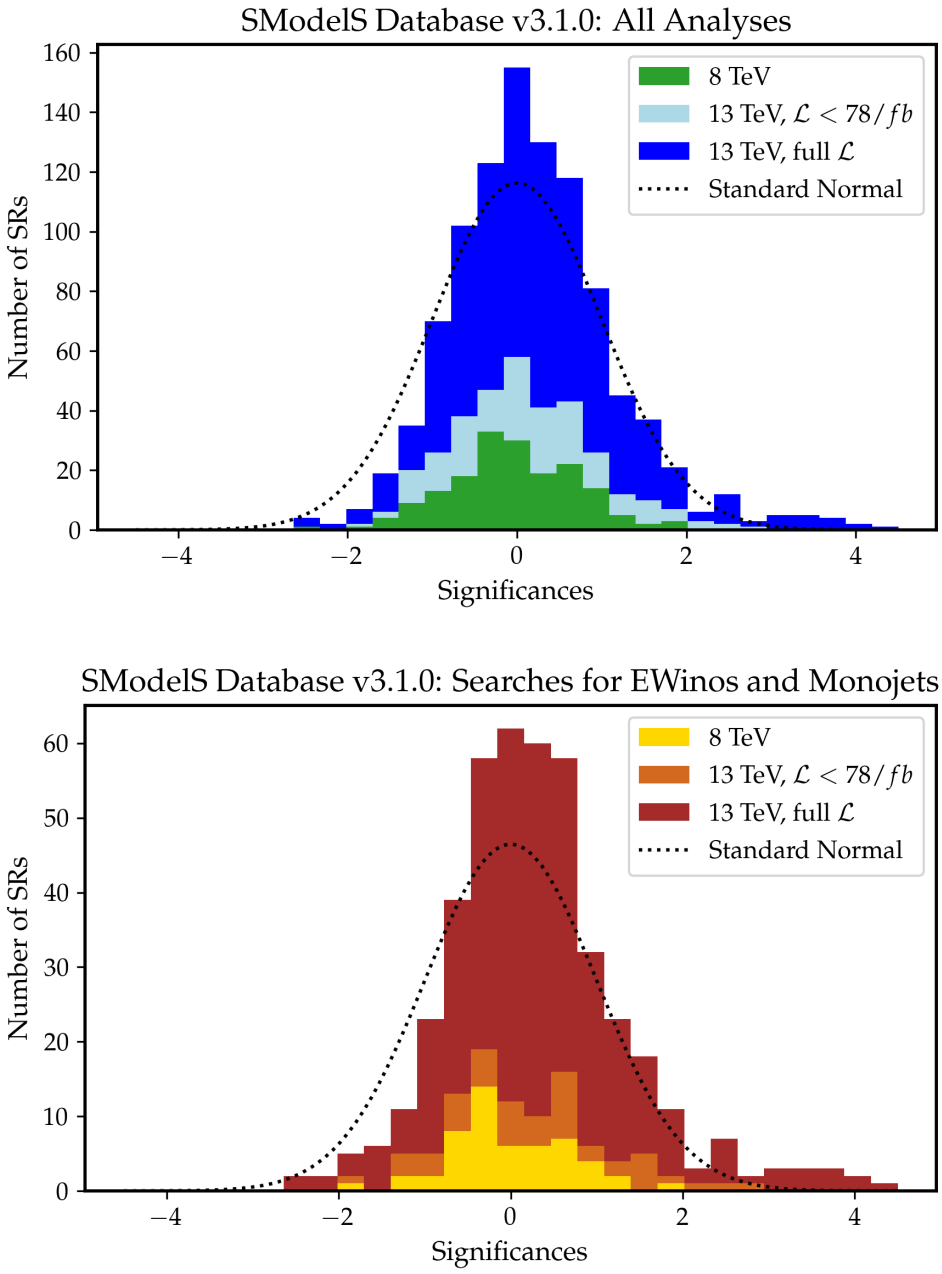


FIGURE 6.2: Distribution of the per-SR significances under the SM hypothesis, for all the validated analyses with EM-type results in the SMODELS database v3.1.0 (top), and for the electroweakino (EWino) and monojet searches only (bottom). A standard normal distribution is expected if no new physics is in the data (shown in black dotted line). New physics would manifest itself as an overabundance of large (positive) significances.

(negative) significances represent over-fluctuations (under-fluctuations) in the respective signal regions, i.e. number of observed events is larger (smaller) than expected SM background events. Note that this distribution is slightly more skewed toward the right tail in searches for EWinos and monojets compared to the full set of EM-type results validated in SModelS database v3.1.0. This is further emphasized when we consider only the 13 TeV full luminosity ($\mathcal{L}$) distribution. This indicates that slightly more excesses are recorded in the EWino plus monojets sector than in the rest of the implemented results, hence motivating the study of this signature space.

We can further look at the SRs from individual analyses that contribute to the tails of the distribution in Figure 6.2. Figure 6.3 presents the individual SR significances under the SM hypothesis for the 10 highest (blue) and 10 lowest (red) significance values. For each analysis presented in the figure, only the maximum and/or minimum signal region significance is shown. The top plot selects the highest/lowest SR significances across all validated analyses with EM-type results, while the bottom panel is restricted to EWino and monojet searches. The analyses appearing in both figures are highlighted in brown. Certain key observations can be made from these plots. In both figures, the positive significances outweigh the negative significances in magnitude. Further, the EWino and monojet searches dominate the distribution of positive significances. Although not depicted in the figure, several SRs of CMS-EXO-20-004 [194], ATLAS-EXOT-2018-06 [74], and ATLAS-SUSY-2018-16 [190] exhibit local significances exceeding $2\sigma$, indicative of over-fluctuations relative to Standard Model predictions.

Lastly, the ability of SModelS to reproduce the experimental limits of the ATLAS soft lepton search differs significantly depending on the scenario considered. For scenarios where the $\tilde{\chi}_2^0$ and $\tilde{\chi}_1^\pm$ are (almost) mass-degenerate, EMs for the exclusive signal regions (extracted from the HEPData patchset) and a full statistical model are available on HEPData. As shown in the left panel of Figure 6.4, this allows SModelS to correctly reproduce the experimental limits. However, for scenarios where the produced particles ($\tilde{\chi}_1^0, \tilde{\chi}_1^2$ and $\tilde{\chi}_1^\pm$) are not mass-degenerate, only EMs for inclusive signal regions are available, without any means for combining them. In this case, the SModelS exclusion is based on the most sensitive signal region only. As shown in the right panel of Figure 6.4, SModelS cannot correctly reproduce the experimental limit under these conditions. What is more, SModelS also cannot reproduce the excess in non-degenerate scenarios. Consequently, it is expected that the Walker algorithm will favour mass degenerate electroweak partner like particles over non-degenerate ones in this region.

Given these considerations, it is particularly interesting to investigate whether our updated Walker algorithm can successfully identify these excesses and construct proto-models that explain them in a statistically consistent manner. Although the Walker algorithm is capable of exploring all available analyses in the SModelS database, this thesis focuses specifically on electroweakino and monojet searches, which exhibit the most compelling excesses.

## 6.2 Walker v2

The Walker algorithm in version 1 explored the space of proto-models via a MCMC-type process, handling the varying dimension of the proto-model states at each step by using a test statistic $K$ that included a penalty term to compare proto-models with

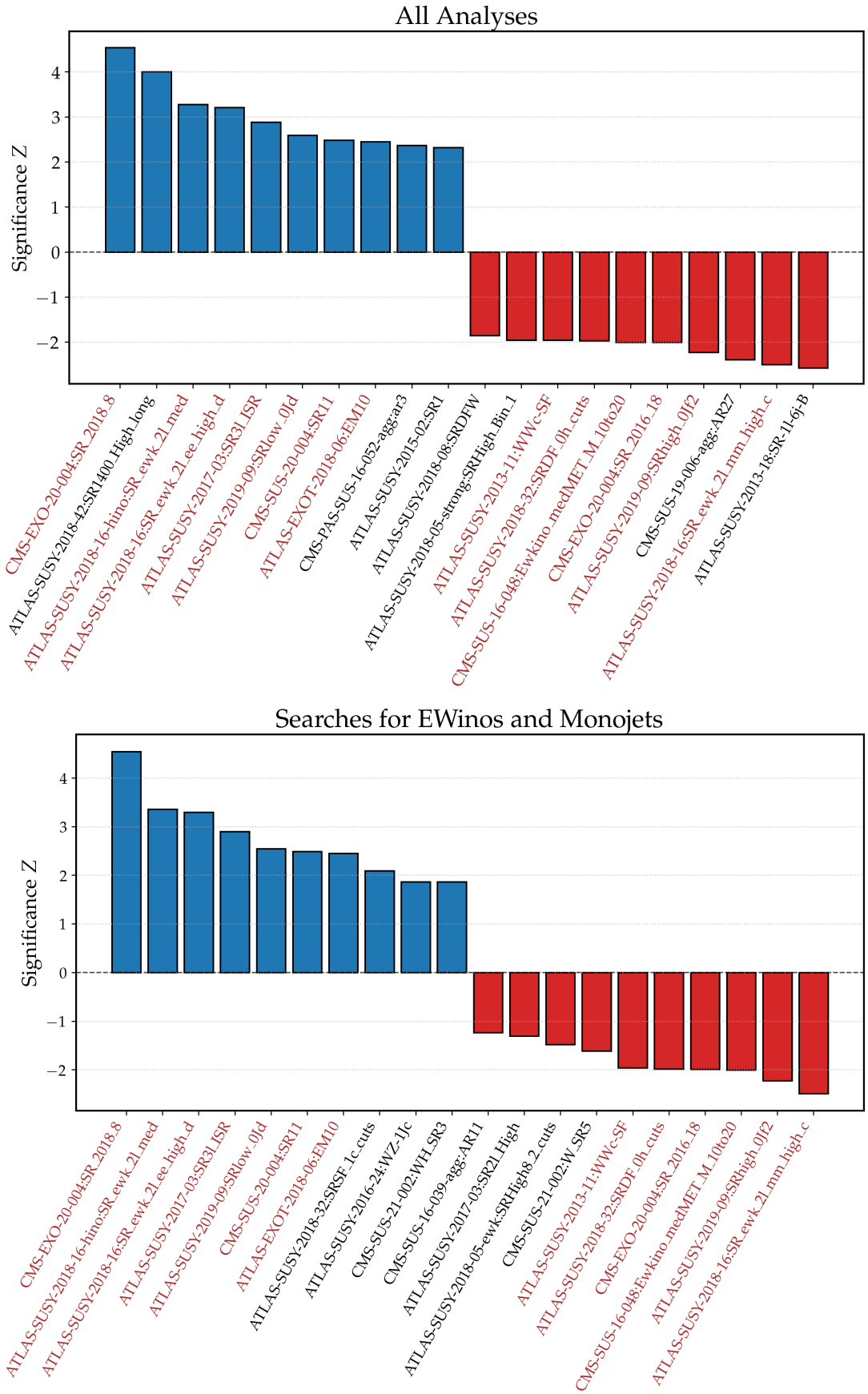


FIGURE 6.3: Individual SR significances under the SM hypothesis for the 10 highest (blue) and 10 lowest (red) significance values. The top plot selects the highest and/or lowest SR significances per analysis across all validated analyses with EM-type results, while the bottom panel is restricted to electroweak-ino (EWino) and monojet searches. Analyses appearing in both figures are highlighted in brown.

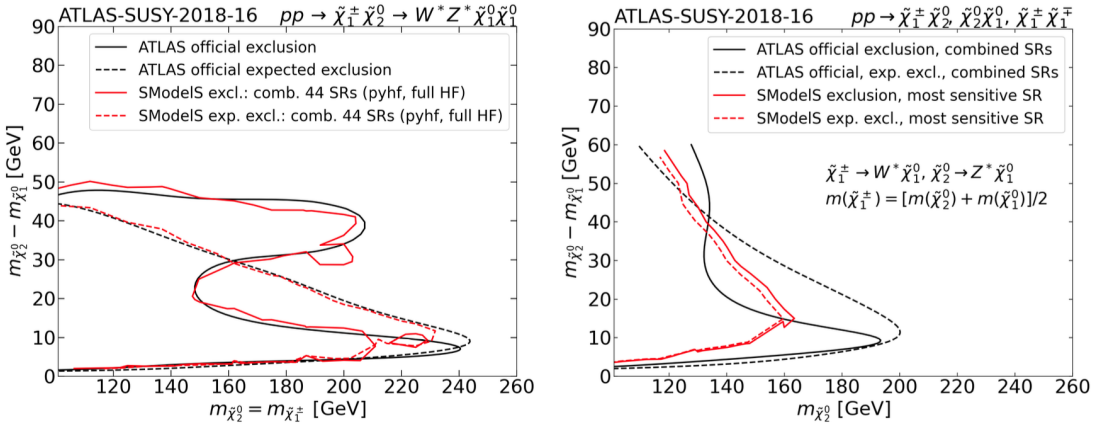


FIGURE 6.4: Comparison of SMODELS exclusions to official ATLAS limits for ATLAS-SUSY-2018-16 [190]. In the left panel, a wino-bino scenario is considered, while in the right panel, a higgsino-LSP scenario is considered, where. In both cases, the heavier electroweakino ($\tilde{\chi}_1^\pm, \tilde{\chi}_2^0$,) decay into off-shell $W/Z$ bosons along with the LSP ($\tilde{\chi}_1^0$). The official ATLAS limits can be correctly reproduced in the wino-bino scenario as EMs are provided for the exclusive SRs along with the full statistical model. However, SMODELS cannot correctly reproduce the ATLAS limits in the higgsino-LSP scenario because only EMs for inclusive SRs are provided for this case, without the capability to combine them.

different degrees of complexity (see Section 5.6). The proposed proto-models of different dimensionality at consecutive steps were compared using this test statistic, with their acceptance/rejection based on the following criterion:

$$\alpha(\mathbf{M}_i \to \mathbf{M}_{i+1}) = \min\left\{1, \quad \exp\left[\frac{1}{2}(K_{i+1} - K_i)\right]\right\}, \tag{6.1}$$

$$= \min\left\{1, \quad \frac{L^{i+1}_{\mathbf{M}}(\hat{\mu})}{L^{i}_{\mathbf{M}}(\hat{\mu})} \frac{L^{i}_{\mathbf{SM}}}{L^{i+1}_{\mathbf{SM}}} \frac{\pi(\mathbf{M}_{i+1})}{\pi(\mathbf{M}_i)}\right\}. \tag{6.2}$$

Here, $\mathbf{M}_i$ corresponds to the proto-model at the $i^{th}$ step of the walk, $L^i_{\mathbf{M}}(\hat{\mu})$ is the maximum likelihood of the $i^{th}$ proto-model evaluated at $\hat{\mu}$ over the optimal combination of predictions, $L^i_{\mathbf{SM}}$ is the SM likelihood ($\mu = 0$) over the optimal combination of predictions for the $i^{th}$ proto-model and $\pi(\mathbf{M}_i)$ is the prior on the $i^{th}$ proto-model.

However, this procedure does not satisfy the detailed balance condition given in Eq. (3.15), which is typically needed to ensure the reversibility of a chain in a MCMC process and obtain meaningful posterior distributions. This was not of utmost priority in v1, as the initial concept focused on developing an algorithm capable of finding excesses in the SMODELS database and building suitable candidate models to explain such excesses. Since no probabilistic interpretation was ever given for the prevalences of the proto-models and their parameters in the chain, the violation of the detailed balance was not considered to be an obstacle and the authors did not expect to get a stationary distribution for the test statistic $K$.

In v2, we aim to make rigorous statistical inferences about the posterior proto-model space. Further, with the help of the proto-model posterior distribution, we would like

to formulate a convergence criterion for the algorithm. To uphold the detailed balance condition in a random walk in which the dimension of the parameter space can vary between iterates of the Markov chain, we adapt ideas from RJMCMC sampling methods to formulate a new acceptance criterion at each step. That is to say, if the condition:

$$\frac{L_c(D|\mu=1,\mathbf{M}_i)}{L_c(D|\mu=0,\mathbf{M}_i)}\frac{\pi(\mathbf{M}_i)}{\pi(\mathbf{SM})}\pi(\theta_i|\mathbf{M}_i)p_U(u)\,q(\mathbf{M}_i\to\mathbf{M}_{i+1}) = \frac{L_{c'}(D|\mu=1,\mathbf{M}_{i+1})}{L_{c'}(D|\mu=0,\mathbf{M}_{i+1})}\frac{\pi(\mathbf{M}_{i+1})}{\pi(\mathbf{SM})}\,\pi(\theta_{i+1}|\mathbf{M}_{i+1})p_V(v)q(\mathbf{M}_{i+1}\to\mathbf{M}_i)\,, \tag{6.3}$$

holds for all proto-models $\mathbf{M}$ at steps $i$ and $i+1$, then we are guaranteed to converge towards a stationary posterior distribution over the proto-model phase space. In Eq. (6.3), $L_c$ is the likelihood of a particular proto-model ($\mu=1$) or SM ($\mu=0$) over the optimal combination $c$ of experimental results, $\pi$ is the prior on the proto-model/SM, and $\pi(\theta|\mathbf{M})$ is the conditional prior on the parameters $\theta$ given the proto-model $\mathbf{M}$.[3] The term $q$ represents the proposal density for jumping between different proto-model states, and $p_U(u)$ and $p_V(v)$ are the probability densities of the latent variables $u$ and $v$ which follow distributions $U$ and $V$, respectively. These latent variables are introduced to account for the potential change in dimensionality between $\mathbf{M}_i$ and $\mathbf{M}_{i+1}$. That is to say, if $\mathbf{M}_i$ and $\mathbf{M}_{i+1}$ have dimensionalities $d_i$ and $d_{i+1}$, respectively, then $u$ and $v$ have to be of dimensionalities $d_u$ and $d_v$ such that $d_i + d_u = d_{i+1} + d_v$. The proposal densities $q$ together with the latent variables take into account the change in dimensionality between different dimensional proto-model states. These terms are implemented in the Builder block, where specific proposal densities are constructed for each move type, ensuring proper handling of trans-dimensional transitions. Note that the distribution which we aim to infer differs from the typical RJMCMC algorithms in that we are more interested in the likelihood ratio $\frac{L(D|\mu=1,\mathbf{M})}{L(D|\mu=0,\mathbf{M})}$, and not just $L(D|\mu=1,\mathbf{M})$.

To go from a proto-model $\mathbf{M}_i$ to a proto-model $\mathbf{M}_{i+1}$, we attempt multiple moves indexed by $m$ with certain probabilities. Following Green, we define the acceptance probability of the new proposed proto-model with respect to the previous as:

$$\alpha(\mathbf{M}_i\to\mathbf{M}_{i+1}) = \min\Bigg\{1, \underbrace{\frac{L_{c'}(\mu=1|\mathbf{M}_{i+1})}{L_{c'}(\mu=0|\mathbf{M}_{i+1})}\frac{L_c(\mu=0|\mathbf{M}_i)}{L_c(\mu=1|\mathbf{M}_i)}}_{\text{likelihood ratio}}\underbrace{\frac{\pi(\mathbf{M}_{i+1})}{\pi(\mathbf{M}_i)}}_{\text{prior ratio}}\underbrace{\frac{\pi(\theta_{i+1}|\mathbf{M}_{i+1})}{\pi(\theta_i|\mathbf{M}_i)}}_{\substack{\text{parameter}\\ \text{prior ratio}}} \frac{p_V(v)}{p_U(u)}\prod_m\underbrace{\frac{q_m(\mathbf{M}_{i+1}\to\mathbf{M}_i)}{q_m(\mathbf{M}_i\to\mathbf{M}_{i+1})}}_{\text{proposal ratio}}\Bigg\}. \tag{6.4}$$

[3] The SM likelihood can differ across proto-model states if their optimal combination of experimental results are different.

The revised Walker algorithm (v2) implements the following iteration structure:

- **Builder:** The Builder block is responsible for defining the proto-model particle content and its parameters, along with implementing functions that propose random changes to the proto-model. In v2, we explicitly define a proposal density for each random change (i.e. a move), which then affects the acceptance probability.
- **Combiner**: The Combiner block is responsible for collecting all the experimental results from the SModelS database that provide theory predictions for the proto-model. It then identifies the optimal combination of experimental results using the PathFinder algorithm with the updated combination matrix as input.
- **Acceptance/Rejection**: With the acceptance probability defined in Eq. (6.4), we either accept the current proto-model and proceed to the next step, or reject it and revert to the previous proto-model.
- **Critic**: We define a separate Critic block that implements two types of critics – one based on UL-type results and one based on EM-type results. The EM-type critic is computationally expensive, and is thus executed after the acceptance/rejection step.

The Walker algorithm terminates after reaching a predefined maximum number of steps. We are currently developing an automatic stopping criterion by evaluating the convergence of proto-models generated both within individual walks and across parallel walks.[4] This iteration procedure is summarised in the flowchart displayed in Figure 6.5.

## 6.3 Builder v2

The Builder module in version 2 maintains its responsibility for defining the BSM particle content and the associated parameters for a proto-model. In v2, we extend the proto-model parameter space to capture additional experimental signatures in the updated SModelS database and define the proposal densities for each move type attempted.

### 6.3.1 Additions to the Proto-models Parameter Space

To capture excesses observed in the soft-lepton signatures and monojets, v2 introduces off-shell decay modes for $X_Z^2$ and $X_W^1$. This allows the algorithm to explore proto-models with compressed mass spectra in the electroweak sector where small mass differences between particles produce characteristically soft decay products. In addition to the decay modes listed in Table 5.1, the following decays are now available in v2:

$$X_Z^2 \to q\bar{q}X_Z^1\,,\; b\bar{b}X_Z^1\,,\; \ell\ell X_Z^1\,,\; \nu_\ell\bar{\nu}_\ell X_Z^1\,; \tag{6.5}$$

$$X_W^1 \to q\bar{q}'X_Z^1\,,\; \ell\nu_\ell X_Z^1\,, \tag{6.6}$$

[4] At the time of writing this thesis, the convergence criterion remains in the testing phase.

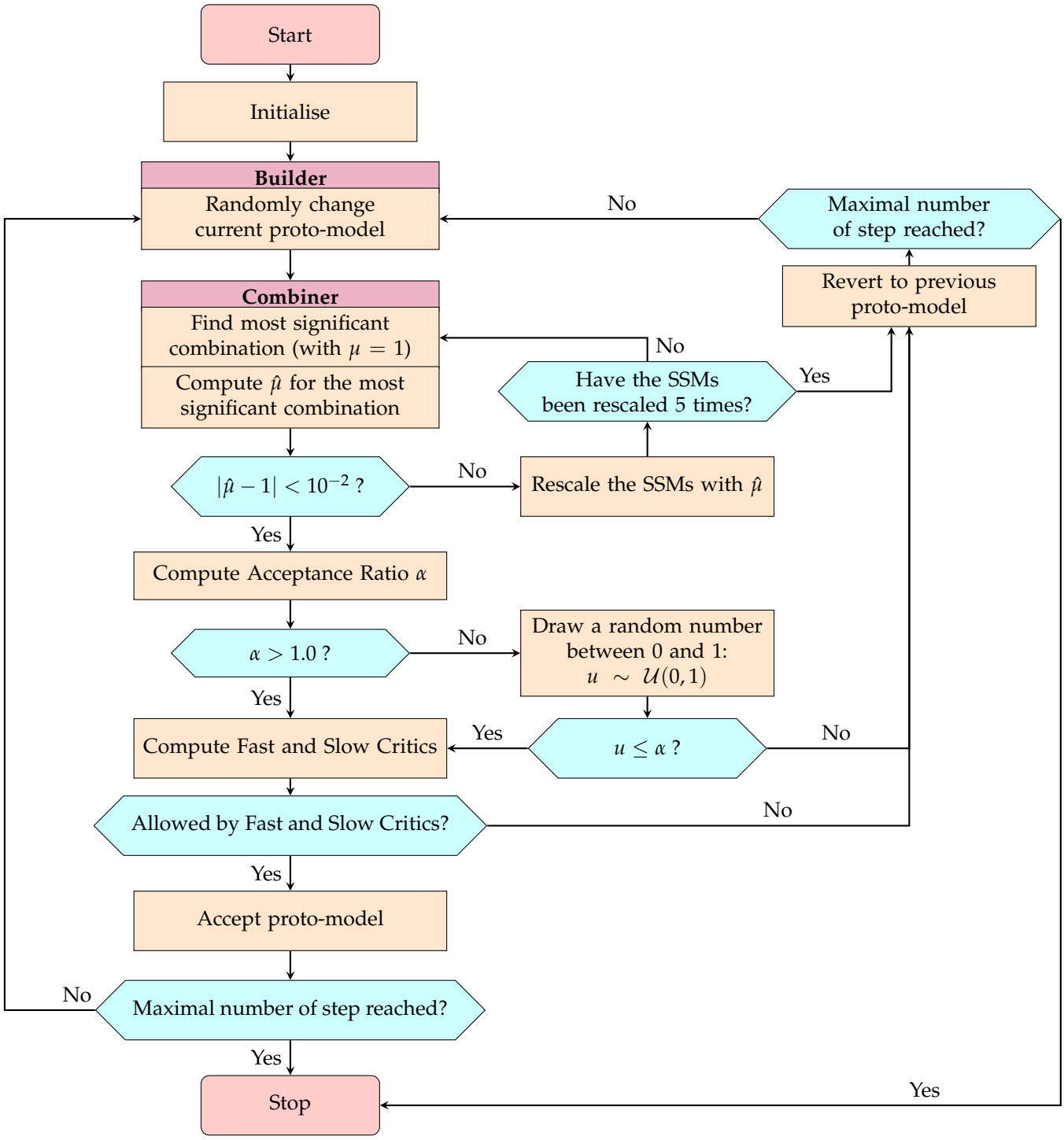


FIGURE 6.5: Simplified flowchart of the Walker algorithm v2.

with $q, q' \in \{u, d, s, c\}$, and $\ell \in \{e, \mu, \tau\}$. We assume the leptonic decays to be flavour democratic, i.e. equal branching ratios for all three off-shell leptonic decays. For decays to light quark, the quark flavour is neglected.

The off-shell decays for $X_W^1$ and $X_Z^2$ are initialised when their mass difference from the LBP is smaller than $m_{W^\pm}$ and $m_Z$, respectively. Upon initialisation, the corresponding on-shell decay channels are disabled. The algorithm incorporates biased sampling to ensure adequate exploration of compressed spectra scenarios. When either $X_Z^2$ or $X_W^1$

is added or their masses are adjusted, there is a 10% chance that they will enter the off-shell region. Additionally, when the mass of either $X_Z^2$ or $X_W^1$ shifts to the off-shell region, there is a 20% chance that the other electroweak partner particle will also shift to the off-shell region and be added to the proto-model. This procedure ensures that the off-shell region is adequately explored, particularly where both $X_Z^2$ and $X_W^1$ are off-shell, preventing under-sampling due to volume effects.

#### Reference Cross Sections

In the previous version, we initialised cross sections via a signal strength multiplier times the corresponding MSSM cross section. This cross section was calculated using Pythia/NLLFast. Instead of calculating via Pythia /NLLFast, we now make use of reference cross sections from [200]. If the required cross section is not available, a similar one is used instead. For example, the 8 TeV cross sections $\sigma(pp \to \tilde{\chi}^0\tilde{\chi}^0)$ are not given by [200], so the $\sigma(pp \to X_Z X_Z)$ cross sections are initialized with $\sigma(pp \to \tilde{\chi}^{\pm}\tilde{\chi}^{\mp})$; for consistency, the same is done for 13 TeV cross sections.

### 6.3.2 Random changes to the proto-model

In each iteration of the Walker algorithm, multiple moves are attempted to change the parameter space of the proto-model. In v1, a probability was assigned to each type of move, but no construction of a proper proposal density was made. In v2, we explicitly define a proposal density for each move, which is then taken into consideration while accepting or rejecting a proto-model. Modifications to a proto-model at a given step can be broadly classified into two categories: (a) trans-dimensional moves that alter the number of parameters of the proto-model and (b) parameter updates that modify existing parameter values without changing dimensionality.

#### Trans-dimensional moves

Whenever we add/remove degrees of freedom (particles, decay channels or production modes) from the current proto-model, we check the probabilities of such changes against the following proposal probabilities:

$$p_{\text{add}}(\mathbf{M}_i \to \mathbf{M}_{i+1}) = \frac{\sigma(-z_{\mathbf{M}_{i+1}})}{\sigma(-z_{\mathbf{M}_i})} = \frac{1+\exp(z_{\mathbf{M}_i})}{1+\exp(z_{\mathbf{M}_{i+1}})}; \qquad \dim(\mathbf{M}_i) < \dim(\mathbf{M}_{i+1})\,, \tag{6.7}$$

$$p_{\text{rem}}(\mathbf{M}_i \to \mathbf{M}_{i+1}) = \frac{\sigma(z_{\mathbf{M}_i})}{\sigma(z_{\mathbf{M}_{i+1}})} = \frac{1+\exp(-z_{\mathbf{M}_{i+1}})}{1+\exp(-z_{\mathbf{M}_i})}; \qquad \dim(\mathbf{M}_i) > \dim(\mathbf{M}_{i+1})\,, \tag{6.8}$$

where

$$z_{\mathbf{M}} = \left(\frac{n_{\text{particles}} - 8}{a_1} + \frac{n_{\text{BRs}}}{a_2} + \frac{n_{\text{SSMs}}}{a_3}\right)_{\mathbf{M}}, \tag{6.9}$$

is inspired from the prior on the dimension of the proto-model as defined in Eq. (5.9) and $a_1, a_2$, and $a_3$ are taken to be 2, 4, and 8 as before. Note that the above probabilities take into account the extra degrees of freedom being added/removed given the current number of degrees of freedom of the proto-model.

There are three move types through which the dimension of a proto-model can be modified. These random moves are implemented independently of each other and are described below.

**1. Adding/Removing Particles**: When we propose to add a particle to a proto-model from the list of allowed particles, we need to initialise its mass, signal strength multipliers for the corresponding production modes, and branching ratios for the allowed decay channels. Therefore, unlike typical RJMCMC processes where the dimension changing move usually alters the dimension of the current state space by 1, adding a particle alters the dimension of the current proto-model by more than 1. The same can be said when we propose to remove a particle from the current proto-model, as we would also need to remove the corresponding production modes and decay channels.

To add a particle to a proto-model, we need to assign values for the parameters associated with the particle. Thus, the new parameters $\theta_{i+1}$ of the proposed proto-model are then:

$$\theta_{i+1} = \theta_i + (m_{\text{new}}, \{b_{\text{new},k}\}, \{\kappa_{\text{new},l}\})\,. \tag{6.10}$$

Here, $\theta_i$ are the parameters associated with the current proto-model $\mathbf{M}_i$, $m_{\text{new}}$ is the mass assigned to the new particle, $\{b_{\text{new},k}\}$ are the branching ratios assigned to $K$ decay channels, and $\{\kappa_{\text{new},l}\}$ are the signal strength multipliers assigned to $L$ production modes. The values of the new parameters are drawn from the distributions of the latent variables. Since $d_i < d_{i+1}$, the dimensions of the latent variables are $d_v = 0$ and $d_u = 1 + K + L$. The distribution of $u = (m, \{b_k\}, \{\kappa_l\})$ is taken to be $U = (\mathcal{U}(0,1), \pi(b), \pi(\kappa))$, where $\mathcal{U}(0,1)$ is a uniform distribution on $[0,1]$, and $\pi(b)$ and $\pi(\kappa)$ are the prior distributions on the branching ratios and the SSMs detailed in Section 6.3.3. The new parameters are then assigned as $m_{\text{new}} = m_{\text{LBP}} + (m_{\text{max}} - m_{\text{LBP}}) \times m$, $b_{\text{new},k} = b_k$, and $\kappa_{\text{new},l} = \kappa_l$. The sum of the initialised branching ratios is required to be normalised to unity.

We then add the particle with all its parameters to the proto-model with the probability defined in Eq. (6.7). As shown in Eq. (6.4), the ratios of the latent variable distributions and the proposal densities for each move type affect the acceptance/rejection step. Thus, adding a new particle with $K$ decay modes and $L$ production modes yields the following terms in the acceptance ratio:

$$\left.\frac{p_V(v)}{p_U(u)}\,\frac{q(\mathbf{M}_{i+1}\to\mathbf{M}_i)}{q(\mathbf{M}_i\to\mathbf{M}_{i+1})}\right|_{\text{add par}} = \frac{1}{p(m)\prod_{k=1}^{K} p(b_k)\prod_{l=1}^{L} p(\kappa_l)}\,\frac{p_{rem}(\mathbf{M}_{i+1}\to\mathbf{M}_i)}{p_{add}(\mathbf{M}_i\to\mathbf{M}_{i+1})}\,\frac{n_{fr}}{n_{un}}\left|\frac{\partial(\theta_{i+1},v)}{\partial(\theta_i,u)}\right|\,. \tag{6.11}$$

Here, the first fraction on the right side represents the ratio of the latent variable distributions. The second fraction reflects the proposal probabilities for changing the dimension of the proto-model defined in Eq. (6.7) and Eq. (6.8). The third fraction is due to the probability of choosing the particle to be added (removed) from the list

of frozen (unfrozen) particles, corresponding to $1/n_{fr}(1/n_{un})$.[5] The final term on the right-hand side is a Jacobian determinant arising from the change of variables from $(\theta_i, u)$ to $(\theta_{i+1}, v)$.

The terms in Eq. (6.11) appear tedious to calculate at first glance, but most factors cancel when we take into account the prior ratios on the proto-model parameters, i.e.:

$$\left.\frac{\pi(\theta_{i+1}|\mathbf{M}_{i+1})}{\pi(\theta_i|\mathbf{M}_i)}\,\frac{p_V(v)}{p_U(u)}\,\frac{q(\mathbf{M}_{i+1}\to\mathbf{M}_i)}{q(\mathbf{M}_i\to\mathbf{M}_{i+1})}\right|_{\text{add par}} = \frac{\pi(m_{\text{new}})\prod_{k=1}^{K}\pi(b_{\text{new},k})\prod_{l=1}^{L}\pi(\kappa_{\text{new},l})}{p(m)\prod_{k=1}^{K}p(b_k)\prod_{l=1}^{L}p(\kappa_l)}\,\frac{p_{rem}(\mathbf{M}_{i+1}\to\mathbf{M}_i)}{p_{add}(\mathbf{M}_i\to\mathbf{M}_{i+1})}\,\frac{n_{fr}}{n_{un}}\left|\frac{\partial(\theta_{i+1},v)}{\partial(\theta_i,u)}\right|,$$

$$= \frac{p_{rem}(\mathbf{M}_{i+1}\to\mathbf{M}_i)}{p_{add}(\mathbf{M}_i\to\mathbf{M}_{i+1})}\,\frac{n_{fr}}{n_{un}}\,. \tag{6.12}$$

In the above equation, the priors on the new branching ratios and SSMs cancel with the probability distributions of the corresponding latent variables. The prior on the mass equals $(m_{\text{new}} - m_{\text{LBP}})^{-1}$, which cancels with the Jacobian determinant. Thus, we are ultimately left with the two fraction terms on the second line of the equation.

The above principle also applies when removing a particle in the proto-model. We remove a particle from a proto-model with all its associated parameters with the probability defined in Eq. (6.8). In this case, the new parameters $\theta_{i+1}$ of the proposedproto-model are:

$$\theta_{i+1} + (m_{\text{old}}, \{b_{\text{old},k}\}, \{\kappa_{\text{old},l}\}) = \theta_i\,, \tag{6.13}$$

where "old" denotes the parameters that are being removed. Since $d_{i+1} < d_i$, the dimension of the latent variables are $d_u = 0$ and $d_v = 1 + K + L$. The proposal ratio, together with the prior ratios and the ratios of the latent variable distributions for the removing a particle, can be obtained by reversing the terms on the right-hand side of Eq. (6.12):

$$\left.\frac{\pi(\theta_{i+1}|\mathbf{M}_{i+1})}{\pi(\theta_i|\mathbf{M}_i)}\,\frac{p_V(v)}{p_U(u)}\,\frac{q(\mathbf{M}_{i+1}\to\mathbf{M}_i)}{q(\mathbf{M}_i\to\mathbf{M}_{i+1})}\right|_{\text{rem par}} = \frac{p(m)\prod_{k=1}^{K}p(b_k)\prod_{l=1}^{L}p(\kappa_l)}{\pi(m_{\text{old}})\prod_{k=1}^{K}\pi(b_{\text{old},k})\prod_{l=1}^{L}\pi(\kappa_{\text{old},l})}\,\frac{p_{add}(\mathbf{M}_{i+1}\to\mathbf{M}_i)}{p_{rem}(\mathbf{M}_i\to\mathbf{M}_{i+1})}\,\frac{n_{un}}{n_{fr}}\left|\frac{\partial(\theta_{i+1},v)}{\partial(\theta_i,u)}\right|,$$

$$= \frac{p_{add}(\mathbf{M}_{i+1}\to\mathbf{M}_i)}{p_{rem}(\mathbf{M}_i\to\mathbf{M}_{i+1})}\,\frac{n_{un}}{n_{fr}}\,. \tag{6.14}$$

Figure 6.6 depicts the probability to add (in blue) and remove (in orange) one particle with two decay modes and two production modes given the current number of particles in the proto-model.

**2. Adding/removing production modes of existing particles**: We add extra production modes or remove existing ones from the current proto-model with the previously defined proposal probabilities to add or remove dimensions. The proposal ratio together with the ratio of the latent variable distributions for attempting to add a particular production mode can be defined as:

[5] Frozen (Unfrozen) particles represent the list of BSM particles absent (present) in the proto-model.

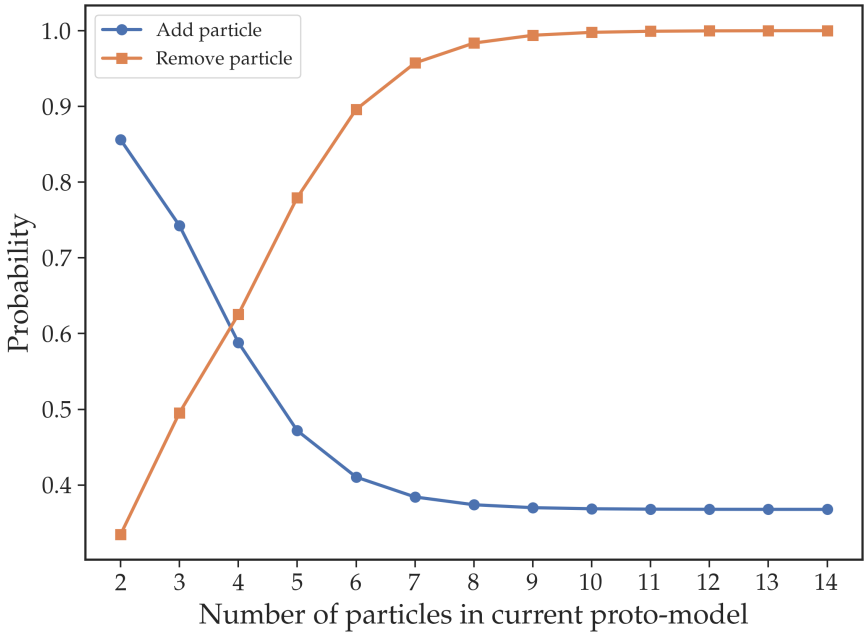


FIGURE 6.6: Probability to add or remove a particle with two decay modes and two production modes given the current number of particles in the proto-model.

$$\left.\frac{p_V(v)}{p_U(u)}\frac{q(\mathbf{M}_{i+1}\to\mathbf{M}_i)}{q(\mathbf{M}_i\to\mathbf{M}_{i+1})}\right|_{\text{add prod}} = \frac{1}{p(\kappa)}\frac{p_{rem}(\mathbf{M}_{i+1}\to\mathbf{M}_i)}{p_{add}(\mathbf{M}_i\to\mathbf{M}_{i+1})}\frac{p(\text{rem prod mode})}{p(\text{add prod mode})}, \quad (6.15)$$

where the probability of adding an allowed production mode (if not already present) is set to occur 70% of the time, and the probability to remove an existing production mode is set to occur 10% of the time:

$$p(\text{add a production mode}) = \frac{0.7}{\text{allowed production modes}}; \quad (6.16)$$

$$p(\text{remove a production mode}) = \frac{0.1}{\text{current number of production modes}}. \quad (6.17)$$

The signal strength multiplier assigned to the added production mode is drawn from the corresponding prior distribution. Consequently, the ratio of the latent variable distributions cancels with the prior on the parameter in the acceptance ratio.

When removing a particular production mode from the current proto-model, the ratios are obtained by inverting the terms on the right-hand side of Eq. (6.15):

$$\left.\frac{p_V(v)}{p_U(u)}\frac{q(\mathbf{M}_{i+1}\to\mathbf{M}_i)}{q(\mathbf{M}_i\to\mathbf{M}_{i+1})}\right|_{\text{rem prod}} = \frac{p_{add}(\mathbf{M}_{i+1}\to\mathbf{M}_i)}{p_{rem}(\mathbf{M}_i\to\mathbf{M}_{i+1})}\frac{p(\text{add prod mode})}{p(\text{rem prod mode})}\frac{p(\kappa)}{1}. \quad (6.18)$$

**3. Adding/Removing decay channels of existing particles**: We attempt to add new (allowed) decay channels or remove existing ones with the previously defined proposal probabilities to add/remove dimensions. There are three possible ways by which we can alter the number of decay channels in the current proto-model:

- Keep one decay channel, closing all others with 5% probability.
- Close a particular channel with 5% probability.
- Add a particular channel with 10% probability.

The ratios for attempting to add a particular decay channel then becomes:

$$\left.\frac{p_V(v)}{p_U(u)}\frac{q(\mathbf{M}_{i+1}\to\mathbf{M}_i)}{q(\mathbf{M}_i\to\mathbf{M}_{i+1})}\right|_{\text{add decay}} = \frac{1}{p(b)}\frac{p_{add}(\mathbf{M}_{i+1}\to\mathbf{M}_i)}{p_{rem}(\mathbf{M}_i\to\mathbf{M}_{i+1})}\frac{p(\text{rem decay channel})}{p(\text{add decay channel})}. \tag{6.19}$$

The branching ratio assigned to the decay channel is drawn from the prior, and thus the latent variable distribution in the denominator of the first term cancels with the prior for the parameter in the acceptance ratio. As before, this ratio is reversed for removing a decay channel.

### Changing existing proto-model parameters

In addition to jumping between different dimensional proto-models, there can be moves that update the existing parameters without any change in the dimensionality, independent of the above trans-dimensional moves. For such a move, we do not need to enter the proposal densities or the latent variable distributions defined for adding/removing dimensions in the acceptance ratio.

- **Changing masses:** If none of the trans-dimensional moves or the other parameter updates have been implemented, we force a change in the mass of a randomly chosen particle in the proto-model. Otherwise, we change the mass of a randomly chosen particle present in the current proto-model with a 5% probability. To modify a particle's mass in the proto-model, we construct a symmetric Gaussian proposal centered on the particle's current mass. The proposal width depends inversely on the current proto-model score (called $TL$, see Eq. (6.24)). If the proto-model has a high score, the width is narrower, enabling fine-tuned exploration near the current mass. Conversely, when the score is low, we permit the algorithm to make broader mass jumps.

  When the mass of the LBP is changed, all other particle masses are shifted correspondingly to maintain fixed mass differences. When changing the masses of other unfrozen particles, the following constraints must be met: (a) all masses must remain between the LBP mass and the maximum allowed mass (2.4 TeV), and (b) mass ordering must be preserved when particles of multiple generations are present.

This move affects only the likelihood ratios in the acceptance ratio calculation. Neither the proposal ratio nor the prior ratio for this move influences the acceptance ratio computation, as we employ a uniform prior on the mass parameter (making the prior ratio unity) and a symmetric Gaussian proposal density.

- **Changing Signal Strength Multipliers** There is a 25% probability of modifying the signal strength multipliers. When this occurs, two scenarios are possible: either all SSMs of production modes for a randomly chosen particle in the proto-model are modified (80% probability), or a random production mode within the proto-model is selected and assigned a new SSM value. Analogous to the branching ratio modification procedure, to maintain a simplified acceptance ratio when changing existing SSMs, new values are sampled from the prior distributions such that the proposal probability for updating the signal strength multiplier cancels with the corresponding prior probability.

- **Changing branching ratios** : There is a 20% probability of modifying the branching ratios for a randomly selected particle in the current proto-model. In most cases (80% probability), existing decay channels are neither removed nor are new possible channels added. Instead, the existing branching ratios for the chosen particle are adjusted. To maintain a simplified acceptance ratio when modifying existing branching ratios of the particle, new values are drawn from the prior distributions such that the proposal probability for updating the branching ratio cancels with the prior probability for the same. Following these modifications, the sum of all branching ratios for the selected particle is normalised to unity.

As mentioned above, multiple moves can be proposed during a single iteration. The total proposal ratio is calculated as the product of the individual proposal ratios for each implemented move type. If the moves indexed by $m$ have been successfully implemented, then:

$$\left.\frac{q(\mathbf{M}_{i+1} \to \mathbf{M}_i)}{q(\mathbf{M}_i \to \mathbf{M}_{i+1})}\right|_{\text{total}} = \prod_m \left.\frac{q(\mathbf{M}_{i+1} \to \mathbf{M}_i)}{q(\mathbf{M}_i \to \mathbf{M}_{i+1})}\right|_m . \tag{6.20}$$

### 6.3.3 Prior Distributions

In v1, a prior was defined on the proto-model that penalised its complexity, which ultimately influenced the computation of the test statistic $K$. Although prior distributions were defined for drawing the parameter values of the proto-model, only the sampled values affected the likelihood computation, while the distributions themselves did not impact comparisons between different proto-models. In v2, prior distributions are explicitly defined for each free parameter, as they directly influence the calculation of the acceptance ratio.

Two distinct sets of priors are established. The first addresses model complexity, through a prior on the dimensionality of the proto-model, which is adopted from the previously defined proto-model prior in Eq. (5.9). The second set of priors governs the sampling of free parameter values within the proto-model, which are subsequently used to initialize these parameters. Given the fixed particles in the proto-model, the free parameters are then their masses, branching ratios for the allowed decay channels, and SSMs for production modes. The prior distributions for each of these parameters

are assumed to be mutually independent and independent of the proto-model dimension.

- **Mass:** The prior distribution on the mass is taken to be a Uniform distribution, $\pi(m) = \mathcal{U}[m_{\text{LBP}}, m_{\text{max}}]$, where $m_{\text{LBP}}$ refers to the mass of the LBP which has a prior $\pi(m_{\text{LBP}}) = \mathcal{U}[100, 500]$ and $m_{\text{max}}$ is the maximum mass allowed for all particles (2400 GeV). If particles of multiple generations are present in the proto-model, they are required to be mass ordered.

- **Branching ratios:** The branching ratios for a particular particle are drawn from a Gaussian prior, $\pi(b) = \text{Gauss}(1/n_{dc}, \sqrt{0.5/n_{dc}})$, where $n_{dc}$ is the number of allowed decay channels for the particle.

- **Signal Strength Multipliers:** The SSMs are drawn from a lognormal distribution with the mean and variance equal to unity, $\pi(\kappa) = \text{LogNorm}(\mu = 1, \sigma^2 = 1)$.

## 6.4 Combiner v2

In v1, the Combiner block collected all possible combinations of experimental results using the binary combination matrix to identify the one that maximally deviated from the SM hypothesis. However, with the significant extension of the SModelS database, this approach quickly became a computational bottleneck due to the exponentially growing number of possible combinations. The updated combination matrices in v2, which incorporate the 13 TeV results from SModelS database v3.1.0 is shown in Figure 6.7 (ATLAS) and Figure 6.8 (CMS). These matrices are significantly larger than those used in v1 (see Figure 5.4). To address the computational constraints imposed by these large matrices, we employ the PathFinder algorithm, originally developed for the Taco framework [159]. This algorithm efficiently selects subsets of minimally correlated results from a large number of analyses or signal regions.

The PathFinder follows a Weighted Hereditary Depth First Search (WHDFS) algorithm that uses the combination matrix and an edge weight to efficiently determine the optimal combination set of experimental results. The edge weight is motivated by the statistical goal being tested, and ideally, should be additive. The additive weights allow for further algorithmic optimisation by (a) ordering the elements in decreasing order of their weights and (b) terminating the search early when no remaining combinations can exceed the current best metric. Thus, the PathFinder algorithm efficiently identifies the optimal combination of statistically non-overlapping results that maximizes the total weight for a given proto-model.

The PathFinder requires an optimal edge weight to be defined, which here corresponds to the maximum deviation from the SM hypothesis. Thus, we can make use of the quantity $Z$ defined in Eq. (5.7), where $Z^2$ is:

$$Z^2 = 2 \ln \frac{L_c^{\text{obs}}(\mu = \hat{\mu}_c)}{L_c^{\text{obs}}(\mu = 0)}, \tag{6.21}$$

where $c$ refers to the optimal combination set, and $\hat{\mu}_c$ is the value of $\mu$ that maximises the combined likelihood. Therefore, we can define the edge weight to be equal to the individual optimised log likelihoods at $\hat{\mu}_i$. However, it is not necessary that the

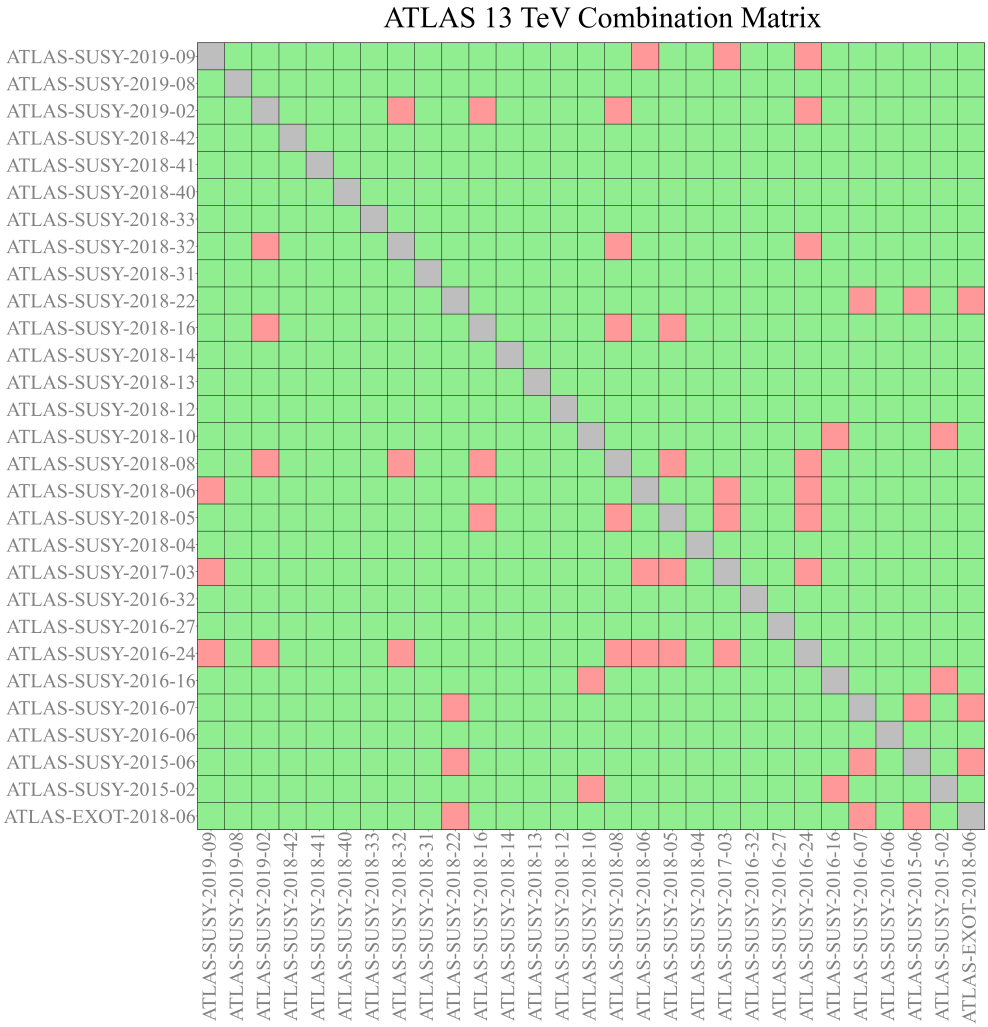


FIGURE 6.7: The updated binary combination matrices used in v2 for the ATLAS 13 TeV results, that describes which analyses are considered to be approximately uncorrelated (green bins) and which are not (red bins). Analyses from different LHC runs or different experiments are always taken as uncorrelated.

combined log likelihood at $\hat{\mu}_c$ is equal to the additive sum of the individual optimised log likelihoods at $\hat{\mu}_i$, i.e.,

$$\ln L_c(\hat{\mu}_c) \;\leq\; \sum_{i \in c} \ln L_i(\hat{\mu}_i)\,. \tag{6.22}$$

Thus, there are two problems with defining the edge weight of the PATHFINDER algorithm to be at the individual maximum log likelihoods at $\hat{\mu}_i$: (a) we need to compute the individual $\hat{\mu}_i$ for each experimental result in the combination matrix which quickly becomes computationally expensive and (b) the sum of the individual optimised log likelihood may not necessarily sit at the combined log likelihood maximised at $\hat{\mu}_c$.

In order to still exploit the attributes of $Z$, we instead evaluate all the individual log likelihoods at $\mu = 1$, and make sure that the combined likelihood is maximised at $\hat{\mu}_c = 1$:

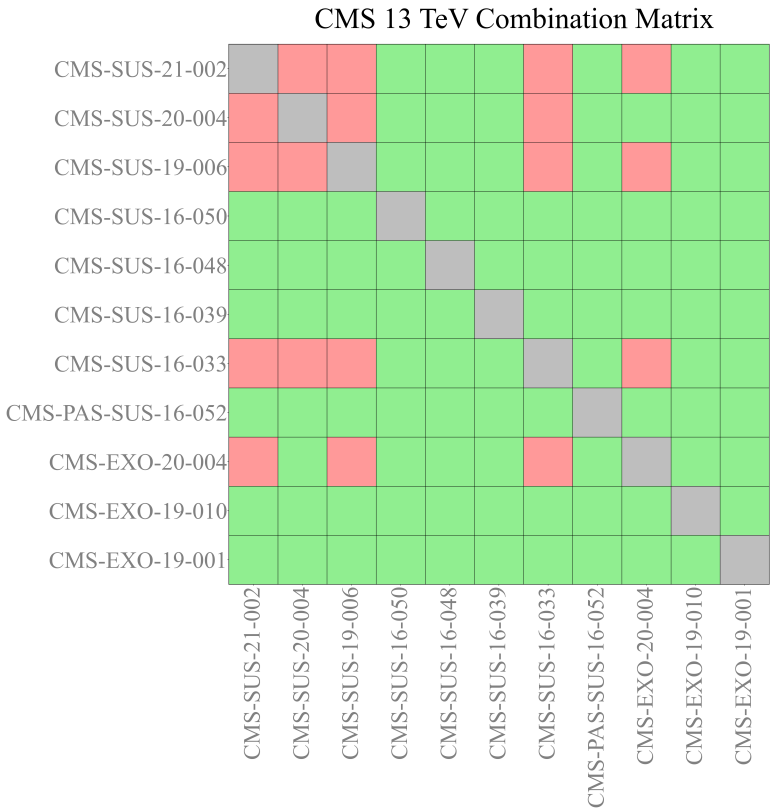


FIGURE 6.8: The updated binary combination matrices used in v2 for the CMS 13 TeV results, that describes which analyses are considered to be approximately uncorrelated (green bins) and which are not (red bins). Analyses from different LHC runs or different experiments are always taken as uncorrelated.

$$\ln L_c(\hat{\mu}_c = 1) \;=\; \sum_{i \in c} \ln L_i(\mu = 1)\,. \tag{6.23}$$

The above condition requires the recursive optimisation of $\hat{\mu}_c$ in order to ensure that the combined log likelihood is maximised at $\hat{\mu}_c = 1$. This is done by using the $\hat{\mu}_c$ computed for a combined set of results to modify the expected signal yields via the cross sections of the proto-model until $\hat{\mu}_c$ converges to unity. This procedure modifies the proto-model point by multiplying the cross sections by the signal strength parameter. It is important to note that $\mu$ is a global signal strength. Therefore, the signal cross-sections are given by $\sigma = \mu \times \kappa \times \sigma_{SUSY}$ , where $\kappa$ is the signal strength multiplier of a given production mode. Technically, once the value of $\mu$ which maximises the likelihood $(\hat{\mu})$ is determined, all signal strength multipliers are rescaled by $\kappa \to \mu \times \kappa$ and $\mu$ is taken as 1.

This modification of yields directly affects the edge weights used in the PATHFINDER. Thus, for each recursion, the optimal combination set has to be re-evaluated, affecting $\hat{\mu}$ for the combined set. This could easily result in an infinite loop where $\hat{\mu}_A$ modifies the model such that a combination set B is chosen whose combined maximum likelihood sits at $\hat{\mu}_B$, which then modifies the proto-model such that set A is chosen with $\hat{\mu}_A$. With this situation in mind, a limit on the number of loops is required, which we currently take to be a maximum of five iterations. If, at the end of five iterations, the

combined $\hat{\mu}_c$ has not converged to 1, we stop the search for the optimal combination set and return to previous proto-model point. In addition, we allow for a minimum tolerance on the optimised $\hat{\mu}_c$ to prevent small non-converging fluctuations around unity.

If the combined $\hat{\mu}_c$ for the optimal combination set converges to unity, then the recursion loop returns the combined set of results for the proto-model point such that,

$$TL = 2\sum_i \ln \frac{L_i(\mu = 1, \hat{\hat{\theta}}_i)}{L_i(\mu = 0, \hat{\hat{\theta}}_i)} \approx 2 \ln \frac{L_c(\mu = \hat{\mu}_c, \hat{\hat{\theta}})}{L_c(\mu = 0, \hat{\theta})}, \tag{6.24}$$

where we now compute the new quantity $TL$ instead of $Z$. The optimal combination of results is then the set which gives the maximum $TL$ for a given proto-model with the combined likelihood sitting at the maximum $\hat{\mu}_c = 1$. The optimal combination of results obtained using this approach is henceforth referred to as the most significant combination.

The test statistic $K$ for the proto-model is now defined using the $TL$ obtained from the most significant combination, incorporating the penalty for model complexity through the prior $\pi(\mathbf{M})$ on the proto-model described in Eq. (5.9):

$$\begin{aligned} K &= TL + 2 \ln \pi(\mathbf{M}), \\ &= 2 \ln \frac{L_c(\mu = 1, \hat{\hat{\theta}})\, \pi(\mathbf{M})}{L_c(\mu = 0, \hat{\hat{\theta}})}, \end{aligned} \tag{6.25}$$

where the prior on the SM is set to 1 as it does not influence the comparison between different proto-models. It is important to note that $K$ appears in the likelihood ratio times the prior ratio in the acceptance probability defined in Eq. (6.4). Therefore, $K$ is reflective of the performance of different proto-models generated across the chain. While presenting the results, we primarily focus on the values and distributions of $K$ and $TL$, as these statistics best reveal the capability of the generated proto-models to identify dispersed signals. While $TL$ measures the performance of a given proto-model, $K$ takes into account the model complexity and penalises for extra degrees of freedom. Thus the value of $K$ is always smaller than the value of $TL$.

Once we compute $K$, we accept the proposed proto-model with the probability defined in Eq. (6.4). If it passes the acceptance criterion, we proceed to check if the proposed proto-model violates any of the constraints in the SModelS database. Otherwise, we revert to the current proto-model and advance to the next iteration.

## 6.5 Critic v2

In v1, the Critic computed an upper limit on the global signal strength $\mu$ by incorporating constraints from all experimental results available in the SModelS database. This maximum permissible signal strength $\mu_{\text{max}}$ was then used to truncate the combined likelihood, ensuring that the combined maximum log likelihood was evaluated under the condition $\hat{\mu}_c \leq \mu_{\text{max}}$.

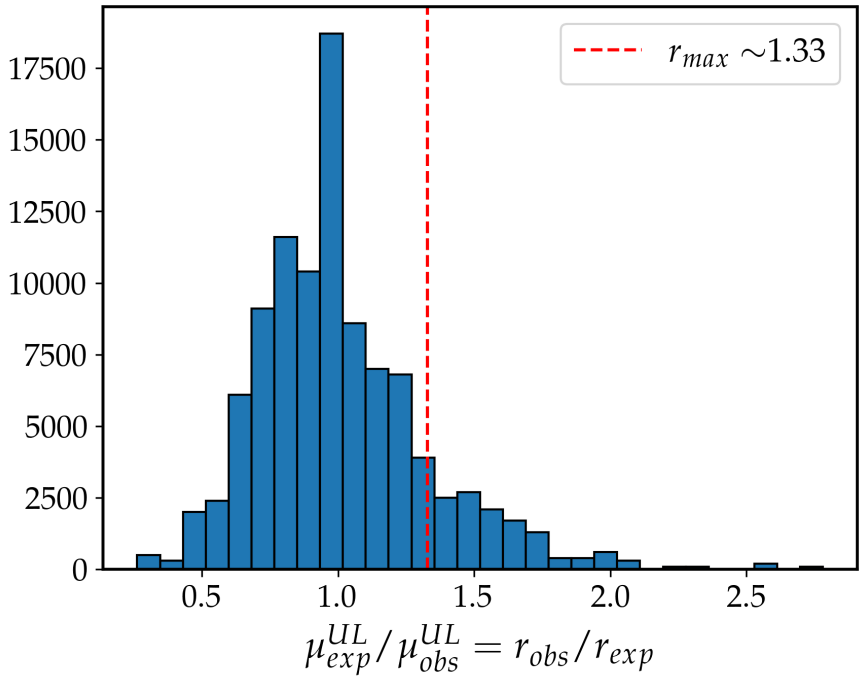


FIGURE 6.9: Distribution of $r_{\text{obs}}/r_{\text{exp}} \equiv \mu^{UL}_{\text{exp}}/\mu^{UL}_{\text{obs}}$ from 100 fake EM-type databases sampled from the SM distribution. The red dotted line indicates the maximum allowed $r_{\text{obs}}$ value for a given proto-model, $r_{\text{max}} \sim 1.33$, which is calculated as 1 $\sigma$ deviation from the mean.

The truncation methodology has since been discontinued in v2, since the Combiner now evaluates the combined log likelihood at $\hat{\mu}_c = 1$. Consequently, the Critic's behaviour has been changed to make a binary acceptance decision for each proto-model. This binary decision is implemented through two sub-components: a *fast critic*, which processes UL-type constraints, and a *slow critic*, which handles EM-type constraints. For a proto-model to be accepted, each critic needs to compute the SModelS observable $r$-value, and the computed $r$-value is required to be below a specified threshold.

### 6.5.1 Fast Critic

This critic checks the proto-models against the LHC upper limit constraints implemented in the SModelS database. The exclusion is only based on UL-type results. However, if an analysis has no UL-type result but an EM-type result has been implemented, then the most sensitive SR from the EM-type result is used to give an upper limit constraint. In this case, we do not compute a likelihood, but only an approximate result. However, this critic has the advantage of quickly rejecting proto-models that violate any of the implemented upper limits.

To say whether an individual result excludes a given proto-model, a 38% violation of the upper limit is allowed. That is to say, an UL- or EM-type result excludes the tested proto-model if it gives $r_{\text{obs}} > 1.33$. This empirical value was obtained by creating 100 fake EM-type result databases sampled from the SM distribution (as described in Section 5.7.1) and computing the 1 sigma deviation of the $r_{\text{obs}}/r_{\text{exp}} \equiv \mu^{UL}_{\text{exp}}/\mu^{UL}_{\text{obs}}$ distribution (computed at the SR level) from the mean, as shown in Figure 6.9.

Since we are checking against constraints from a large number of experimental results,

we also allow for statistical violations of the ULs by computing the maximal number of ULs that are allowed to be violated. This number is modelled as a binomial distribution $\equiv \text{Binom}(n, 0.05)$ where $n$ denotes the number of sensitive results constraining the proto-model. Here, the sensitive results are the ones with an $r_{\text{exp}} \geq 0.7$. If expected upper limit constraints are not available, we substitute $r_{\text{exp}}$ with the observed value. We allow for this substitution as no abnormally large deviation from the SM has been observed and we want to take into account only sensitive analyses in the fast critic.

In this case, the mean of the binomial distribution corresponds to 5% of the sensitive results excluding a proto-model point due to statistical fluctuations (since the upper limits are given as 95% CL ULs). Therefore, we take the maximal number of violations allowed before excluding the proto-model as the lowest number for which the cumulative distribution function of the binomial distribution is one sigma above the mean, i.e. above 66%. However, we require at least $n = 20$ results before allowing any violations; otherwise, all UL constraints must be satisfied. Thus, when the number of UL constraints is small, we ensure that at least one violation is permitted. If the number of sensitive results excluding the proto-model is below the maximal allowed violations, the proto-model passes the fast critic and we then proceed to compute the slow critic. Otherwise, the proto-model is excluded and we return to the previous step, bypassing the computation of the slow critic.

### 6.5.2 Slow Critic

This critic is evaluated only if the fast critic does not exclude the proto-model point. It tests the proto-model point against the observed $r$-value obtained from the most sensitive combination of experimental results. Here, we use only EM-type results (as we can build likelihoods) but relax the sensitivity limit compared to the fast critic, taking only results with $r_{\text{exp}} \geq 0.1$.

We define the most sensitive combination as the one with the lowest expected limit on the signal strength $\mu^{95}_{\text{exp}}$ (or, equivalently, highest $r_{\text{exp}}$). Since the computation of $\mu^{95}_{\text{exp}}$ can be time consuming, we take the combination that minimises $L^{\text{exp}}(\mathbf{M})/L^{\text{exp}}(\text{SM})$ as the one with the lowest $\mu^{95}_{\text{exp}}$. Even though the insensitive analyses could have been used in the combination, they do not impact the result and hence were removed for technical stability and reduction of the computation time. To find the most sensitive combination, we once again make use of the PATHFINDER algorithm, however, this time modifying the edge weight to be:

$$TL^{\text{exp}} = 2\sum_i \ln \frac{L_i^{\text{exp}}(\mu = 0, \hat{\hat{\theta}}_i)}{L_i^{\text{exp}}(\mu = 1, \hat{\hat{\theta}}_i)}\,. \tag{6.26}$$

The most sensitive combination is then the set of experimental results that maximises $TL^{\text{exp}}$ value (i.e minimizes $L^{\text{exp}}(\mathbf{M})/L^{\text{exp}}(\mathbf{SM})$). We then compute the combined observed $r$-value for the combination of results. If the observed $r$-value is below 1.2, or if it is below 1.5 and the $r_{\text{exp}}$ is at least twice $r_{\text{obs}}$, the proto-model point is not excluded and we finally accept the proposed proto-model and proceed to the next step in the chain. Otherwise, the proposed proto-model is rejected, and we revert to the current proto-model before starting the next step.

Finding the most sensitive combination and computing the combined observed $r$-value is expensive, hence we compute it at the very end. However, it is much more robust than the slow critic.

## 6.6 Running the Proto-model framework

The proto-model framework is implemented entirely in `Python` programming language. The blocks described in Section 6.2 are implemented in three main folders consisting of several modules:

- `builder/`: This folder contains the Builder block, which sets the groundwork for proto-model construction and modification. The `protomodel.py` module is responsible for defining all properties of a proto-model object, such as the number and type of BSM particles and associated parameters. The `manipulator.py` module contains functions responsible for implementing random changes (manipulations) on the current proto-model. This module also defines the proposal density that guide the proto-model transitions and prior distributions for the proto-model parameters. In addition, this folder contains the `template.slha` files which set the proto-model parameter space that is allowed to be explored during a walk.

- `tester/`: This folder contains both the Combiner and the Critic blocks and utilizes the SModelS framework for systematic comparison between the theory predictions and experimental constraints for a given proto-model. The `predictor.py` module computes the list of SModelS theory predictions for a proto-model generated by the `builder` block. The most significant combination of these theory predictions is then given by the `combiner.py` module with the help of the PathFinder module. The `critic.py` module evaluates the proto-model's exclusion status by computing the constraint violations via the fast and slow critics. This folder additionally incorporates the combination matrix, defined in terms of four `YAML` files separated by experiment (ATLAS/CMS) and center-of-mass energy (8 TeV/13 TeV).

- `walker/`: This folder contains the Walker, which orchestrates the overall algorithmic exploration. The `randomwalker.py` module initialises the walk either from the SM, or from a predefined proto-model, and computes the acceptance ratio at each step. It serves as the central coordinator and calls appropriate functions from the modules in builder and tester folders. The module `factoryOfWalkers.py` can be used to deploy multiple concurrent walks to allow parallel exploration of different parameter space regions, thus maximising coverage and efficiency. A comprehensive documentation of each step in a walk is maintained in dedicated log files in a specified `rundir` directory. After each walk, a `hiscore.dict` file is produced which preserves the top 10 best performing (highest $K$) proto-models.

As mentioned above, the `factoryOfWalkers.py` can be used to set up multiple parallel walks through calls to the main `randomwalker.py` module. A subset of configuration parameters that influence a set of walks is given below:

- `nmin`: Specifies the walker ID of the first walker in the ensemble. It establishes the starting point for walker identification when setting up parallel walks.

- `nmax`: Specifies the walker ID of the last walker in the ensemble. Together with `nmin`, it determines the total number of parallel walks that will be executed in a single run.
- `maxsteps`: Set the maximum number of steps in each individual walk.
- `dbpath`: Specifies the path to the experimental database containing constraints for proto-model evaluation. The default setting `"official"` references the current official SModelS database repository, though alternative databases can be specified for specialized studies.
- `rundir`: Specifies the path to the output directory where all walk results are stored. This directory contains comprehensive documentation of each walk in a `logs` subdirectory, along with exception reports and hiscore.dict files that save the best performing proto-models generated during a run.
- `select`: Selects only a subset of results from the database according to specific criteria. Options include `all` to select all results, `em`(`ul`) to select only results that have efficiency maps (upper limits), or topology-specific filtering using syntax like `"txnames:electroweakinos"` to select constraints on particular SMS topologies.
- `forbiddenparticles`: Reduces parameter space dimensionality by accepting lists of proto-model particle IDs to exclude from exploration. This feature is valuable for managing computational complexity in large parameter spaces or investigating scenarios where specific particle types are theoretically absent.
- `cheatcode`: Controls the initial conditions for walker deployment. The default value `"0"` initiates all walks from the SM baseline. Alternatively, we can specify dictionary file paths containing predefined proto-model configurations to enable exploration around interesting parameter regions.
- `runmcmc`: Switches the sampling procedure from a varying-dimensional sampling to MCMC sampling when set to `True`. This mode maintains fixed theoretical dimensionality of a proto-model, making it suitable for detailed investigation of specific parameter regions rather than broad parameter space surveys.

In this thesis, we focus on building proto-models that can exploit the excesses found in the monojet/compressed electroweakino phase space. The results discussed in the next section therefore focus on the subset of available proto-model parameter space.

## 6.7 Results

In this section, we present the results of running the Walker algorithm v2 over the SModelS database v3.1.0. This database includes simplified model results from 61 ATLAS and 64 CMS analyses, as detailed in Appendix B. As mentioned before, we focus on building proto-models that can explain the small excesses found in the monojet/soft-lepton channels. We thus restrict the exploration of the proto-model parameter space by only considering the particles, decay channels, and production modes listed in Table 6.1. We further restrict the experimental results to those that exhibit signatures within this phase space. This selection is implemented using the code parameters `select = "txnames:electroweakinos"` and forbidding particles that are not listed in

Table 6.1. This selection thus limits the SModelS database to experimental results that search for electroweakinos and monojet signatures, corresponding to a total of 20 ATLAS and 17 CMS analyses. Of these, 20 analyses provide efficiency maps (14 from ATLAS and 6 from CMS) enabling likelihood computation for proto-model signals.

| Particle | Decay channels |
|---|---|
| $X_Z^1$ | – |
| $X_Z^{j\neq 1}$ | $W\,X_W^i,\ Z\,X_Z^k,\ h\,X_Z^k$ |
| $X_Z^2$ | $q\bar{q}X_Z^1\ ,\ b\bar{b}X_Z^1\ ,\ \ell\ell\ X_Z^1\ ,\ \nu_\ell\bar{\nu}_\ell X_Z^1$ (off-shell) |
| $X_W^1$ | $W\,X_Z^j, q\bar{q}'\,X_Z^1\ ,\ \ell\nu_\ell X_Z^1$ |
| $X_W^2$ | $W\,X_Z^j,\ Z\,X_W^1,\ h\,X_W^1$ |

| | |
|---|---|
| Pair production | $(X_Z^i, X_Z^i),\ (X_W^{j+}, X_W^{j-})$ |
| Associated production | $(X_Z^i, X_Z^j)\ (X_Z^i, X_W^{j\pm}),$ |

TABLE 6.1: The restricted BSM parameter space considered for building proto-models with Walker v2. Note that the newly added off-shell decay modes for $X_Z^2$ and $X_W^1$ are included alongside the on-shell decay modes.

In the proof-of-concept paper, the authors performed 50 parallel walks, each with a 1000 steps. The walk producing the best performing proto-model, i.e., the one with the highest $K$ value, was then analysed in detail. To assess the significance of the $K$ value obtained, the authors estimated the distribution of $K$ under the SM-only hypothesis by creating an ensemble of "fake SM" databases. Section 5.7.1 detailed the procedures used to create an ensemble of fake SM databases and the estimation of the density of the test statistic $K$ under the SM hypothesis. We repeat this procedure here, first running the Walker algorithm on the ensemble of fake SM databases before running it on the real SModelS database to set baseline expectations. As before, we run 50 parallel walkers; however, each walk now executes 20000 steps. This increase is necessary to enable thorough exploration of the proto-model parameter space.

Before presenting the results, we introduce two definitions for categorising proto-models based on their test statistic $K$:

1. **Best performing proto-model** is the proto-model that has the maximum $K$ value within a single walk on a given database (real or fake).

2. **Absolute best performing proto-model** is the proto-model that has the maximum $K$ value across all walks on a given database, defined as $\max\{\mathbf{M}_{\text{best}}^{(i)}\}$, where $\mathbf{M}_{\text{best}}^{(i)}$ is the proto-model with the maximum $K$ from walk $i$.

### 6.7.1 Runs across fake SM Databases

Following the method described in Section 5.7.1, we create an ensemble of 15 "fake SM" databases. We perform 50 parallel walks (one run) on each of the 15 fake SM databases, with each walk executing 20000 steps. From each walk on a fake database, we collect the best performing proto-model, i.e., the one with the highest $K$ value ($K_{fake}$), and estimate its distribution using a Kernel Density Estimator.

Before constructing the KDE under the SM hypothesis, it is interesting to examine the evolution of the test statistics $K$ and $TL$ as a function of step on the fake SM databases. Figure 6.10 shows two such plots for walks generating the best performing proto-model over two different fake SM databases. We observe that most walks exhibit typical behaviour, with values of $K$ and $TL$ being mostly $K \lesssim 0$ and $TL \lesssim 2.5$, with occasional peaks at higher values reaching $K \lesssim 10$ and $TL \lesssim 15$. However, extreme deviations from this pattern is observed in some walks on one database out of 750 total walks (15 databases $\times$ 50 walkers). Figure 6.11 depicts this extreme behaviour for one walk on a fake SM database, where $K$ and $TL$ converge to approximately 10 and 15, respectively. This walk produced the absolute best performing proto-model across all 15 runs on fake SM databases.

This extreme result was due to certain SRs in this particular fake SM database whose sampled observed values were larger than the expected SM events. These SRs then entered the most significant combination driving the upward trend in $K$ and $TL$. Such extreme deviations are expected to occur, as the Walker algorithm is optimised to identify dispersed signals, with $K$ and $TL$ representing the maximum deviation from the SM across all possible combinations of results. Since the fake SM databases are sampled from the SM distribution, it is possible to have databases where the observed number of events exceed the expected SM background events. Such upward background fluctuations can mimic dispersed signals. Thus, it is important to see the possible $K$ and $TL$ values obtained for proto-models generated from walks on fake SM databases in order to compare them with results from the real database and distinguish between statistical fluctuations and genuine physics signals.

Figure 6.12 shows the $K_{fake}$ values obtained for the best performing proto-models from each of 50 walks across 15 fake SM databases. The red points represent the "absolute" best performing proto-model from each database. The orange curve represents the density $\rho(K)$ obtained under the SM hypothesis using a Gaussian Kernel Density Estimator. From this figure, we observe that the density of $K$ under the SM hypothesis shows a peak near 5 while values close to 15 can be expected with the Walker algorithm v2. It is also interesting to note that there exists best performing proto-models with negative $K$ values from the fake SM runs. $K$ being negative implies that the SM is favoured over the proto-model signal. This means that in some walks on the fake SM databases, the algorithm could not build a proto-model that was favoured over the SM.

### 6.7.2 Runs across SModelS database v3.1.0

We now apply the Walker algorithm v2 to the SModelS database v3.1.0, selecting only the subset of experimental results that constrains the aforementioned proto-model parameter space. We perform 50 parallel walks with 20000 steps/walker. The best performing proto-model from each walk is then collected. Figure 6.13 displays the particle content, masses, and the corresponding $K$ values for the top ten best performing proto-models across all 50 walks. From this figure, we see that all the best performing proto-models include $X_Z^2$ alongside the LBP, $X_Z^1$. Two proto-models also include $X_W^1$ with masses close to that of $X_Z^2$, and one proto-model includes $X_Z^3$. The masses of $X_Z^1$ remain near 100 GeV for most of the top 10 proto-models, with the masses being close to 250 GeV for Walker IDs 18 and 24. Only the first proto-model in the figure, generated by Walker ID 3 at step 4947, has $X_Z^2$ and $X_W^1$ masses in the off-shell region. This proto-model is the "absolute" best performing proto-model with $K = 18.29$ and the

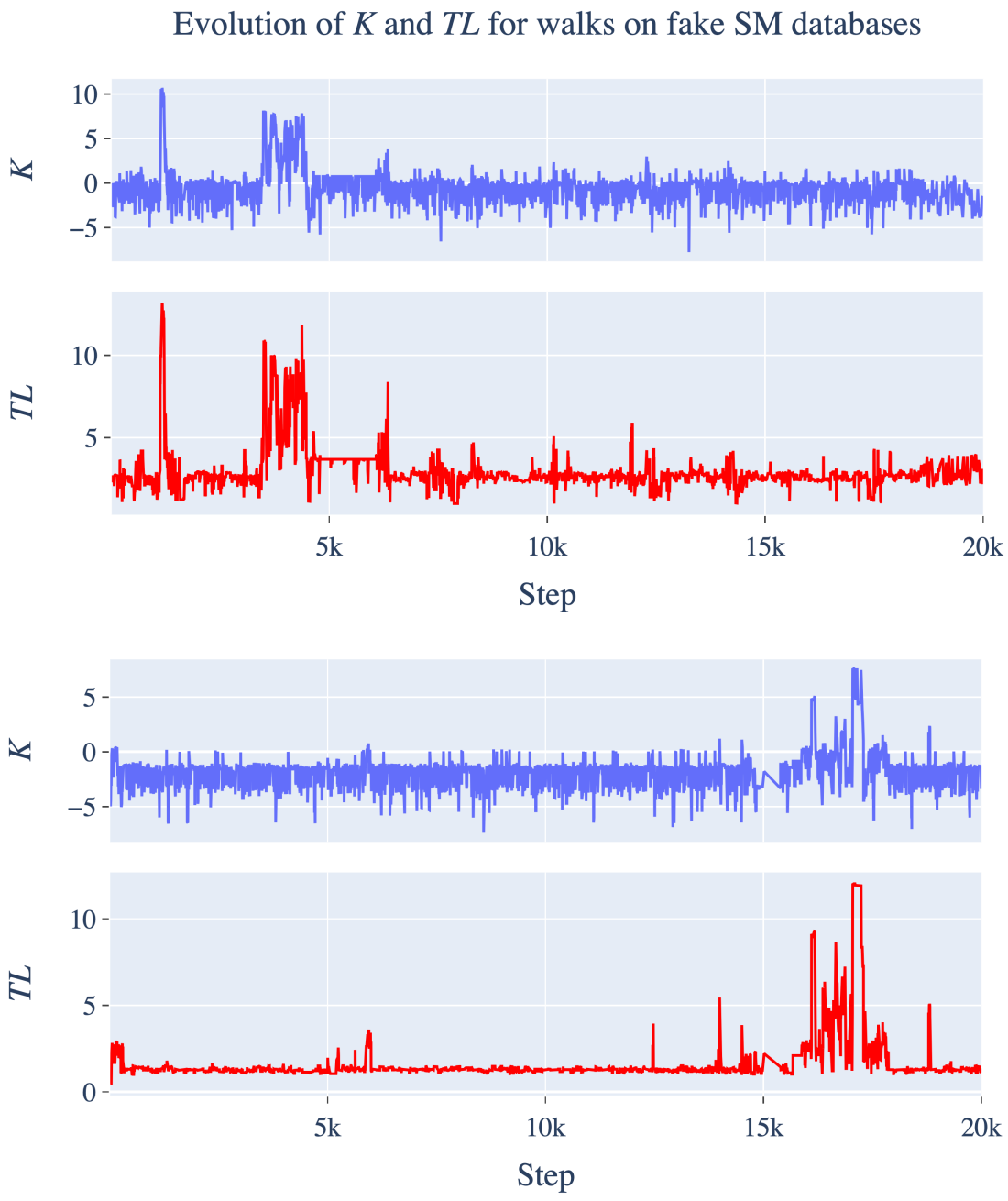


FIGURE 6.10: Evolution of $K$ (blue) and $TL$ (red) for individual walks across two fake SM databases. On average, proto-models generated across walks on different fake SM databases have $K \lesssim 0$ and $TL \lesssim 2.5$. However, occasional deviations from this baseline behaviour are observed.

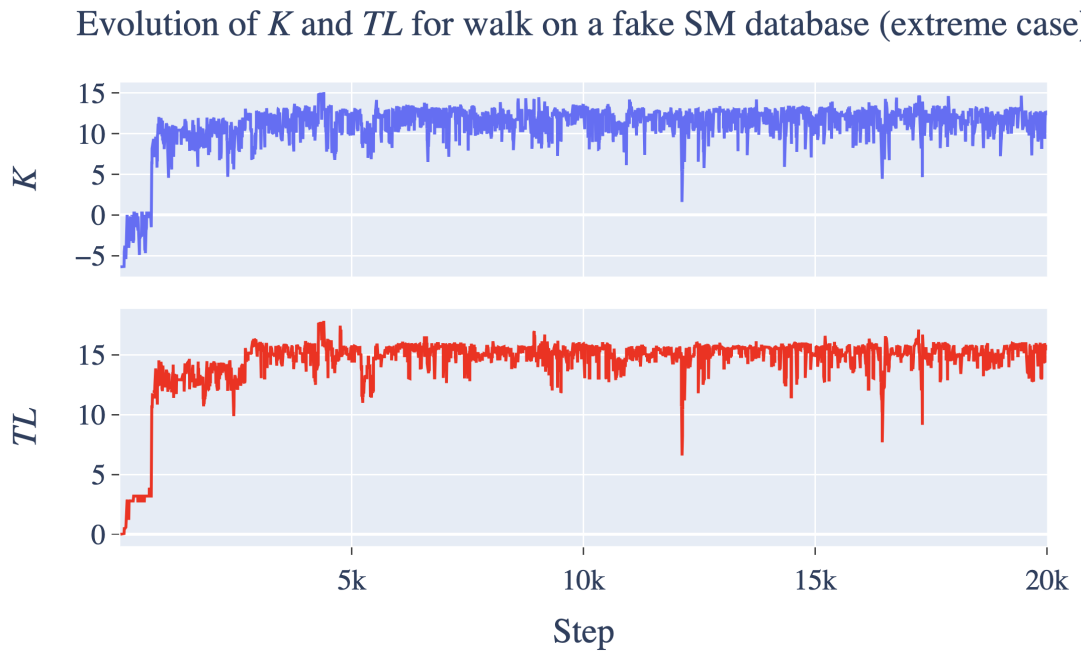


FIGURE 6.11: An extreme case of $K$ and $TL$ evolution from a single walk on a fake SM database. $K$ and $TL$ converge to approximately 13 and 15, respectively. This run produced the highest scoring proto-model across all 15 fake SM databases.

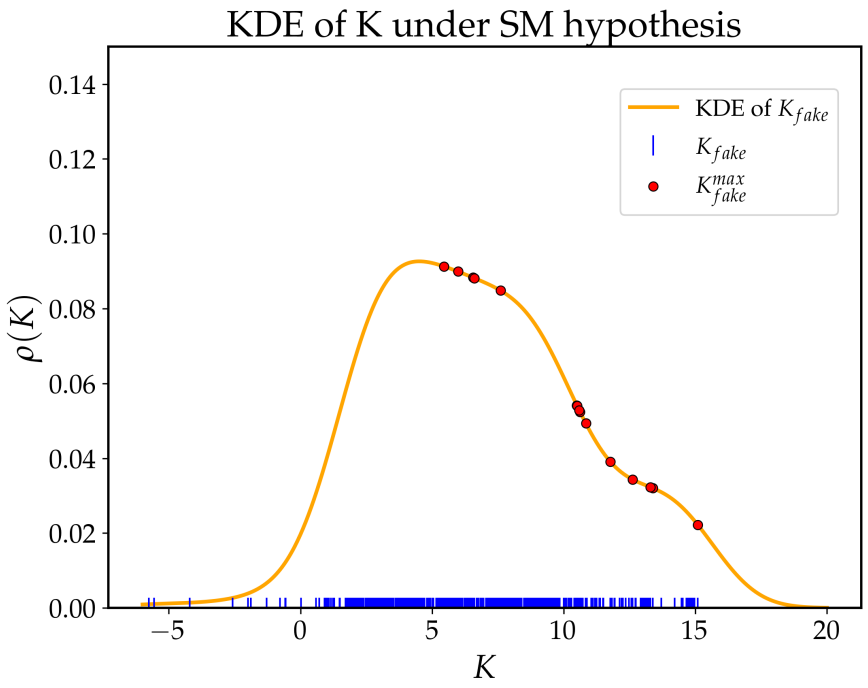


FIGURE 6.12: The distribution of $K$ under the SM-only hypothesis, estimated using a Kernel Density Estimator. The red points denote the highest $K$ values ($K_{fake}$) of proto-models generated across 50 parallel runs on 15 fake SM databases. The blue marks on the x-axis represent the $K$ values ($K_{fake}$) of the best performing proto-models from each of the 50 walks across 15 fake SM databases.

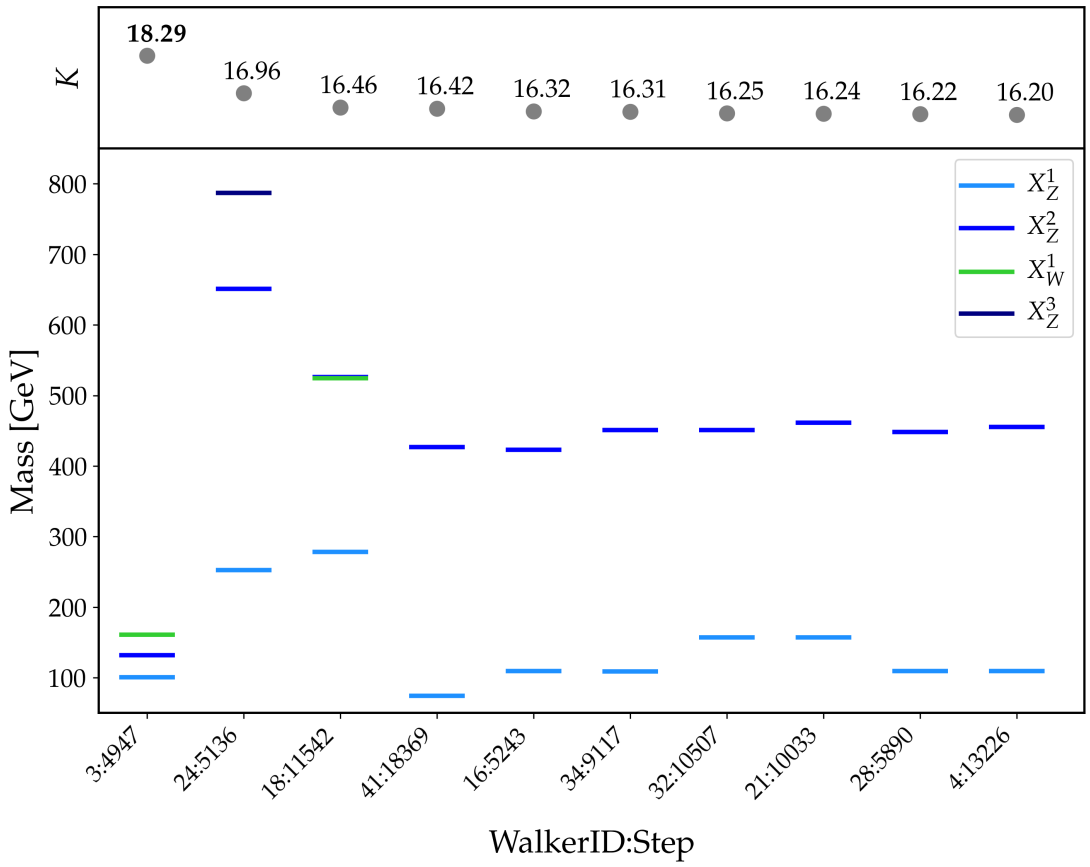


FIGURE 6.13: Top ten proto-models with particle content and masses with the highest $K$ obtained across 50 walks on the real database. The corresponding $K$ values are shown in the top.

corresponding $TL = 22.31$. The $K$ values for the remaining proto-models are nearly the same and between 16 and 17. Notably, apart from the top three, the remaining seven proto-models share the same particle content with nearly the same masses. The difference in $K$ values are primarily due to slight variations in $TL$ values, with the prior on model complexity playing a negligible role for these seven proto-models.

The combinations of experimental results that contribute to these particle configurations are also noteworthy. Figure 6.14 displays the analyses that enter the most significant combination for the top ten proto-models. The excesses in monojet channels in ATLAS-EXOT-2018-16 and CMS-EXO-20-004 are captured in all proto-models. CMS-SUS-20-004 contributes to all proto-models except the best performing one, as the electroweak partner particles in this proto-model lies in the off-shell region not constrained by CMS-SUS-20-004. The proto-models with only two particles, $X_Z^1$ and $X_Z^2$, share identical combinations.

We would first like to understand the significance of the excess and the $K$ values for the proto-models in Figure 6.13. Figure 6.15 shows the density of $K$ under the SM-only hypothesis obtained from the runs on the fake SM databases (orange curve). The $K$ values for all the best performing proto-models from each of the 50 walks on the real SMODELS database are shown as green points overlaid on the curve. We see that all the best performing proto-models lie well above those from the fake runs (above 15.0), with the top ten extending even further into the tail of the distribution. To quantify

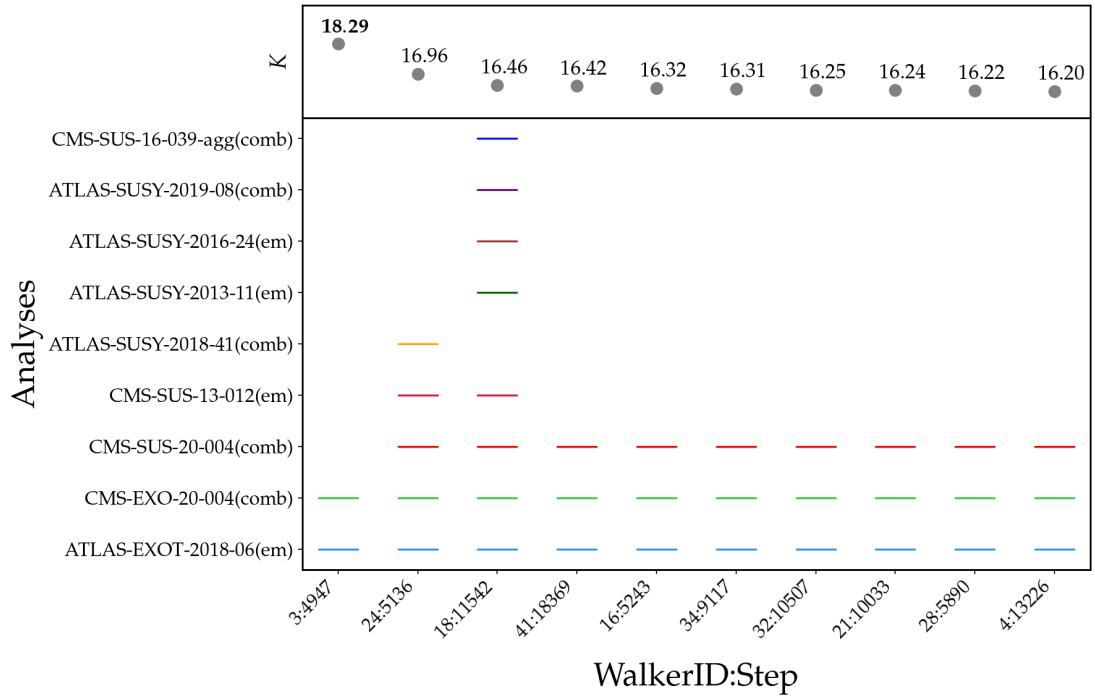


FIGURE 6.14: The experimental results that enter the most significant combination for the top ten best performing proto-models across 50 walks. The corresponding $K$ values are shown in the top.

the compatibility of the observed $K$ values with those found from the fake runs ($K_{fake}$), we compute the $p$-value, given by the relative frequency of $K$ values under the SM hypothesis that exceed the average of the observed $K$ values:

$$p_{\text{global}} := \int_{\bar{K}_{\text{obs}}}^{\infty} dK \rho(K) \,. \tag{6.27}$$

Here, $\bar{K}_{\text{obs}}$ is the average of the observed $K$ values from 50 walks on the SModelS database. It is represented as a light blue star overlaid on the density of $K$ values obtained from the SM runs. The resulting $p$-value corresponds to the light-blue shaded region in Figure 6.15. Evaluating the integral in Eq. (6.27), we obtain the global $p$-value for the SM hypothesis:

$$p_{\text{global}} \approx 0.013 \,. \tag{6.28}$$

Thus, the results obtained with the Walker algorithm v2 on the restricted proto-model parameter space indicate a stronger disagreement with the SM hypothesis than the proof-of-concept version. This strong disagreement warrants closer examination of the best-performing proto-models, particularly the absolute best-performing proto-model. Thus, the following discussion focuses on the walk that generated this proto-model, i.e., Walker ID 3.

The "absolute" best performing proto-model has three BSM particles with $K = 18.29$, generated at step 4947 by Walker ID 3. The proto-model with its particle content and

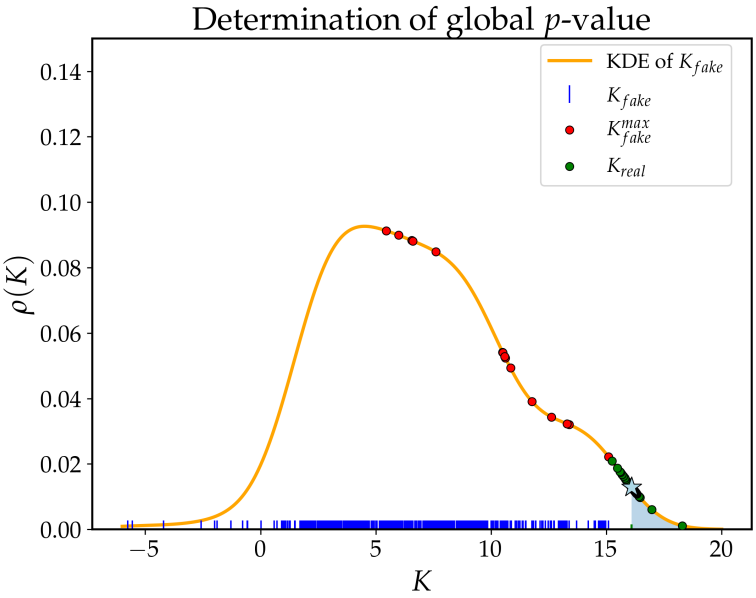


FIGURE 6.15: $K$ values obtained from walks on the SMODELS database (green points) overlaid on the density obtained from the fake SM runs (orange curve). The blue marks on the x-axis represent the $K$ values ($K_{fake}$) of the best performing proto-models from each of the 50 walks across 15 fake SM databases. The red points represent the $K$ values of the "absolute" best performing proto-model ($K_{fake}^{max}$) from each of the 15 fake SM databases. The shaded region corresponds to the global $p$-value for the average $K$ values (light blue star) from the walks on the real database.

decay channels is displayed in the left panel of Figure 6.16. The right panel shows how much the likelihood of the proto-model at different values of the signal strength $\mu$ exceeds that of SM ($\mu = 0$) for three different cases. The dotted lines represent the likelihood ratio for the individual analyses entering the most significant combination, and the solid blue line represents the combined likelihood ratio. There are two key takeaways from the plot: (1) All likelihood ratios are maximum near $\mu = 1$, depicting the maximum deviation of the proto-model signal from the SM. (2) CMS-EXO-20-004 is the primary driver of the combined likelihood. Note that the likelihood obtained from CMS-EXO-20-004 is the combined simplified likelihood of all SRs implemented in this analysis, whereas only the most significant SR of ATLAS-EXOT-2018-16 contributes to the combined likelihood.[6]

The best performing proto-model includes particles $X_Z^1$, $X_Z^2$, and $X_W^1$ with masses of 100.92, 131.72, and 161.21 GeV, respectively. Since $\Delta(m_{X_Z^2}, m_{X_Z^1})$ and $\Delta(m_{X_W^1}, m_{X_Z^1})$ are less than the masses of $Z$ and $W$ bosons, respectively, both $X_Z^2$ and $X_W^1$ decay to the LBP via off-shell channels. In particular, $X_Z^2$ decays invisibly (via neutrinos) to $X_Z^1$, while $X_W^1$ decays via light quarks to $X_Z^1$. This proto-model can give rise to two experimental signatures: (a) final states with only $E_T^{\text{miss}}$, and (b) final states with light jets and $E_T^{\text{miss}}$. Thus, this proto-model is able to capture excesses found in such final state signatures, particularly in the monojet searches.

[6]The most significant SR corresponds to the SR which shows the maximum deviation from the SM hypothesis.

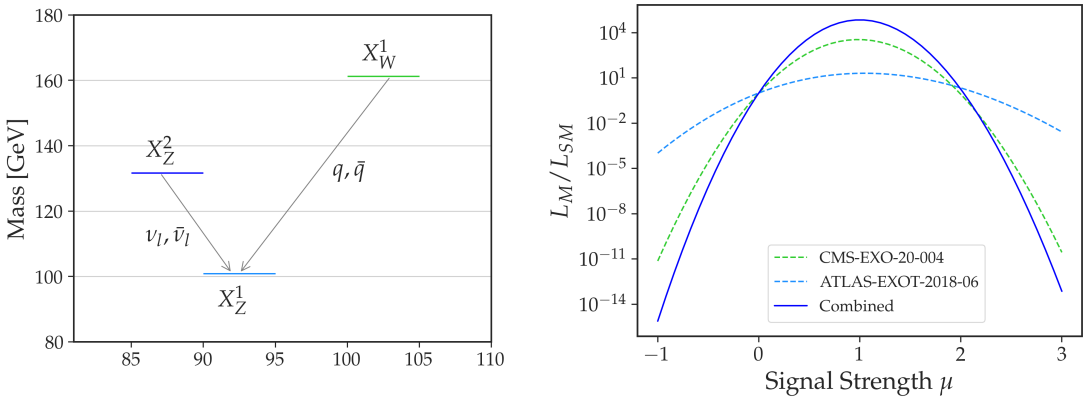


FIGURE 6.16: The "absolute" best-performing proto-model across all 50 walks. Left: particle content with masses and decay modes. Right: Likelihood ratio $L_{\mathbf{M}}(\mu)/L_{\mathbf{SM}}(\mu = 0)$ as a function of the signal strength $\mu$ for individual analyses (dotted lines) and their combination (solid line).

| Pair | SSM | 8 TeV [pb] | 13 TeV [pb] |
|---|---|---|---|
| $(X_Z^1, X_Z^2)$ | 0.31 | 1.03 | 2.28 |
| $(X_Z^1, X_W^1)$ | 1.55 | 4.05 | 8.57 |
| $(X_Z^2, X_Z^2)$ | 0.92 | 1.85 | 4.07 |
| $(X_Z^2, X_W^1)$ | 3.94 | 6.81 | 14.6 |
| $(X_W^1, X_W^1)$ | 0.91 | 0.829 | 1.92 |

TABLE 6.2: The production modes for the absolute best performing proto-model. The signal strength multipliers and the corresponding cross sections at 8 and 13 TeV are displayed.

It is interesting to see which production modes are included in this proto-model. Table 6.2 lists all production modes contained in the proto-model along with the corresponding SSMs and cross sections at 8 and 13 TeV (in pb). From the values listed in the table, we see that the production cross sections are in the same order of magnitude as the corresponding SUSY cross sections. Concretely, the effective signal strength multipliers are $\kappa_{(X_W^1, X_W^1)} = 0.91$, $\kappa_{(X_Z^1, X_Z^2)} = 0.31$, $\kappa_{(X_Z^1, X_W^1)} = 1.55$, $\kappa_{(X_Z^2, X_Z^2)} = 0.92$ and $\kappa_{(X_Z^2, X_Z^2)} = 3.94$. These production modes are relevant because the monojet searches target signals with final states containing either all $E_T^{\text{miss}}$– captured by $(X_Z^1, X_Z^2)$ and $(X_Z^2, X_Z^2)$ production where $X_Z^2$ decays invisibly, or jets and $E_T^{\text{miss}}$– captured by pair and associated production modes of $X_W^1$.

Figure 6.17 shows the evolution of $K$ and $TL$ for this walk. The $K$ and $TL$ values converge near 10 and 12, respectively, with frequent large upward fluctuations reaching approximately 15 and 18. Such behaviour was also observed in other walks on the real database. This contrasts sharply with most walks on fake SM databases, except for the extreme case discussed previously. The step at which $K$ is maximum is marked with a green point and the corresponding $K$ and $TL$ values are mentioned in the plot. We also see that when the Walker traverses poorly performing regions, it quickly jumps back to the better performing regions within a few steps.

It is unclear why the Walker algorithm does not remain in better performing regions

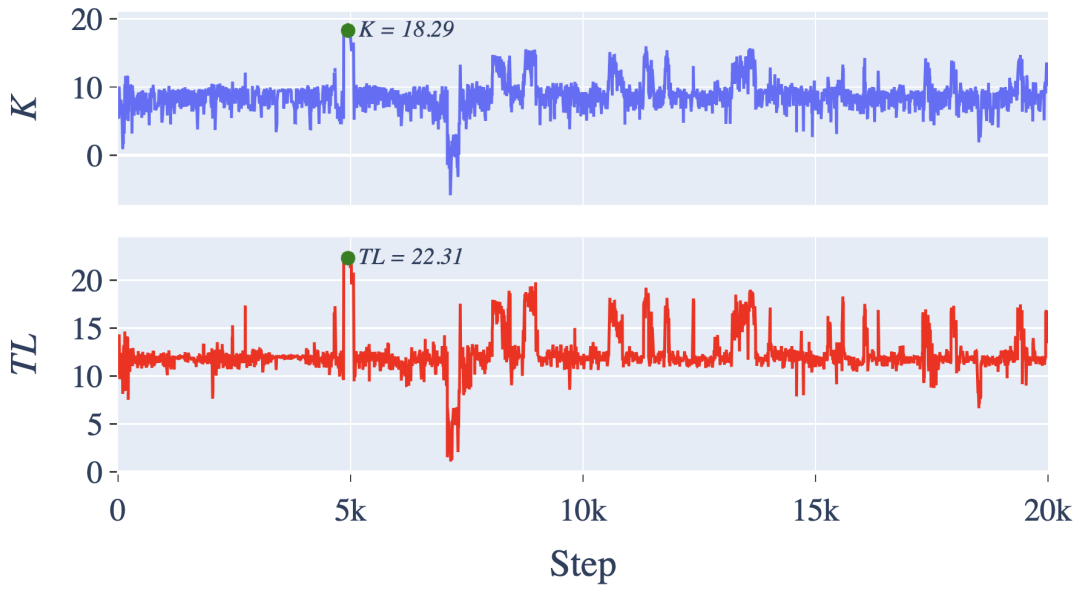


FIGURE 6.17: Evolution of $K$ and $TL$ for walker number 3 on the real SMODELS database. The highest $K$ value obtained and the corresponding $TL$ value are marked in the plot.

for extended periods. One possible diagnosis is that our acceptance probability is too high. Nearly 60% of the proposed proto-models are accepted on average. This causes the walker to jump rapidly between different phase space regions rather than thoroughly exploring interesting regions. Another possible reason is that off-shell regions occupy a much smaller volume than the rest of the phase space, making them more difficult for the sampler to access. We previously imposed a 10% probability of jumping to off-shell regions to facilitate their exploration, but this may be insufficient for the Walker algorithm. This could also explain why other parallel walks failed to find the best performing proto-models in the off-shell region.

So far, we have discussed the performance of the best performing proto-models generated across different walks. It is also important to see what proto-model configurations are generated during the walk, and whether the Walker algorithm is biased toward certain regions of phase space. Figure 6.18 shows the evolution of the proto-model particle content across the Walker 3 for the accepted proto-models. The y-axis represents the integrated probability, which indicates the cumulative frequency with which each particle configuration has been accepted up to the current step. We observe that three proto-model particle configurations occur most frequently: $X^1_Z$,$X^2_Z$; $X^1_Z$ and $X^1_W$; and $X^1_Z$, $X^2_Z$,$X^1_W$. Although other particle configurations are still accepted, their acceptance probabilities decrease sharply as the walk progresses. This indicates that exploration of different proto-model configurations occurs primarily in the initial steps, while later steps predominantly explore the three configurations mentioned above. The remaining particle configurations can occur in later steps, however, the probability of their occurrence is lower. From this plot, we consider the first 3500 steps as a "burn-in" period, where the Walker algorithm is still exploring the available phase space. Thus, the distribution plots shown in the remaining of this section discards the first 3500 steps.

The posterior distributions for Walker ID 3 are noteworthy. We treat the first 3500 steps as a "burn-in" phase and exclude them from all distributions shown. Figure 6.19

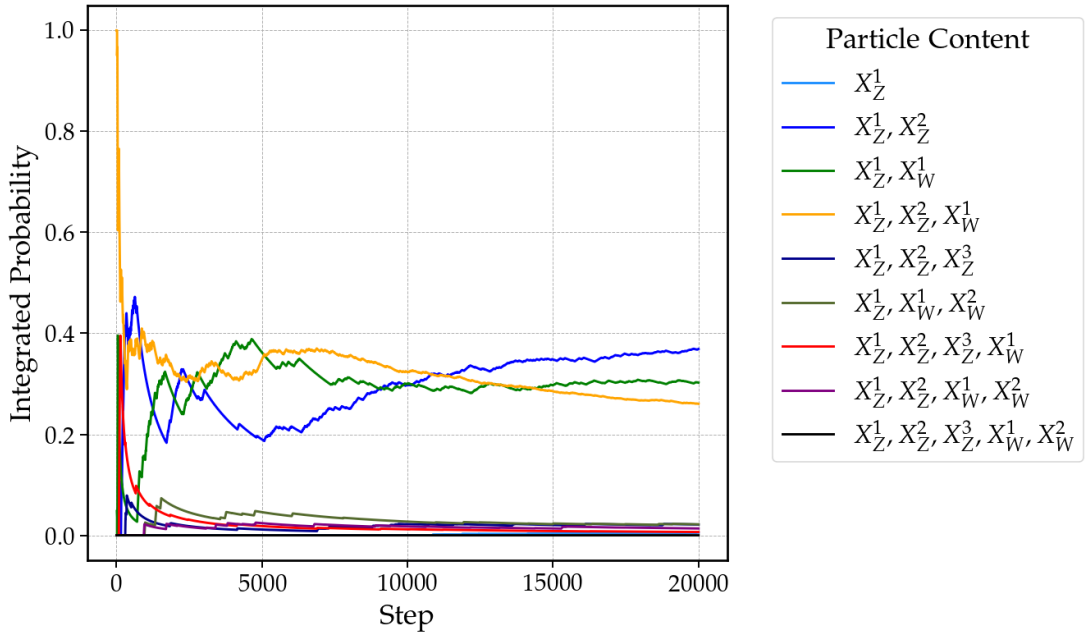


FIGURE 6.18: An evolution of the integrated probabilities of the different proto-model particle spectra as a function of the step for Walker ID 3. The integrated probability indicates the cumulative frequency with which each particle spectrum has been accepted up to the current step.

shows the distribution of the proto-model counts over the allowed particle content. In each block, the top label shows the number of times the proto-model particle configuration appears in the walk (after the "burn-in" period), while the bottom label indicates the particles present in the corresponding proto-model. Except for proto-models containing only the LBP $X_Z^1$ (which is possible as $(X_Z^1, X_Z^1)$ production is allowed), proto-models with fewer particles occur more frequently. We see that no proto-models with all five particles present are accepted in this walk. The most frequent particle configurations include $X_Z^1$ and $X_Z^2$. The next most frequent configuration contains $X_Z^1$ and $X_W^1$, followed by configurations including $X_Z^1$, $X_Z^2$, and $X_W^1$. After these leading cases, the model counts drop sharply, though additional proto-model particle configurations are accepted with a modest frequency. This pattern is observed across all walks on the real database.

The posterior mass distributions for Walker ID 3 are shown in Figure 6.20. We treat the first 3500 steps as a "burn-in" phase and exclude them from these distributions. The proto-model points shown here all contain $X_Z^1$, $X_Z^2$, and $X_W^1$, corresponding to 4043 out of 16500 points. The region where the best performing proto-model is found is marked with a blue open circle. The colour scale represents the range of $K$ values, with darker (redder) points indicating higher $K$ values. The top left plot shows the distribution of $m_{X_W^1}$ vs. $m_{X_Z^2}$. The bottom left plot shows $m_{X_W^1}$ vs. $m_{X_Z^1}$. The bottom right plot shows $m_{X_Z^2}$ vs. $m_{X_Z^1}$.

Several interesting patterns can be seen in these plots. The masses of $X_Z^2$ and $X_W^1$ always lie above the mass of $X_Z^1$ as enforced, and can reach up to 2500 GeV, demonstrating the Walker algorithm's capability to explore the entire available phase space. The masses of $X_Z^1$ vary from 10 to 600 GeV. Low masses of $X_Z^1$, especially near 10 GeV, have extremely low values of $K$, with $K$ even reaching negative values. The negative $K$

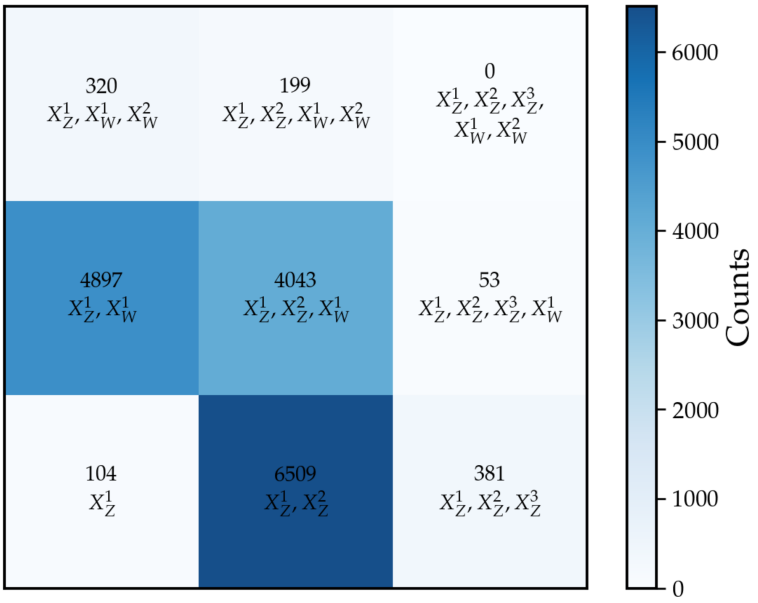


FIGURE 6.19: The distribution of the BSM particle content of the proto-models generated after the initial 3500 steps ("burn-in" period) for walker number 3. Proto-models having only $X_Z^1$ and $X_Z^2$ are the ones that are most favoured while proto-models with a high number of particles are discouraged.

values indicate strong disfavour for these proto-model points with respect to the SM. These low $K$ regions are independent of the mass values of $X_Z^2$ or $X_W^1$, as seen near the bottom of the lower plots.

An interesting pattern appears in the bottom right plot, which displays the distribution of $m_{X_Z^2}$ vs. $m_{X_Z^1}$. Two distinct bands of high $K$ values are evident. The best performing proto-model lies in the orange band, within the mass region where $X_Z^2$ is off-shell. The red band has $m_{X_Z^2}$ close to 500 GeV with $m_{X_Z^1}$ ranging from 100 to 400 GeV. The $K$ values for proto-model points in this band lie between 12 and 15. This red band is also visible in the top left plot ($m_{X_W^1}$ vs. $m_{X_Z^2}$), where $m_{X_Z^2}$ is again near 500 GeV while $m_{X_W^1}$ ranges from 150 to nearly 2500 GeV. Consequently, this distinct red band does not appear in the bottom left plot ($m_{X_W^1}$ vs. $m_{X_Z^1}$), but rather manifests as scattered red points across these mass ranges. A closer inspection of the proto-model points in the red band reveals that, alongside the monojet searches, CMS-SUS-20-004 appears in the most significant combination for all these points. These proto-model points have $X_Z^2$ primarily decaying via $Z/H$ to the LBP $X_Z^1$, or via $W/H$ to $X_W^1/X_Z^1$ when $m_{X_Z^2} > m_{X_W^1}$. This analysis does not appear in the most significant combination for many proto-model points in the orange band, indicating that the excess in CMS-SUS-20-004 significantly enhances the $K$ values in the red band.

The orange bands occur in all three plots and correspond to points with $m_{X_W^1} \sim m_{X_Z^2}$. Some points in the orange band where both the $X_Z^2$ and $X_W^1$ masses lie in the off-shell region have the highest $K$ values, ranging from 12 to 18, with 18.29 being the maximum. These points exhibit similar mass and decay patterns as depicted in Figure 6.16 (left plot), with $X_Z^2$ decaying invisibly to $X_Z^1$ and $X_W^1$ decaying via light quarks to $X_Z^1$. The SSMs are also in similar ranges to those listed in Table 6.2. However, most points in the off-shell region outside these high-$K$ regions have $K$ values between 7 and 9

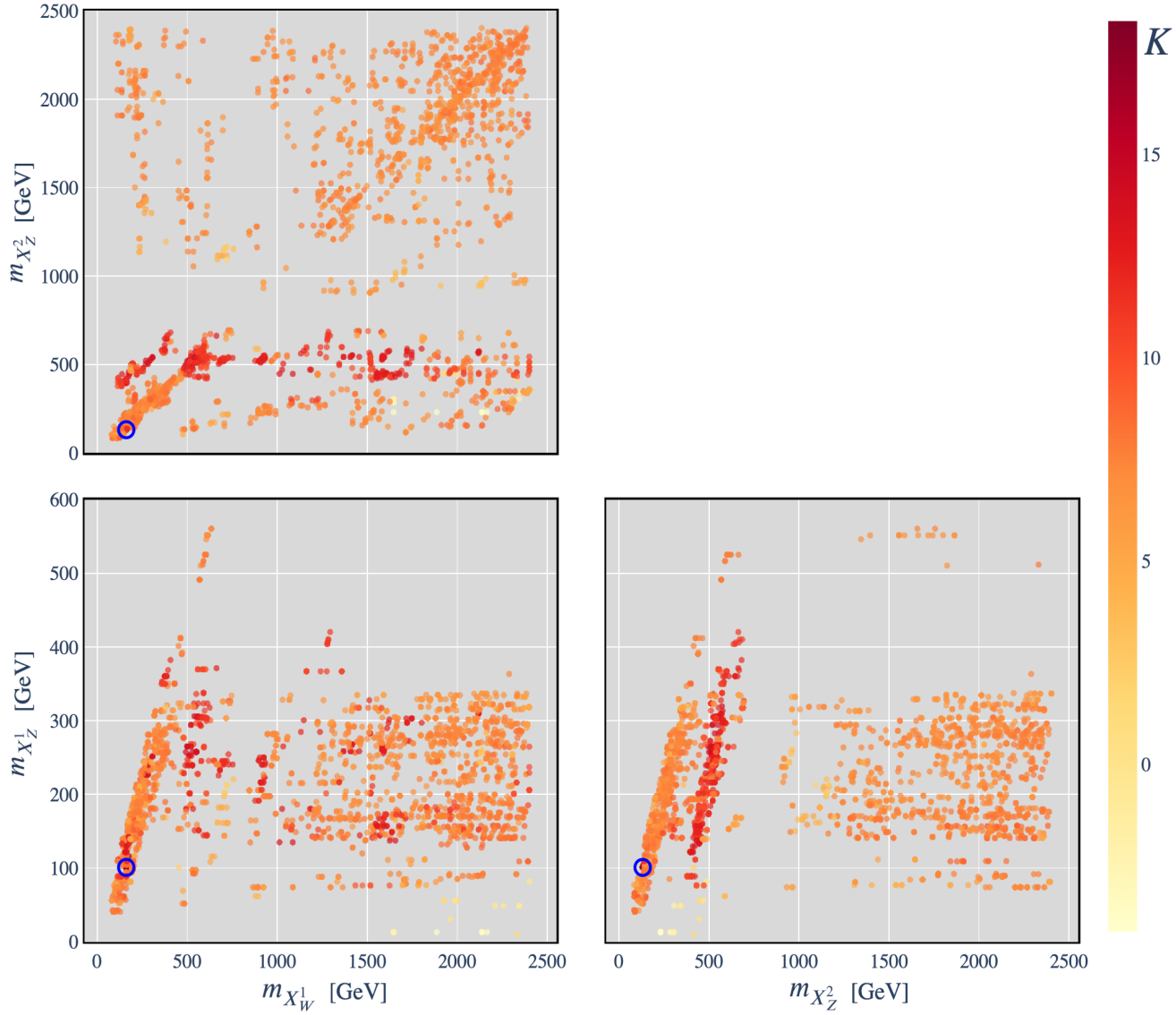


FIGURE 6.20: Mass distributions for the particles $X_Z^1$, $X_Z^2$ and $X_W^1$ in proto-models containing all three particles for walker number 3. The blue open circle marks the region where the best performing proto-model lies. The colour of the points reflect the $K$ values, with darker points having higher $K$ values. The first 3500 steps are considered as a "burn-in" phase and are removed.

(appearing orange in the plot). Although the same experimental results (primarily monojet searches) contribute to these points, differences in masses, decays, or signal strength multipliers lower the $K$ value. This indicates that while the orange band is the most densely populated, more thorough exploration of certain phase space regions is required to generate proto-model points with higher $K$ values.

A puzzling observation across all plots in this section is the absence of the ATLAS soft-lepton search (ATLAS-SUSY-2018-16) from the most significant combination for most proto-model points, especially in the off-shell regions. Given its combinability with the monojet searches, we had expected the Walker algorithm to include it. To capture the excess in this search, the Walker algorithm would need to generate a proto-model where $X^2_Z$ is off-shell and decays leptonically to the LBP. However, we observe that while this proto-model is generated in the walk, their $TL$ and subsequently $K$ values are much lower than those with invisible decays. The invisible decay mode is strongly preferred for $X^2_Z$ over the leptonic decay mode. We are currently investigating this discrepancy and do not yet have a clear explanation for why our expectation does not match the observations.

From all the evolution and distribution plots shown in this section, it is evident that the walks have not converged. Although, with 20000 steps, the Walker algorithm has explored the available phase space, we require substantially more steps to make more robust statements about the posterior distributions. We restricted the runs to 20000 steps because running the Walker algorithm is computationally very expensive, particularly since we must now evaluate large statistical models.

In the next section, we discuss a few closure tests, and a proto-model obtained by focusing on thorough exploration.

### 6.7.3 Closure tests

The $K$ values obtained from the walks on the real database are in notable disagreement with the SM hypothesis. However, to determine whether this disagreement represents a genuine physics signal, it is essential to verify whether the Walker algorithm can reproduce an underlying signal when we artificially inject a signal model into the database. For this closure test, we employ a scheme similar to that used to create fake databases under the SM-only hypothesis. However, this time we create fake observations under a "BSM hypothesis". Specifically, we sample observations from a signal plus background model and assume the corresponding uncertainties to be dominated by background errors. This procedure is described in the proof-of-concept version (see Section 5.3 of[7]).

We generate one such "fake signal" database where we inject a proto-model signal containing $X^1_Z$ at 150 GeV and $X^2_Z$ and $X^1_W$ at 300 GeV. We perform 20 parallel walks (with IDs from 21-40) on this database for a reduced number of steps (roughly 10000).[7] Figure 6.21 shows the particle spectra of the best performing proto-models from these fake signal runs and compares them to the injected proto-model signal. We see that all best performing proto-models reconstruct the injected particle spectrum, with mass differences properly reproduced across the different proto-models. However, while the injected proto-model has $K = 13.3$, the best performing proto-models generated across different walks have significantly higher $K$ values, ranging from approximately 20 to 24, with the particle masses shifted lower on average. The differences between

[7]The number of walks and steps for the closure test was reduced due to time constraints.

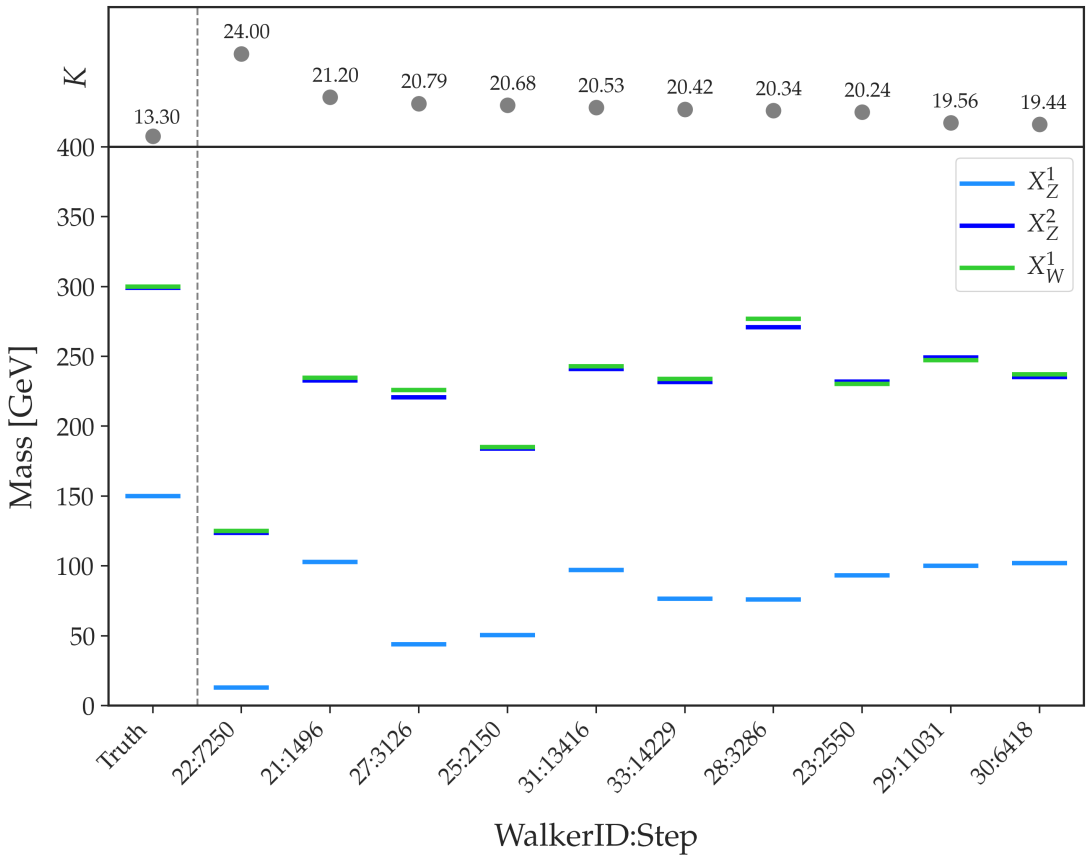


FIGURE 6.21: Particle spectrum and masses for the top ten best performing proto-models across 20 walks on one fake database generated under the "BSM hypothesis". The corresponding $K$ values are shown at the top. The particle spectrum of the proto-model used for the injected signal is shown on the left, and is labelled "Truth".

the injected and reconstructed signals shown in Figure 6.21 are statistical in nature and can be expected in our procedure, given that the injected signal is of the same order as the background uncertainties.

### 6.7.4 Finding the global optimum

In Section 6.7.2, we obtained the absolute best-performing proto-model by running 50 parallel walks for 20000 steps. However, we note that thorough exploration near this proto-model is limited, given the small volume available for off-shell region exploration and the high acceptance probability of the walk. To investigate whether we can achieve a better performing proto-model by focusing on high-$K$ regions, we performed another walk, this time starting not from the Standard Model but from a proto-model from the high-$K$ regions. Here, we do not walk continuously for 20000 steps; instead, we run for a minimum number of steps, identify where the walker reached a new maximum $K$, and then restart the next walk from this region. Hence, this is not strictly a sequential RJMCMC walk, as we force the Walker to explore only high-$K$ regions. Consequently, we cannot provide robust statistical significance for the best performing proto-model obtained this way, but we gain better insight into the type of proto-model that can be constructed to capture the excesses.

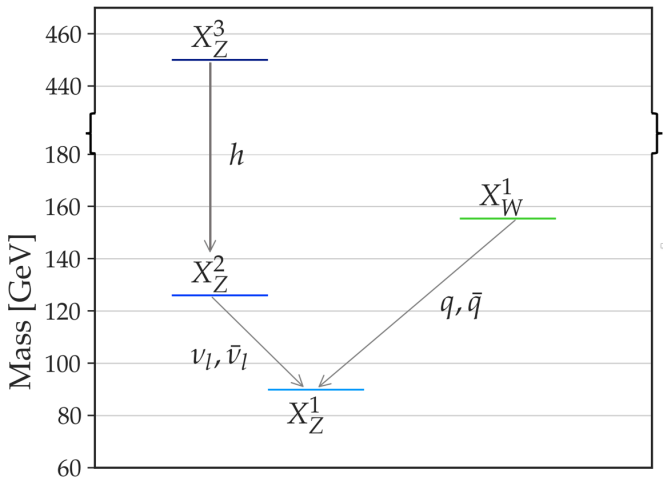


FIGURE 6.22: The best performing proto-model obtained by repeatedly walking near the high $K$ regions. Note that the mass axis has a discontinuity at 180 GeV to accommodate $X_Z^3$ at higher mass in the same plot.

Figure 6.22 shows the proto-model obtained using this method. Besides $X_Z^1, X_Z^2$ and $X_W^1$, this proto-model also includes $X_Z^3$. Interestingly, the decays of $X_Z^2$ and $X_W^1$ are identical to those in Figure 6.16. The $X_Z^3$ decays via a Higgs boson to $X_Z^2$. This particular decay, coupled with $X_Z^2$ decaying invisibly to $X_Z^1$, captures the excess in the CMS-SUS-20-004 analysis. Thus, this proto-model effectively combines the excesses in monojet searches and CMS-SUS-20-004. Although the addition of an extra particle with its corresponding parameters incurs a penalty, the significant deviation from the SM makes this proto-model very attractive. The test statistic obtained for this proto-model lies at $K = 28.39$ and $TL = 33.69$, much higher than the values obtained for the "absolute" best performing proto-model in Section 6.7.2.

### Getting a MCMC posterior distribution

Having found the proto-model which sits at a global optimum in the previous section, we seek to better understand it by collecting posterior samples through a MCMC walk starting from the proto-model point. This is accomplished by setting the parameter `runmcmc=True`, which forces the Walker algorithm to maintain fixed parameter content (no addition or removal of any parameters) while allowing thorough exploration of the proto-model parameters. We performed 50 parallel MCMC walks, this time for a smaller number of steps (approximately 10000), as we observed faster convergence in the test statistics. The masses and signal strength multipliers are allowed to vary freely as before. However, since each particle has only one decay mode, the branching ratios remain fixed.

Figure 6.23 depicts the 1D and 2D marginalised posterior distributions for the particle masses in the proto-model. The top panels show the 1D marginalised posterior mass distributions for each particle, with central values indicating the mean point estimates and $\pm$ indicating the $1\sigma$ band. The off-diagonal panels show the $1\sigma$ and $2\sigma$ credible regions corresponding to the highest posterior density regions. The scatter points outside these regions are raw samples that lie in low probability regions. The black marker indicates the best-fit point (the proto-model with the highest $K/TL$), and the gray dotted lines denote the corresponding masses.[8]

[8]Note that maximising $K$ is equivalent to maximising $TL$, as we are not changing dimensions.

Interestingly, the masses of $X_Z^1$, $X_Z^2$, and $X_W^1$ are highly correlated, while $X_Z^3$ exhibits weaker correlation with all three. This is expected because $X_Z^2$ and $X_W^1$ must remain off-shell to maintain their characteristic decay channels. The best-fit point has masses close to that of the proto-model found from the previous exploration; however, it achieves higher $TL$ and correspondingly higher $K$ values through adjustment of one of the signal strength multipliers for a production mode.

## 6.8 Conclusions

In the absence of clear new physics signals at the LHC and other experiments, and with an ever increasing number of theoretical models being proposed to address the tensions in the Standard Model, it becomes increasingly relevant to change our perspective in the quest for new physics. The artificial proto-modelling framework presents a data driven, relatively model independent approach to address this problem. This chapter presents the significant upgrades made to this framework beyond the proof-of-concept stage, enabling a more statistically robust interpretation of mutually compatible, dispersed signals.

We highlight the importance of formulating a robust acceptance criterion, with well motivated proposal densities and prior distributions. These upgrades have significantly enhanced the Walker algorithm's ability to explore the proto-model parameter space. The algorithm itself has undergone extensive restructuring, incorporating ideas from the RJMCMC method while maintaining computational efficiency. Significant updates to the Builder, Combiner, and Critic blocks have been made relative to the proof-of-concept version. The Builder now explicitly defines proposal and prior probabilities, directly influencing the acceptance probability. The Combiner integrates the PATHFINDER algorithm to reduce computational time in identifying the most significant combination set of experimental results. The Critic is redesigned into two binary decision metrics based on the type of experimental constraints.

For the preliminary results obtained with the Walker algorithm v2, we restrict the proto-model parameter space, inspired by excesses observed in monojet and soft-lepton searches. To understand the results obtained by running the updated Walker algorithm on the restricted proto-model space, we first evaluate its performance on an ensemble of fake SM databases. Each walk is made to run for 20000 steps, with 50 parallel walkers operating across 15 such databases. Even on fake SM databases, statistical fluctuations generate proto-model signals, though most exhibit weak deviations from the SM, with $K \approx 0$ and $TL \approx 2.5$. In one extreme case, such fluctuations allowed for proto-model signals to have test statistic values as high as 10 and 15, respectively.

However, in runs on the real database, such values represent the average, with large upward fluctuations reaching 18 and 20, respectively. The best-performing proto-model has $K = 18.29$. This "absolute" best performing proto-model includes $X_Z^2$ and $X_W^1$ with masses in the off-shell region close to 130 and 160 GeV, respectively, and $X_Z^1$ close to 100 GeV. The cross-sections for the corresponding production modes are of the same order as the corresponding SUSY cross sections. Each particle except the LBP has a simple decay mode, with $X_Z^2$ decaying invisibly, and $X_W^1$ decaying via soft quarks. This proto-model signal is motivated by the excesses in the monojet signal regions which show strong deviation from the expected SM. The global $p$-value for

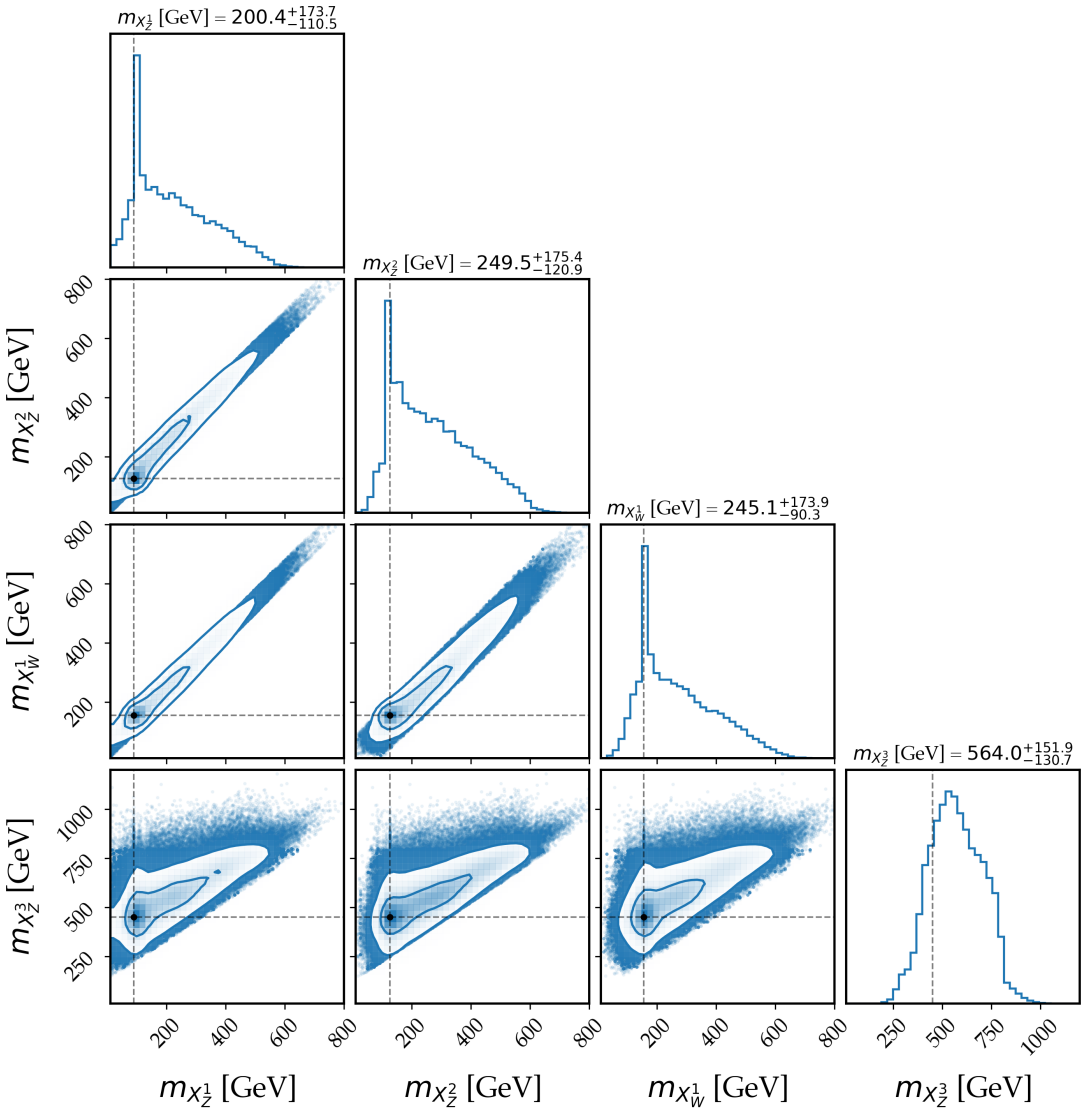


FIGURE 6.23: The 1D and 2D marginalised posterior distributions for the particle masses in the proto-model. The top panels represent the 1D marginalized posterior mass distributions for each particle, with central values indicating the mean point estimates and the $\pm$ indicating the $1\sigma$ band. The off-diagonal panels show the $1\sigma$ and $2\sigma$ credible regions that correspond to the highest posterior density regions for each 2D marginalized posterior distribution. The scatter points outside these regions are raw samples that lie in low probability regions. The black marker indicates the best-fit point, or the proto-model with the highest $K/TL$ and the gray dotted lines indicate the corresponding masses.

the average observed $K$ of 50 best-performing proto-models stood at $p_{\text{global}} \approx 0.013$ under the SM hypothesis.

We also verified the algorithm's capability to reproduce a proto-model signal when one was artificially introduced into a database. Moreover, observing the Walker algorithm's inability to remain in high-performing regions of parameter space, we artificially constrained the algorithm to thoroughly explore interesting phase-space regions of the results.

Despite these promising results, several challenges remain. We are currently puzzled as to why the Walker algorithm does not stay in high performing regions for a longer period of time. We do observe that one cause could be that the current acceptance rate is high. Approximately 60% of proposed proto-models are accepted. While this facilitates wide exploration of parameter space, it also makes locating the global optimum more difficult. Thus, we execute the Walker algorithm to repeatedly probe high-$K$ regions, allowing faster, though less statistically rigorous, identification of optimal proto-models.

Running multiple parallel walkers for extended chains does improve exploration but comes at a significant computational cost. The results described here required continuous computation for over two months on the CLIP cluster, with extensive memory and processing demands. One of the most resource-intensive steps is the likelihood calculation for proto-model signals at each iteration, particularly when the likelihood involves complex HISTFACTORY statistical models combining multiple signal regions. Ongoing work aims to replace these models with machine-learned surrogates to accelerate this step.

We also want to formulate a robust convergence diagnostic based on the posterior distribution. From the results presented here, it is evident that the chain has not fully converged even after 20000 steps. Studies which use RJMCMC principles suggest that at least 50000 steps are typically required for reliable convergence [138, 139]. New diagnostics, including chi-squared–based tests on proto-model samples, are currently under development to address this.

Although these results represent a substantial advancement beyond the initial proof-of-concept version (which focused mainly on proto-model generation) many open questions remain. For instance, the absence of the soft lepton excess observed in SRs of ATLAS-SUSY-2018-16 among those identified by the Walker algorithm warrants further investigation. Nevertheless, this version marks a significant step forward in both scope and methodological rigour. We expect future iterations to address the current limitations and deepen our understanding of the dispersed signals present in various search channels.

# Chapter 7

# Conclusions and Outlook

The Standard Model of particle physics is one of the most successful theories of modern physics and has been tested to a great degree of precision. Nonetheless, strong evidence points to BSM physics, both on the theoretical and experimental side. Many BSM theories have been proposed to address the shortcomings of the SM, but no definite signal from any of them has been observed to date, despite intensive experimental search programs. Thus, this thesis presents a novel approach to complement the traditional searches for new physics.

Searches for new physics at the ATLAS and CMS experiments are often pursued in a channel-by-channel approach, with limits on new physics parameters interpreted within simplified model frameworks. Several reinterpretation tools then utilise these results to extend limits on simplified models to full theories. SModelS is one such public reinterpretation tool that constrains BSM theories by decomposing them into a collection of simplified models, which are then confronted against simplified model results implemented in its database. The advantage of SModelS is its fast reinterpretation of simplified model results as it does not depend on any Monte Carlo simulation. Thus, it is suitable for large scans.

The work presented in this thesis comprises contributions to the development of the SModelS framework from v2 to v3, which implements a graph-based description of simplified model topologies that extends beyond simple $\mathbb{Z}_2$-like structures. We also presented the contributions to the SModelS database extension, implementation, and validation of experimental results, and improvements to statistical treatments in Chapter 4. The end of this chapter focused on a top-down approach, utilising SModelS framework to constrain BSM theories. Specifically, it highlighted the importance of combining different experimental results to build a global likelihood for testing the electroweakino parameter space of supersymmetry. A comprehensive phenomenological study was subsequently presented, which applied global LHC constraints to the MSSM electroweakino sector through dynamical combination of 16 ATLAS and CMS Run 1 and Run 2 searches. The most sensitive combination of analyses was identified dynamically for each model point, with analyses considered approximately uncorrelated if from different runs, different experiments, or with non-overlapping signal region selections. At high chargino masses, ATLAS and CMS hadronic searches drove sensitivity and exclusion, while for compressed mass spectra, the ATLAS three-lepton plus missing energy Run 2 search dominated.

For models with a bino-like LSP, $m_{\tilde{\chi}_1^0}$ values up to approximately 1 TeV were excluded when $m_{\tilde{\chi}_1^0} \approx 0$, but no points with $m_{\tilde{\chi}_1^0} \gtrsim 400$ GeV were excluded. The combination of

different analyses resulted in a clear excluded region whose extent depended on the nature of NLSP nature. The exclusion limits for higgsino-bino models were approximately 100 GeV weaker than limits for wino-bino models due to smaller production cross section of higgsino-like particles. Indeed, the production cross section of the h being smaller than for wino-like particles, For models with a non-bino-like LSP, $m_{\tilde{\chi}_2^\pm}$ values up to approximately 950 GeV were excluded when $m_{\tilde{\chi}_1^0} \approx 100$ GeV, though LEP constraints on light charginos forbade most non-bino-like LSP points with $m_{\tilde{\chi}_1^0} \lesssim 100$ GeV. However, no points with $m_{\tilde{\chi}_1^\pm} \gtrsim 350$ GeV were excluded. Analysis combination increased the number of excluded points by 35% (48% expected) compared to using only the most sensitive single analysis, with the improvement more pronounced for bino-like LSP models.

Chapters 5 and 6 presented a novel methodology called "*Artificial Proto-modelling*" that goes beyond the usual top-down approach to test BSM theories. This data driven, model independent method was designed to construct simple BSM models by searching for dispersed signals manifesting across a collection of simplified model results. More precisely, we developed an algorithm that searched for hints of new physics by constructing proto-models, (collection of simplified model topologies not bound by higher level theoretical assumptions) by confronting them against the simplified model results in the SModelS database. Proto-models were constructed to identify mutually compatible over-fluctuations from different LHC search channels via dynamical analysis combination while being consistent with the current experimental limits. They were designed to be as model independent as possible. Since the algorithm was developed to operate on the SModelS database, the proto-model particle content was SUSY-inspired.

While Chapter 5 introduced the concept of artificial proto-modelling and presented the first version of the Walker algorithm, Chapter 6 presented a major restructuring of the Walker algorithm, advancing it beyond the proof-of-concept stage. The algorithm evolved from a MCMC-like random walk to implementing RJMCMC methods. Major upgrades included significant expansion of the SModelS database, particularly incorporating analyses for which likelihoods could be constructed (often with the possibility of combining signal regions within an analysis). Another important improvement concerned the combination matrix: rather than only considering analyses with trivially orthogonal search channels as combinable, signal region overlap was carefully scrutinized through selection cut analysis when necessary. Additionally, the proto-model parameter space was extended off-shell decay modes for the lightest electroweak partner particles were included.

Although the proto-modelling framework's core components remained unchanged from v1 to v2 (a builder building proto-models, a combiner identifying optimal analysis combinations, and a critic setting constraints on proto-models), the code architecture was considerably improved. Proper proposal densities were constructed for each allowed random modification, along with appropriate prior distributions from which proto-model parameter values were drawn. The acceptance criterion was redesigned based on RJMCMC principles to provide more robust statistical inference. The PathFinder algorithm [159] was employed to identify optimal analysis combinations both in the Combiner, to find the most significant combination, and in the Critic, to find the most sensitive combination. The Critic makes binary decisions and is split into two sub-components: a "fast critic" that primarily enforces constraints from UL-type results, and a "slow critic" that utilises likelihood information from constraints

to identify the most sensitive analysis combination.

For getting the results with the updated algorithm, the proto-model phase space was restricted to monojet and electroweakino searches, as these regions have exhibited the most interesting excesses. The Walker algorithm v2 was first run on an ensemble of fake databases drawn from Standard Model backgrounds to establish baseline expectations for the types of proto-models that could be constructed and the test statistic values that could be obtained. Two main scores were recorded for each proto-model: $TL$, which measured how much the proto-model signal deviated from the expected SM, and $K$, which incorporated $TL$ while adding a penalty for model complexity. From the ensemble of fake SM runs, we observed that $K$ and $TL$ values of 10 and 15 could be expected from background over-fluctuations mimicking dispersed signals. Most runs yielded values fluctuating near 0 and 5, while some runs reached 10 and 15, respectively.

This stood in sharp contrast to running on the real SModelS database. Values of $K$ and $TL$ fluctuated between 10 and 15, with some reaching up to 18 and 20, respectively. The top ten best performing proto-models all included the lightest neutral electroweakino partner particles $X_Z^1$ and $X_Z^2$. The "absolute" best performing proto-model additionally included $X_W^1$, with the masses of $X_Z^2$ and $X_W^1$ lying in the off-shell region. This proto-model was primarily driven by excesses found in the monojet search channels of CMS-EXO-20-004 and ATLAS-EXOT-2018-16. The global $p$-value for the average observed $K$ of 50 best-performing proto-models stood at $p_{\text{global}} \approx 0.013$ under the SM hypothesis. This notable disagreement with Standard Model expectations compels us to probe the excesses in these search channels more thoroughly. The absence of soft-lepton excesses in ATLAS-SUSY-2018-16 in any of the best performing proto-models is particularly puzzling, given the compatibility of the parameter region with excesses observed in monojet search channels. It should be noted, however, that these results originated from preliminary test runs on a restricted parameter space and require further validation.

Although these results are more statistically robust than those obtained with v1, there are several areas that could be improved further. First, we plan to implement formal convergence diagnostics that would provide more rigorous assessments of whether the algorithm has adequately explored the proto-model parameter space. Second, as experimental results increasingly provide detailed statistical models for SR combination, computing the likelihood of the proto-model signal becomes computationally expensive, contributing to the major bottleneck in the iteration process. We are currently investigating whether these models could be replaced by machine-learned surrogates to improve efficiency. Third, the Walker algorithm itself can be further refined, particularly regarding the proposal and prior distributions. Stricter acceptance criteria might be required to encourage the algorithm to remain in high-performing regions of parameter space. Fourth, the current SModelS database v3.1.0 includes searches for long-lived particles (LLPs), monojet resonances, and other exotic signatures. To capture potential excesses in these channels, the parameter space would need to be expanded to include width-dependent effects, resonance structures, and displaced vertices. We plan to incorporate these extensions in the next version of the proto-model algorithm. Lastly, it would also be interesting to see if the proto-models obtained could be mapped to existing effective BSM theories or even to full UV complete theories.

As a concluding remark, the absence of clear BSM signals combined with the increasing diversity of theoretically-motivated scenarios necessitates a shift in perspective for the quest for new physics. The proto-modelling framework represents a step in this direction, offering a more model-independent, data-driven approach to identifying potential dispersed signals. We also note that appropriate reinterpretation materials play a crucial role in this endeavour: accurate likelihood reconstruction requires both efficiency maps and complete statistical models. As experimental collaborations continue to provide richer statistical information, the potential for data-driven discovery methods will only grow, offering complementary sensitivity to traditional theory-driven searches.

# Appendix A

# Neutralino and chargino masses

We denote neutralinos and charginos as $\tilde{\chi}^0_{1\ldots4}$ and $\tilde{\chi}^\pm_{1,2}$, respectively. They are the mass eigenstates that form from the higgsinos and electroweak gauginos (the fermionic superpartners of the Higgs and electroweak gauge bosons, respectively) due to the effects of electroweak symmetry breaking. Concretely, neutralinos are linear combinations of the bino $\widetilde{B}$, neutral wino $\widetilde{W}^0$ and neutral higgsino $\widetilde{H}^0_u$ and $\widetilde{H}^0_d$ gauge eigenstates, while charginos are linear combinations of the charged wino ($\widetilde{W}^+$ and $\widetilde{W}^-$) and charged higgsino ($\widetilde{H}^+_u$ and $\widetilde{H}^-_d$) gauge eigenstates.

In the basis $\psi^0 = (\widetilde{B}, \widetilde{W}^0, \widetilde{H}^0_d, \widetilde{H}^0_u)^T$, $\psi^\pm = (\widetilde{W}^+, \widetilde{H}^+_u, \widetilde{W}^-, \widetilde{H}^-_d)^T$, the relevant part of the Lagrangian is [70, 201]

$$\mathcal{L}_{\text{mass}} = -\frac{1}{2}(\psi^0)^T \mathcal{M}_N \psi^0 - \frac{1}{2}(\psi^\pm)^T \mathcal{M}_C \psi^\pm + \text{c.c.}\,, \tag{A.1}$$

where

$$\mathcal{M}_N = \begin{pmatrix} M_1 & 0 & -c_\beta\, s_W\, m_Z & s_\beta\, s_W\, m_Z \\ 0 & M_2 & c_\beta\, c_W\, m_Z & -s_\beta\, c_W\, m_Z \\ -c_\beta\, s_W\, m_Z & c_\beta\, c_W\, m_Z & 0 & -\mu \\ s_\beta\, s_W\, m_Z & -s_\beta\, c_W\, m_Z & -\mu & 0 \end{pmatrix} \tag{A.2}$$

and

$$\mathcal{M}_C = \begin{pmatrix} \mathbf{0} & \mathbf{X}^T \\ \mathbf{X} & \mathbf{0} \end{pmatrix}, \qquad \mathbf{X} = \begin{pmatrix} M_2 & \sqrt{2}\, s_\beta\, m_W \\ \sqrt{2}\, c_\beta\, m_W & \mu \end{pmatrix}, \tag{A.3}$$

are the neutralino and chargino mass matrices. Here, $M_1$, $M_2$ and $\mu$ are the bino, wino and higgsino mass parameters, respectively, and we have introduced the abbreviations $s_\beta = \sin\beta$, $c_\beta = \cos\beta$, $s_W = \sin\theta_W$, and $c_W = \cos\theta_W$, with $\theta_W$ the weak mixing angle and $\tan\beta = v_u/v_d$ the ratio of the Higgs vacuum expectation values. The chargino mass matrix is written in $2 \times 2$ block form for convenience.

The mass eigenstates are related to the gauge eigenstates by the unitary matrices $N$, $U$ and $V$, which diagonalise the mass matrices:

$$N^* \mathcal{M}_N N^{-1} = \text{diag}\left(m_{\tilde{\chi}^0_1}, \ldots, m_{\tilde{\chi}^0_4}\right), \tag{A.4}$$

$$U^* \mathbf{X} V^{-1} = \text{diag}\left(m_{\tilde{\chi}^\pm_1}, m_{\tilde{\chi}^\pm_2}\right), \tag{A.5}$$

so that

$$\tilde{\chi}_i^0 = N_{ij}\psi_j^0\,, \qquad \begin{pmatrix}\tilde{\chi}_1^+\\ \tilde{\chi}_2^+\end{pmatrix} = V\begin{pmatrix}\widetilde{W}^+\\ \widetilde{H}_u^+\end{pmatrix}, \quad \begin{pmatrix}\tilde{\chi}_1^-\\ \tilde{\chi}_2^-\end{pmatrix} = U\begin{pmatrix}\widetilde{W}^-\\ \widetilde{H}_d^-\end{pmatrix}. \tag{A.6}$$

By convention, the physical states are mass ordered: $|m_{\tilde{\chi}_i^0}| < |m_{\tilde{\chi}_j^0}|$ for $i < j$ and $m_{\tilde{\chi}_1^\pm} < m_{\tilde{\chi}_2^\pm}$. Following the SUSY Les Houches Accord (SLHA) [144] conventions, in the absence of CP violation we choose the mixing matrices to be real, allowing for *signed* (negative) mass eigenvalues for the neutralinos. The lightest neutralino, $\tilde{\chi}_1^0$, is typically also the Lightest Supersymmetric Particle (LSP) and the dark matter candidate.

If the mass parameters $M_1$, $M_2$ and $\mu$ in eqs. (A.2) and (A.3) are sufficiently different from each other, the mixing is small and one ends up with a bino-like neutralino with mass of about $M_1$, an almost mass-degenerate pair of wino-like chargino/neutralino with mass of about $M_2$, and a triplet of higgsino-like neutralinos and chargino with mass of about $\mu$. The bino, wino and higgsino contents of neutralino $\tilde{\chi}_i^0$ are given by $|N_{i1}|^2$, $|N_{i2}|^2$ and $|N_{i3}|^2 + |N_{i4}|^2$, respectively. Likewise, the wino and higgsino admixtures of chargino $\tilde{\chi}_i^+$ are given by $|V_{i1}|^2$ and $|V_{i2}|^2$.

## Appendix B

# Complete list of analyses in the SModelS database v3.1.0

| ID | Short Description | $\mathcal{L}$ [fb$^{-1}$] | $UL_{obs}$ | $UL_{exp}$ | EM | comb. |
|---|---|---|---|---|---|---|
| ATLAS-EXOT-2018-06 [74] | monojet | 139.0 | ✓ | | ✓ | |
| ATLAS-EXOT-2018-48 [202] | di-top resonance | 139.0 | ✓ | ✓ | | |
| ATLAS-EXOT-2019-03 [203] | dijet resonance | 139.0 | ✓ | ✓ | | |
| ATLAS-SUSY-2015-01 [204] | 2 $b$-jets | 3.2 | ✓ | | | |
| ATLAS-SUSY-2015-02 [205] | 1$\ell$ stop | 3.2 | ✓ | | ✓ | |
| ATLAS-SUSY-2015-06 [206] | 0$\ell$ + 2–6 jets | 3.2 | | | ✓ | |
| ATLAS-SUSY-2015-09 [207] | jets + 2 SS or $\geq 3\ell$ | 3.2 | ✓ | | | |
| ATLAS-SUSY-2016-06 [208] | disappearing track | 36.1 | | | ✓ | |
| ATLAS-SUSY-2016-07 [182] | 0$\ell$ + jets | 36.1 | ✓ | | ✓ | |
| ATLAS-SUSY-2016-08 [209] | displaced vertices | 32.8 | ✓ | | | |
| ATLAS-SUSY-2016-14 [210] | 2 SS or 3$\ell$ + jets | 36.1 | ✓ | | | |
| ATLAS-SUSY-2016-15 [211] | 0$\ell$ stop | 36.1 | ✓ | | | |
| ATLAS-SUSY-2016-16 [183] | 1$\ell$ stop | 36.1 | ✓ | | ✓ | |
| ATLAS-SUSY-2016-17 [212] | 2 OS $\ell$ | 36.1 | ✓ | | | |
| ATLAS-SUSY-2016-19 [213] | 2 $b$-jets + $\tau$ | 36.1 | ✓ | | | |
| ATLAS-SUSY-2016-24 [180] | 2–3$\ell$, EWK | 36.1 | ✓ | | ✓ | |
| ATLAS-SUSY-2016-26 [214] | $\geq 2$ $c$-jets | 36.1 | ✓ | | | |
| ATLAS-SUSY-2016-27 [215] | jets + $\gamma$ | 36.1 | ✓ | | ✓ | |
| ATLAS-SUSY-2016-28 [216] | 2 $b$-jets | 36.1 | ✓ | | | |
| ATLAS-SUSY-2016-32 [217] | HSCP | 31.6 | ✓ | ✓ | ✓ | |
| ATLAS-SUSY-2016-33 [218] | 2 SFOS $\ell$ | 36.1 | ✓ | | | |
| ATLAS-SUSY-2017-01 [219] | $W$ $h(bb)$, EWK | 36.1 | ✓ | | | |
| ATLAS-SUSY-2017-02 [220] | 0$\ell$ + jets | 36.1 | ✓ | ✓ | | |
| ATLAS-SUSY-2017-03 [221] | multi-$\ell$ EWK | 36.1 | ✓ | | ✓ | |
| ATLAS-SUSY-2018-04 [222] | 2 hadronic $\tau$ | 139.0 | ✓ | | ✓ | PyHF |
| ATLAS-SUSY-2018-05 [223] | 2$\ell$ + jets, EWK | 139.0 | ✓ | | ✓ | PyHF |
| ATLAS-SUSY-2018-06 [128] | 3$\ell$, EWK | 139.0 | ✓ | ✓ | ✓ | |
| ATLAS-SUSY-2018-08 [224] | 2 OS $\ell$ | 139.0 | ✓ | | ✓ | |
| ATLAS-SUSY-2018-09 [225] | 2 SS $\ell$ | 139.0 | ✓ | | | |
| ATLAS-SUSY-2018-10 [226] | 1$\ell$ + jets | 139.0 | ✓ | | ✓ | |
| ATLAS-SUSY-2018-12 [227] | 0$\ell$ + jets | 139.0 | ✓ | ✓ | ✓ | |
| ATLAS-SUSY-2018-13 [228] | displaced jets | 139.0 | | | ✓ | SLv1 |
| ATLAS-SUSY-2018-14 [229] | displaced vertices | 139.0 | | | ✓ | PyHF |
| ATLAS-SUSY-2018-16 [190] | 2 soft $\ell$ + jets, EWK | 139.0 | ✓ | ✓ | ✓ | PyHF |
| ATLAS-SUSY-2018-22 [230] | multi-jets | 139.0 | ✓ | | ✓ | |
| ATLAS-SUSY-2018-23 [231] | $Wh(\gamma\gamma)$, EWK | 139.0 | ✓ | ✓ | | |
| ATLAS-SUSY-2018-31 [232] | 2 $b$-jets + 2 h | 139.0 | ✓ | | ✓ | PyHF |
| ATLAS-SUSY-2018-32 [233] | 2 OS $\ell$ | 139.0 | ✓ | | ✓ | PyHF |
| ATLAS-SUSY-2018-33 [234] | DV with $\geq 1$ muon | 136.0 | | | ✓ | |
| ATLAS-SUSY-2018-40 [235] | 2 $b$-jets + 2 h | 139.0 | ✓ | ✓ | ✓ | |
| ATLAS-SUSY-2018-41 [236] | hadr. EWK | 139.0 | ✓ | ✓ | ✓ | SLv1 |
| ATLAS-SUSY-2018-42 [237] | charged LLPs, dE/dx | 139.0 | ✓ | ✓ | ✓ | |
| ATLAS-SUSY-2019-02 [238] | 2 soft $\ell$, EWK | 139.0 | ✓ | | ✓ | SLv1 |
| ATLAS-SUSY-2019-08 [239] | 1$\ell$ + $h(bb)$, EWK | 139.0 | ✓ | | ✓ | PyHF |
| ATLAS-SUSY-2019-09 [191] | 3$\ell$, EWK | 139.0 | ✓ | ✓ | ✓ | PyHF |

TABLE B.1: List of ATLAS Run 2 analyses and their types of results in the SModelS v3.1.0 database. Apart from the HSCP, disappearing tracks and displaced lepton searches, all analyses require $E_T^{\text{miss}}$ in the final state (for conciseness omitted in the short descriptions). EW stands for electroweak (-ino or slepton) production. The last column specifies whether and how SRs are combined: "PyHF " means a HistFactory model is used through interface with PyHF; "SLv1"("SLv2") means that a covariance matrix (with a third moment) is used; and a blank means only the most sensitive SR is used.

| ID | Short Description | $\mathcal{L}$ [fb$^{-1}$] | UL$_{\text{obs}}$ | UL$_{\text{exp}}$ | EM | comb. |
|---|---|---|---|---|---|---|
| CMS-EXO-19-001 [240] | non-prompt jets | 137.0 | | | ✓ | |
| CMS-EXO-19-010 [241] | disappearing track | 101.0 | | | ✓ | |
| CMS-EXO-19-012 [242] | dijet resonance | 137.0 | ✓ | | | |
| CMS-EXO-20-004 [194] | monojet | 137.0 | | | ✓ | SLv1 |
| CMS-EXO-20-008 [243] | di-b resonance | 138.0 | ✓ | ✓ | | |
| CMS-PAS-EXO-16-036 [244] | HSCP | 12.9 | ✓ | | | |
| CMS-PAS-SUS-16-052 [245] | ISR jet + soft $\ell$ | 35.9 | ✓ | | ✓ | SLv1 |
| CMS-SUS-16-009 [246] | $0\ell$ + jets, top tag | 2.3 | ✓ | ✓ | | |
| CMS-SUS-16-032 [247] | 2 $b$- or 2 $c$-jets | 35.9 | ✓ | | | |
| CMS-SUS-16-033 [186] | $0\ell$ + jets | 35.9 | ✓ | ✓ | ✓ | |
| CMS-SUS-16-034 [248] | 2 SFOS $\ell$ | 35.9 | ✓ | | | |
| CMS-SUS-16-035 [249] | 2 SS $\ell$ | 35.9 | ✓ | | | |
| CMS-SUS-16-036 [187] | $0\ell$ + jets | 35.9 | ✓ | ✓ | | |
| CMS-SUS-16-037 [250] | $1\ell$ + jets with MJ | 35.9 | ✓ | | | |
| CMS-SUS-16-039 [251] | multi-$\ell$, EWK | 35.9 | ✓ | | ✓ | SLv1 |
| CMS-SUS-16-041 [252] | multi-$\ell$ + jets | 35.9 | ✓ | | | |
| CMS-SUS-16-042 [253] | $1\ell$ + jets | 35.9 | ✓ | | | |
| CMS-SUS-16-043 [254] | $W\,h(bb)$, EWK | 35.9 | ✓ | | | |
| CMS-SUS-16-045 [255] | 2 $b$-jets + 2 $h(\gamma\gamma)$ | 35.9 | ✓ | | | |
| CMS-SUS-16-046 [256] | high-$p_T$ $\gamma$ | 35.9 | ✓ | | | |
| CMS-SUS-16-047 [257] | $\gamma$ + jets, high $H_T$ | 35.9 | ✓ | | | |
| CMS-SUS-16-048 [258] | soft OS $\ell$ | 35.9 | | | ✓ | SLv1 |
| CMS-SUS-16-050 [185] | $0\ell$ + top tag | 35.9 | ✓ | ✓ | ✓ | SLv1 |
| CMS-SUS-16-051 [189] | $1\ell$ stop | 35.9 | ✓ | ✓ | | |
| CMS-SUS-17-003 [259] | 2 $\tau$ | 35.9 | ✓ | | | |
| CMS-SUS-17-004 [260] | EWK comb. | 35.9 | ✓ | | | |
| CMS-SUS-17-005 [261] | $1\ell$ + jets, top tag | 35.9 | ✓ | ✓ | | |
| CMS-SUS-17-006 [262] | jets + boosted $h(bb)$ | 35.9 | ✓ | ✓ | | |
| CMS-SUS-17-009 [179] | SFOS $\ell$ | 35.9 | ✓ | ✓ | | |
| CMS-SUS-17-010 [263] | $2\ell$ stop | 35.9 | ✓ | ✓ | | |
| CMS-SUS-18-002 [264] | $\gamma$ + ($b$-)jets, top tag | 35.9 | ✓ | ✓ | | |
| CMS-SUS-18-004 [192] | 2–3 soft $\ell$ | 137.0 | ✓ | ✓ | | |
| CMS-SUS-18-007 [265] | 2 $h(\gamma\gamma)$, EWK | 77.5 | ✓ | ✓ | | |
| CMS-SUS-19-006 [188] | $0\ell$ + jets, $\not{H}_T$ | 137.0 | ✓ | ✓ | ✓ | SLv1 |
| CMS-SUS-19-008 [266] | 2–3$\ell$ + jets | 137.0 | ✓ | ✓ | | |
| CMS-SUS-19-009 [267] | $1\ell$ + jets, $\not{H}_T$ | 137.0 | ✓ | ✓ | | |
| CMS-SUS-19-010 [268] | jets + top- and $W$-tag | 137.0 | ✓ | ✓ | | |
| CMS-SUS-19-011 [269] | $2\ell$ stop | 137.0 | ✓ | ✓ | | |
| CMS-SUS-19-013 [270] | jets + boosted $Z$ | 137.0 | ✓ | ✓ | | |
| CMS-SUS-20-001 [271] | SFOS $\ell$ | 137.0 | ✓ | ✓ | | |
| CMS-SUS-20-002 [272] | stop combination | 137.0 | ✓ | ✓ | | |
| CMS-SUS-20-004 [8] | 2 $h(bb)$, EWK | 137.0 | ✓ | ✓ | ✓ | SLv2 |
| CMS-SUS-21-002 [273] | hadr. EWK | 137.0 | ✓ | ✓ | ✓ | SLv1 |
| CMS-SUS-21-007 [274] | $1\ell$ + top- or $W$-tag | 138.0 | ✓ | | | |

TABLE B.2: List of CMS Run 2 analyses and their types of results in the SModelS v3.1.0 database. Apart from the HSCP, disappearing tracks and displaced lepton searches, all analyses require $E_T^{\text{miss}}$ in the final state (for conciseness omitted in the short descriptions). EW stands for electroweak (-ino or slepton) production. The last column specifies whether and how SRs are combined: "SLv1"("SLv2") means that a covariance matrix (with a third moment) is used; and a blank means only the most sensitive SR is used

| ID | Short Description | $\mathcal{L}$ [fb$^{-1}$] | UL$_{\text{obs}}$ | UL$_{\text{exp}}$ | EM |
|---|---|---|---|---|---|
| ATLAS-EXOT-2013-11 [275] | dijets | 20.3 | ✓ | | |
| ATLAS-SUSY-2013-02 [181] | $0\ell$ + 2–6 jets | 20.3 | ✓ | | ✓ |
| ATLAS-SUSY-2013-04 [276] | $0\ell$ + 7–10 jets | 20.3 | ✓ | | ✓ |
| ATLAS-SUSY-2013-05 [277] | $0\ell$ + 2 $b$-jets | 20.1 | ✓ | | ✓ |
| ATLAS-SUSY-2013-08 [278] | $Z(\ell\ell)$ + $b$-jets | 20.3 | ✓ | | |
| ATLAS-SUSY-2013-09 [279] | 2 SS $\ell$ + 0–3 $b$-jets | 20.3 | ✓ | | ✓ |
| ATLAS-SUSY-2013-11 [280] | $2\ell$ ($e, \mu$), EWK | 20.3 | ✓ | | ✓ |
| ATLAS-SUSY-2013-12 [281] | $3\ell$ ($e, \mu, \tau$), EWK | 20.3 | ✓ | | ✓ |
| ATLAS-SUSY-2013-15 [282] | $1\ell$ + 4 (1 $b$-)jets | 20.3 | ✓ | | ✓ |
| ATLAS-SUSY-2013-16 [283] | $0\ell$ + 6 (2 $b$-)jets | 20.1 | ✓ | | ✓ |
| ATLAS-SUSY-2013-18 [284] | jets + $\geq 3$ $b$-jets | 20.1 | ✓ | | ✓ |
| ATLAS-SUSY-2013-19 [285] | 2 OS $\ell$ + ($b$-)jets | 20.3 | ✓ | | |
| ATLAS-SUSY-2013-20 [286] | $2\ell$ ($e, \mu$) + jets | 20.0 | ✓ | | |
| ATLAS-SUSY-2013-21 [287] | monojet or $c$-jet | 20.3 | | | ✓ |
| ATLAS-SUSY-2013-23 [288] | $1\ell$ + 2 $b$-jets (or 2 $\gamma$) | 20.3 | ✓ | | |
| ATLAS-SUSY-2014-03 [289] | $\geq 2$ ($c$-)jets | 20.3 | | | ✓ |
| CMS-EXO-12-026 [290] | HSCP | 18.8 | ✓ | | |
| CMS-EXO-12-059 [291] | dijet resonance | 19.7 | ✓ | ✓ | |
| CMS-EXO-13-006 [292] | HSCP | 18.8 | | | ✓ |
| CMS-EXO-16-057 [293] | di $b$-jet resonance | 19.7 | ✓ | ✓ | |
| CMS-PAS-SUS-13-015 [294] | $\geq 5$ (1 $b$-)jets | 19.4 | | | ✓ |
| CMS-PAS-SUS-13-016 [295] | 2 OS $\ell$ + $\geq 4$ (2 $b$-)jets | 19.7 | ✓ | | ✓ |
| CMS-PAS-SUS-13-018 [296] | 1–2 $b$-jets, $M_{\text{CT}}$ | 19.4 | ✓ | | |
| CMS-PAS-SUS-13-023 [297] | $0\ell$ stop | 18.9 | ✓ | | |
| CMS-SUS-12-024 [298] | $0\ell$ + $\geq 3$ (1 $b$-)jets | 19.4 | ✓ | | ✓ |
| CMS-SUS-12-028 [299] | multi ($b$-)jets, $\alpha_T$ | 11.7 | ✓ | ✓ | |
| CMS-SUS-13-002 [300] | $\geq 3\ell$ (+ jets) | 19.5 | ✓ | ✓ | |
| CMS-SUS-13-004 [301] | $\geq 1$ $b$-jet, Razor | 19.3 | ✓ | | |
| CMS-SUS-13-006 [302] | multi-$\ell$, EWK | 19.5 | ✓ | | |
| CMS-SUS-13-007 [303] | $1\ell$ + $\geq 2$ $b$-jets | 19.3 | ✓ | | ✓ |
| CMS-SUS-13-011 [304] | $1\ell$ + $\geq 4$ (1 $b$-)jets | 19.5 | ✓ | | ✓ |
| CMS-SUS-13-012 [184] | jets + $\not{H}_T$ | 19.5 | ✓ | ✓ | ✓ |
| CMS-SUS-13-013 [305] | 2 SS $\ell$ + ($b$-)jets | 19.5 | ✓ | ✓ | ✓ |
| CMS-SUS-13-019 [306] | $\geq 2$ jets, $M_{\text{T2}}$ | 19.5 | ✓ | | |
| CMS-SUS-14-010 [307] | $b$-jets + 4 $W$ | 19.5 | ✓ | ✓ | |
| CMS-SUS-14-021 [308] | soft $\ell$, low jet mult. | 19.7 | ✓ | ✓ | ✓ |

TABLE B.3: List of 15 ATLAS and 18 CMS Run 1 analyses and their types of results in the SModelS v3.1.0 database. Apart from the HSCP searches, all analyses require $E_T^{\text{miss}}$ in the final state (for conciseness omitted in the short descriptions). EW stands for electroweak(-ino) production. The column Comb. from Tables B.1- B.2 is omitted because none of the Run 1 analyses provides any information on background correlations.

# Appendix C

# Combination Matrix

This appendix details the combinations considered for the Artificial Proto-modelling v2. Only the combinations for 13 TeV analyses are detailed, as there are no updates from the 8 TeV results already used in v1.

For each experiment, searches are split into groups based on the number of leptons in the final state. An analysis in one group is typically considered to be combinable with an analysis in another, unless they are in multiple groups.

## C.1 ATLAS 13 TeV

### Zero-Lepton Final States

This category of searches encompasses thirteen ATLAS searches targeting final states with no leptons, characterised primarily by hadronic activity and missing transverse momentum. Based on their experimental signatures and selection criteria, three different subcategories can be made which we consider to be orthogonal to one another.

#### General Hadronic Searches

The analyses within this subgroup cannot be combined with one another due to overlapping selection criteria. However, they can be combined with all analyses outside the subgroup.

- **ATLAS-SUSY-2015-06** and its successor **ATLAS-SUSY-2016-07** employ inclusive signal regions with increasing jet multiplicities (2-6 jets), targeting generic hadronic SUSY signatures.
- **ATLAS-SUSY-2018-22** is an extension of the above two searches employing a "multi-bin" search approach with at least two energetic jets across three signal region sets.
- **ATLAS-EXOT-2018-06** searches for new phenomena in events containing an energetic jet and large missing transverse momentum. The final-state monojet signature requires at least one energetic jet with upto three additional jets.

#### Final states with $b$-jets

This subcategory focuses on final states enriched in $b$-tagged jets.

- **ATLAS-SUSY-2015-01** selects events with exactly two $b$-jets in two sets of SRs. The first set of SRs enforces the invariant mass of the two $b$-jets to be greater than 200 GeV. The second set of SRs requires the presence of a high $p_T$ leading jet that is not $b$-tagged along with the $b$-jets.

- **ATLAS-SUSY-2016-15** targets all-hadronic final states with at least four jets, requiring at least one $b$-jet across five signal region sets.

  This analysis is not combinable with **ATLAS-SUSY-2015-01** due to overlapping selection requirements, particularly in SRs demanding two or more $b$-jets.

- **ATLAS-SUSY-2017-01** searches for electroweakino pair production via hadronic $W$ and Higgs boson decays in events containing four or five jets, with exactly two identified as $b$-jets. The analysis requires the invariant mass of the $b$-jet pair to be compatible with the Higgs boson mass ($[105, 135]$ GeV) and the dijet masses to be consistent with the $W$ boson mass ($[75, 90]$ GeV).

  Despite requiring exactly two $b$-jets, the specific mass requirements create sufficient orthogonality to allow combination with the above analyses.

- **ATLAS-SUSY-2018-12** targets all-hadronic $t\bar{t}$ signatures characterized by multiple jets, including one or two b-tagged jets, across four distinct signal region sets.

  The analysis employs selection requirements similar to **ATLAS-SUSY-2016-15**, preventing combination with both **ATLAS-SUSY-2015-01** and **ATLAS-SUSY-2016-15**.

- **ATLAS-SUSY-2018-31** focuses on final states with three or more $b$-jets, defining three overlapping signal regions to capture signatures with up to six b-jets.

  The requirement of three or more $b$-jets in the final state events makes this analyses combinable with all other analyses in this subcategory.

- **ATLAS-SUSY-2018-41** is an extension of the **ATLAS-SUSY-2017-01** hadronic search by targeting hadronic $Z$ boson decays along with $W$ and Higgs bosons. The search considers two specific fully hadronic scenarios: the $qqqq$ final state, where two $W/Z$ bosons each decay into light-flavor quark pairs, and the $bbqq$ final state, where one $W/Z$ boson produces light-flavor quarks while a second $Z/h$ boson decays into $b\bar{b}$. Thus, two sets of SRs are defined based on the absence/presence of exactly two $b$-jets. Further, jets are required to be "boson-tagged", to ensure that they arise from the respective bosons.

  As this analysis is an extension of **ATLAS-SUSY-2017-01**, these two analyses are not combinable with one another. However, it is combinable with the rest of the analyses due to the specific 'boson-tagging' criteria.

**Specialized Signatures**

The analyses in this group have distinct final state signatures, and thus are orthogonal with respect to each other and with all the other analyses.

- **ATLAS-SUSY-2016-06** searches for disappearing-track signatures, requiring tracks with specific disappearance conditions alongside additional jets.

- **ATLAS-SUSY-2016-27** searches for photonic signatures with isolated photons and missing transverse momentum.
- **ATLAS-SUSY-2018-13** targets events with displaced vertices alongside multiple energetic jets.
- **ATLAS-SUSY-2018-42** searches for hypothetical charged, long-lived particles characterised by high transverse momenta and large specific ionisation losses.

### Single-Lepton Final States

This category comprises five ATLAS supersymmetry searches targeting final states with exactly one isolated electron or muon, characterized by hadronic activity and missing transverse momentum.

- **ATLAS-SUSY-2015-02** and **ATLAS-SUSY-2016-16** both target direct top squark pair production. These analyses select events with one light lepton (from $W$ boson decay), at least four jets with typically one $b$-jet required, and large missing transverse momentum. The experimental signature resembles top quark pair production with additional missing energy. Due to overlapping selection requirements, these analyses cannot be statistically combined.
- **ATLAS-SUSY-2017-01** searches for chargino-neutralino production decaying via $W$ and Higgs boson. Along with fully hadronic final state signatures, this analysis targets single lepton final states requiring exactly one lepton, 2-3 jets with exactly two $b$-jets. The $b$-jet invariant mass is required to be consistent with the Higgs boson (105-135 GeV).

  The specific two $b$-jet requirement with mass constraints enables combination with the above stop searches.
- **ATLAS-SUSY-2018-10** searches for gluino and squark pair production decaying via charginos to two $W$ bosons plus neutralinos. The analysis selects events with one lepton from $W$ decay, at least two jets, and defines four signal regions with increasing jet multiplicities ($\geq$ 2 to $\geq$ 6 jets). Signal regions are further categorized by $b-$tagging requirements: $b-$tag regions requiring $\geq$ 1 b-jet, and $b$-veto regions explicitly rejecting $b$-tagged jets.

  The $b$-tag signal regions overlap with **ATLAS-SUSY-2015-02** and **ATLAS-SUSY-2016-16**, preventing combination.
- **ATLAS-SUSY-2019-08** searches for electroweakino pair production decaying into final states with a $W$ and Higgs boson. The signal selection requires a pair of $b$-tagged jets consistent with those from a Higgs boson decay, and either an electron or a muon from the $W$ boson decay, together with missing transverse momentum.

  This analysis extends the parameter space covered by **ATLAS-SUSY-2017-01** and employs similar selection criteria. Thus, it is not combinable with **ATLAS-SUSY-2017-01**, but is combinable with the other analyses in this group.

### Two-Lepton Final States

This category encompasses nine ATLAS supersymmetry searches targeting final states with exactly two leptons, primarily focusing on electroweakino production.

- **ATLAS-SUSY-2016-24** searches for electroweak production of SUSY particles decaying via $W/Z$ bosons in final states consisting of multiple leptons, jets and missing transverse momentum. The channels requiring two leptons in final states are divided into two based on the absence or presence of non $b$-jets. The two leptons are required to be of opposite sign and can be of same flavour (SF) or different flavour (DF). The invariant mass of the two leptons should be consistent with the $Z$ boson mass and the $W$ boson is reconstructed from the jets.

- **ATLAS-SUSY-2017-01** searches for electroweakino production decaying via $W$ and Higgs bosons. Along with fully hadronic and single-lepton final state signatures, this analysis targets multilepton final states. In the two lepton selection, the SRs require two same-sign leptons in the final state events. Events are further required to have one to three non $b$-jets.

  Though the two lepton final state SRs are combinable with the same final state SRs of **ATLAS-SUSY-2016-24**, the three lepton final state SRs do overlap (see below). Thus, they are not considered to be combinable.

- **ATLAS-SUSY-2017-03** searches for electroweak production of SUSY particles decaying via $W/Z$ bosons in final states consisting of multiple leptons, jets and missing transverse momentum. The SRs require two opposite-sign, same-flavour leptons (OSSF) with an invariant mass consistent with arising from a $Z$ boson ($[80-100]$ GeV). In addition, two or more non $b$-jets are required with the dijet mass consistent with the $W$ boson mass ($[70, 90]$ GeV)

  As this analysis shares similar selection requirements as the same flavour SRs of **ATLAS-SUSY-2016-24**, they are not combinable with one another.

- **ATLAS-SUSY-2018-04** searches for direct stau production in final states with exactly two hadronically decaying $\tau$-leptons. Signal events are characterized by the presence of exactly two $\tau$-leptons and large missing transverse momentum. The events are required to have exactly two $\tau$-lepton candidates with opposite-sign electric charge and invariant masses above 120 GeV. Additionally, a light lepton veto and a $b$-jet veto are applied.

  The $\tau$-lepton requirement ensures combinability with the above analyses.

- **ATLAS-SUSY-2018-05** searches for electroweak and strong production of sparticles in events with exactly two OSSF leptons, jets, and missing transverse momentum. The invariant mass of the leptons need to be consistent with the $Z$ boson mass. Some SRs do define the invariant mass to be below the $Z$ peak to capture offshell decays of electroweakino models. Additionally, events are required to have at least two jets and both $b$-tag and $b$-veto SRs are defined.

  Similar selection requirements with **ATLAS-SUSY-2016-24** and **ATLAS-SUSY-2017-03** prevent combination with these analyses.

- **ATLAS-SUSY-2018-08** searches for top squarks and dark matter in final states with two opposite-charge leptons (SF or DF), jets, and missing transverse momentum. The analysis requires lepton invariant masses above 10 GeV while explicitly rejecting $Z$-peak events (71-111 GeV) for same-flavour pairs, implementing both $b$-tag and $b$-veto signal regions.

  This analysis has some SRs that overlap with the non-$b$-jet different flavour regions **ATLAS-SUSY-2016-24** and offshell SRs of **ATLAS-SUSY-2018-05**, thus preventing combination.

- **ATLAS-SUSY-2018-16** searches for electroweak production of sparticles in final states with two OSSF low $p_T$ leptons, along with hadronic signatures and missing transverse momentum. Signal events require the invariant mass of the leptons to be less than 60 GeV.

  Some signal regions overlap with same-flavor regions of **ATLAS-SUSY-2018-08** and offshell SRs of **ATLAS-SUSY-2018-05** preventing combination, but the analysis remains combinable with all others listed above.

- **ATLAS-SUSY-2018-32** searches for electroweak production of sparticles in final states with two opposite-charge leptons (SF or DF), jets, and significant missing transverse momentum. Lepton invariant masses must be greater than 100 GeV, with same-flavor events required to have masses far from the $Z$ peak ($>$ 121.2 GeV). All events are required to have no more than one non-$b$-jet.

  As an update to **ATLAS-SUSY-2016-24**, it cannot be combined with its predecessor or with **ATLAS-SUSY-2018-08** due to similar selection requirements.

- **ATLAS-SUSY-2018-40** searches for bottom squark pair production in events with hadronically decaying $\tau$-leptons, $b$-tagged jets, and large missing transverse momentum. Events are required to have at least three jets, among which at least two must be $b$-tagged. All SRs require at least two hadronically decaying $\tau$-leptons with opposite electric charge. The invariant mass of the $\tau$-leptons must satisfy $55\ \text{GeV} < m(\tau_1, \tau_2) < 120\ \text{GeV}$.

  As the signal selection requirements do not overlap with any other analyses in this group, it is combinable with all the analyses.

- **ATLAS-SUSY-2019-02** searches for electroweak production of sparticles in final states with two leptons and missing transverse momentum. The leptons can be of both same flavour or different flavour. SF events are required to have a dilepton invariant mass far from the Z peak, $|m_{ll} - 91\ \text{GeV}| > 15\ \text{GeV}$. Additionally, events must also have no more than one non $b$-tag jet.

  This analysis is complementary to **ATLAS-SUSY-2018-32** and hence is not combinable with it. In addition, it cannot be combined with **ATLAS-SUSY-2016-24**, **ATLAS-SUSY-2018-08** and **ATLAS-SUSY-2018-16**.

### Three lepton final states

All the four analyses listed below target trilepton signatures from electroweakino production of sparticles.

- **ATLAS-SUSY-2016-24** searches for final state signatures with three leptons in addition to the two lepton channels. In the three lepton channel, events can have have $0- \geq 1$ non $b$-jets. In addition, two of the leptons must form an OSSF pair.

- **ATLAS-SUSY-2017-01** searches for electroweakino production decaying via $W$ and Higgs bosons. Along with fully hadronic and single-lepton final state signatures, this analysis targets multi-lepton final states. Events in the $3\ell$ signal regions are categorized according to flavor and charge-sign combinations of the leptons in the event. In opposite-sign different-flavor (OSDF) signal regions, two of the leptons are required to have same sign and same flavor (the SSSF lepton pair), while the third lepton (the OSDF lepton) must have opposite charge and different flavor to the other two leptons. In the OSSF signal regions, there must be at least one pair of leptons of the same flavor and with opposite-sign charge whose invariant mass lies outside the $Z$ peak.

  While the two-lepton final state regions could be combined with the non-overlapping **ATLAS-SUSY-2016-24** regions, the three-lepton regions overlap due to both analyses having OSSF pair requirements with potential $Z$-peak exclusions. Thus, they cannot be combined.

- **ATLAS-SUSY-2017-03** is an update of **ATLAS-SUSY-2016-24** in the same final state signature. An OSSF lepton pair is required, formed by finding the pair with invariant mass closest to the $Z$-boson mass along with the requirement of zero to three non-$b$-jets.

  Due to overlapping signal region definitions and similar selection strategies, this analysis cannot be combined with **ATLAS-SUSY-2016-24**.

- **ATLAS-SUSY-2018-06** targets leptonically decaying W and Z bosons from the electroweakinos in final states with exactly three leptons. The leptons must have at least one OSSF pair with an invariant mass consistent with the $Z$ boson mass. Events containing $b$-tagged jets are rejected.

  Due to overlapping signal region definitions and similar selection strategies, this analysis cannot be combined with **ATLAS-SUSY-2016-24** and **ATLAS-SUSY-2017-03**.

- **ATLAS-SUSY-2019-09** provides complementary coverage to **ATLAS-SUSY-2018-06** with three distinct decay scenarios: on-shell $WZ$, off-shell $WZ$, and $Wh$-mediated processes. Final state events consists consists of exactly three leptons, possible ISR jets, and missing transverse energy. For $W^*Z^*$-mediated scenarios, two leptons are assigned to the $Z^*$-boson candidate by selecting a OSSF lepton pair, and the remaining lepton is assigned to the $W^*$ boson. In $Wh$-mediated scenarios, the opposite-sign leptons are the indirect product of the Higgs boson decay and can be of either the same or different flavour.

  Due to overlapping signal region definitions and similar selection strategies, this analysis cannot be statistically combined with any analysis in this group.

## C.2 CMS 13 TeV

### Zero Lepton Final States

This category of searches encompasses eight CMS 13 TeV searches targeting final states with no leptons, characterised primarily by hadronic activity and missing transverse momentum.

- **CMS-EXO-19-001**: Searches for long-lived particles decaying to displaced, non-prompt jets along with missing transverse momentum. The analysis selects potential signal jets that do not originate from the primary vertex, implementing a signal region requirement of jet timing greater than 3 ns to identify signatures of particles with measurable lifetimes.

  Due to the special timing requirement on the jets, this analysis is combinable with all the other analyses in this group.

- **CMS-EXO-19-010**: Targets long-lived charged particles that decay within the silicon tracker volume, producing a distinctive "disappearing track" signature. Events are characterized by isolated tracks with missing hits in the outermost tracker layers, minimal calorimeter energy deposition, and no muon detector hits, indicating particles that decay before reaching the outer detector systems.

  Due to the disappearing track signature, this analysis is combinable with all the other analyses in this group.

- **CMS-EXO-20-004**: Searches for new phenomena in events with energetic jets and large missing transverse momentum. The analysis requires boson-tagged jets to identify $W/Z$ boson signatures while implementing a $b$-jet veto.

- **CMS-SUS-16-033** and its extension **CMS-SUS-19-006** target supersymmetric scenarios through multijet final states with large missing transverse momentum. These complementary analyses examine events containing 2 to $\geq 9$ jets with 0 to $\geq 3$ $b$-jets.

- **CMS-SUS-16-050** searches for supersymmetric scenarios involving top quark production by selecting events with hadronically decaying top quarks, zero leptons, and significant missing transverse momentum. Selection criteria require at least four jets with at least one identified as $b$-jet and one reconstructed top quark.

  Due to the top reconstruction criteria, this analysis is combinable with all other analysis in this group

- **CMS-SUS-20-004**: Selects final states containing two Higgs bosons decaying to $b\bar{b}$ pairs. The analysis vetoes leptons and isolated charged particle tracks while selecting the four $b$-jets to reconstruct two Higgs boson candidates.

  This analysis is combinable with **CMS-EXO-20-004** as it explictly requires $b$-jets. However, it is not combinable with **CMS-SUS-16-033**, **CMS-SUS-19-006** and **CMS-SUS-21-002** due to similar selection criteria.

- **CMS-SUS-21-002**: Searches for direct chargino and neutralino production in final states with large missing transverse momentum and pairs of hadronically

decaying bosons ($WW$, $WZ$, $Wh$). The search requires boson-tagged jets and implements both $b$-veto signal regions (requiring boson-tagged jets) and $b$-tagged signal regions (combining boson-tagged and $b$-tagged jets).

Due to similar selection criteria, it cannot be combined with **CMS-EXO-20-004**, **CMS-SUS-16-033**, **CMS-SUS-19-006**, and **CMS-SUS-20-004**.

### Multi-lepton Final States

This category of searches encompasses three 13 TeV searches targeting final states with one or more leptons. These analyses exploit distinct final state signatures provided by different lepton multiplicities and charge configurations, creating orthogonal search strategies and thus, can be statistically combined with one another.

- **CMS-PAS-SUS-16-052**: Searches for supersymmetry with a compressed mass spectrum using events containing a high-momentum jet from initial state radiation, large missing transverse momentum, and a single low-momentum lepton.
- **CMS-SUS-16-039**: Searches for the direct electroweak production of charginos and neutralinos through two distinct final state signatures. The first targets events with two or more same-sign (SS) leptons (electrons or muons). The second selects events with three or more leptons, where up to two may be hadronically decaying tau leptons.
- **CMS-SUS-16-048**: Searches for new physics signatures in events containing two low-momentum, oppositely charged (OS) leptons (electrons or muons) along with missing transverse momentum.

# Bibliography


[1] S. Kraml et al. "SModelS: a tool for interpreting simplified-model results from the LHC and its application to supersymmetry". In: *Eur. Phys. J. C* 74 (2014), p. 2868. DOI: 10.1140/epjc/s10052-014-2868-5. arXiv: 1312.4175.

[2] S. Kraml et al. *SModelS v1.0: a short user guide*. 2014. arXiv: 1412.1745.

[3] F. Ambrogi et al. "SModelS v1.1 user manual: Improving simplified model constraints with efficiency maps". In: *Comput. Phys. Commun.* 227 (2018), pp. 72–98. DOI: 10.1016/j.cpc.2018.02.007. arXiv: 1701.06586.

[4] F. Ambrogi et al. "SModelS v1.2: long-lived particles, combination of signal regions, and other novelties". In: *Comput. Phys. Commun.* 251 (2020), p. 106848. DOI: 10.1016/j.cpc.2019.07.013. arXiv: 1811.10624.

[5] G. Alguero et al. "Constraining new physics with SModelS version 2". In: *JHEP* 08 (2022), p. 068. DOI: 10.1007/JHEP08(2022)068. arXiv: 2112.00769.

[6] M. M. Altakach et al. "SModelS v2.3: Enabling global likelihood analyses". In: *SciPost Phys.* 15.5 (2023), p. 185. DOI: 10.21468/SciPostPhys.15.5.185. arXiv: 2306.17676.

[7] W. Waltenberger, A. Lessa, and S. Kraml. "Artificial Proto-Modelling: Building Precursors Of A Next Standard Model From Simplified Model Results". In: *Journal of High Energy Physics* 3 (2021). ISSN: 1029-8479. DOI: 10.1007/jhep03(2021)207.

[8] A. Tumasyan et al. "Search for higgsinos decaying to two Higgs bosons and missing transverse momentum in proton-proton collisions at $\sqrt{s} = 13$ TeV". In: *JHEP* 05 (2022), p. 014. DOI: 10.1007/JHEP05(2022)014. arXiv: 2201.04206 [hep-ex].

[9] J. J. Thomson. "XL. Cathode Rays". In: *The London, Edinburgh, and Dublin Philosophical Magazine and Journal of Science* 44.269 (1897), pp. 293–316. DOI: 10.1080/14786449708621070.

[10] J. C. Maxwell. "A Treatise on Electricity and Magnetism". In: *Nature* 7 (1873), pp. 478–480. DOI: 10.1038/007478a0.

[11] A. Einstein. "Über einen die Erzeugung und Verwandlung des Lichtes betreffenden heuristischen Gesichtspunkt". In: *Annalen der Physik* 322 (1905), pp. 132–148. DOI: 10.1002/andp.19053220607.

[12] A. H. Compton. "A Quantum Theory of the Scattering of X-Rays by Light Elements". In: *Physical Review* 21.5 (May 1923), pp. 483–502. DOI: 10.1103/PhysRev.21.483.

[13] J. Schwinger. "On Quantum-Electrodynamics and the Magnetic Moment of the Electron". In: *Physical Review* 73 (Feb. 1948), pp. 416–417. DOI: 10.1103/PhysRev.73.416.

[14] S.-I. Tomonaga and J. R. Oppenheimer. "On Infinite Field Reactions in Quantum Field Theory". In: *Physical Review* 74 (1948), pp. 224–225. DOI: 10.1103/PhysRev.74.224.

[15] R. P. Feynman. "Space–Time Approach to Quantum Electrodynamics". In: *Physical Review* 76 (Sept. 1949), p. 769. DOI: 10.1103/PhysRev.76.769.

[16] J. Chadwick. "The Intensity Distribution in the Magnetic Spectrum of $\beta$ Particles from Radium (B + C)". In: *Verh. Phys. Gesell.* 16 (1914), pp. 383–391.

[17] W. Pauli. "Dear Radioactive Ladies and Gentlemen". In: *Physics Today* 31.9 (1978), p. 27.

[18] E. Fermi. "Tentativo di una teoria dell'Emissione dei raggi beta". In: *Ric. Sci.* 4 (1933), pp. 491–495.

[19] E. Fermi. "Versuch einer Theorie der $\beta$-Strahlen. I". In: *Zeitschrift für Physik* 88 (1934), pp. 161–177. DOI: 10.1007/BF01351864.

[20] J. Schwinger. "A theory of the fundamental interactions". In: *Annals of Physics* 2 (1957), pp. 407–434. DOI: 10.1016/0003-4916(57)90015-5.

[21] R. P. Feynman and M. Gell-Mann. "Theory of the Fermi Interaction". In: *Phys. Rev.* 109.1 (Jan. 1958), pp. 193–198. DOI: 10.1103/PhysRev.109.193.

[22] E. C. G. Sudarshan and R. E. Marshak. "Chirality Invariance and the Universal Fermi Interaction". In: *Phys. Rev.* 109.5 (Mar. 1958), pp. 1860–1862. DOI: 10.1103/PhysRev.109.1860.2.

[23] C. N. Yang and R. L. Mills. "Conservation of Isotopic Spin and Isotopic Gauge Invariance". In: *Physical Review* 96.1 (Oct. 1954), pp. 191–195. DOI: 10.1103/PhysRev.96.191.

[24] S. L. Glashow. "Partial-symmetries of weak interactions". In: *Nuclear Physics* 22 (1961), pp. 579–588. DOI: 10.1016/0029-5582(61)90469-2.

[25] F. Englert and R. Brout. "Broken Symmetry and the Mass of Gauge Vector Mesons". In: *Phys. Rev. Lett.* 13.9 (Aug. 1964), pp. 321–323. DOI: 10.1103/PhysRevLett.13.321.

[26] P. W. Higgs. "Broken symmetries, massless particles and gauge fields". In: *Physics Letters* 12.2 (1964), pp. 132–133. DOI: 10.1016/0031-9163(64)91136-9.

[27] P. W. Higgs. "Broken Symmetries and the Masses of Gauge Bosons". In: *Phys. Rev. Lett.* 13.16 (Oct. 1964), pp. 508–509. DOI: 10.1103/PhysRevLett.13.508.

[28] G. S. Guralnik, C. R. Hagen, and T. W. B. Kibble. "Global Conservation Laws and Massless Particles". In: *Phys. Rev. Lett.* 13.20 (Nov. 1964), pp. 585–587. DOI: 10.1103/PhysRevLett.13.585.

[29] S. Weinberg. "A Model of Leptons". In: *Phys. Rev. Lett.* 19 (21 Nov. 1967), pp. 1264–1266. DOI: 10.1103/PhysRevLett.19.1264.

[30] G. 't Hooft. "Renormalizable Lagrangians for massive Yang-Mills fields". In: *Nuclear Physics B* 35.1 (1971), pp. 167–188. DOI: 10.1016/0550-3213(71)90139-8.

[31] UA1 Collaboration. "Experimental observation of isolated large transverse energy electrons with associated missing energy at $s = 540$ GeV". In: *Physics Letters B* 122.1 (1983), pp. 103–116. DOI: 10.1016/0370-2693(83)91177-2.

[32] UA2 Collaboration. "Observation of single isolated electrons of high transverse momentum in events with missing transverse energy at the CERN pp collider". In: *Physics Letters B* 122.5 (1983), pp. 476–485. DOI: https://doi.org/10.1016/0370-2693(83)91605-2.

[33] UA1 Collaboration. "Experimental observation of lepton pairs of invariant mass around 95 GeV/$c^2$ at the CERN SPS collider". In: *Physics Letters B* 126.5 (1983), pp. 398–410. DOI: https://doi.org/10.1016/0370-2693(83)90188-0.

[34] UA2 Collaboration. "Evidence for $Z^0 \to e^+e^-$ at the CERN pp Collider". In: *Physics Letters B* 129.1 (1983), pp. 130–140. DOI: 10.1016/0370-2693(83)90744-X.

[35] H. Yukawa. "On the Interaction of Elementary Particles. I". In: *Progress of Theoretical Physics Supplement* 1 (1955), pp. 1–10. DOI: 10.1143/PTPS.1.1.

[36] M. Gell-Mann. *The Eightfold Way: A Theory of Strong Interaction Symmetry*. Tech. rep. California Institute of Technology, Mar. 1961. DOI: 10.2172/4008239.

[37] M. Gell-Mann. "A Schematic Model of Baryons and Mesons". In: *Phys. Lett.* 8 (1964), pp. 214–215. DOI: 10.1016/S0031-9163(64)92001-3.

[38] G. Zweig. *An SU(3) Model for Strong Interaction Symmetry and Its Breaking*. Tech. rep. An updated version is available as CERN-TH-412, Feb. 1964. Geneva: CERN, 1964. DOI: 10.17181/CERN-TH-401.

[39] O. W. Greenberg. "Spin and Unitary-Spin Independence in a Paraquark Model of Baryons and Mesons". In: *Phys. Rev. Lett.* 13.20 (Nov. 1964), pp. 598–602. DOI: 10.1103/PhysRevLett.13.598.

[40] G. Danby et al. "Observation of High-Energy Neutrino Reactions and the Existence of Two Kinds of Neutrinos". In: *Phys. Rev. Lett.* 9.1 (July 1962), pp. 36–44. DOI: 10.1103/PhysRevLett.9.36.

[41] J. D. Bjorken and S. L. Glashow. "Elementary Particles and SU(4)". In: *Phys. Lett.* 11 (1964), pp. 255–257. DOI: 10.1016/0031-9163(64)90433-0.

[42] S. L. Glashow, J. Iliopoulos, and L. Maiani. "Weak Interactions with Lepton-Hadron Symmetry". In: *Phys. Rev. D* 2.7 (Oct. 1970), pp. 1285–1292. DOI: 10.1103/PhysRevD.2.1285.

[43] J. J. Aubert et al. "Experimental Observation of a Heavy Particle $J$". In: *Phys. Rev. Lett.* 33.23 (Dec. 1974), pp. 1404–1406. DOI: 10.1103/PhysRevLett.33.1404.

[44] J.-E. Augustin et al. "Discovery of a Narrow Resonance in $e^+e^-$ Annihilation". In: *Phys. Rev. Lett.* 33.23 (Dec. 1974), pp. 1406–1408. DOI: 10.1103/PhysRevLett.33.1406.

[45] H. Fritzsch, M. Gell-Mann, and H. Leutwyler. "Advantages of the Color Octet Gluon Picture". In: *Phys. Lett. B* 47 (1973), pp. 365–368. DOI: 10.1016/0370-2693(73)90625-4.

[46] M. L. Perl et al. "Evidence for Anomalous Lepton Production in $e^+e^-$ Annihilation". In: *Phys. Rev. Lett.* 35.22 (Dec. 1975), pp. 1489–1492. DOI: 10.1103/PhysRevLett.35.1489.

[47] S. W. Herb et al. "Observation of a Dimuon Resonance at 9.5 GeV in 400-GeV Proton-Nucleus Collisions". In: *Phys. Rev. Lett.* 39.5 (Aug. 1977), pp. 252–255. DOI: 10.1103/PhysRevLett.39.252.

[48] C. Berger et al. "Observation of a Narrow Resonance Formed in $e^+e^-$ Annihilation at 9.46-GeV". In: *Phys. Lett. B* 76 (1978), pp. 243–245. DOI: 10.1016/0370-2693(78)90287-3.

[49] D0 Collaboration. "Observation of the Top Quark". In: *Phys. Rev. Lett.* 74 (14 Apr. 1995), pp. 2632–2637. DOI: 10.1103/PhysRevLett.74.2632.

[50] CDF Collaboration. "Observation of Top Quark Production in $\bar{p}p$ Collisions with the Collider Detector at Fermilab". In: *Phys. Rev. Lett.* 74 (14 Apr. 1995), pp. 2626–2631. DOI: 10.1103/PhysRevLett.74.2626.

[51] DONUT Collaboration. "Observation of tau neutrino interactions". In: *Phys. Lett. B* 504.3 (Apr. 2001), pp. 218–224. ISSN: 0370-2693. DOI: 10.1016/s0370-2693(01)00307-0. URL: http://dx.doi.org/10.1016/S0370-2693(01)00307-0.

[52] ATLAS Collaboration. "Observation of a new particle in the search for the Standard Model Higgs boson in proton–proton collisions at $\sqrt{s} = 7$ TeV with the ATLAS detector". In: *Phys. Lett. B* 716 (2012), pp. 1–29. DOI: 10.1016/j.physletb.2012.08.020.

[53] CMS Collaboration. "Observation of a new boson at a mass of 125 GeV with the CMS experiment at the LHC". In: *Phys. Lett. B* 716 (2012), pp. 30–61. DOI: 10.1016/j.physletb.2012.08.021.

[54] J. Ellis. "Higgs Physics". In: *2013 European School of High-Energy Physics*. 2015, pp. 117–168. DOI: 10.5170/CERN-2015-004.117. arXiv: 1312.5672 [hep-ph].

[55] Super-Kamiokande Collaboration. "Evidence for oscillation of atmospheric neutrinos". In: *Phys. Rev. Lett.* 81 (1998), pp. 1562–1567. DOI: 10.1103/PhysRevLett.81.1562. arXiv: hep-ex/9807003 [hep-ex].

[56] SNO Collaboration. "Measurement of the rate of $\nu_e + d \rightarrow p + p + e^-$ interactions produced by $^8$B solar neutrinos at the Sudbury Neutrino Observatory". In: *Phys. Rev. Lett.* 87 (2001), p. 071301. DOI: 10.1103/PhysRevLett.87.071301. arXiv: nucl-ex/0106015 [nucl-ex].

[57] SNO Collaboration. "Direct evidence for neutrino flavor transformation from neutral current interactions in the Sudbury Neutrino Observatory". In: *Phys. Rev. Lett.* 89 (2002), p. 011301. DOI: 10.1103/PhysRevLett.89.011301.

[58] V. Cirigliano et al. *Neutrinoless Double-Beta Decay: A Roadmap for Matching Theory to Experiment*. 2022. arXiv: 2203.12169 [hep-ph].

[59] F. Zwicky. "The Redshift of Extragalactic Nebulae". In: *General Relativity and Gravitation* 41 (2009). English translation and republication of the original 1933 paper in *Helv. Phys. Acta*, pp. 207–224. DOI: 10.1007/s10714-008-0707-4.

[60] V. C. Rubin and W. K. Jr. Ford. "Rotation of the Andromeda Nebula from a Spectroscopic Survey of Emission Regions". In: *Astrophysical Journal* 159 (1970), pp. 379–403. DOI: 10.1086/150317.

[61] K. C. Freeman. "On the Disks of Spiral and S%0 Galaxies". In: *Astrophysical Journal* 160 (1970), pp. 811–830. DOI: 10.1086/150474.

[62] V. C. Rubin, Jr. Ford W. K., and N. Thonnard. "Rotational Properties of 21 SC Galaxies with a Large Range of Luminosities and Radii, from NGC 4605 (R = 4 kpc) to UGC 2885 (R = 122 kpc)". In: *Astrophysical Journal* 238 (1980), pp. 471–487. DOI: 10.1086/158003.

[63] T. S. van Albada et al. "Distribution of dark matter in the spiral galaxy NGC 3198". In: *Astrophysical Journal* 295 (1985), pp. 305–313. DOI: 10.1086/163375.

[64] Adam G. Riess et al. "Observational evidence from supernovae for an accelerating universe and a cosmological constant". In: *Astron. J.* 116 (1998), pp. 1009–1038. DOI: 10.1086/300499. arXiv: astro-ph/9805201.

[65] S. Perlmutter et al. "Measurements of $\Omega$ and $\Lambda$ from 42 High Redshift Supernovae". In: *Astrophys. J.* 517 (1999), pp. 565–586. DOI: 10.1086/307221. arXiv: astro-ph/9812133.

[66] DESI Collaboration. *DESI DR2 Results II: Measurements of Baryon Acoustic Oscillations and Cosmological Constraints*. Part of the DESI Data Release 2 publication series. 2025. DOI: 10.48550/arXiv.2503.14738. arXiv: 2503.14738 [astro-ph.CO].

[67] P. Fayet. "Supersymmetry and Weak, Electromagnetic and Strong Interactions". In: *Phys. Lett. B* 64 (1976), pp. 159–162. DOI: 10.1016/0370-2693(76)90319-1.

[68] P. Fayet. "Spontaneously Broken Supersymmetric Theories of Weak, Electromagnetic and Strong Interactions". In: *Phys. Lett. B* 69 (1977), pp. 489–494. DOI: 10.1016/0370-2693(77)90852-8.

[69] H. P. Nilles. "Minimal Supersymmetric Standard Model and Grand Unification". In: *Theoretical Advanced Study Institute in Elementary Particle Physics (TASI 93): The Building Blocks of Creation — From Microfermius to Megaparsecs*. 1993.

[70] S. P. Martin. "A Supersymmetry Primer". In: *Perspectives on Supersymmetry*. World Scientific, July 1998, pp. 1–98. DOI: 10.1142/9789812839657_0001.

[71] ATLAS Collaboration. "ATLAS Run 2 searches for electroweak production of supersymmetric particles interpreted within the pMSSM". In: *JHEP* 05 (2024), p. 106. DOI: 10.1007/JHEP05(2024)106. arXiv: 2402.01392 [hep-ex].

[72] A. Djouadi et al. *The Minimal Supersymmetric Standard Model: Group Summary Report*. 1999. arXiv: hep-ph/9901246 [hep-ph].

[73] N. Arkani–Hamed, S. Dimopoulos, and G. Dvali. "The hierarchy problem and new dimensions at a millimeter". In: *Physics Letters B* 429.3–4 (June 1998), pp. 263–272. ISSN: 0370-2693. DOI: 10.1016/s0370-2693(98)00466-3.

[74] G. Aad et al. "Search for new phenomena in events with an energetic jet and missing transverse momentum in $pp$ collisions at $\sqrt{s}$ =13 TeV with the ATLAS detector". In: *Phys. Rev. D* 103.11 (2021), p. 112006. DOI: 10.1103/PhysRevD.103.112006. arXiv: 2102.10874 [hep-ex].

[75] CMS Collaboration. *Search for new physics in the final state of a single photon and large missing transverse energy in pp collisions at $\sqrt{s} = 13$ TeV (CMS-PAS-SUS-23-016)*. Preliminary result, 28 March 2025. Mar. 2025. URL: https://cms-results.web.cern.ch/cms-results/public-results/preliminary-results/SUS-23-016/index.html (visited on 09/26/2025).

[76] L. Randall and R. Sundrum. "Large Mass Hierarchy from a Small Extra Dimension". In: *Phys. Rev. Lett.* 83 (17 Oct. 1999), pp. 3370–3373. DOI: 10.1103/PhysRevLett.83.3370.

[77] H. Georgi and D. B. Kaplan. "Composite Higgs and Custodial SU(2)". In: *Physics Letters B* 145.3 (1984), pp. 216–220. DOI: 10.1016/0370-2693(84)90341-1.

[78] K. Agashe, R. Contino, and A. Pomarol. "The Minimal Composite Higgs Model". In: *Nuclear Physics B* 719 (2005), pp. 165–187. DOI: 10.1016/j.nuclphysb.2005.04.040. arXiv: hep-ph/0412089 [hep-ph].

[79] R. Contino, Y. Nomura, and A. Pomarol. "Higgs as a Holographic Pseudo-Goldstone Boson". In: *Nuclear Physics B* 671 (Nov. 2003), pp. 148–174. DOI: 10.1016/j.nuclphysb.2003.08.027.

[80] D. B. Kaplan. "Flavor at SSC Energies: A New Mechanism for Dynamically Generated Fermion Masses". In: *Nuclear Physics B* 365.2 (1991), pp. 259–278. DOI: 10.1016/S0550-3213(05)80021-5.

[81] A. Pomarol and F. Riva. "The Composite Higgs and Light Resonance Connection". In: *Journal of High Energy Physics* 2012.8 (Aug. 2012), p. 135. DOI: 10.1007/JHEP08(2012)135.

[82] C. K. Khosa and V. Sanz. "On the Impact of the LHC Run 2 Data on General Composite Higgs Scenarios". In: *arXiv preprint* (2021). arXiv: 2102.13429 [hep-ph].

[83] F. del Aguila and M. J. Bowick. "The Possibility of New Fermions with $\Delta I = 0$ Mass". In: *Nucl. Phys. B* 224 (1983), pp. 107–121. DOI: 10.1016/0550-3213(83)90316-4.

[84] P. M. Fishbane, R. E. Norton, and M. J. Rivard. "Experimental Implications of Heavy Isosinglet Quarks and Leptons". In: *Phys. Rev. D* 33 (1986), pp. 2632–2639. DOI: 10.1103/PhysRevD.33.2632.

[85] P. M. Fishbane and P. Q. Hung. "Lepton Masses in a Dynamical Model of Family Symmetry". In: *Z. Phys. C* 38 (1988), pp. 663–668. DOI: 10.1007/BF01624371.

[86] K. Fujikawa. "A Vector-like Extension of the Standard Model". In: *Prog. Theor. Phys.* 92 (1994), pp. 1149–1156. DOI: 10.1143/PTP.92.1149.

[87] P. Schwaller, T. M. P. Tait, and R. Vega-Morales. "Dark Matter and Vectorlike Leptons from Gauged Lepton Number". In: *Phys. Rev. D* 88.3 (2013), p. 035001. DOI: 10.1103/PhysRevD.88.035001.

[88] J. Halverson, N. Orlofsky, and A. Pierce. "Vectorlike Leptons as the Tip of the Dark Matter Iceberg". In: *Phys. Rev. D* 90.1 (2014), p. 015002. DOI: 10.1103/PhysRevD.90.015002.

[89] S. Bahrami et al. "Dark matter and collider studies in the left-right symmetric model with vectorlike leptons". In: *Phys. Rev. D* 95.9 (2017), p. 095024. DOI: 10.1103/PhysRevD.95.095024.

[90] S. Bhattacharya et al. "Mini Review on Vector-Like Leptonic Dark Matter, Neutrino Mass, and Collider Signatures". In: *Front. Phys.* 7 (2019), p. 80. DOI: 10.3389/fphy.2019.00080.

[91] K. Agashe, T. Okui, and R. Sundrum. "A Common Origin for Neutrino Anarchy and Charged Hierarchies". In: *Phys. Rev. Lett.* 102 (2009), p. 101801. DOI: 10.1103/PhysRevLett.102.101801. arXiv: 0810.1277 [hep-ph].

[92] M. Redi. "Leptons in Composite MFV". In: *JHEP* 09 (2013), p. 060. DOI: 10.1007/JHEP09(2013)060. arXiv: 1306.1525 [hep-ph].

[93] D. B. Kaplan and H. Georgi. "SU(2) $\times$ U(1) Breaking by Vacuum Misalignment". In: *Physics Letters B* 136.3 (1984). Published in Physics Letters B, Volume 136, Pages 183–186, 1984, pp. 183–186. DOI: 10.1016/0370-2693(84)91177-8.

[94] ATLAS Collaboration. "Exploration at the high-energy frontier: ATLAS Run 2 searches investigating the exotic jungle beyond the Standard Model". In: *Physics Reports* 1116 (2025), pp. 301–385. DOI: 10.1016/j.physrep.2024.10.001. arXiv: 2403.09292 [hep-ex].

[95] CMS Collaboration. "Review of searches for vector-like quarks, vector-like leptons, and heavy neutral leptons in proton-proton collisions at $\sqrt{s}$ = 13 TeV at the CMS Experiment". In: *Physics Reports* 1115 (2025), p. 570. DOI: 10.1016/j.physrep.2024.09.012. arXiv: 2405.17605 [hep-ex].

[96] A. Banerjee et al. "Vector-like quarks: status and new directions at the LHC". In: *SciPost Phys. Core* 7 (2024), p. 079. DOI: 10.21468/SciPostPhysCore.7.4.079. arXiv: 2406.09193 [hep-ph].

[97] T. Asaka, W. Buchmüller, and L. Covi. "Quarks and leptons between branes and bulk". In: *Physics Letters B* 563 (2003), pp. 209–216. DOI: 10.1016/S0370-2693(03)00944-0. arXiv: hep-ph/0304142 [hep-ph].

[98] F. Gürsey, P. Ramond, and P. Sikivie. "A universal gauge theory model based on $E_6$". In: *Physics Letters B* 60.2 (1976). Published in Physics Letters B, Volume 60, Pages 177-180, 1976, pp. 177–180. DOI: 10.1016/0370-2693(76)90417-2.

[99] T. Moroi and Y. Okada. "Radiative corrections to Higgs masses in the supersymmetric model with an extra family and antifamily". In: *Modern Physics Letters A* 7 (1992). Report No. TU-379, pp. 187–200. DOI: 10.1142/S0217732392000124.

[100] M. Endo et al. "Higgs mass and muon anomalous magnetic moment in supersymmetric models with vectorlike matters". In: *Physical Review D* 84 (2011), p. 075017. DOI: 10.1103/PhysRevD.84.075017. arXiv: 1108.3071 [hep-ph].

[101] E. Megias, M. Quiros, and L. Salas. "Muon $g-2$ from Vector-Like Leptons in Warped Space". In: *JHEP* 05 (2017), p. 016. DOI: 10.1007/JHEP05(2017)016. arXiv: 1701.05072 [hep-ph].

[102] J. Kawamura, S. Raby, and A. Trautner. "Complete Vectorlike Fourth Family and new $U(1)'$ for Muon Anomalies". In: *Phys. Rev. D* 100 (2019), p. 055030. DOI: 10.1103/PhysRevD.100.055030. arXiv: 1906.11297 [hep-ph].

[103] G. Hiller, D. Loose, and I. Söding. "Model Building from Asymptotic Safety with Higgs and Flavor Portals". In: *Phys. Rev. D* 102 (2020), p. 095023. DOI: 10.1103/PhysRevD.102.095023. arXiv: 2008.08606 [hep-ph].

[104] B. Abi et al. "Measurement of the Positive Muon Anomalous Magnetic Moment to 0.46 ppm". In: *Phys. Rev. Lett.* 126 (2021), p. 141801. DOI: 10.1103/PhysRevLett.126.141801. arXiv: 2104.03281 [hep-ex].

[105] Armen Tumasyan et al. "Inclusive nonresonant multilepton probes of new phenomena at $\sqrt{s}$=13 TeV". In: *Phys. Rev. D* 105.11 (2022), p. 112007. DOI: 10.1103/PhysRevD.105.112007. arXiv: 2202.08676 [hep-ex].

[106] H. Georgi and S. L. Glashow. "Unity of All Elementary-Particle Forces". In: *Physical Review Letters* 32.8 (Feb. 1974), pp. 438–441. DOI: 10.1103/PhysRevLett.32.438.

[107] H. Fritzsch and P. Minkowski. "Unified Interactions of Leptons and Hadrons". In: *Annals of Physics* 93 (1975), pp. 193–266. DOI: 10.1016/0003-4916(75)90211-0.

[108] S. Weinberg. "Supersymmetry at Ordinary Energies: Masses and Conservation Laws". In: *Physical Review D* 26.1 (July 1982), pp. 287–302. DOI: 10.1103/PhysRevD.26.287.

[109] G. R. Farrar and P. Fayet. "Phenomenology of the Production, Decay, and Detection of New Hadronic States Associated with Supersymmetry". In: *Physics Letters B* 76 (1978), pp. 575–579. DOI: 10.1016/0370-2693(78)90858-4.

[110] R. Barbier et al. "R-Parity Violating Supersymmetry". In: *Physics Reports* 420 (2005), pp. 1–202. DOI: 10.1016/j.physrep.2005.08.006. arXiv: hep-ph/0406039 [hep-ph].

[111] J. P. Lees et al. "Measurement of an Excess of $\bar{B} \to D^{(*)}\tau^-\bar{\nu}_\tau$ Decays and Implications for Charged Higgs Bosons". In: *Physical Review D* 88.7 (2013), p. 072012. DOI: 10.1103/PhysRevD.88.072012. arXiv: 1303.0571 [hep-ex].

[112] A. Bozek et al. "Observation of $B^+ \to \bar{D}^{*0}\tau^+\nu_\tau$ and Evidence for $B^+ \to \bar{D}^0\tau^+\nu_\tau$ at Belle". In: *Physical Review D* 82 (2010), p. 072005. DOI: 10.1103/PhysRevD.82.072005. arXiv: 1005.2302 [hep-ex].

[113] R. Aaij et al. "Measurement of the Ratios of Branching Fractions $\mathcal{R}(D^*)$ and $\mathcal{R}(D^0)$". In: *Physical Review Letters* 131 (2023), p. 111802. DOI: 10.1103/PhysRevLett.131.111802. arXiv: 2302.02886 [hep-ex].

[114] C. Cornella, J. Fuentes-Martin, and G. Isidori. "Revisiting the Vector Leptoquark Explanation of the B-Physics Anomalies". In: *Journal of High Energy Physics* 07 (2019), p. 168. DOI: 10.1007/JHEP07(2019)168. arXiv: 1903.11517 [hep-ph].

[115] A. Greljo, P. Stangl, and A. E. Thomsen. "A Model of Muon Anomalies". In: *Physics Letters B* 820 (2021), p. 136554. DOI: 10.1016/j.physletb.2021.136554. arXiv: 2103.13991 [hep-ph].

[116] Albert M Sirunyan et al. "Search for singly and pair-produced leptoquarks coupling to third-generation fermions in proton-proton collisions at s=13 TeV". In: *Phys. Lett. B* 819 (2021), p. 136446. DOI: 10.1016/j.physletb.2021.136446. arXiv: 2012.04178 [hep-ex].

[117] Georges Aad et al. "Search for pair production of scalar leptoquarks decaying into first- or second-generation leptons and top quarks in proton–proton collisions at $\sqrt{s}$ = 13 TeV with the ATLAS detector". In: *Eur. Phys. J. C* 81.4 (2021), p. 313. DOI: 10.1140/epjc/s10052-021-09009-8. arXiv: 2010.02098 [hep-ex].

[118] Georges Aad et al. "Search for pair production of third-generation scalar leptoquarks decaying into a top quark and a $\tau$-lepton in $pp$ collisions at $\sqrt{s}$ = 13 TeV with the ATLAS detector". In: *JHEP* 06 (2021), p. 179. DOI: 10.1007/JHEP06(2021)179. arXiv: 2101.11582 [hep-ex].

[119] L. R. Evans and P. Bryant. "LHC Machine". In: *Journal of Instrumentation* 3.08 (2008), S08001. DOI: 10.1088/1748-0221/3/08/S08001.

[120] CERN. *The accelerator complex*. 2025. URL: https://home.cern/science/accelerators/accelerator-complex.

[121] A. A. Alves et al. "The LHCb Detector at the LHC". In: *JINST* 3 (2008), S08005. DOI: 10.1088/1748-0221/3/08/S08005.

[122] E. Jans. "The LHCb detector". In: *Meeting of the Division of Particles and Fields of the American Physical Society (DPF 2009)*. 2009. arXiv: 0910.1740 [hep-ex].

[123] K. Aamodt et al. "The ALICE experiment at the CERN LHC". In: *JINST* 3 (2008), S08002. DOI: 10.1088/1748-0221/3/08/S08002.

[124] G. Aad et al. "The ATLAS Experiment at the CERN Large Hadron Collider". In: *JINST* 3 (2008), S08003. DOI: 10.1088/1748-0221/3/08/S08003.

[125] S. Chatrchyan et al. "The CMS Experiment at the CERN LHC". In: *JINST* 3 (2008), S08004. DOI: 10.1088/1748-0221/3/08/S08004.

[126] ATLAS Collaboration. *ATLAS event selection system readies for LHC Run 3*. 2022. URL: https://atlas.cern/updates/briefing/run-3-trigger.

[127] S. R. Davis. *Interactive Slice of the CMS detector*. 2016. URL: https://cds.cern.ch/record/2205172.

[128] G. Aad et al. "Search for chargino-neutralino production with mass splittings near the electroweak scale in three-lepton final states in $\sqrt{s}$=13 TeV $pp$ collisions with the ATLAS detector". In: *Phys. Rev.* D101.7 (2020), p. 072001. DOI: 10.1103/PhysRevD.101.072001. arXiv: 1912.08479 [hep-ex].

[129] J. Neyman and E. S. Pearson. "On the Problem of the Most Efficient Tests of Statistical Hypotheses". In: *Philosophical Transactions of the Royal Society of London. Series A, Containing Papers of a Mathematical or Physical Character* 231 (1933), pp. 289–337. DOI: 10.1098/rsta.1933.0009.

[130] S. S. Wilks. "The Large-Sample Distribution of the Likelihood Ratio for Testing Composite Hypotheses". In: *Annals of Mathematical Statistics* 9.1 (1938), pp. 60–62. DOI: 10.1214/aoms/1177732360.

[131] A. L. Read. "Presentation of search results: The $CL_s$ technique". In: *Journal of Physics G: Nuclear and Particle Physics* 28.10 (2002). Ed. by M. R. Whalley and L. Lyons, pp. 2693–2704. DOI: 10.1088/0954-3899/28/10/313.

[132] Joshua S. Speagle. *A Conceptual Introduction to Markov Chain Monte Carlo Methods*. Sept. 2019. arXiv: 1909.12313 [stat.OT].

[133] D. Gamerman and H. F. Lopes. *Markov Chain Monte Carlo: Stochastic Simulation for Bayesian Inference*. 2nd ed. Vol. 68. Texts in Statistical Science. Boca Raton, Florida, USA: Chapman & Hall/CRC, 2006.

[134] W. K. Hastings. "Monte Carlo Sampling Methods Using Markov Chains and Their Applications". In: *Biometrika* 57.1 (1970), pp. 97–109. DOI: 10.1093/biomet/57.1.97.

[135] N. Metropolis et al. "Equation of State Calculations by Fast Computing Machines". In: *The Journal of Chemical Physics* 21.6 (1953), pp. 1087–1092. DOI: 10.1063/1.1699114.

[136] J. Zhang, Y. Yang, and J. Ding. "Information Criteria for Model Selection". In: *Wiley Interdisciplinary Reviews: Computational Statistics* 15.5 (2023), e1607. DOI: 10.1002/wics.1607.

[137] H. Akaike. "Information Theory and an Extension of the Maximum Likelihood Principle". In: *Selected Papers of Hirotugu Akaike*. Ed. by Emanuel Parzen, Kunio Tanabe, and Genshiro Kitagawa. New York, NY: Springer New York, 1998, pp. 199–213. ISBN: 978-1-4612-1694-0. DOI: 10.1007/978-1-4612-1694-0_15.

[138] P. J. Green. "Reversible Jump Markov Chain Monte Carlo Computation and Bayesian Model Determination". In: *Biometrika* 82.4 (1995), pp. 711–732. ISSN: 0006-3444. DOI: 10.2307/2337340.

[139] D. I. Hastie and P. J. Green. "Model choice using reversible jump Markov chain Monte Carlo". In: *Statistica Neerlandica* 66.3 (2012), pp. 309–338. DOI: 10.1111/j.1467-9574.2012.00516.x.

[140] S. Chatrchyan et al. "Interpretation of Searches for Supersymmetry with Simplified Models". In: *Phys. Rev. D* 88.5 (2013), p. 052017. DOI: 10.1103/PhysRevD.88.052017. arXiv: 1301.2175 [hep-ex].

[141] J. Alwall, P. Schuster, and N. Toro. "Simplified Models for a First Characterization of New Physics at the LHC". In: *Physical Review D* 79.7 (2009), p. 075020. DOI: 10.1103/PhysRevD.79.075020. arXiv: 0810.3921 [hep-ph].

[142] LHC New Physics Working Group Collaboration, Daniel Alves, et al. "Simplified Models for LHC New Physics Searches". In: *Journal of Physics G* 39.10 (2012), p. 105005. DOI: 10.1088/0954-3899/39/10/105005. arXiv: 1105.2838 [hep-ph].

[143] A. Tumasyan et al. "Search for electroweak production of charginos and neutralinos at s=13TeV in final states containing hadronic decays of WW, WZ, or WH and missing transverse momentum". In: *Phys. Lett. B* 842 (2023), p. 137460. DOI: 10.1016/j.physletb.2022.137460. arXiv: 2205.09597 [hep-ex].

[144] P. Z. Skands et al. "SUSY Les Houches Accord: Interfacing SUSY spectrum calculators, decay packages, and event generators". In: *JHEP* 07 (July 2004), p. 036. DOI: 10.1088/1126-6708/2004/07/036. arXiv: hep-ph/0311123.

[145] J. Alwall et al. "A Standard format for Les Houches event files". In: *Comput. Phys. Commun.* 176 (Mar. 2007), pp. 300–304. DOI: 10.1016/j.cpc.2006.11.010. arXiv: hep-ph/0609017.

[146] M. M. Altakach et al. "SModelS v3: going beyond Z2 topologies". In: *JHEP* 11 (2024), p. 074. DOI: 10.1007/JHEP11(2024)074. arXiv: 2409.12942.

[147] G. Cowan et al. "Asymptotic formulae for likelihood-based tests of new physics". In: *Eur. Phys. J. C* 71 (2011), p. 1554. DOI: 10.1140/epjc/s10052-011-1554-0. arXiv: 1007.1727.

[148] CMS Collaboration. *Simplified likelihood for the re-interpretation of public CMS results*. CMS Note CMS-NOTE-2017-001. Geneva: CERN, 2017. URL: https://cds.cern.ch/record/2242860.

[149] A. Buckley et al. "The Simplified Likelihood Framework". In: *JHEP* 04 (2019), p. 064. DOI: 10.1007/JHEP04(2019)064. arXiv: 1809.05548 [hep-ph].

[150] W. Ford. "Reproducing a CMS higgsino search from public data". Talk at the 7th workshop of the LHC Reinterpretation Forum, CERN, 12–15 Dec 2022. 2022. URL: https://indico.cern.ch/event/1197680/contributions/5164689/.

[151] K. Cranmer et al. *HistFactory: A tool for creating statistical models for use with RooFit and RooStats*. Tech. rep. CERN-OPEN-2012-016. CERN, June 2012.

[152] G. Alguero, S. Kraml, and W. Waltenberger. "A SModelS interface for pyhf likelihoods". In: *Comput. Phys. Commun.* 264 (2021), p. 107909. DOI: 10.1016/j.cpc.2021.107909. arXiv: 2009.01809.

[153] L. Heinrich et al. "pyhf: pure-Python implementation of HistFactory statistical models". In: *J. Open Source Softw.* 6.58 (2021), p. 2823. DOI: 10.21105/joss.02823.

[154] ATLAS Collaboration. *Implementation of simplified likelihoods in HistFactory for searches for supersymmetry*. Tech. rep. ATL-PHYS-PUB-2021-038. CERN, 2021.

[155] E. Schanet. *simplify: v0.1.6*. https://github.com/eschanet/simplify. Accessed: 2025-06-14. 2022.

[156] G. Aad et al. "Searches for electroweak production of supersymmetric particles with compressed mass spectra in $\sqrt{s} = 13$ TeV $pp$ collisions with the ATLAS

detector". In: *Phys. Rev. D* 101.5 (2020), p. 052005. DOI: 10.1103/PhysRevD.101.052005. arXiv: 1911.12606 [hep-ex].

[157] G. Aad et al. "Search for direct production of electroweakinos in final states with one lepton, missing transverse momentum and a Higgs boson decaying into two $b$-jets in $pp$ collisions at $\sqrt{s} = 13$ TeV with the ATLAS detector". In: *Eur. Phys. J. C* 80.8 (2020), p. 691. DOI: 10.1140/epjc/s10052-020-8050-3. arXiv: 1909.09226 [hep-ex].

[158] G. Aad et al. "Search for chargino–neutralino pair production in final states with three leptons and missing transverse momentum in $\sqrt{s} = 13$ TeV $pp$ collisions with the ATLAS detector". In: *Eur. Phys. J. C* 81.12 (2021), p. 1118. DOI: 10.1140/epjc/s10052-021-09749-7. arXiv: 2106.01676 [hep-ex].

[159] J. Y. Araz et al. "Strength in numbers: optimal and scalable combination of LHC new-physics searches". In: *SciPost Phys.* 14.4 (2023), p. 077. DOI: 10.21468/SciPostPhys.14.4.077. arXiv: 2209.00025 [hep-ph].

[160] G. Aad et al. "Summary of the ATLAS experiment's sensitivity to supersymmetry after LHC Run 1 – interpreted in the phenomenological MSSM". In: *JHEP* 10 (2015), p. 134. DOI: 10.1007/JHEP10(2015)134. arXiv: 1508.06608 [hep-ex].

[161] CMS Collaboration. *Phenomenological MSSM interpretation of the CMS 7 and 8 TeV results*. CMS Physics Analysis Summary CMS-PAS-SUS-13-020. Preliminary results. Geneva: CERN, 2014. URL: https://cms-results.web.cern.ch/cms-results/public-results/preliminary-results/SUS-13-020/index.html.

[162] The GAMBIT Collaboration. "A global fit of the MSSM with GAMBIT". In: *Eur. Phys. J. C* 77.12 (2017), p. 879. DOI: 10.1140/epjc/s10052-017-5196-8. arXiv: 1705.07917 [hep-ph].

[163] P. Athron et al. "Combined collider constraints on neutralinos and charginos". In: *Eur. Phys. J. C* 79.5 (2019), p. 395. DOI: 10.1140/epjc/s10052-019-6837-x. arXiv: 1809.02097 [hep-ph].

[164] V. Ananyev et al. "Collider constraints on electroweakinos in the presence of a light gravitino". In: *Eur. Phys. J. C* 83.6 (2023), p. 493. DOI: 10.1140/epjc/s10052-023-11574-z. arXiv: 2303.09082 [hep-ph].

[165] A. Kvellestad, P. Scott, and M. White. "GAMBIT and its Application in the Search for Physics Beyond the Standard Model". In: *Prog. Part. Nucl. Phys.* (2020). DOI: 10.1016/j.ppnp.2020.103769. arXiv: 1912.04079 [hep-ph].

[166] M. M. Altakach et al. "Global LHC constraints on electroweak-inos with SModelS v2.3". In: *SciPost Phys.* 16.4 (2024), p. 101. DOI: 10.21468/SciPostPhys.16.4.101. arXiv: 2312.16635 [hep-ph].

[167] CMS Collaboration et al. "Search for Supersymmetry in Proton-Proton Collisions at 13 TeV in Final States with Jets and Missing Transverse Momentum". In: *Journal of High Energy Physics* 2019.10 (2019), p. 244. DOI: 10.1007/JHEP10(2019)244. arXiv: 1908.04722 [hep-ex].

[168] T. Sjöstrand et al. "An introduction to PYTHIA 8.2". In: *Comput. Phys. Commun.* 191 (2015), pp. 159–177. DOI: 10.1016/j.cpc.2015.01.024. arXiv: 1410.3012 [hep-ph].

[169] W. Beenakker et al. "Squark and gluino production at hadron colliders". In: *Nucl.Phys.* B492 (1997), pp. 51–103. DOI: 10.1016/S0550-3213(97)80027-2. arXiv: hep-ph/9610490 [hep-ph].

[170] W. Beenakker et al. "Stop production at hadron colliders". In: *Nucl.Phys.* B515 (1998), pp. 3–14. DOI: 10.1016/S0550-3213(98)00014-5. arXiv: hep-ph/9710451 [hep-ph].

[171] A. Kulesza and L. Motyka. "Threshold resummation for squark-antisquark and gluino-pair production at the LHC". In: *Phys.Rev.Lett.* 102 (2009), p. 111802. DOI: 10.1103/PhysRevLett.102.111802. arXiv: 0807.2405 [hep-ph].

[172] A. Kulesza and L. Motyka. "Soft gluon resummation for the production of gluino-gluino and squark-antisquark pairs at the LHC". In: *Phys.Rev.* D80 (2009), p. 095004. DOI: 10.1103/PhysRevD.80.095004. arXiv: 0905.4749 [hep-ph].

[173] W. Beenakker et al. "Soft-gluon resummation for squark and gluino hadroproduction". In: *JHEP* 0912 (2009), p. 041. DOI: 10.1088/1126-6708/2009/12/041. arXiv: 0909.4418 [hep-ph].

[174] W. Beenakker et al. "Supersymmetric top and bottom squark production at hadron colliders". In: *JHEP* 1008 (2010), p. 098. DOI: 10.1007/JHEP08(2010)098. arXiv: 1006.4771 [hep-ph].

[175] W. Beenakker et al. "Squark and Gluino Hadroproduction". In: *Int.J.Mod.Phys.* A26 (2011), pp. 2637–2664. DOI: 10.1142/S0217751X11053560. arXiv: 1105.1110 [hep-ph].

[176] W. Beenakker et al. "NLO+NLL squark and gluino production cross-sections with threshold-improved parton distributions". In: *Eur. Phys. J.* C76.2 (2016), p. 53. DOI: 10.1140/epjc/s10052-016-3892-4. arXiv: 1510.00375 [hep-ph].

[177] Aleksandr Azatov, Roberto Contino, and Jamison Galloway. "Model-Independent Bounds on a Light Higgs". In: *JHEP* 04 (2012). [Erratum: JHEP 04, 140 (2013)], p. 127. DOI: 10.1007/JHEP04(2012)127. arXiv: 1202.3415 [hep-ph].

[178] D. W. Scott. *Multivariate Density Estimation: Theory, Practice, and Visualization*. 2nd ed. New York, Chichester: John Wiley & Sons, 2015.

[179] A. M. Sirunyan et al. "Search for supersymmetric partners of electrons and muons in proton-proton collisions at $\sqrt{s} = 13$ TeV". In: *Phys. Lett.* B790 (2019), pp. 140–166. DOI: 10.1016/j.physletb.2019.01.005. arXiv: 1806.05264 [hep-ex].

[180] M. Aaboud et al. "Search for electroweak production of supersymmetric particles in final states with two or three leptons at $\sqrt{s} = 13$ TeV with the ATLAS detector". In: *Eur. Phys. J.* C78.12 (2018), p. 995. DOI: 10.1140/epjc/s10052-018-6423-7. arXiv: 1803.02762 [hep-ex].

[181] G. Aad et al. "Search for squarks and gluinos with the ATLAS detector in final states with jets and missing transverse momentum using $\sqrt{s} = 8$ TeV proton–proton collision data". In: *JHEP* 09 (2014), p. 176. DOI: 10.1007/JHEP09(2014)176. arXiv: 1405.7875 [hep-ex].

[182] M. Aaboud et al. "Search for squarks and gluinos in final states with jets and missing transverse momentum using 36 fb$^{-1}$ of $\sqrt{s} = 13$ TeV pp collision data with the ATLAS detector". In: *Phys. Rev.* D97.11 (2018), p. 112001. DOI: 10.1103/PhysRevD.97.112001. arXiv: 1712.02332 [hep-ex].

[183] M. Aaboud et al. "Search for top-squark pair production in final states with one lepton, jets, and missing transverse momentum using 36 fb$^{-1}$ of $\sqrt{s} = 13$ TeV pp collision data with the ATLAS detector". In: *JHEP* 06 (2018), p. 108. DOI: 10.1007/JHEP06(2018)108. arXiv: 1711.11520 [hep-ex].

[184] S. Chatrchyan et al. "Search for new physics in the multijet and missing transverse momentum final state in proton-proton collisions at $\sqrt{s}$= 8 TeV". In: *JHEP* 06 (2014), p. 055. DOI: 10.1007/JHEP06(2014)055. arXiv: 1402.4770 [hep-ex].

[185] A. M. Sirunyan et al. "Search for supersymmetry in proton-proton collisions at 13 TeV using identified top quarks". In: *Phys. Rev. D* 97.1 (2018), p. 012007. DOI: 10.1103/PhysRevD.97.012007. arXiv: 1710.11188 [hep-ex].

[186] A. M. Sirunyan et al. "Search for supersymmetry in multijet events with missing transverse momentum in proton-proton collisions at 13 TeV". In: *Phys. Rev.*

D96.3 (2017), p. 032003. DOI: 10.1103/PhysRevD.96.032003. arXiv: 1704.07781 [hep-ex].

[187] A. M. Sirunyan et al. "Search for new phenomena with the $M_{T2}$ variable in the all-hadronic final state produced in proton–proton collisions at $\sqrt{s} = 13$ TeV". In: *Eur. Phys. J.* C77.10 (2017), p. 710. DOI: 10.1140/epjc/s10052-017-5267-x. arXiv: 1705.04650 [hep-ex].

[188] A. M. Sirunyan et al. "Search for supersymmetry in proton-proton collisions at 13 TeV in final states with jets and missing transverse momentum". In: *JHEP* 10 (2019), p. 244. DOI: 10.1007/JHEP10(2019)244. arXiv: 1908.04722 [hep-ex].

[189] A. M. Sirunyan et al. "Search for top squark pair production in pp collisions at $\sqrt{s} = 13$ TeV using single lepton events". In: *JHEP* 10 (2017), p. 019. DOI: 10.1007/JHEP10(2017)019. arXiv: 1706.04402 [hep-ex].

[190] G. Aad et al. "Searches for electroweak production of supersymmetric particles with compressed mass spectra in $\sqrt{s} = 13$ TeV $pp$ collisions with the ATLAS detector". In: *Phys. Rev. D* 101.5 (2020), p. 052005. DOI: 10.1103/PhysRevD.101.052005. arXiv: 1911.12606 [hep-ex].

[191] G. Aad et al. "Search for chargino–neutralino pair production in final states with three leptons and missing transverse momentum in $\sqrt{s} = 13$ TeV pp collisions with the ATLAS detector". In: *Eur. Phys. J. C* 81.12 (2021), p. 1118. DOI: 10.1140/epjc/s10052-021-09749-7. arXiv: 2106.01676 [hep-ex].

[192] A. Tumasyan et al. "Search for supersymmetry in final states with two or three soft leptons and missing transverse momentum in proton-proton collisions at $\sqrt{s} = 13$ TeV". In: (Nov. 2021). arXiv: 2111.06296 [hep-ex].

[193] A. Tumasyan et al. "Search for electroweak production of charginos and neutralinos in proton-proton collisions at $\sqrt{s} = 13$ TeV". In: *JHEP* 04 (2022), p. 147. DOI: 10.1007/JHEP04(2022)147. arXiv: 2106.14246 [hep-ex].

[194] A. Tumasyan et al. "Search for new particles in events with energetic jets and large missing transverse momentum in proton-proton collisions at $\sqrt{s} = 13$ TeV". In: *JHEP* 11 (2021), p. 153. DOI: 10.1007/JHEP11(2021)153. arXiv: 2107.13021 [hep-ex].

[195] D. Agin et al. "Monojets reveal overlapping excesses for light compressed higgsinos". In: *Phys. Lett. B* 853 (2024), p. 138597. DOI: 10.1016/j.physletb.2024.138597. arXiv: 2311.17149 [hep-ph].

[196] D. Agin et al. "Seeking a coherent explanation of LHC excesses for compressed spectra". In: *Eur. Phys. J. C* 84.11 (2024), p. 1218. DOI: 10.1140/epjc/s10052-024-13594-9. arXiv: 2404.12423 [hep-ph].

[197] B. Fuks, M. D. Goodsell, and T. Murphy. "Monojets from compressed weak frustrated dark matter". In: *Phys. Rev. D* 111.5 (2025), p. 055010. DOI: 10.1103/PhysRevD.111.055010. arXiv: 2409.03014 [hep-ph].

[198] D. Agin et al. "A joint explanation for the soft lepton and monojet LHC excesses in the wino-bino model". In: *The European Physical Journal C* (June 2025). DOI: 10.1140/epjc/s10052-025-14886-4. arXiv: 2506.21676 [hep-ph].

[199] A. Hayrapetyan et al. "Search for supersymmetry in final states with disappearing tracks in proton-proton collisions at $\sqrt{s} = 13$ TeV". In: *Phys. Rev. D* 109.7 (2024), p. 072007. DOI: 10.1103/PhysRevD.109.072007. arXiv: 2309.16823 [hep-ex].

[200] LHC SUSY Cross Section Working Group. *LHC SUSY Cross Section Working Group: SUSY Cross Sections*. n.d. URL: https://twiki.cern.ch/twiki/bin/view/LHCPhysics/SUSYCrossSections (visited on 08/27/2025).

[201] H. E. Haber and G. L. Kane. "The Search for Supersymmetry: Probing Physics Beyond the Standard Model". In: *Physics Reports* 117 (1985), pp. 75–263. DOI: 10.1016/0370-1573(85)90051-1.

[202] G. Aad et al. "Search for $t\bar{t}$ resonances in fully hadronic final states in $pp$ collisions at $\sqrt{s}$ = 13 TeV with the ATLAS detector". In: *JHEP* 10 (2020), p. 061. DOI: 10.1007/JHEP10(2020)061. arXiv: 2005.05138 [hep-ex].

[203] G. Aad et al. "Search for new resonances in mass distributions of jet pairs using 139 fb$^{-1}$ of $pp$ collisions at $\sqrt{s} = 13$ TeV with the ATLAS detector". In: *JHEP* 03 (2020), p. 145. DOI: 10.1007/JHEP03(2020)145. arXiv: 1910.08447 [hep-ex].

[204] M. Aaboud et al. "Search for bottom squark pair production in proton–proton collisions at $\sqrt{s} = 13$ TeV with the ATLAS detector". In: *Eur. Phys. J.* C76.10 (2016), p. 547. DOI: 10.1140/epjc/s10052-016-4382-4. arXiv: 1606.08772 [hep-ex].

[205] M. Aaboud et al. "Search for top squarks in final states with one isolated lepton, jets, and missing transverse momentum in $\sqrt{s} = 13$ TeV $pp$ collisions with the ATLAS detector". In: *Phys. Rev.* D94.5 (2016), p. 052009. DOI: 10.1103/PhysRevD.94.052009. arXiv: 1606.03903 [hep-ex].

[206] M. Aaboud et al. "Search for squarks and gluinos in final states with jets and missing transverse momentum at $\sqrt{s} = 13$ TeV with the ATLAS detector". In: *Eur. Phys. J.* C76.7 (2016), p. 392. DOI: 10.1140/epjc/s10052-016-4184-8. arXiv: 1605.03814 [hep-ex].

[207] G. Aad et al. "Search for supersymmetry at $\sqrt{s} = 13$ TeV in final states with jets and two same-sign leptons or three leptons with the ATLAS detector". In: *Eur. Phys. J.* C76.5 (2016), p. 259. DOI: 10.1140/epjc/s10052-016-4095-8. arXiv: 1602.09058 [hep-ex].

[208] M. Aaboud et al. "Search for long-lived charginos based on a disappearing-track signature in pp collisions at $\sqrt{s} = 13$ TeV with the ATLAS detector". In: *JHEP* 06 (2018), p. 022. DOI: 10.1007/JHEP06(2018)022. arXiv: 1712.02118 [hep-ex].

[209] M. Aaboud et al. "Search for long-lived, massive particles in events with displaced vertices and missing transverse momentum in $\sqrt{s}$ = 13 TeV $pp$ collisions with the ATLAS detector". In: *Phys. Rev.* D97.5 (2018), p. 052012. DOI: 10.1103/PhysRevD.97.052012. arXiv: 1710.04901 [hep-ex].

[210] M. Aaboud et al. "Search for supersymmetry in final states with two same-sign or three leptons and jets using 36 fb$^{-1}$ of $\sqrt{s} = 13$ TeV $pp$ collision data with the ATLAS detector". In: *JHEP* 09 (2017). [Erratum: JHEP08,121(2019)], p. 084. DOI: 10.1007/JHEP09(2017)084, 10.1007/JHEP08(2019)121. arXiv: 1706.03731 [hep-ex].

[211] M. Aaboud et al. "Search for a scalar partner of the top quark in the jets plus missing transverse momentum final state at $\sqrt{s}$=13 TeV with the ATLAS detector". In: *JHEP* 12 (2017), p. 085. DOI: 10.1007/JHEP12(2017)085. arXiv: 1709.04183 [hep-ex].

[212] M. Aaboud et al. "Search for direct top squark pair production in final states with two leptons in $\sqrt{s} = 13$ TeV $pp$ collisions with the ATLAS detector". In: *Eur. Phys. J.* C77.12 (2017), p. 898. DOI: 10.1140/epjc/s10052-017-5445-x. arXiv: 1708.03247 [hep-ex].

[213] M. Aaboud et al. "Search for top squarks decaying to tau sleptons in $pp$ collisions at $\sqrt{s} = 13$ TeV with the ATLAS detector". In: *Phys. Rev.* D98.3 (2018), p. 032008. DOI: 10.1103/PhysRevD.98.032008. arXiv: 1803.10178 [hep-ex].

[214] M. Aaboud et al. "Search for supersymmetry in final states with charm jets and missing transverse momentum in 13 TeV $pp$ collisions with the ATLAS

detector". In: *JHEP* 09 (2018), p. 050. DOI: 10.1007/JHEP09(2018)050. arXiv: 1805.01649 [hep-ex].

[215] M. Aaboud et al. "Search for photonic signatures of gauge-mediated supersymmetry in 13 TeV $pp$ collisions with the ATLAS detector". In: *Phys. Rev.* D97.9 (2018), p. 092006. DOI: 10.1103/PhysRevD.97.092006. arXiv: 1802.03158 [hep-ex].

[216] M. Aaboud et al. "Search for supersymmetry in events with $b$-tagged jets and missing transverse momentum in $pp$ collisions at $\sqrt{s} = 13$ TeV with the ATLAS detector". In: *JHEP* 11 (2017), p. 195. DOI: 10.1007/JHEP11(2017)195. arXiv: 1708.09266 [hep-ex].

[217] M. Aaboud et al. "Search for heavy charged long-lived particles in the ATLAS detector in 36.1 fb$^{-1}$ of proton-proton collision data at $\sqrt{s} = 13$ TeV". In: *Phys. Rev.* D99.9 (2019), p. 092007. DOI: 10.1103/PhysRevD.99.092007. arXiv: 1902.01636 [hep-ex].

[218] M. Aaboud et al. "Search for new phenomena using the invariant mass distribution of same-flavour opposite-sign dilepton pairs in events with missing transverse momentum in $\sqrt{s} = 13$ TeV pp collisions with the ATLAS detector". In: *Eur. Phys. J.* C78.8 (2018), p. 625. DOI: 10.1140/epjc/s10052-018-6081-9. arXiv: 1805.11381 [hep-ex].

[219] M. Aaboud et al. "Search for chargino and neutralino production in final states with a Higgs boson and missing transverse momentum at $\sqrt{s} = 13$ TeV with the ATLAS detector". In: *Phys. Rev.* D100.1 (2019), p. 012006. DOI: 10.1103/PhysRevD.100.012006. arXiv: 1812.09432 [hep-ex].

[220] M. Aaboud et al. "Search for pair production of higgsinos in final states with at least three $b$-tagged jets in $\sqrt{s} = 13$ TeV $pp$ collisions using the ATLAS detector". In: *Phys. Rev.* D98.9 (2018), p. 092002. DOI: 10.1103/PhysRevD.98.092002. arXiv: 1806.04030 [hep-ex].

[221] M. Aaboud et al. "Search for chargino-neutralino production using recursive jigsaw reconstruction in final states with two or three charged leptons in proton-proton collisions at $\sqrt{s} = 13$ TeV with the ATLAS detector". In: *Phys. Rev.* D98.9 (2018), p. 092012. DOI: 10.1103/PhysRevD.98.092012. arXiv: 1806.02293 [hep-ex].

[222] G. Aad et al. "Search for direct stau production in events with two hadronic $\tau$-leptons in $\sqrt{s} = 13$ TeV $pp$ collisions with the ATLAS detector". In: *Phys. Rev.* D101.3 (2020), p. 032009. DOI: 10.1103/PhysRevD.101.032009. arXiv: 1911.06660 [hep-ex].

[223] G. Aad et al. "Searches for new phenomena in events with two leptons, jets, and missing transverse momentum in 139 fb$^{-1}$ of $\sqrt{s} = 13$ TeV $pp$ collisions with the ATLAS detector". In: *Eur. Phys. J. C* 83.6 (2023), p. 515. arXiv: 2204.13072 [hep-ex].

[224] G. Aad et al. "Search for new phenomena in events with two opposite-charge leptons, jets and missing transverse momentum in pp collisions at $\sqrt{s}$ = 13 TeV with the ATLAS detector". In: *JHEP* 04 (2021), p. 165. DOI: 10.1007/JHEP04(2021)165. arXiv: 2102.01444 [hep-ex].

[225] G. Aad et al. "Search for squarks and gluinos in final states with same-sign leptons and jets using 139 fb$^{-1}$ of data collected with the ATLAS detector". In: *JHEP* 06 (2020), p. 046. DOI: 10.1007/JHEP06(2020)046. arXiv: 1909.08457 [hep-ex].

[226] G. Aad et al. "Search for squarks and gluinos in final states with one isolated lepton, jets, and missing transverse momentum at $\sqrt{s} = 13$ with the ATLAS

detector". In: *Eur. Phys. J. C* 81.7 (2021), p. 600. DOI: 10.1140/epjc/s10052-021-09344-w. arXiv: 2101.01629 [hep-ex].

[227] G. Aad et al. "Search for a scalar partner of the top quark in the all-hadronic $t\bar{t}$ plus missing transverse momentum final state at $\sqrt{s} = 13$ TeV with the ATLAS detector". In: *Eur. Phys. J. C* 80.8 (2020), p. 737. DOI: 10.1140/epjc/s10052-020-8102-8. arXiv: 2004.14060 [hep-ex].

[228] G. Aad et al. "Search for long-lived, massive particles in events with displaced vertices and multiple jets in pp collisions at $\sqrt{s}$ = 13 TeV with the ATLAS detector". In: *JHEP* 06 (2023), p. 200. DOI: 10.1007/JHEP06(2023)200. arXiv: 2301.13866 [hep-ex].

[229] G. Aad et al. "Search for Displaced Leptons in $\sqrt{s} = 13$ TeV $pp$ Collisions with the ATLAS Detector". In: *Phys. Rev. Lett.* 127.5 (2021), p. 051802. DOI: 10.1103/PhysRevLett.127.051802. arXiv: 2011.07812 [hep-ex].

[230] G. Aad et al. "Search for squarks and gluinos in final states with jets and missing transverse momentum using 139 fb$^{-1}$ of $\sqrt{s}$ =13 TeV $pp$ collision data with the ATLAS detector". In: *JHEP* 02 (2021), p. 143. DOI: 10.1007/JHEP02(2021)143. arXiv: 2010.14293 [hep-ex].

[231] G. Aad et al. "Search for direct production of electroweakinos in final states with missing transverse momentum and a Higgs boson decaying into photons in pp collisions at $\sqrt{s}$ = 13 TeV with the ATLAS detector". In: *JHEP* 10 (2020), p. 005. DOI: 10.1007/JHEP10(2020)005. arXiv: 2004.10894 [hep-ex].

[232] G. Aad et al. "Search for bottom-squark pair production with the ATLAS detector in final states containing Higgs bosons, $b$-jets and missing transverse momentum". In: *JHEP* 12 (2019), p. 060. DOI: 10.1007/JHEP12(2019)060. arXiv: 1908.03122 [hep-ex].

[233] G. Aad et al. "Search for electroweak production of charginos and sleptons decaying into final states with two leptons and missing transverse momentum in $\sqrt{s} = 13$ TeV $pp$ collisions using the ATLAS detector". In: *Eur. Phys. J.* C80.2 (2020), p. 123. DOI: 10.1140/epjc/s10052-019-7594-6. arXiv: 1908.08215 [hep-ex].

[234] G. Aad et al. "Search for long-lived, massive particles in events with a displaced vertex and a muon with large impact parameter in $pp$ collisions at $\sqrt{s} = 13$ TeV with the ATLAS detector". In: *Phys. Rev. D* 102.3 (2020), p. 032006. DOI: 10.1103/PhysRevD.102.032006. arXiv: 2003.11956 [hep-ex].

[235] G. Aad et al. "Search for bottom-squark pair production in $pp$ collision events at $\sqrt{s} = 13$ TeV with hadronically decaying $\tau$-leptons, $b$-jets and missing transverse momentum using the ATLAS detector". In: *Phys. Rev. D* 104.3 (2021), p. 032014. DOI: 10.1103/PhysRevD.104.032014. arXiv: 2103.08189 [hep-ex].

[236] G. Aad et al. "Search for charginos and neutralinos in final states with two boosted hadronically decaying bosons and missing transverse momentum in $pp$ collisions at $\sqrt{s}$ = 13 TeV with the ATLAS detector". In: *Phys. Rev. D* 104.11 (2021), p. 112010. DOI: 10.1103/PhysRevD.104.112010. arXiv: 2108.07586 [hep-ex].

[237] G. Aad et al. "Search for heavy, long-lived, charged particles with large ionisation energy loss in $pp$ collisions at $\sqrt{s} = 13$ TeV using the ATLAS experiment and the full Run 2 dataset". In: *JHEP* 2306 (2023), p. 158. DOI: 10.1007/JHEP06(2023)158. arXiv: 2205.06013 [hep-ex].

[238] G. Aad et al. "Search for direct pair production of sleptons and charginos decaying to two leptons and neutralinos with mass splittings near the $W$-boson mass in $\sqrt{s} = 13$ TeV $pp$ collisions with the ATLAS detector". In: *JHEP* 06 (2023), p. 031. DOI: 10.1007/JHEP06(2023)031. arXiv: 2209.13935 [hep-ex].

[239] G. Aad et al. "Search for direct production of electroweakinos in final states with one lepton, missing transverse momentum and a Higgs boson decaying into two $b$-jets in $pp$ collisions at $\sqrt{s} = 13$ TeV with the ATLAS detector". In: *Eur. Phys. J.* C80.8 (2020), p. 691. DOI: 10.1140/epjc/s10052-020-8050-3. arXiv: 1909.09226 [hep-ex].

[240] A. M. Sirunyan et al. "Search for long-lived particles using nonprompt jets and missing transverse momentum with proton-proton collisions at $\sqrt{s} = 13$ TeV". In: *Phys. Lett.* B797 (2019), p. 134876. DOI: 10.1016/j.physletb.2019.134876. arXiv: 1906.06441 [hep-ex].

[241] A. M. Sirunyan et al. "Search for disappearing tracks in proton-proton collisions at $\sqrt{s} = 13$ TeV". In: *Phys. Lett. B* 806 (2020), p. 135502. DOI: 10.1016/j.physletb.2020.135502. arXiv: 2004.05153 [hep-ex].

[242] A. M. Sirunyan et al. "Search for high mass dijet resonances with a new background prediction method in proton-proton collisions at $\sqrt{s} = 13$ TeV". In: *JHEP* 05 (2020), p. 033. DOI: 10.1007/JHEP05(2020)033. arXiv: 1911.03947 [hep-ex].

[243] A. Tumasyan et al. "Search for narrow resonances in the b-tagged dijet mass spectrum in proton-proton collisions at s=13 TeV". In: *Phys. Rev. D* 108.1 (2023), p. 012009. DOI: 10.1103/PhysRevD.108.012009. arXiv: 2205.01835 [hep-ex].

[244] *Search for heavy stable charged particles with* 12.9 $\text{fb}^{-1}$ *of 2016 data*. Tech. rep. CMS-PAS-EXO-16-036. Geneva: CERN, 2016. URL: https://cds.cern.ch/record/2205281.

[245] *Search for supersymmetry in events with at least one soft lepton, low jet multiplicity, and missing transverse momentum in proton-proton collisions at* $\sqrt{s} = 13$ TeV. Tech. rep. CMS-PAS-SUS-16-052. Geneva: CERN, 2017. URL: https://cds.cern.ch/record/2273394.

[246] V. Khachatryan et al. "Search for supersymmetry in the all-hadronic final state using top quark tagging in pp collisions at $\sqrt{s} = 13$ TeV". In: *Phys. Rev.* D96.1 (2017), p. 012004. DOI: 10.1103/PhysRevD.96.012004. arXiv: 1701.01954 [hep-ex].

[247] A. M. Sirunyan et al. "Search for the pair production of third-generation squarks with two-body decays to a bottom or charm quark and a neutralino in proton–proton collisions at $\sqrt{s}$ = 13 TeV". In: *Phys. Lett.* B778 (2018), pp. 263–291. DOI: 10.1016/j.physletb.2018.01.012. arXiv: 1707.07274 [hep-ex].

[248] A. M. Sirunyan et al. "Search for new phenomena in final states with two opposite-charge, same-flavor leptons, jets, and missing transverse momentum in pp collisions at $\sqrt{s} = 13$ TeV". In: *JHEP* 03 (2018), p. 076. DOI: 10.1007/s13130-018-7845-2,10.1007/JHEP03(2018)076. arXiv: 1709.08908 [hep-ex].

[249] A. M. Sirunyan et al. "Search for physics beyond the standard model in events with two leptons of same sign, missing transverse momentum, and jets in proton–proton collisions at $\sqrt{s} = 13$ TeV". In: *Eur. Phys. J.* C77.9 (2017), p. 578. DOI: 10.1140/epjc/s10052-017-5079-z. arXiv: 1704.07323 [hep-ex].

[250] A. M. Sirunyan et al. "Search for Supersymmetry in $pp$ Collisions at $\sqrt{s} = 13$ TeV in the Single-Lepton Final State Using the Sum of Masses of Large-Radius Jets". In: *Phys. Rev. Lett.* 119.15 (2017), p. 151802. DOI: 10.1103/PhysRevLett.119.151802. arXiv: 1705.04673 [hep-ex].

[251] A. M. Sirunyan et al. "Search for electroweak production of charginos and neutralinos in multilepton final states in proton-proton collisions at $\sqrt{s} = 13$ TeV". In: *JHEP* 03 (2018), p. 166. DOI: 10.1007/JHEP03(2018)166. arXiv: 1709.05406 [hep-ex].

[252] A. M. Sirunyan et al. "Search for supersymmetry in events with at least three electrons or muons, jets, and missing transverse momentum in proton-proton collisions at $\sqrt{s} = 13$ TeV". In: *JHEP* 02 (2018), p. 067. DOI: 10.1007/JHEP02(2018)067. arXiv: 1710.09154 [hep-ex].

[253] A. M. Sirunyan et al. "Search for supersymmetry in events with one lepton and multiple jets exploiting the angular correlation between the lepton and the missing transverse momentum in proton-proton collisions at $\sqrt{s} = 13$ TeV". In: *Phys. Lett.* B780 (2018), pp. 384–409. DOI: 10.1016/j.physletb.2018.03.028. arXiv: 1709.09814 [hep-ex].

[254] A. M. Sirunyan et al. "Search for electroweak production of charginos and neutralinos in WH events in proton-proton collisions at $\sqrt{s} = 13$ TeV". In: *JHEP* 11 (2017), p. 029. DOI: 10.1007/JHEP11(2017)029. arXiv: 1706.09933 [hep-ex].

[255] A. M. Sirunyan et al. "Search for supersymmetry with Higgs boson to diphoton decays using the razor variables at $\sqrt{s} = 13$ TeV". In: *Phys. Lett.* B779 (2018), pp. 166–190. DOI: 10.1016/j.physletb.2017.12.069. arXiv: 1709.00384 [hep-ex].

[256] A. M. Sirunyan et al. "Search for gauge-mediated supersymmetry in events with at least one photon and missing transverse momentum in pp collisions at $\sqrt{s} = 13$ TeV". In: *Phys. Lett.* B780 (2018), pp. 118–143. DOI: 10.1016/j.physletb.2018.02.045. arXiv: 1711.08008 [hep-ex].

[257] A. M. Sirunyan et al. "Search for supersymmetry in events with at least one photon, missing transverse momentum, and large transverse event activity in proton-proton collisions at $\sqrt{s} = 13$ TeV". In: *JHEP* 12 (2017), p. 142. DOI: 10.1007/JHEP12(2017)142. arXiv: 1707.06193 [hep-ex].

[258] A. M. Sirunyan et al. "Search for new physics in events with two soft oppositely charged leptons and missing transverse momentum in proton-proton collisions at $\sqrt{s} = 13$ TeV". In: *Phys. Lett. B* 782 (2018), pp. 440–467. DOI: 10.1016/j.physletb.2018.05.062. arXiv: 1801.01846 [hep-ex].

[259] A. M. Sirunyan et al. "Search for supersymmetry in events with a $\tau$ lepton pair and missing transverse momentum in proton-proton collisions at $\sqrt{s} = 13$ TeV". In: *JHEP* 11 (2018), p. 151. DOI: 10.1007/JHEP11(2018)151. arXiv: 1807.02048 [hep-ex].

[260] A. M. Sirunyan et al. "Combined search for electroweak production of charginos and neutralinos in proton-proton collisions at $\sqrt{s} = 13$ TeV". In: *JHEP* 03 (2018), p. 160. DOI: 10.1007/JHEP03(2018)160. arXiv: 1801.03957 [hep-ex].

[261] A. M. Sirunyan et al. "Search for top squarks decaying via four-body or chargino-mediated modes in single-lepton final states in proton-proton collisions at $\sqrt{s} = 13$ TeV". In: *JHEP* 09 (2018), p. 065. DOI: 10.1007/JHEP09(2018)065. arXiv: 1805.05784 [hep-ex].

[262] A. M. Sirunyan et al. "Search for Physics Beyond the Standard Model in Events with High-Momentum Higgs Bosons and Missing Transverse Momentum in Proton-Proton Collisions at 13 TeV". In: *Phys. Rev. Lett.* 120.24 (2018), p. 241801. DOI: 10.1103/PhysRevLett.120.241801. arXiv: 1712.08501 [hep-ex].

[263] A. M. Sirunyan et al. "Searches for pair production of charginos and top squarks in final states with two oppositely charged leptons in proton-proton collisions at $\sqrt{s} = 13$ TeV". In: *JHEP* 11 (2018), p. 079. DOI: 10.1007/JHEP11(2018)079. arXiv: 1807.07799 [hep-ex].

[264] A. M. Sirunyan et al. "Search for supersymmetry in events with a photon, jets, b -jets, and missing transverse momentum in proton–proton collisions at 13 TeV". In: *Eur. Phys. J.* C79.5 (2019), p. 444. DOI: 10.1140/epjc/s10052-019-6926-x. arXiv: 1901.06726 [hep-ex].

[265] A. M. Sirunyan et al. "Search for supersymmetry using Higgs boson to diphoton decays at $\sqrt{s}$ = 13 TeV". In: *JHEP* 11 (2019), p. 109. DOI: 10.1007/JHEP11(2019)109. arXiv: 1908.08500 [hep-ex].

[266] A. M. Sirunyan et al. "Search for physics beyond the standard model in events with jets and two same-sign or at least three charged leptons in proton-proton collisions at $\sqrt{s}$ = 13 TeV". In: *Eur. Phys. J. C* 80.8 (2020), p. 752. DOI: 10.1140/epjc/s10052-020-8168-3. arXiv: 2001.10086 [hep-ex].

[267] A. M. Sirunyan et al. "Search for direct top squark pair production in events with one lepton, jets, and missing transverse momentum at 13 TeV with the CMS experiment". In: *JHEP* 05 (2020), p. 032. DOI: 10.1007/JHEP05(2020)032. arXiv: 1912.08887 [hep-ex].

[268] A. M. Sirunyan et al. "Search for top squark production in fully-hadronic final states in proton-proton collisions at $\sqrt{s}$ = 13 TeV". In: *Phys. Rev. D* 104.5 (2021), p. 052001. DOI: 10.1103/PhysRevD.104.052001. arXiv: 2103.01290 [hep-ex].

[269] A. M. Sirunyan et al. "Search for top squark pair production using dilepton final states in pp collision data collected at $\sqrt{s}$ = 13 TeV". In: *Eur. Phys. J. C* 81.1 (2021), p. 3. DOI: 10.1140/epjc/s10052-020-08701-5. arXiv: 2008.05936 [hep-ex].

[270] A. M. Sirunyan et al. "Search for supersymmetry in proton-proton collisions at $\sqrt{s}$ = 13 TeV in events with high-momentum Z bosons and missing transverse momentum". In: *JHEP* 09 (2020), p. 149. DOI: 10.1007/JHEP09(2020)149. arXiv: 2008.04422 [hep-ex].

[271] A. M. Sirunyan et al. "Search for supersymmetry in final states with two oppositely charged same-flavor leptons and missing transverse momentum in proton-proton collisions at $\sqrt{s}$ = 13 TeV". In: *JHEP* 04 (2021), p. 123. DOI: 10.1007/JHEP04(2021)123. arXiv: 2012.08600 [hep-ex].

[272] A. Tumasyan et al. "Combined searches for the production of supersymmetric top quark partners in proton–proton collisions at $\sqrt{s}$ = 13 TeV". In: *Eur. Phys. J. C* 81.11 (2021), p. 970. DOI: 10.1140/epjc/s10052-021-09721-5. arXiv: 2107.10892 [hep-ex].

[273] A. Tumasyan et al. "Search for electroweak production of charginos and neutralinos at $\sqrt{s}$ =13 TeV in final states containing hadronic decays of WW, WZ, or WH and missing transverse momentum". In: *Phys. Lett. B* 842 (2023), p. 137460. DOI: 10.1016/j.physletb.2022.137460. arXiv: 2205.09597 [hep-ex].

[274] A. Tumasyan et al. "Search for supersymmetry in final states with a single electron or muon using angular correlations and heavy-object identification in proton-proton collisions at $\sqrt{s}$ = 13 TeV". In: *JHEP* 09 (2023), p. 149. DOI: 10.1007/JHEP09(2023)149. arXiv: 2211.08476 [hep-ex].

[275] G. Aad et al. "Search for new phenomena in the dijet mass distribution using $p - p$ collision data at $\sqrt{s}$ = 8 TeV with the ATLAS detector". In: *Phys. Rev. D* 91.5 (2015), p. 052007. DOI: 10.1103/PhysRevD.91.052007. arXiv: 1407.1376 [hep-ex].

[276] G. Aad et al. "Search for new phenomena in final states with large jet multiplicities and missing transverse momentum at $\sqrt{s}$=8 TeV proton-proton collisions using the ATLAS experiment". In: *JHEP* 10 (2013). [Erratum: JHEP01,109(2014)], p. 130. DOI: 10.1007/JHEP10(2013)130, 10.1007/JHEP01(2014)109. arXiv: 1308.1841 [hep-ex].

[277] G. Aad et al. "Search for direct third-generation squark pair production in final states with missing transverse momentum and two $b$-jets in $\sqrt{s}$ = 8 TeV $pp$ collisions with the ATLAS detector". In: *JHEP* 10 (2013), p. 189. DOI: 10.1007/JHEP10(2013)189. arXiv: 1308.2631 [hep-ex].

[278] G. Aad et al. "Search for direct top squark pair production in events with a Z boson, b-jets and missing transverse momentum in sqrt(s)=8 TeV pp collisions with the ATLAS detector". In: *Eur. Phys. J.* C74.6 (2014), p. 2883. DOI: 10.1140/epjc/s10052-014-2883-6. arXiv: 1403.5222 [hep-ex].

[279] G. Aad et al. "Search for supersymmetry at $\sqrt{s}$=8 TeV in final states with jets and two same-sign leptons or three leptons with the ATLAS detector". In: *JHEP* 06 (2014), p. 035. DOI: 10.1007/JHEP06(2014)035. arXiv: 1404.2500 [hep-ex].

[280] G. Aad et al. "Search for direct production of charginos, neutralinos and sleptons in final states with two leptons and missing transverse momentum in $pp$ collisions at $\sqrt{s} = 8$ TeV with the ATLAS detector". In: *JHEP* 05 (2014), p. 071. DOI: 10.1007/JHEP05(2014)071. arXiv: 1403.5294 [hep-ex].

[281] G. Aad et al. "Search for direct production of charginos and neutralinos in events with three leptons and missing transverse momentum in $\sqrt{s} = 8$ TeV $pp$ collisions with the ATLAS detector". In: *JHEP* 04 (2014), p. 169. DOI: 10.1007/JHEP04(2014)169. arXiv: 1402.7029 [hep-ex].

[282] G. Aad et al. "Search for top squark pair production in final states with one isolated lepton, jets, and missing transverse momentum in $\sqrt{s}$ =8 TeV $pp$ collisions with the ATLAS detector". In: *JHEP* 11 (2014), p. 118. DOI: 10.1007/JHEP11(2014)118. arXiv: 1407.0583 [hep-ex].

[283] G. Aad et al. "Search for direct pair production of the top squark in all-hadronic final states in proton-proton collisions at $\sqrt{s} = 8$ TeV with the ATLAS detector". In: *JHEP* 09 (2014), p. 015. DOI: 10.1007/JHEP09(2014)015. arXiv: 1406.1122 [hep-ex].

[284] G. Aad et al. "Search for strong production of supersymmetric particles in final states with missing transverse momentum and at least three $b$-jets at $\sqrt{s}$= 8 TeV proton-proton collisions with the ATLAS detector". In: *JHEP* 10 (2014), p. 024. DOI: 10.1007/JHEP10(2014)024. arXiv: 1407.0600 [hep-ex].

[285] G. Aad et al. "Search for direct top-squark pair production in final states with two leptons in pp collisions at $\sqrt{s} = 8$ TeV with the ATLAS detector". In: *JHEP* 06 (2014), p. 124. DOI: 10.1007/JHEP06(2014)124. arXiv: 1403.4853 [hep-ex].

[286] G. Aad et al. "Search for squarks and gluinos in events with isolated leptons, jets and missing transverse momentum at $\sqrt{s} = 8$ TeV with the ATLAS detector". In: *JHEP* 04 (2015), p. 116. DOI: 10.1007/JHEP04(2015)116. arXiv: 1501.03555 [hep-ex].

[287] G. Aad et al. "Search for pair-produced third-generation squarks decaying via charm quarks or in compressed supersymmetric scenarios in $pp$ collisions at $\sqrt{s} = 8$ TeV with the ATLAS detector". In: *Phys. Rev.* D90.5 (2014), p. 052008. DOI: 10.1103/PhysRevD.90.052008. arXiv: 1407.0608 [hep-ex].

[288] G. Aad et al. "Search for direct pair production of a chargino and a neutralino decaying to the 125 GeV Higgs boson in $\sqrt{s} = 8$ TeV $pp$ collisions with the ATLAS detector". In: *Eur. Phys. J.* C75.5 (2015), p. 208. DOI: 10.1140/epjc/s10052-015-3408-7. arXiv: 1501.07110 [hep-ex].

[289] G. Aad et al. "Search for Scalar Charm Quark Pair Production in $pp$ Collisions at $\sqrt{s} = 8$ TeV with the ATLAS Detector". In: *Phys. Rev. Lett.* 114.16 (2015), p. 161801. DOI: 10.1103/PhysRevLett.114.161801. arXiv: 1501.01325 [hep-ex].

[290] S. Chatrchyan et al. "Searches for Long-Lived Charged Particles in $pp$ Collisions at $\sqrt{s}$=7 and 8 TeV". In: *JHEP* 07 (2013), p. 122. DOI: 10.1007/JHEP07(2013)122. arXiv: 1305.0491 [hep-ex].

[291] V Khachatryan et al. "Search for resonances and quantum black holes using dijet mass spectra in proton-proton collisions at $\sqrt{s} = 8$ TeV". In: *Phys. Rev. D*

91.5 (2015), p. 052009. DOI: 10.1103/PhysRevD.91.052009. arXiv: 1501.04198 [hep-ex].

[292] V. Khachatryan et al. "Constraints on the pMSSM, AMSB model and on other models from the search for long-lived charged particles in proton-proton collisions at sqrt(s) = 8 TeV". In: *Eur. Phys. J.* C75.7 (2015), p. 325. DOI: 10.1140/epjc/s10052-015-3533-3. arXiv: 1502.02522 [hep-ex].

[293] A. M. Sirunyan et al. "Search for narrow resonances in the b-tagged dijet mass spectrum in proton-proton collisions at $\sqrt{s} = 8$ TeV". In: *Phys. Rev. Lett.* 120.20 (2018), p. 201801. DOI: 10.1103/PhysRevLett.120.201801. arXiv: 1802.06149 [hep-ex].

[294] *Search for top squarks in multijet events with large missing momentum in proton-proton collisions at 8 TeV*. Tech. rep. CMS-PAS-SUS-13-015. Geneva: CERN, 2013. URL: http://cds.cern.ch/record/1635353.

[295] *Search for supersymmetry in pp collisions at sqrt(s) = 8 TeV in events with two opposite sign leptons, large number of jets, b-tagged jets, and large missing transverse energy*. Tech. rep. CMS-PAS-SUS-13-016. Geneva: CERN, 2013. URL: http://cds.cern.ch/record/1623818.

[296] *Search for direct production of bottom squark pairs*. Tech. rep. CMS-PAS-SUS-13-018. Geneva: CERN, 2014. URL: https://cds.cern.ch/record/1693164.

[297] *A Search for Scalar Top Quark Production and Decay to All Hadronic Final States in pp Collisions at sqrt(s) = 8 TeV*. Tech. rep. CMS-PAS-SUS-13-023. Geneva: CERN, 2015. URL: http://cds.cern.ch/record/2044441.

[298] S. Chatrchyan et al. "Search for Gluino Mediated Bottom- and Top-Squark Production in Multijet Final States in $pp$ Collisions at 8 TeV". In: *Phys. Lett.* B725 (2013), pp. 243–270. DOI: 10.1016/j.physletb.2013.06.058. arXiv: 1305.2390 [hep-ex].

[299] S. Chatrchyan et al. "Search for Supersymmetry in Hadronic Final States with Missing Transverse Energy Using the Variables $\alpha_T$ and b-Quark Multiplicity in $pp$ collisions at $\sqrt{s} = 8$ TeV". In: *Eur. Phys. J.* C73.9 (2013), p. 2568. DOI: 10.1140/epjc/s10052-013-2568-6. arXiv: 1303.2985 [hep-ex].

[300] S. Chatrchyan et al. "Search for anomalous production of events with three or more leptons in $pp$ collisions at $\sqrt{(s)} = 8$ TeV". In: *Phys. Rev.* D90 (2014), p. 032006. DOI: 10.1103/PhysRevD.90.032006. arXiv: 1404.5801 [hep-ex].

[301] V. Khachatryan et al. "Search for Supersymmetry Using Razor Variables in Events with $b$-Tagged Jets in $pp$ Collisions at $\sqrt{s} = 8$ TeV". In: *Phys. Rev.* D91 (2015), p. 052018. DOI: 10.1103/PhysRevD.91.052018. arXiv: 1502.00300 [hep-ex].

[302] V. Khachatryan et al. "Searches for electroweak production of charginos, neutralinos, and sleptons decaying to leptons and W, Z, and Higgs bosons in pp collisions at 8 TeV". In: *Eur. Phys. J.* C74.9 (2014), p. 3036. DOI: 10.1140/epjc/s10052-014-3036-7. arXiv: 1405.7570 [hep-ex].

[303] S. Chatrchyan et al. "Search for Supersymmetry in pp Collisions at $\sqrt{s}$=8 TeV in Events with a Single Lepton, Large Jet Multiplicity, and Multiple b Jets". In: *Phys. Lett.* B733 (2014), pp. 328–353. DOI: 10.1016/j.physletb.2014.04.023. arXiv: 1311.4937 [hep-ex].

[304] S. Chatrchyan et al. "Search for Top-Squark Pair Production in the Single-Lepton Final State in pp Collisions at $\sqrt{s}$ = 8 TeV". In: *Eur. Phys. J.* C73.12 (2013), p. 2677. DOI: 10.1140/epjc/s10052-013-2677-2. arXiv: 1308.1586 [hep-ex].

[305] S. Chatrchyan et al. "Search for New Physics in Events with Same-Sign Dileptons and Jets in pp Collisions at $\sqrt{s}$ = 8 TeV". In: *JHEP* 01 (2014). [Erratum:

JHEP01,014(2015)], p. 163. DOI: 10.1007/JHEP01(2015)014,10.1007/JHEP01(2014)163. arXiv: 1311.6736.

[306] V. Khachatryan et al. "Searches for Supersymmetry using the $M_{T2}$ Variable in Hadronic Events Produced in pp Collisions at 8 TeV". In: *JHEP* 05 (2015), p. 078. DOI: 10.1007/JHEP05(2015)078. arXiv: 1502.04358 [hep-ex].

[307] V. Khachatryan et al. "Searches for supersymmetry based on events with b jets and four W bosons in pp collisions at 8 TeV". In: *Phys. Lett.* B745 (2015), pp. 5–28. DOI: 10.1016/j.physletb.2015.04.002. arXiv: 1412.4109 [hep-ex].

[308] V. Khachatryan et al. "Search for supersymmetry in events with soft leptons, low jet multiplicity, and missing transverse energy in proton–proton collisions at $\sqrt{s}$=8 TeV". In: *Phys. Lett.* B759 (2016), pp. 9–35. DOI: 10.1016/j.physletb.2016.05.033. arXiv: 1512.08002 [hep-ex].

# List of Figures


2.1 The Higgs potential described in Eq. (2.4) in the case that $\mu^2 < 0$ [54] . . 9
2.2 Distribution of the star velocities in the galaxy NGC 3198 with respect to the distance from the centre of the same galaxy [63]. . . . . 12
2.3 Fraction of pMSSM electroweakino model points excluded by ATLAS across the masses of each electroweakino particle. Figure adapted from [71]. . . . . 15
2.4 95% CL lower limits on the fundamental Planck scale in $4 + n$ dimensions, $M_D$, as a function of the number of extra dimensions. Figure adapted from [74]. . . . . 17
2.5 95% CL upper limits on the production cross section for the vector-like leptons coupled to third-generation SM leptons in the doublet model (left) and singlet model (right). Figures adapted from [105]. . . . . 19
2.6 95% CL upper limits on pair production cross sections for scalar leptoquarks ($LQ_S$) as a function of the mass of the LQ. The solid blue curve indicates the theoretical predictions for pair-produced $LQ_S$. Figure adapted from [116]. . . . . 20
2.7 The CERN accelerator complex [120]. . . . . 21
2.8 Particle interactions in a transverse slice of the ATLAS detector [126] from the beam interaction region to the muon detector. . . . . 23
2.9 Particle interactions in a transverse slice of the CMS detector [127] from the beam interaction region to the muon detector. . . . . 24
2.10 SR event selection criteria and Monte Carlo (MC) generator-weighted yields defined for a BSM model point in ATLAS-SUSY-2018-06 [128]. . . 26

3.1 Illustration of the $CL_s$ method. . . . . 30
3.2 Illustration of Bayes' Theorem. The posterior density $P(\theta)$ of model parameters $\theta$ results from combining the prior distribution $\pi(\theta)$ (blue) with the likelihood $L(\theta) = P(X|\theta)$ (red), normalised by the overall evidence $Z = \pi(\theta)L(\theta)d\theta$ (purple) for the particular model. Figure adapted from [132]. . . . . 32

4.1 An example of a CMS search for electroweak production of charginos and neutralinos using simplified models [143]. The simplified model topology depicting chargino-neutralino pair production and their subsequent decays is shown in the top plot. Here, the chargino always decays to a $W$ boson and the lightest neutralino $\tilde{\chi}_1^0$ while the heavier neutralino decays 100% of the time to either a $Z$ or Higgs boson along with the $\tilde{\chi}_1^0$. . . . . 40
4.2 The 95% CL exclusion contour from CMS-SUS-21-002 [143] for the simplified model topology depicted in Figure 4.1. . . . . 41
4.3 Schematic representation of the working principle of SModelS. . . . . 42

4.4 The representation of a simplified model topology as a graph in SModelS v3 along with its elements: root node, SM and BSM nodes, and edges representing the decays. . . . . 43
4.5 The structure of the SModelS database. Database entries are categorised according to the center-of-mass energy (currently, 8 or 13 TeV) and the experiment (ATLAS or CMS) of their analyses. They are further categorised based on the type of results they contain (UL- or EM-type results). . . . . 45
4.6 SModelS reproducing the expected (top) and observed (bottom) experimental limits using the most sensitive SR, the full statistical model and the simplified one. The plots on the left shows the simplified likelihood working well for ATLAS-SUSY-2019-09 [158] and plots on the right shows the failure of the simplified likelihood computation for ATLAS-SUSY-2018-16 [156]. . . . . 51
4.7 Distributions of $M_1$, $M_2$ and $\mu$ in the set of EW-ino scan points used in this study; on the left for points with a bino-like LSP, on the right for points with a non-bino-like LSP. Only values up to 2 TeV are shown. . . 54
4.8 Non-bino-like LSP points, on the left in the $\mu$ vs. $M_2$ plane and on the right in the $M_2/M_1$ vs. $M_2/\mu$ plane. The colour code shows higgsino content of the LSP. In the left plot, the $x$- and $y$-axes go only up to 1.2 TeV for better visibility of the mixed region, but in both directions scan points extend up to 3 TeV. . . . . 55
4.9 Matrix displaying the combinability of the searches considered in this study. Green means the two analyses are assumed to be approximately uncorrelated and can be combined, while red means that they are not and shouldn't be combined. . . . . 56
4.10 Number of points expected to be excluded (top) and number of points actually excluded (bottom) as determined by the most sensitive analysis (pink area) and the best combination of analyses (purple line). In addition, the left panel shows the impact of the two hadronic searches: CMS-SUS-21-002 (light blue) and ATLAS-SUSY-2018-41 (light red), along with the $3\ell + \not{E}_T$ search ATLAS-SUSY-2019-09 (orange). On the other hand, the right panel also displays the observed exclusion with respect to the most constraining analysis (grey). . . . . 58
4.11 Most sensitive combinations in the $m_{\tilde{\chi}_1^0}$ vs. $m_{\tilde{\chi}_1^\pm}$ plane for points excluded by the combination and featuring a bino-like LSP. Only the combinations appearing at least 25 times are shown. The combinations that appeared less than 25 times fall into the "Others" category. . . . . 59
4.12 Most sensitive combinations in the $m_{\tilde{\chi}_1^0}$ vs. $m_{\tilde{\chi}_2^\pm}$ plane for points excluded by the combination and featuring a non-bino-like LSP. Only the combinations appearing at least 2 times are shown. The other combinations that appeared 2 times or less fall into the "Others" category. . . . . 60

5.1 A strategy of how we may envisage to construct a Next Standard Model (NSM) Lagrangian from LHC data: the outcomes of specific searches, which are interpreted through simplified models, can be used to construct proto-models. . . . . 64
5.2 Simplified flowchart of the Walker algorithm v1. . . . . 69

5.3 Left: an illustration of the signal likelihood as a function of the signal strength ($\mu$) for two results (A and B) and the corresponding combined likelihood. The value of $\hat{\mu}$ given by the maximum of the combined likelihood (green curve) is also shown as well as the upper limit on $\mu$ ($\mu_{max}$) given by Result B alone. Right: a similar example, but where it is not possible to combine both likelihoods, or the likelihood for Result B is not available. In this case, the likelihood for Result A is truncated at $\mu_{max}$ (obtained from Result B). All the curves are normalised to the corresponding SM likelihood value ($\mu = 0$). . . . . 72
5.4 Binary combination matrices used in v1, that describes which analyses are considered to be approximately uncorrelated (green bins) and which are not (red bins). Analyses from different LHC runs or different experiments are always taken as uncorrelated. White bins denote analyses, for which no likelihood can be computed (observed UL only). 73
5.5 The density of the test statistic $K$ under the SM-only hypothesis obtained using a Kernel Density Estimator (KDE). The red points denote the $K$ values generated by the runs over 50 fake databases. . . . . 77
5.6 The particle content and mass spectrum for the proto-models having the highest test statistic $K$ obtained from each of the 10 runs over real SModelS database. The top block displays the corresponding $K$ for each proto-model and the highest $K$ is highlighted in bold text for walker 9. . . . . 78
5.7 Values of the test statistic $K$ obtained for the walks discussed in the text. The green stars represent the $K$ values for the highest scoring proto-models from 10 runs over the real database, while the red open circles show the values obtained under the "BSM hypothesis" (see Section 5.3 in [7]). The solid orange curve shows the distribution obtained under the SM-only hypothesis. The shaded green area corresponds to the global $p$-value for average $K$ from the runs over the real database. . . . . 80

6.1 Exclusion regions in the ($m_{\tilde{\chi}_2^0}$, $\Delta m$) plane presented in the study [195] through the reinterpretation of the results of several LHC analyses. . . . 85
6.2 Distribution of the per-SR significances under the SM hypothesis, for all the validated analyses with EM-type results in the SModelS database v3.1.0 (top), and for the electroweakino (EWino) and monojet searches only (bottom). A standard normal distribution is expected if no new physics is in the data (shown in black dotted line). New physics would manifest itself as an overabundance of large (positive) significances. . . 87
6.3 Individual SR significances under the SM hypothesis for the 10 highest (blue) and 10 lowest (red) significance values. The top plot selects the highest and/or lowest SR significances per analysis across all validated analyses with EM-type results, while the bottom panel is restricted to electroweak-ino (EWino) and monojet searches. Analyses appearing in both figures are highlighted in brown. . . . . 89

6.4 Comparison of SModelS exclusions to official ATLAS limits for ATLAS-SUSY-2018-16 [190]. In the left panel, a wino-bino scenario is considered, while in the right panel, a higgsino-LSP scenario is considered, where. In both cases, the heavier electroweakino ($\tilde{\chi}_1^{\pm}, \tilde{\chi}_2^0$,) decay into off-shell $W/Z$ bosons along with the LSP ($\tilde{\chi}_1^0$). The official ATLAS limits can be correctly reproduced in the wino-bino scenario as EMs are provided for the exclusive SRs along with the full statistical model. However, SModelS cannot correctly reproduce the ATLAS limits in the higgsino-LSP scenario because only EMs for inclusive SRs are provided for this case, without the capability to combine them. . . . . 90
6.5 Simplified flowchart of the Walker algorithm v2. . . . . 93
6.6 Probability to add or remove a particle with two decay modes and two production modes given the current number of particles in the proto-model. . . . . 97
6.7 The updated binary combination matrices used in v2 for the ATLAS 13 TeV results, that describes which analyses are considered to be approximately uncorrelated (green bins) and which are not (red bins). Analyses from different LHC runs or different experiments are always taken as uncorrelated. . . . . 101
6.8 The updated binary combination matrices used in v2 for the CMS 13 TeV results, that describes which analyses are considered to be approximately uncorrelated (green bins) and which are not (red bins). Analyses from different LHC runs or different experiments are always taken as uncorrelated. . . . . 102
6.9 Distribution of $r_{\text{obs}}/r_{\text{exp}} \equiv \mu_{\text{exp}}^{UL}/\mu_{\text{obs}}^{UL}$ from 100 fake EM-type databases sampled from the SM distribution. The red dotted line indicates the maximum allowed $r_{\text{obs}}$ value for a given proto-model, $r_{\text{max}} \sim 1.33$, which is calculated as 1 $\sigma$ deviation from the mean. . . . . 104
6.10 Evolution of $K$ (blue) and $TL$ (red) for individual walks across two fake SM databases. On average, proto-models generated across walks on different fake SM databases have $K \lesssim 0$ and $TL \lesssim 2.5$. However, occasional deviations from this baseline behaviour are observed. . . . . 110
6.11 An extreme case of $K$ and $TL$ evolution from a single walk on a fake SM database. $K$ and $TL$ converge to approximately 13 and 15, respectively. This run produced the highest scoring proto-model across all 15 fake SM databases. . . . . 111
6.12 The distribution of $K$ under the SM-only hypothesis, estimated using a Kernel Density Estimator. The red points denote the highest $K$ values ($K_{fake}$) of proto-models generated across 50 parallel runs on 15 fake SM databases. The blue marks on the x-axis represent the $K$ values ($K_{fake}$) of the best performing proto-models from each of the 50 walks across 15 fake SM databases. . . . . 111
6.13 Top ten proto-models with particle content and masses with the highest $K$ obtained across 50 walks on the real database. The corresponding $K$ values are shown in the top. . . . . 112
6.14 The experimental results that enter the most significant combination for the top ten best performing proto-models across 50 walks. The corresponding $K$ values are shown in the top. . . . . 113

6.15 $K$ values obtained from walks on the SModelS database (green points) overlaid on the density obtained from the fake SM runs (orange curve). The blue marks on the x-axis represent the $K$ values ($K_{fake}$) of the best performing proto-models from each of the 50 walks across 15 fake SM databases. The red points represent the $K$ values of the "absolute" best performing proto-model ($K^{max}_{fake}$) from each of the 15 fake SM databases. The shaded region corresponds to the global $p$-value for the average $K$ values (light blue star) from the walks on the real database. . . . . 114
6.16 The "absolute" best-performing proto-model across all 50 walks. Left: particle content with masses and decay modes. Right: Likelihood ratio $L_{\mathbf{M}}(\mu)/L_{\mathbf{SM}}(\mu = 0)$ as a function of the signal strength $\mu$ for individual analyses (dotted lines) and their combination (solid line). . . . . 115
6.17 Evolution of $K$ and $TL$ for walker number 3 on the real SModelS database. The highest $K$ value obtained and the corresponding $TL$ value are marked in the plot. . . . . 116
6.18 An evolution of the integrated probabilities of the different proto-model particle spectra as a function of the step for Walker ID 3. The integrated probability indicates the cumulative frequency with which each particle spectrum has been accepted up to the current step. . . . . 117
6.19 The distribution of the BSM particle content of the proto-models generated after the initial 3500 steps ("burn-in" period) for walker number 3. Proto-models having only $X^1_Z$ and $X^2_Z$ are the ones that are most favoured while proto-models with a high number of particles are discouraged. . . . . 118
6.20 Mass distributions for the particles $X^1_Z$, $X^2_Z$ and $X^1_W$ in proto-models containing all three particles for walker number 3. The blue open circle marks the region where the best performing proto-model lies. The colour of the points reflect the $K$ values, with darker points having higher $K$ values. The first 3500 steps are considered as a "burn-in" phase and are removed. . . . . 119
6.21 Particle spectrum and masses for the top ten best performing proto-models across 20 walks on one fake database generated under the "BSM hypothesis". The corresponding $K$ values are shown at the top. The particle spectrum of the proto-model used for the injected signal is shown on the left, and is labelled "Truth". . . . . 121
6.22 The best performing proto-model obtained by repeatedly walking near the high $K$ regions. Note that the mass axis has a discontinuity at 180 GeV to accommodate $X^3_Z$ at higher mass in the same plot. . . . . 122
6.23 The 1D and 2D marginalised posterior distributions for the particle masses in the proto-model. The top panels represent the 1D marginalized posterior mass distributions for each particle, with central values indicating the mean point estimates and the $\pm$ indicating the $1\sigma$ band. The off-diagonal panels show the $1\sigma$ and $2\sigma$ credible regions that correspond to the highest posterior density regions for each 2D marginalized posterior distribution. The scatter points outside these regions are raw samples that lie in low probability regions. The black marker indicates the best-fit point, or the proto-model with the highest $K/TL$ and the gray dotted lines indicate the corresponding masses. . . . . 124

# List of Tables

2.1 Field content of the Standard Model and their gauge quantum numbers. There are three generations (families) of quarks and leptons, differing by their mass. . . . . 8
2.2 Particle content of the MSSM. The particles that are new compared to the SM are written in blue. The rows are organised in supermultiplets. For chiral supermultiplets, a symbol representing the whole supermultiplet is denoted in the "Names" column. Adapted from [70]. . . . . 14

5.1 The BSM particles and their decay channels considered for building proto-models in the paper [7]. . . . . 66
5.2 The effect on the proto-model test statistic $K$ by the choice of prior in Eq. (5.9) for different proto-model parameters. The last column displays the decrease in the test statistic: $\Delta K = 2 \ln \pi(\mathbf{M})$. . . . . 75
5.3 Analyses that contribute to the $K$ value of the highest scoring proto-model from Fig. 5.6. The **Dataset** column lists the contributing signal region (SR) where applicable. The **Obs** and **Exp** columns list the number of observed events or the observed upper limit and the expected background and its uncertainty or the expected upper limit, respectively. The column **Z** lists the significance of the excess, and the column **P** lists the proto-model particle introduced for fitting the observed data. The last column, **Signal** shows the predicted contribution of the proto-model, in number of events for EM results (ATLAS, ATL for short) and in fb for UL results (CMS). . . . . 79
5.4 List of the most constraining results for the highest scoring proto-model. The second column displays the constrained production mode, while the third column shows the respective cross section value. The corresponding observed and expected upper limits and the ratio $r_{\text{obs}} = \sigma_{XX}/\sigma^{\text{UL}}_{\text{obs}}$ are also presented. . . . . 79

6.1 The restricted BSM parameter space considered for building proto-models with Walker v2. Note that the newly added off-shell decay modes for $X^2_Z$ and $X^1_W$ are included alongside the on-shell decay modes. . . . . 108
6.2 The production modes for the absolute best performing proto-model. The signal strength multipliers and the corresponding cross sections at 8 and 13 TeV are displayed. . . . . 115

B.1 List of ATLAS Run 2 analyses and their types of results in the SModelS v3.1.0 database. Apart from the HSCP, disappearing tracks and displaced lepton searches, all analyses require $E_T^{\text{miss}}$ in the final state (for conciseness omitted in the short descriptions). EW stands for electroweak (-ino or slepton) production. The last column specifies whether and how SRs are combined: "PYHF " means a HistFactory model is used through interface with PYHF; "SLv1"("SLv2") means that a covariance matrix (with a third moment) is used; and a blank means only the most sensitive SR is used. . . . . 134
B.2 List of CMS Run 2 analyses and their types of results in the SModelS v3.1.0 database. Apart from the HSCP, disappearing tracks and displaced lepton searches, all analyses require $E_T^{\text{miss}}$ in the final state (for conciseness omitted in the short descriptions). EW stands for electroweak (-ino or slepton) production. The last column specifies whether and how SRs are combined: "SLv1"("SLv2") means that a covariance matrix (with a third moment) is used; and a blank means only the most sensitive SR is used . . . . . 135
B.3 List of 15 ATLAS and 18 CMS Run 1 analyses and their types of results in the SModelS v3.1.0 database. Apart from the HSCP searches, all analyses require $E_T^{\text{miss}}$ in the final state (for conciseness omitted in the short descriptions). EW stands for electroweak(-ino) production. The column Comb. from Tables B.1- B.2 is omitted because none of the Run 1 analyses provides any information on background correlations. . . . . 136